# Wetland Hydrologic Modeling through Physically-based and Data-driven Approaches

by

Mehdi Rezaeianzadeh

A dissertation submitted to the Graduate Faculty of
Auburn University
in partial fulfillment of the
requirements for the Degree of
Doctor of Philosophy

Auburn, Alabama
August 5, 2017

Keywords: Wetland hydrology, Water level prediction, Climate change and variability, Model development, Unsaturated flow, *WetQual*

Copyright 2017 by Mehdi Rezaeianzadeh

Approved by

Latif Kalin, Chair, Professor of School of Forestry and Wildlife Sciences
Mohamed M. Hantush, Senior Research Scientist, USEPA
Christopher J. Anderson, Associate Professor of School of Forestry and Wildlife Sciences
Puneet Srivastava, Professor of Biosystems Engineering

Abstract

Hydrology influences vegetation composition, species richness, primary productivity, accumulation of organic material, and nutrient availability and cycling in wetlands. Any alteration to wetland hydrology can change the biogeochemistry of wetlands and the dominant nutrient removal pathways. A better understanding of wetland hydrologic processes offers valuable insights into the study and modeling of wetland nutrient removal and cycling. This study, performed in four stages, was undertaken to advance the current knowledge of wetland hydrologic modeling by introducing various models.

In Chapter 2, two artificial neural network (ANN)-based models were developed and validated for predicting hourly water levels (WLs) in wetlands characterized by water tables at or near the surface that respond rapidly to precipitation. The first method makes use of hourly precipitation data and WL data from nearby sites. The second method is a combination of ANN, recursive digital filter, and recession curve method and does not require any nearby site. The proposed methods were tested at two headwater wetlands in coastal Alabama. Site 17 had two nearby sites whose WLs were highly correlated with Site 17's. The root-mean-square error and Nash–Sutcliffe efficiencies were 2.9 cm and 0.98, respectively, when the first method was applied to Site 17. The second method was tested at Site 32. A combination of ANN and base-flow separation methods proved to be very efficient for WL prediction at this site, especially when the duration of quick-response components of individual events was less than 6 h. The proposed methodologies, therefore, proved useful in predicting WLs in wetlands dominated by

both surface water and groundwater. This chapter has been published in *Journal of Hydrologic Engineering*.

In Chapter 3, we built on the previous stage of the study by eliminating the need for WL data from nearby wetlands as inputs to the model. A hybrid modeling approach was developed for improved WL predictions in wetlands, by coupling the watershed model SWAT with ANNs. To demonstrate the utility of this approach, the developed model was used to assess the potential impacts of climate change on WL fluctuations at the headwater wetland site 17. Model results forecast potential increase in medium ($20^{th}$-$80^{th}$ percentile) WLs and a decreasing trend for low ($0^{th}$-$20^{th}$ percentile) and high ($80^{th}$-$100^{th}$ percentile) WLs. Water levels predicted with this hybrid model were also used to explore possible teleconnections between El Niño Southern Oscillation (ENSO) and WLs in the study wetland. Results showed that both precipitation and the variations in WLs were partially affected by ENSO. The findings suggested wetter conditions in winter during El Nino in Coastal Alabama. However, WL reduction in spring during El Nino is expected. Hence, understanding the hydrologic processes in wetlands going through wetting and drying cycles and the biochemical and ecological implications of those cycles is a critical task. A manuscript written from this chapter is currently under review in *Hydrological Sciences*.

In wetlands going through wetting/drying cycles, simulation of nutrient processes and biogeochemical reactions in both ponded and unsaturated wetland zones are needed for an improved understanding of wetland functioning for water quality improvement. Sharifi et al. (2017) extended the ponded version of *WetQual* model (Hantush et al. 2013, Kalin et al. 2013, Sharifi et al. 2013) by adding a soil moisture accounting module and biogeochemical relationships for improved N and C cycles in variably saturated zones of wetlands. He used Richards' Equation (RE) to calculate soil moisture dynamics. This resulted in an unnecessarily

complex model because not only RE equation is notoriously complex and numerically difficult to deal with, but also *WetQual* only needs average moisture content (it is a lumped model). In Chapter 4, a depth-averaged solution to the RE (called DARE) for one-dimensional vertical unsaturated flow is presented to predict the temporal variation of the average moisture content of the root zone and the layer below it in unsaturated parts of wetlands. This will make Sharifi et al. (2017) version of *WetQual* more practical and computationally efficient. The DARE model was verified versus Hydrus-1D which utilizes the full RE, using field data from the Hupselse Beek watershed in the Netherlands. Gravity drainage version of DARE works well with a comparison to Hydrus-1D, under all the assigned atmospheric boundary conditions of varying fluxes for all examined soil types including sandy loam, loam, sandy clay loam, and sand. A full-term version of DARE offers reasonable accuracy dominantly in the root zone.

The focus of Chapter 5 was adding a flow routing module to ponded version of *WetQual* and creating a graphical user interface (GUI) that brings the hydrologic and water quality modeling under one umbrella. Earlier versions of *WetQual* required users take care of wetland hydrology independently. The developed GUI also provides opportunities for processing and visualization of input/outputs and helps the users identify any source of error in inputs or model simulations. In addition, the *WetQual* GUI was equipped with powerful post-processing and sensitivity analysis modules. The GUI performs Generalized Likelihood Uncertainty Estimation (GLUE) and Bayesian Monte Carlo simulation and Maximum Likelihood estimation (BMCML) analyses. The utility of the *WetQual* GUI was demonstrated through a case study in a small restored wetland called Barnstable wetland, located in Kent Island, Maryland. This GUI can be used as a learning tool for hydrology and water quality processes in wetlands.

Acknowledgments

I would like to acknowledge the support and advice I received from many people during my Ph.D., without which completing this doctoral dissertation would not have been conceivable. Firstly, I express my deep gratitude to my advisor, Dr. Latif Kalin, who sustained me scientifically with his moral guidance over this long and challenging endeavor. My committee member, Dr. Mohamed M. Hantush likewise made an invaluable contribution to this dissertation, and I would like to thank him for being such a great mentor. I learned a lot from Dr. Kalin and Dr. Hantush all of which will be pertinent for my future career. I am correspondingly very thankful to other members of my dissertation advisory committee, especially Dr. Christopher J. Anderson and Dr. Puneet Srivastava for their backing and helpful recommendations for improving this research. I would like to appreciate the time Dr. Luke J. Marzen, my university reader, took to review my dissertation.

Friends and colleagues were important to me during development of this dissertations with my special thanks going to Dr. Ammirreza Sharifi, Chunzhang Mo, Dr. Sabahattin Isik, Rajesh Sawant, Dr. Hamed Majidzadeh, Dr. Navideh Noori, Rasika Ramesh, Hossein Ahmadian, Dr. Fatemeh Baratian and Dr. Hooman Ghasemi.

I will forever be thankful to my other mentors and friends who have aided me from the commencement of my academic studies and positions. My thanks are also extended to Dr. E. Zia Hosseinipour, Dr. Amir AghaKouchak, Dr. Navid Jalalkamali, Hossein Tabari, Dr. Hirad

Abghari, Dr. Ali Asghari Tabrizi, Dr. Jonathan Peter Cox, Dr. Alfred Stein, and Dr. Vijay P. Singh.

Unconditional love and support from my parents have always been the greatest strengths I have been carrying throughout my whole life. I have learned honesty and responsibility in performing my works and owe the entire achievements of my life to them. I will never forget the love and support from my parents, two sisters and my brother.

Lastly but most importantly, I would like to thank my soul mate and wife, Maryam Shakeri, who was the most important supporter during my Ph.D. studies and who helped me in the most challenging parts of this difficult venture. At the time of writing this acknowledgment, we are getting close to our $10^{th}$ wedding anniversary. I appreciate her unconditional love and care, companionship and support over the past ten years.

*The research described in this dissertation has been partially funded by the U.S. Environmental Protection Agency (U.S. EPA) through its Office of Research and Development and the Center for Environmental Studies at the Urban-Rural Interface (CESURI) at Auburn University.*

Table of Contents

List of Tables

List of Figures

# Chapter 1 : Introduction

Wetlands are areas in the landscape that are fully or partially saturated at least part of the year. They are transitional between terrestrial and open-water aquatic ecosystems. Wetlands provide many important ecosystem services including water quality improvement through filtering, water storage and providing habitat to many animals and plants. Wetlands can function as a sink, source, or transformer for nutrients. They act as transformers through processes such as denitrification, methanogenesis, and the microbial breakdown of organic matter (Reddy and Delaune, 2008). Wetlands also contribute to flood mitigation and they recharge aquifers, allowing stored groundwater to sustain base flow in streams during dry periods (Hantush et al. 2013).

It is widely accepted that wetlands have a significant influence on the hydrologic cycle. Studies of chemical input-output relationships in wetlands are heavily dependent on hydrologic data (LaBaugh, 1986). Any alteration to wetland hydrology can change biogeochemistry of wetlands and dominant nutrient removal pathways (Kalin et al. 2017). Hence, wetland hydrology is of more importance when nutrient cycling/removal and their modeling are the ultimate goals of a study. Hydrology influences the physiochemical environment by transporting sediments, nutrients, and even toxic materials into wetlands (Mitsch and Gosselink, 2007). As a result, any significant changes in hydrologic conditions can lead to considerable disturbances in the wetland functionality.

Hydrologic signature of a wetland (or hydroperiod) is the result of the balance between inflows and outflows of the water (called water budget), the wetland basin geomorphology and the subsurface conditions (Mitsch and Gosselink, 2000). In most wetland systems, water levels, as one of the most important hydrologic indices, are generally not constant and fluctuate

seasonally (riparian wetlands), daily or semi-daily (various types of tidal wetlands/marshes) or unpredictably (wetlands in low-order streams and coastal wetlands with wind-driven tides) (Mitsch and Gosselink, 2000). Constructed treatment wetlands, on the other hand, typically have some forms of water level control structure, thus there is little or no variation in the water level, except in stormwater treatment wetlands (Kadlec and Wallace, 2009). Wetlands in arid and semi-arid areas are especially sensitive to hydrology. Interruption of a wetland's inflow in such environments not only affects its hydrological regime, but can also significantly harm its ecological functions (Sarhadi and Soltani 2013).

Alteration to wetland hydrology as a result of changes in the land use and land cover (LULC) of the watersheds draining to wetlands can include reduced groundwater recharge and increased surface runoff. These changes have been shown to cause increased flashiness, flow velocities, soil erosion and storm-flow frequencies while reducing baseflow levels (Ehrenfeld et al. 2003; Barksdale et al. 2014). For instance, if the watershed of a wetland urbanizes, the wetland in time can become channelized and turn into a flow-through system. This will reduce the retention time and change how the wetland filters pollutants. Also, the potential for hydrological export of particulate organic matter increases as a result of increase in magnitude and frequency of floods due to LULC changes (Barksdale et al. 2014). There is also considerable evidence that watersheds that drain wetland regions export more organic material but retain more nutrients than do watersheds that do not have wetlands (Mitsch and Gosselink, 2015). Furthermore, the impacts of climate change and variability on the hydrology of wetlands and the related alterations must be considered because those alterations can lead to a large shift in wetland distribution, extent and functioning. Accurately modeling the hydrology of wetlands can help better understand the potential impacts of any alterations to these important ecosystems.

Depending on the availability of data and understanding of the underlying processes, wetland hydrology studies can be performed through either data-driven or physically-based models. Data-driven modeling is focused on computational intelligence and machine learning techniques that can be utilized to construct models for complementing or replacing physically-based models (Solomatine et al. 2008). Two types of modeling approaches can be distinguished in physically-based wetland hydrology modeling; one is developing wetland hydrology/hydraulic models, and the other is utilizing available watershed models by adding a wetland hydrology module or modifying their available modules. The first approach is limited in its application to natural wetlands because inflows to the wetlands, such as surface runoff, and groundwater discharge need to be provided by the user, which is usually done by running a watershed model.

Hydrology is the main driving force for many physical, chemical and biological processes in wetlands. To account for biogeochemical processes and their cycling in wetlands, two aspects of wetland hydrology should be considered; *i*) the effects of groundwater fluctuations on wetland soil moisture, and *ii*) the effects of seasonal water level patterns in wetlands and the rise and fall of wetland surface and subsurface water (Sharifi, 2013). In the latter, wetland soil transitions between saturated and unsaturated conditions, which requires consideration of soil moisture dynamics to capture the effects of unsaturated zones on the wetland hydrology and eventually wetland biogeochemistry.

## 1. Problem Definition and Objectives of the Study

Headwater wetlands are the source of many of our rivers and streams. Although not often displayed on maps, small headwater streams may account for more than 70% of the overall stream channel length in the United States (Lowe and Likens, 2005). Headwater wetlands are

also considered as one of the most important subclasses of wetlands located in coastal plains of the Southeastern U.S. They are critical components to the landscape because they occur at the interface of uplands and coastal creeks. Headwater wetlands have both ground and surface water dynamics. Quantifying the groundwater component of a wetland water budget is a very difficult endeavor (McKillop et al. 1999). To have a better understanding of groundwater/surface water contributions to headwater systems, there is a need to assess long-term WL data. WL prediction and assessment are of great importance especially in headwater wetlands because of their susceptibility to (i.e., more frequent, rapid, substantial changes in WL) changes in catchment land use/cover. When there is insufficient knowledge of the soil physical properties and hydrogeologic characteristics of the system, and accurate prediction is more important than understanding the physical processes, physically-based modeling may not be feasible; instead, data-driven models can replace physically-based models to obtain important hydrologic components of wetlands such as water level dynamics. Despite the widespread applications of data-driven models, especially ANNs in hydrology and water resources field, very few studies have been reported on ANN applications to wetlands, particularly in headwater wetlands. None of them attempted to predict WLs at sub-weekly time scale.

Given the facts above, the **first objective** of this study was to develop models to predict hourly WLs in wetlands characterized by water tables at or near the surface that respond rapidly to rainfall events. Consequently, two ANN-based methodologies are proposed for wetlands whose WLs show (i) high correlation, and (ii) low to no correlation with WLs from nearby sites. Unlike most previous studies, the first methodology does not require antecedent WL. Instead, this method benefits from the WL data from nearby sites and can be used to predict time series of WLs. The second method, on the other hand, requires antecedent WLs. It is a combination of

ANN, recursive digital filter and recession curve method and is more useful for predicting WL response to individual rain events or for filling short period data gaps under the absence of highly correlated nearby site. Development, application, and validation of such models are explained in Chapter 2.

It is now widely accepted that climate is changing and by the end of this century, altered temperature and precipitation patterns can have considerable implications for all ecosystems, especially wetlands, whose ecological characters rely heavily on their hydrological regime (Acreman et al. 2009). Changes in wetland water balance due to climate change could alter wetland extent or cause wetland loss (Records et al. 2014). Wetlands are responsible for 20 to 25 percent of global methane emissions to the earth's atmosphere, yet they also have the best capacity of any ecosystem to retain carbon through permanent burial (sequestration); both processes have implications for climate change (Mitsch and Gosselink 2015). Among all eco-hydrologic indices, WL plays a key role in controlling $CH_4$ emissions by determining the interface between aerobic and anaerobic processes (above- vs. below-ground, respectively) (Kang et al. 2012). WL also determines the degree of $CO_2$ production (Daulat and Clymo 1998; Chimner and Cooper 2003). Hence, having knowledge about WL changes under the future projected climate can provide the researchers with valuable insight into the probable $CH_4$ and $CO_2$ dynamics in wetlands. Climate variability is also known to have a significant impact on wetland $CH_4$ emissions. Hodson et al. (2011) showed that global wetland $CH_4$ variability is strongly related to El Niño Southern Oscillation (ENSO) variability. The large-scale response of wetland $CH_4$ emissions to ENSO variability using satellite retrievals was reported by Pandey et al. (2017). To the best of my knowledge, there are limited number of studies that considered the global climate models (GCMs) in evaluating climate change effects on wetland hydrology; most

studies rely on scenario-based definition of climate change (i.e., degree changes in temperature or/and percentages of changes in precipitation). For instance, van der Valk et al. (2015) performed a scenario-based evaluation of climate change impacts on the Florida Everglades. Scenario-based modeling of climate change lacks capturing the variations in temperature and in particular the precipitation patterns.

To build a predictive model capable of capturing physical processes to some levels, coupling a watershed model with ANN would be useful for wetland water level prediction. By running a watershed model, the hydrologic inputs from the contributing watershed to the wetland (i.e., slow and quick flow components) can be simulated. Input combinations to ANN play a crucial role in developing a robust model. In that sense, importing the baseflow and stormflow simulated by a watershed model as inputs to ANN can improve the accuracy of ANNs. To the best of my knowledge, no study has considered combining a watershed model with ANN to predict wetland WL, although there are studies that coupled watershed models and ANNs for streamflow prediction.

The **second objective** of my dissertation was to develop a coupled SWAT-ANN model to predict WLs in headwater wetlands. The model was applied to a headwater wetland in coastal Alabama, USA to predict the WL dynamics of the wetland. The coupled model of this study overcomes some of the limitations of the two previously developed WL prediction models (which are explained in Chapter 2), which either required WL data from nearby wetlands or antecedent WL data from the target wetland itself as input. None of those models are suited for long-term predictions, which is needed to explore impacts of climate change and variability on wetland hydrology. The utility of the developed model was demonstrated with two applications. In the first application, potential impacts of future climate change on WLs were assessed. The

second application is related to climate variability rather than change where we explored the potential teleconnections between El Niño Southern Oscillation (ENSO) and WL fluctuations in the study wetland. This study is the first attempt, to the best of my knowledge, at evaluating the hydrologic function of a headwater wetland in Coastal Alabama under varying ENSO conditions. Chapter 3 explains the methodology behind coupled SWAT-ANN model and those two applications. The potential impacts of climate change and variability could have considerable implications on the wetland water budget and could make a flooded wetland become a non-flooded wetland or vice versa.

In wetlands going through wetting and drying cycles, simulation of nutrient removal and cycling in both ponded and unsaturated section of wetlands are needed. Sharifi et al. (2017) extended the ponded version of *WetQual* model to account for soil moisture dynamics in vadose zone of wetlands and consequently updated the N and C relationships for an improved wetland water quality modeling. They utilized a numerical solution of highly non-linear Richards' (1931) Equation (RE). They reported frequent crashes in the numerical solution, specifically when a soil is close to saturation due to the hyperbolic nature of RE and high non-linearity of soil hydraulic functions. Hence, numerical solution of RE for the infiltration-redistribution cycle is extremely challenging and is not recommended for vadose zone hydrological processes in wetlands. Furthermore, Sharifi et al. (2017) considered a head-controlled boundary condition for the bottom node, assuming the existence of a non-fluctuating perched water table at the bottom of the soil column. There is a need for a model of less computationally intensive with a simpler mathematical representation that can account for soil moisture dynamics in the unsaturated zone of wetlands.

The **third objective** of this study was to utilize a depth-averaged solution to RE for vertical unsaturated flow to develop a less computationally intensive solution for unsaturated flow conditions which can be used in *WetQual* model. This model is more efficient in computation time because of its simpler mathematical representation compared to the RE. This depth-averaged solution can also be a reliable replacement for highly non-linear RE utilized in some watershed scale models such as Gridded Surface Subsurface Hydrological Analysis (GSSHA) and MIKE SHE. A two-layer **D**epth-**A**veraged **RE**, called DARE was utilized and examined in this study. This method considers impact of groundwater level fluctuations. To that end, a gravity drainage condition, which assumes a uniform, vertical unit-gradient and ignores suction force was first considered. In the next step, negative pressure head component was added which led to the full version of DARE. The two layers include the root zone and the zone between roots and the water table. Heun's method was adopted to discretize and solve the equations numerically. The methodology, verification of the model and the related case study are presented in Chapter 4.

Although most of the commonly used hydrology and water quality models were initially developed using programming languages such as FORTRAN, they have some types of graphical user interfaces to help the users apply those models to their projects within a user-friendly environment. Over the years with the emerging of object-oriented languages (such as C++, and C#), user-friendly versions of those models have been developed. For instance, two well-known watershed hydrology and water quality models, SWMM and HSPF, were initially prepared in the FORTRAN environment, but they also have Windows-based (written in C/C++ languages) versions developed in the last two decades which give the user greater flexibility and more advanced interactive capabilities. A Graphical User Interface (GUI) can also be used for training

and educational purposes. Visualizing inputs/outputs, importing and exporting the data from/to other platforms, which include the outputs from other models to be used in the target model or vice versa, are some of the capabilities of the user interfaces developed for those models. Soil and Water Assessment Tool (SWAT; which is written originally in FORTRAN), as an example, has a user interface called ArcSWAT which was developed based on Geographic Information System (GIS) in Visual Basic (VB) (Olivera et al. 2004) which help divide watershed into subbasins and further into hydrologic response units.

The ponded version of *WetQual* does not include a hydrology component which limits its application. Hydrologic information (flow in and out of the wetland, depth-area-volume time series, etc.) needs to be provided as an input, which could be observed data or modeled. Adding a hydrology component is required in case the users do not have the pre-defined/measured hydrologic inputs for the wetland which is mostly the case. By solving continuity equation through a flow routing module, a hydrology component should read in the incoming time series (i.e., inflow, evapotranspiration (ET), precipitation and subsurface/groundwater flow), and geometry table (i.e., depth-area-volume-outflow relationship), to calculate the times series of outflow, wetland water level, surface area, and volume. An inclusion of the hydrology component in the *WetQual* will help conduct a smoother water quality modeling by providing the users with a better understanding of hydrologic processes in the study wetland. Furthermore, the users do not need to perform wetland hydrologic modeling individually outside the *WetQual*.

A better representation of physics and natural processes comes with a higher complexity in the model and consequently more uncertainties, and that is why a robust wetland water quality model can benefit from uncertainty and sensitivity analyses embedded into its graphical interface. *WetQual* as a process-based model includes a large number of parameters, and those

have to be estimated from a limited information or data available from wetland hydrology and water quality measurements. For a proper application of *WetQual* model, a Monte Carlo (MC) simulation of 50,000 or 100,000 runs are highly recommended. Generating an ensemble of *WetQual* outputs by conducting MC simulations is the first step in conducting uncertainty analyses. With the current format, the users have to do random parameter generation for a successful Monte Carlo simulation, uncertainty and sensitivity analyses outside of the *WetQual* in other software such as Excel. They also need to export their data to other platforms for qualitative and quantitative assessment of their results. It has text-based input/output interactions with no visualization interface which makes its application more complicated. A GUI would help to extend the model's accessibility for public use.

The **fourth objective** of this study was adding a flow routing module to ponded version of *WetQual* and creating a GUI that bring the hydrologic and water quality modeling under one umbrella. The process-based *WetQual* model simulates the water quality including nitrogen, phosphorous, carbon and sediment cycles in natural and constructed wetlands. *WetQual* can be used in continuously flooded environments or wetlands going through wetting and drying cycles. The GUI is being developed to handle flooded type of wetlands. The GUI is written in the C#.NET environment (within Visual Studio 2015). "C# is an elegant and type-safe object-oriented language that enables developers to build a variety of secure and robust applications that run on the Microsoft .NET Framework" (MSDN 2015). The developed *WetQual* GUI has a hydrologic component that can calculate wetland outflow, depth, area and volume time series through flow routing. The GUI also simplifies the input/output transfer and provides users with a powerful visualization and post processing tool which include uncertainty and sensitivity analyses. By utilizing this GUI, users can perform the Generalized Likelihood Uncertainty

Estimation (GLUE) and Bayesian Monte Carlo simulation and maximum likelihood estimation (BMCML) analyses. GUI in its post processing module provides a tool for model predictive uncertainty analysis. By conducting GLUE, it provides estimate for the 95% prediction interval. Through BMCML it can provide 95% confidence limits. Sensitivity analysss based on Kolmogorov-Smirnov (K-S) test and dotty plots are also available in the GUI. The development of the GUI and its demonstration through a case study are explained in Chapter 5.

## 2. Dissertation organization

This dissertation is organized based on the following structure. Chapter 1 provides an introduction on the motivations behind this research and presents the research objectives. Chapter 2 describes the methodology and the application of ANN-based models for wetland WL predictions in response to objective 1. This chapter has already been published in "special issue: Advances in Wetland Hydrology and Water Quality Processes Modeling" in *Journal of Hydrologic Engineering*. Chapter 3 explains the methodology behind the coupled SWAT-ANN model, its verification, and two applications in response to the second objective of the study. In the first application, potential impacts of future climate change on WLs are assessed. The second application is related to climate variability rather than change. This chapter has been submitted to *Hydrological Sciences Journal* and it is currently under review. Chapter 4 explains the development and verification of depth-averaged Richards' equation and the associated case study, in response to the third objective of the study. The target journal for chapter 4 is *Journal of Hydrology*. Chapter 5 provides the details on the development of *WetQual* GUI, and the structure of the GUI is explained in depth with a case study. We hope we can publish this chapter in *Environmental Modeling & Software*. Chapter 6 presents a summary of the entire research and

provides a conclusion with major findings of this study. It also provides suggestions for relevant research in the future.

# Appendix

## A Review on Wetland Hydrology/Hydraulic Modeling

### Introduction

Studies of chemical input-output relationships in wetlands are heavily dependent on hydrologic data (LaBaugh, 1986). Even slight changes in wetland hydrologic conditions can affect soil biogeochemistry and consequently nutrient cycles; the biota may respond with considerable changes in species composition and richness and in ecosystem productivity (Mitsch and Gosselink, 2000). The flow rate across a wetland is controlled by topography and ground slope, water depths, vegetation type and density, and the degree and type of channelization (Hammer and Kadlec, 1986). Hence, hydrology and hydraulics of wetlands need to be understood well for modeling wetland biogeochemical processes as well as for defining hydrologic connectivity of wetlands and their functionality at a broader scale, (e.g., watershed scale). In this section, by focusing on the philosophical progression of modeling approaches, we review various types of wetland hydrology/hydraulic models and approaches with various levels of complexity.

The history of contemporary wetland hydrology modeling goes back to the 1980s when the wetland vegetation effects on overland flow were explicitly taken into account by Kadlec et al. (1981) and Hammer and Kadlec (1986). Before that, hydrologic modeling in wetlands were limited to ecosystem and regional models for general water budget calculation purposes, and hydrodynamic transport models to simulate streamflow and storm runoff. However, none of these models were truly capable of describing overland flow of a thin water sheet impeded by wetland vegetation (Hammer and Kadlec, 1986). Generally, two types of modeling approaches

can be simply distinguished; one is developing wetland hydrology/hydraulic models, and the other is utilizing available watershed models by adding a wetland hydrology module or modifying their available modules. The first approach is limited in its application to natural wetlands because inflow to the wetland, such as surface runoff, groundwater discharge, etc., needs to be provided by the user, which is usually done by running a watershed model.

**Wetland hydrology/hydraulics**

Hydrologic signature of a wetland (or hydroperiod) is the result of the balance between inflows and outflows of the water (called water budget), the wetland basin geomorphology and the subsurface conditions (Mitsch and Gosselink, 2000). In most wetland systems water levels, as one of the most important hydrologic indices, are generally not constant and fluctuate seasonally (riparian wetlands), daily or semi-daily (various types of tidal wetlands/marshes) or unpredictably (wetlands in low-order streams and coastal wetlands with wind-driven tides) (Mitsch and Gosselink, 2000). Constructed treatment wetlands, on the other hand, typically have some forms of water level control structure, thus there is little or no variation in the water level, except in stormwater treatment wetlands (Kadlec and Wallace, 2009). However, many have climatic or seasonal variations that result in WL changes. Wetlands in arid and semi-arid areas are especially sensitive to hydrology. Interruption of a wetland's inflow in such environments not only affects its hydrological regime, but also can significantly harm its ecological functions (Sarhadi and Soltani 2013).

Water can enter a wetland via streamflow, overland runoff, groundwater discharge and precipitation. Similarly, wetlands can lose water via streamflow, groundwater recharge, and evapotranspiration. Being stochastic in nature, the inflows and outflows could be extremely

variable in most wetlands (Kadlec and Wallace, 2009). Surface flow routing in a wetland system can be described using a simple flow continuity equation (Hantush et al. 2013) with adding tidal effects:

$$\phi_w \frac{dV_w}{dt} = Q_i \pm Q_g - Q_o - AE_T + Ai_P \pm Q_T \quad (1)$$

where, $V_w$ is the water volume of wetland surface water ($L^3$); $A$ is the wetland surface area ($L^2$); $Q_i$ is the volumetric surface inflow rate (including flooding streams) ($L^3T^{-1}$), $Q_g$ is groundwater discharge or recharge ($L^3T^{-1}$), $Q_o$ is wetland discharge (outflow) rate ($L^3T^{-1}$), $i_p$ is precipitation rate ($LT^{-1}$), $E_T$ is evapotranspiration rate ($LT^{-1}$), $Q_T$ is tidal inflow or outflow and $\phi_w$ is effective porosity of wetland surface water (since biomass occupies a part of the submerged wetland volume). The terms in the equation vary in importance depending on the type of wetland. Furthermore, not all the terms in the above hydrologic budget equation apply to all wetlands.

Wetlands can be highly heterogeneous systems. Therefore, when modeling movement of the surface water, there may be a need to compartmentalize the wetland into small homogenous units or cells. Often, the major factor in deciding whether to compartmentalize or not is the available knowledge or the lack of knowledge about the wetland characteristics and the data availability. In the single compartment case, the movement of water is modeled with a simple water budget, similar to Eq. (1), to quantify the changes in average water depth and volume in time. When heterogeneity cannot be ignored, efficiency can be increased by subdividing the wetland into a number of cells that interact with each other. A dynamic water mass balance model calculates the water level at each cell. In the water balance calculations flow exchanges among the cells should be considered, which can be expressed by Eq (2). Two examples of compartmental wetland model are Dall'O' et al. (2001) and Sharifi (2013), which will be scrutinized in detail later on.

$$\phi_w \frac{\partial V_w}{\partial t} = \sum Q_{exchange} + \sum Q_{boundary} + (Q_i + Q_g - Q_o - AE_T + Ai_P \pm Q_T) \quad (2)$$

where, $Q_{exchange}$ is the flow exchanged between neighboring cells and $Q_{boundary}$ is the flow across the cell boundary.

**Mathematical Representation of developed/applied wetland Hydrology/Hydraulics models/modules**

Several mathematical models have been developed within the past three to four decades for modeling hydrology and hydraulics of wetlands. Table 1.1 provides a summary of some of the promising wetland hydrology/hydraulic models and modules (i.e., a new component added to an existing model). In the table information about the type or dimension of the developed/applied models, specific wetland types for which these models have been developed for and the study area where the models were applied to are also given. A water balance (budget) equation, as discussed earlier, is usually the first step in almost all models. Zero-dimensional water balance models cannot represent spatial variability and multiscale hydrological processes (Moffett et al. 2012). Examples to the zero-dimensional, lumped wetland hydrology/hydraulic modeling are Konyha et al. (1995), Zhang and Mitsch (2005), Dadaser-Celik et al. (2006), Liu et al. (2008), Villa and Tobon (2012), Feng et al. (2013) and Hughes et al. (2014). Dall'O' et al. (2001) developed a zero-dimensional model, but the model allows for multiple compartments in horizontal and vertical directions. Sharifi (2013) also provided a zero-dimensional but compartmentalized model in horizontal direction. Since the inflows and outflows at many wetlands sites have been observed in more than one direction (Kazezyilmaz-Alhan et al. 2007), the zero-dimensional models may not be the best viable option to accurately capture the water depth changes in space and time.

Vegetation mats present an obstruction to flow, comprising a doubly porous medium, with plant stems and litter forming fine-scale porosity, while hummocks, islands, and channels resulting in a coarse-scale porosity (Hammer and Kadlec, 1986). To account for the effects of vegetation density and bed-shape irregularities (hummocks and depressions) on the flow and from hydraulic standpoint, the general approach is the utilization of continuity of mass, and momentum conservation equations, coupled with an equation for frictional resistance. The earlier studies on overland flow in wetlands mainly adapted open channel flow formulas (Kadlec and Wallace 2009). Manning's equation is the most widely used flow equation for uniform open channel and overland flows. However, there is a fundamental problem with the utilization of the Manning's equation to wetland surface water flows. Manning's equation requires flow to be turbulent, whereas free water surface (FWS) wetlands are almost always in a laminar or transitional flow regime (based on the open channel flow criteria of $Re$<2000) (Kadlec and Wallace, 2009). The other difficulty in the application of open channel concepts to wetlands is that the frictional effects in open channels are associated primarily with drag exerted by channel bottom and sides while the resistance to flow in wetlands is dominated by drag exerted by the stems and litters (Kadlec and Wallace, 2009). As a result of the difficulties inherent in the application of the Manning equation to wetland systems, Kadlec's (1990) proposed the following power law equation for overland flow in wetlands:

$$q_i = K d^{\beta} {S_{f,i}}^{\alpha} \tag{3}$$

where $q_i$ is specific discharge (m/s), with three constants: a depth component $\beta$, a slope component $\alpha$, and a premultiplier (or conductance coefficient of equation) $K$ ($m^{(1-\beta)}s^{-1}$). In the equation $d$ is the average depth of water in meters and $S_{f,i}$ is the friction slope in direction $i$. The values of $\alpha$, $\beta$ and $K$ are ranging from 0.7 to 1.0, 2.5 to 3.75 and $0.37*10^8$ to $28.5*10^8$,

respectively, according to Kadlec (1990). More information regarding these values can be found in Kadlec (1990) while to the best of author's knowledge, these values have been reported from very limited studies and there is a need to gather more information from different types of wetlands having various vegetation densities. Therefore, modelers must be cautious in their applications with these range of values.

The transient surface water flow can be modeled by the equations of continuity and momentum (Restrepo et al. 1998). For wetlands, where ground-surface slopes are gentle, the acceleration terms in Saint Venant equations are likely to be very small and can be neglected (Weinmann and Laurenson, 1979; McKillop et al. 1999). Thus, the "diffusive wave" approximation works well in most wetlands. The diffusion wave equation is obtained by combining the continuity and momentum equations and neglecting the local and convective acceleration terms. With the frictional and gravity effects in balance, flows through a wetland environment can be modeled using an appropriate mass balance and a relationship between velocity and hydraulic gradient (as an expression of power law) (Hammer and Kadlec, 1986). Hammer and Kadlec (1986) adapted the friction (or power) and Darcy's laws into the 1-D diffusion wave equation to model surface and subsurface flows. Another application of friction law by using 1-D diffusion-based model is the work of McKillop et al. (1999). For the sake of clarity, a clean version of the equations mixing power law with diffusion wave equation can be expressed as

$$\phi_w \frac{\partial h}{\partial t} = \frac{\partial}{\partial x}\left(K d^{\beta+1} \frac{\partial h}{\partial x}\right) \pm (F) \tag{4}$$

where, $F$ is the inflow/outflow fluxes ($LT^{-1}$) (precipitation, evapotranspiration, etc.).

When no terms in the Saint Venant equation are ignored, it becomes dynamic wave equation. Several wetland hydrology models implemented the full dynamic wave equation in one

dimension. For instance, the Wetland Dynamic Water Budget Model (WDWBM) developed by Walton et al. (1996) utilized 1-D dynamic wave for surface water flow and Darcy's law for the variably-saturated horizontal groundwater flow. As presented in Table 1.1, Kazezyilmaz-Alhan et al. (2007) used 1-D diffusion wave equation for water quantity and 1-D advection-dispersion-reaction equations for water quality modeling. Kazezyilmaz-Alhan et al. (2007) utilized Darcy's law to quantify the groundwater recharge/discharge where the unsaturated layer is thin and groundwater levels are close to the wetland elevations (shallow water table).

Flows in wetlands can be characterized as shallow flow where the horizontal dimensions are dominant compared to the vertical extent. This is because the vertical component of water particle acceleration is negligible and the pressure variations can be assumed hydrostatic. In shallow flows horizontal mixing is of particular importance (Arega 2013). Wetlands are usually subject to periodic flooding (pulsing water levels) and drying events, which cause dynamic changes in water surface elevation, and as a response to this variation, the boundary lines between the water body and the land surface change position with time. Thus, one must deal with a so-called 'moving boundary problem' (Feng and Molz, 1997). Yuan et al. (2008) also emphasized that the moving boundary problem is a very important phenomenon in shallow water flows over wetlands and floodplains, particularly with regard to flooding. Hence, 2-D modeling is often needed to capture the horizontal mixing effects and to deal with the moving boundary conditions.

Few studies on overland flow in wetlands have utilized the diffusive wave equations in 2-D (e.g., Restrepo et al. 1998; Feng and Molz, 1997; Wilsnack et al., 2001; Min et al., 2010; Bolster and Saiers, 2002). The application of dynamic wave equations was also reported by Guardo and Tomasello (1995) and Thompson et al. (2004). Another examples is Arega (2013),

who coupled depth-integrated continuity and momentum equations with Lagrangian particle tracking for a tidal wetland.

In the most complex case, a 2-D surface flow model is coupled with a 3-D subsurface flow model. These types of applications are the most computationally demanding ones and require a high level of expertise. For instance, Thompson et al. (2004) combined the 2-D Saint-Venant (dynamic wave) equation for surface flow with the 1-D Richards' equation for unsaturated flow and 3-D saturated subsurface flow.

**Quantifying the Effects of Groundwater in Wetlands**

As mentioned before, hydrology is the main driving force for many physical, chemical and biological processes in wetlands. To account for biogeochemical processes and their cycling in wetlands, two aspects of wetland hydrology should be considered; i) the effects of groundwater fluctuations on wetland soil moisture and ii) the effects of seasonal pattern of water level in wetlands and the rise and fall of wetland surface and subsurface water (Sharifi, 2013). In the latter, the wetland soil transitions between saturated or unsaturated conditions, which require consideration of soil moisture dynamics to capture the effects of unsaturated zone in wetland modeling.

A new compartmentalization scheme can be employed in wetlands exhibiting wetting and drying cycles following Sharifi (2013). In this scheme the wetland is divided into ponded and unponded compartments. To track the mass exchange between these two compartments, a temporary, transition compartment is needed, also called dummy compartment (Sharifi, 2013). Furthermore, to address wetland soil heterogeneity, non-linearity of physical properties in wetland soil and non-uniform root water uptake of wetland plants, a numerical solution of

Richards's equation (Richards, 1931) was found to be useful and it was an example of 1-D modeling (in vertical direction) of unsaturated zone in WetQual model (Sharifi 2013). Thompson et al. (2004) had already reported the utilization of 1-D Richards' equation for unsaturated flow and 3-D saturated subsurface flows using Boussinesq equation but they had used an existing model, MIKE SHE. These two studies, in theory are superior to those that utilized Darcy's law in their 1-D mass balance equations (Hammer and Kadlec 1986; Kazezyilmaz-Alhan et al. 2007) because of the better representation of the physics. However, a key component, plant uptake effects on soil moisture redistribution, is missing in Thompson et al. (2004). On the contrary, the multidimensional WETLANDS model developed by Mansell et al. (2000) uses the 2-D surface flow equations and the Richards's equation for subsurface porous media by considering the effects of plant uptake.

It is necessary to mention that depending on the hydrogeologic formations of the study area beneath the wetland, utilization of non-linear and computationally demanding equations such as the Richard's may not always be the best viable option. For example, application of the Richard's equation to regional hydrologic systems that encompass hundreds to thousands of square kilometers will not result in a proper understanding of the surface/groundwater interaction.

**Wetland Hydrology/hydraulic modeling and its impact at the watershed scale**

Wetlands are one of the most important watershed microtopographic features that alter hydrologic processes (e.g., routing) and the fate and transport of various water quality constituents (e.g., sediment and nutrients) (Wang et al. 2010). Only a handful of watershed models consider wetlands in their computations, and they mostly do so by simply considering

zero-dimensional water balance equations. For instance, the SWAT (Soil and Water Assessment Tool) model treats wetlands and ponds similar and allows for only one wetland within each subbasin (Neitsch et al. 2011). Clearly, representation of wetland processes in SWAT is not sufficient, and has to be improved (Krysanova and Arnold, 2008). Hattermann et al. (2008) added a wetland module to the SWIM (Soil and Water Integrated Model) model, which is an adaptation of SWAT (Krysanova and Arnold, 2008). Hattermann et al. (2008) present two approaches which allow integration of the most important wetland processes in the SWIM model. Both approaches consider water and nutrient fluxes, but have different levels of complexity. The first (and simpler) approach considers seasonal river discharge and nutrient loads in catchments with wetlands. The second, more advanced approach is introduced at the level of hydrologic response units (HRUs), and takes into account fluctuations of groundwater table (Krysanova and Arnold, 2008). The Hydrological Simulation Program–Fortran (HSPF), although does not have a wetland module, some applications has been reported representing wetlands either as pervious landforms or as reach reservoirs with storage-attenuation characteristics. The former allows groundwater levels and the interaction between the saturated and unsaturated zones to be modeled where groundwater can rise through the original unsaturated zone and inundate the surface which is subject to evaporation and surface runoff (Said et al. 2007). The latter approach allows stage-dependent flow from the wetlands and interaction with the shallow groundwater system. Similar to HSPF, another widely used watershed model MIKE-SHE although does not have an individual wetland module, it has been used to model water movement in wetlands by coupling it with MIKE-11 (Thompson et al. 2004). It's worth noting that there is an option of "Two-layer water balance" for unsaturated flow calculations in MIKE-SHE for shallow water tables (such as swamps or wetlands areas) (MIKE

SHE, DHI, 2007). Fossey et al. (2015) is another good example to efforts integrating wetland hydrology modules into watershed models, in which they modified the HYDROTEL watershed model to better represent impacts of wetlands on the watershed hydrology. Through building the hydrologic equivalent wetlands (HEWs) using HYSITEL (a geographic information system), isolated and riparian wetlands are defined in HYDROTEL by a zero-dimensional, lumped water budget model, very similar to wetland modeling work of Liu et al. (2008).

To the best of our knowledge, limited studies have tried to address the aggregate impacts of wetlands at watershed level and they mostly did this with lumped water budget models (e.g., Liu et al. 2008; Feng et al. 2013). Furthermore, quantifying the hydrologic functions of wetlands at the watershed scale cannot be achieved without assessing the surface water/groundwater interactions. Coupled surface water-groundwater models are important for assessing complex watershed scale questions because they consider feedbacks among the various water balance components (e.g. surface runoff, evapotranspiration and groundwater flows) (Golden et al. 2014). In a watershed with a sufficiently dense distribution of geographically isolated wetlands (GIW), their hydrologic connections and the hydrologic functions they provide, could have important implications for flood regulation and mitigation of the future effects of climate and land use change; while quantifying the extent to which GIWs are measurably linked to surface water via surface and/or groundwater connections remains a fundamental research gap for informing unresolved science and policy questions (Golden et al. 2014). Golden et al. (2014) reported several watershed models that could be readily adapted to answer questions concerning geographically isolated wetland hydrologic connectivity which include SWAT, HSPF, DRAINMOD for Watershed (DRAINWAT) (Skaggs, 1978; Amatya, 1993; Amatya et al., 1997), TOPMODEL (Beven and Kirkby, 1979), Grid Based Mercury Model (GBMM) (Dai et al., 2005;

Tetra Tech, 2006) and Visualizing Ecosystems for Land Management Assessment (VELMA) (Abdelnour et al., 2011).

**Summary of Discussion/Future Outlook**

Several significant challenges that pose difficulties in wetland hydrology/hydraulic studies are non-linearity of soil characteristics in horizontal and vertical directions, impacts of vegetation communities on flow of water and nutrient cycling in water and soil (aerobic and anaerobic) columns. One of the most appreciable efforts related to soil moisture redistribution was done by Sharifi (2013). He reported frequent crashes in the numerical solution, specifically when soil is close to saturation due to the hyperbolic nature of Richard's equation and high non-linearity of soil hydraulic functions. Hence, numerical solution of Richard's equation for the infiltration-redistribution cycle is extremely difficult and is not recommended for wetland modeling at watershed scale. There is a need for introducing a simplified model that can account for soil moisture redistribution in unsaturated zone and can be linked with watershed scale models such as SWAT (Arnold et al. 1998).

The stochastic and dynamic nature of the water table in certain type of wetlands, such as tidal wetlands and ones with significant groundwater-surface water interaction, makes the problem more complicated. Bullock and Acreman (2003) reported that there is strong evidence that wetlands evaporate more water than other land types such as forests, savannah grassland or arable land. The other gap that can be addressed here is regarding evapotranspiration (ET) estimations especially when the water table falls below the ground surface. It seems that the previously developed wetland hydrology models have not utilized a dynamic procedure for ET

calculations based on shallow and deep water table. A stochastic description of water table fluctuations can be considered (Tamea et al. 2010; Laio et al. 2009; Tamea et al. 2009).

The aggregate effect of wetlands in landscapes where many wetlands are hydrologically connected is particularly challenging. The connectivity of various hydrologic systems and the groundwater/surface water interactions at the watershed scale are influenced by many factors such as topology, topography, geology, and the climate of the region. Such interactions in wetlands are complex and an understanding of basic principles and physical laws governing exchange between groundwater and surface water is needed for modeling the interactions at multiple scales (Hantush et al. 2011). However, to deal with such complexities and to capture their relevant effects, utilization of the fully-integrated approaches or 3-D modeling efforts may not always be the best option, because of the need for detailed understanding of hydrogeology of underlying geologic formations of the wetlands and hydro-climatic forcings. Physically-based watershed models vary in complexity in handling surface water/groundwater interactions. Although Golden et al. (2014) have listed SWAT, HSPF, etc. as examples of watershed models that can be readily adaptable to address GIWs and their hydrologic connectivity, the lack of more detailed wetland hydrology modules and accordingly water quality components for wetland processes and nutrient cycling, limit their capabilities to accurately address this issue. Furthermore, one big challenge in incorporating a comprehensive wetland module to such watershed models is the complexity issue. Any wetland module should be consistent with their philosophy. Artificial intelligence (AI) models such as artificial neural networks (ANNs) can be viable options where observed hydrologic data (e.g. inflow, outflow, water depth, etc.) exists but there are no/lack of information on soil and hydrogeology of the system. Two examples of ANN

applications in wetland hydrology studies are Dadaser-Celik and Cengiz (2013) and Rezaeianzadeh et al. (2015).

As discussed in this review, there is still a gap regarding the development of wetland hydrology models/modules that can be linked with large-scale watershed models. Because, watershed responses are partly controlled by the number of wetlands, area, and distribution, as well as connection paths (i.e., surface vs. subsurface). Furthermore, watershed discharge integrates the entire continuum of hydrological connectivity, not just rapid or surface-connected flow paths (Cohen et al. 2016). Most of the reported studies have treated the wetlands as a geographically isolated wetland (GIW) without any hydrologic connectivity, whereas the eco-hydrological effects of wetlands and their hydrologic connectivity via surface and/or groundwater (Golden et al. 2014) should be considered at watershed scale. The study by McLaughlin et al. (2014) clearly shows GIWs can have significant nexus to navigable waters through wetland-groundwater interactions. Furthermore, existing watershed models often use zero-dimensional water balance equations that may not sufficiently capture inflow/outflow to/from the wetlands. Golden et al. (2016) for instance clearly showed the relative attenuating impacts of GIWs on streamflow through a watershed-scale analysis. To understand the aggregate impacts of GIWs, Rains et al. (2016) suggested the development of a classification system as the first step to defining regions or conditions under which GIWs have expected behaviors that can be studied in aggregate. They emphasized on regional-scale data collection and improving the resolution of remote-sensing datasets, and finally improving the sensitivity and accessibility of modelling/analytical tools that can be used to evaluate the aggregate effects of the portfolio of GIWs that emerge at the watershed scale. Eventually, although not discussed here, the impacts of climate change on the hydrology of wetlands and the related alterations must be considered

because those alterations as discussed by can lead to a large shift in wetland distribution, extent and functioning.

Table 1.1: Sample of wetland hydrology/hydraulic models/modules

| Model name/title | Dimension/Scale | Author(s) year | *Remarks |
|---|---|---|---|
| Dynamic Hydrologic Model of the Örtülüakar Marsh in Turkey | Zero/monthly | Dadaser-Celik et al. (2006) | Lumped model, Marsh, Turkey, MATLAB software |
| FEUWAnet | Zero/daily | Dall'O' et al. (2001) | Multi-box model, Riparian wetlands, Germany, C language |
| A wetland module incorporated into SWAT model | Zero/monthly | Feng et al. (2013) | Lumped in [1]HRUs, Marsh, China |
| MODFLOW Wetlands Package | 2-D/daily | Wilsnack et al. (2001) | Diffusion-wave equation, Florida Everglades, USA |
| A Model for Wetland Surface Water Dynamics | 1-D/daily | Hammer and Kadlec (1986) | Friction law in conjunction with mass balance, Peatland (also constructed wetlands), Michigan, USA |
| Wetland water balance sub-model incorporated into Pitman monthly rainfall–runoff model | Zero/monthly | Hughes et al. (2014) | Lumped model, wetlands, southern Africa where the downstream impacts of wetland storage are expected to be evident at the monthly time scale |
| Wetland Solute Transport Dynamics (WETSAND) for both water quantity and quality modeling | 1-D/flexible | Kazezyilmaz-Alhan et al. (2007) | Diffusion wave equation for water quantity model, advection-dispersion-reaction (ADV) equations for water quality model, restored wetland system at Duke University, North Carolina, USA |
| Riparian wetland hydrologic module for embedding in SWAT | Zero/daily | Liu et al. (2008) | Lumped model, riparian wetlands, southern Ontario of Canada, FORTRAN |
| Modeling the rainfall-runoff response of a headwater wetland | 1-D/hourly | McKillop et al. (1999) | Friction law in conjunction with mass balance, headwater wetland, southern Ontario, Canada |
| Regional Simulation Model (RSM) | 2-D/daily | Min et al. (2010) | Mass and momentum conservation (St. Venant equations), spatially distributed, Florida Everglades, USA, C++ |

| | | | |
|---|---|---|---|
| STELLA | Zero/daily | Zhang and Mitsch (2005) | Lumped model, created freshwater wetlands in Ohio, USA |
| STELLA | Zero/hourly | Villa and Tobon (2012) | Lumped model, created wetland, Colombia |
| A coupled hydraulic–hydrologic modelling approach using MIKE21 and a water balance model | **2-D and Zero/daily | Rayburg and Thoms (2009) | Reynolds-averaged Navier–Stokes equations in hydraulic model and a lumped model for hydrology, floodplain–lake–wetland complex, New South Wales, Australia |
| SWAMPMOD | Zero/daily | Konyha et al. (1995) | Lumped model, hypothetical stormwater wetland design located at the outlet of a 20-ha watershed in central Illinois, USA, MicroSoft QuickBASIC. |
| Wetlands Dynamic Water Budget Model (WDWBM) | 1-D/daily | Walton et al. (1996) | Momentum conservation equation, Swamp wetlands, Arkansas, USA |
| 2-D hydrodynamic model | 2-D/hourly interpolated probably based on daily time scale | Arega (2013) | depth-integrated continuity and momentum equations, tidal wetlands, South Carolina, USA |
| Coupled MIKE SHE/MIKE 11 | Multi-dimension/daily | Thompson et al. (2004) | 2-D overland flow using full Saint-Venant (dynamic wave) equation, 1-D Richards' equation for unsaturated flow and 3-D saturated subsurface flows using Boussinesq equation, grassland wetlands, southeast England |
| WetQual | 1-D/daily | Sharifi (2013) | 1-D Richards's equation for unsaturated flow, restored wetland, Maryland, USA, FORTRAN |
| WETLANDS | Multi-dimension/daily | Mansell et al. (2000) | 2-D Richards's equation for subsurface flow, cypress pond, Florida, USA |
| WETFLOW | 2-D/flexible | Feng and Molz (1997) | Diffusion-based continuity, together with momentum equations for surface flow, upland wetland, |

| | | | |
|---|---|---|---|
| | | | Moundville, Alabama, USA |
| A Wetland Simulation Module for the MODFLOW | 2-D/flexible | Restrepo et al. (1998) | Diffusion equation, hypothetical isolated wetland, South Florida Water Management District (SFWMD), USA |
| SHEET2D | 2-D/flexible | Guardo and Tomasello (1995) | Continuity and momentum ( Saint Venant) equations, Florida Everglades, USA |
| A surface-water flow model in wetlands | 2-D/daily | Bolster and Saiers (2002) | Diffusion-based continuity/momentum equations considering friction law, Florida Everglades, USA |

[1]Hydrologic response unit

[*]**Remarks:** Three or four types of information are provided in this column; 1) the types of equations they are utilizing in one or higher dimensions, 2) the type of wetland where the models have been applied 3) the country of study 4) the language/software of programming/developing the models (was not available for all studies). Note: lumped models refer to utilization of mass balance water budget equation without compartmentalization.

[**] Two and zero-dimension for hydraulic and hydrology models.

[***] One and zero-dimension for hydraulic and hydrology models.

# Chapter 2 : Wetland Water Level Prediction using ANN in Conjunction with Baseflow Recession Analysis


## Abstract

This study introduces two artificial neural network (ANN) based methodologies to predict hourly water levels (WLs) in wetlands characterized by water tables at or near the surface that respond rapidly to precipitation. The first method makes use of hourly precipitation data and WL data from nearby sites. The second method is a combination of ANN, recursive digital filter and recession curve method and does not require any nearby site. The proposed methods were tested at two headwater wetlands in coastal Alabama. Site 17 had two nearby sites whose WLs were highly correlated to site 17's. The RMSE and Nash-Sutcliffe efficiencies were 2.9 cm and 0.98, respectively when the first method was applied to site 17. The second method was tested at site 32. For this the WL time series was separated into quick and slow response components. A combination of ANN and baseflow separation methods proved to be very efficient for WL prediction at this site, especially when the duration of quick response components of individual events were less than 6 hours. The proposed methodologies, therefore, proved useful in predicting WLs in wetlands dominated by both surface and groundwater.

## 1. Introduction

Coastal wetlands are among the most important ecosystems in terms of the services they provide (e.g., water quality improvement, water storage, habitat), but they are also among the most vulnerable. One of the most important subclass of wetlands located in coastal plains of the southeastern U.S. are headwater wetlands because of their importance in protecting downstream aquatic resources by acting as natural filters for water quality (Savage and Baker 2007). Headwater wetlands are critical components to the landscape because they occur at the interface of uplands and coastal creeks. They are characterized by water tables at or near the surface that respond rapidly to precipitation (direct and/or return flow) and evapotranspiration (ET) (Noble et al. 2007). Conversion of forested land for urban development or agricultural production can result in significant alterations to streams, wetlands and other aquatic systems (DeLaney 1995; Messina and Conner 1998; Faulkner 2004; Barksdale et al. 2014). Changes in wetland hydrology as a result of modifications in watershed land use/cover can include reduced groundwater recharge, increased surface runoff and flashy behavior (Ehrenfeld et al. 2003; Barksdale et al. 2014).

Water levels (WL) in most wetlands are generally not constant and fluctuate seasonally (riparian wetlands), daily or semi-daily (various types of tidal wetlands/marshes) or unpredictably (wetlands in low-order streams and coastal wetlands with wind-driven tides) (Mitsch and Gosselink 2000). Headwater wetlands have both ground and surface water dynamics. Thus, WLs can be above or below the ground at any given time depending on the season and climatic conditions. The role of groundwater in maintaining the wetland character is a vital element of its support for wetland ecological functions, managing wildlife habitat (Taylor and Alley 2001) and maintaining the physical and chemical characteristics/conditions in the root

zone (Hunt et al. 1999). However, quantifying the groundwater component of a wetland water budget is a very difficult endeavor (McKillop et al. 1999). To have a better understanding of groundwater/surface water contributions to headwater systems, there is a need to assess long-term WL data. WL prediction and assessment are of great importance especially in headwater wetlands because of their susceptibility to change (i.e., more frequent, rapid, large changes in WL) caused by changes in catchment land use/cover.

Models can be used to simulate WLs when there is a need to assess wetlands under various conditions (Dadaser-Celik and Cengiz 2013). WLs can be predicted through physically-based or data-driven models. Developing a physically-based model for assessing WL fluctuations requires proper characterization and synthesis of the aquifer parameters to describe the spatial variability of the subsurface hydrogeology and soil. (Taormina et al. 2012; Dadaser-Celik and Cengiz 2013). When there is insufficient knowledge of the soil and hydrogeologic characteristics of the system, and accurate prediction is more important than understanding the physical processes, black-box type models can be viable options (Nourani and Mano 2007). Artificial neural networks (ANNs) are among the black-box type models that can be applied to capture non-linear behavior of complex systems. ANN models have been used in rainfall-runoff processes (Hsu et al. 1995; Dawson and Wilby 1998; Kumar et al. 2005; Rezaeian Zadeh et al. 2010), streamflow forecasting (Kisi 2007; Yonaba et al. 2010; Isik et al. 2013), water quality (Singh et al. 2009; Kalin et al. 2010), and evaporation estimation (Kisi 2009; Tabari et al. 2010).

Due to the complexity of hydrogeological systems, modeling groundwater levels using data-driven methods has been an attractive option to researchers lately. Previous studies have focused on predicting groundwater levels at monthly (Nayak et al. 2006; Nourani et al. 2008; Jalalkamali et al. 2011; Shirmohammadi et al. 2013), weekly (Mohanty et al. 2010; Karthikeyan

et al. 2013; Mohanty et al. 2013), daily (Sahoo and Jha 2013; Shiri and Kisi 2011; Shiri et al. 2013) and six-hourly time intervals (Yoon et al. 2011). To the best of the authors' knowledge, the only study on predicting hourly groundwater levels using ANN models is Taormina et al. (2012). They developed feed forward neural networks for long term simulation (up to several months) of hourly groundwater levels in a coastal unconfined aquifer near the Lagoon of Venice, Italy.

Since headwater wetlands are dynamic systems, hourly WL data (which could again be below or above ground surface at a given moment, i.e. both surface and groundwater hydrology play key roles in WL fluctuations) are crucial in understanding the behavior of these systems under varying conditions. When they transition from more stable to flashier hydroperiods, they may lose their functioning capabilities. For instance, variations in WL within a given day were detected in wetlands influenced by varying levels of surrounding land use (Barksdale et al. 2014). These variations are partially responsible for differences detected in amphibian habitat (Alix et al. 2014), forest connectivity composition and soil conditions (Barksdale and Anderson 2014). The studies listed in the previous paragraph have all relied upon antecedent WL data as input to predict groundwater levels only. Therefore, they are not suitable for predicting WLs in wetlands impacted by surface and groundwater at hourly time scale.

Despite the widespread applications of data-driven models, especially ANNs in hydrology and water resources field, very few studies on ANN applications to wetlands have been reported, particularly in headwater wetlands. One such study was carried out by Karthikeyan et al. (2013), who evaluated weekly time series of groundwater levels of a well in the uplands of a tropical coastal wetland. They used four and eight variables including rainfall, streamflow, evaporation and water level of the well with one-week lag (case one) and one-and

two-week lags (case two) as inputs to the ANNs and concluded that the model with four inputs (case one) outperformed the other combination. In another study, Dadaser-Celik and Cengiz (2013) developed a multi-layer perceptron (MLP) scheme to model monthly average WLs at the Sultan Marshes wetland in Turkey. The model inputs consisted of climatic (precipitation, air temperature, evapotranspiration) and hydrologic data (groundwater levels, spring flow rates, and preceding water levels). They concluded that ANN models have the potential to simulate monthly WLs in wetlands. Another example of data-driven method application for WL of wetlands is the study performed by Ali (2009). A dynamic multivariate Nonlinear Auto Regressive network with eXogenous inputs (NARX) combined with principal component analysis (PCA) was developed to predict weekly WLs in the Florida Everglade's wetland systems. None of these studies attempted to predict WL at sub-weekly time scale.

The objective of this study was to develop models to predict hourly WLs in wetlands characterized by water tables at or near the surface that respond rapidly to precipitation events. Consequently, two ANN-based methodologies are proposed for wetlands whose WLs show (i) high correlation, and (ii) low to no correlation with WLs from nearby sites. Unlike most previous studies, the first methodology does not require antecedent WL. Instead this method benefits from the WL data from nearby sites and can be used to predict time series of WLs. The second method, on the other hand, requires antecedent WLs. It is a combination of ANN, recursive digital filter and recession curve method and is more useful for predicting WL response to individual rain events or for filling short period data gaps under the absence of highly correlated nearby site.

## 2. Study Area and Data Sets

The study wetlands are located in coastal Alabama in Southeast USA (Figure 2.1). This region is characterized by mild winters and hot and humid summers with mean annual temperatures ranging from 15 to 21˚C, and annual precipitation ranging from 125 to 180 cm which is fairly evenly distributed throughout the year (Noble et al. 2007). Headwater wetlands in coastal Alabama are groundwater driven and are usually located at the headwater reaches of first order streams (Noble et al. 2007). They tend to be fairly flat, however they normally occupy gradual slopes and often have hummock/hollow microtopography. These wetlands are typically comprised of alluvial soils that are classified as “wet loamy alluvial lands”, while the uplands are generally sandy soils derived from marine deposits (McBride and Burgess 1964). As part of a previous study to assess the impact of upland land use/cover on the behavior of headwater wetlands and their associated functions (Barksdale et al. 2014), hourly WLs in 15 headwater wetlands were monitored for 1 year (Figure 2.1). All the headwater wetlands were naturally groundwater driven, represented the upstream origin of local creeks and had no natural channel inflows. Historically, they were all fed primarily by shallow groundwater (except under more severe rain events). With development and other land use changes, the drainage has become enhanced into these wetlands and this has made many of the wetlands much more responsive to precipitation. In all cases, the small size and proximity of the catchments to these wetlands make them respond quickly to rainfall events as was evident in the monitoring data. Wetland water levels (relative to ground surface) were monitored in shallow wells using In-Situ Mini-Troll 500 pressure transducers from February 2011 to March 2012 (Barksdale et al. 2014). Wells were located in the interior to best approximate conditions throughout the wetland. During the summer

and fall (June through November) of 2011, drought conditions persisted across the study area with the driest period occurring May–June (National Climatic Data Center, 2012).

Most of the sites had periods of omitted data caused by pressure sensor drift or potential sensor fouling, varying from less than one to several months. In order to have a better understanding of the hydrology in these wetlands and relate them to the land use/cover conditions of their watersheds, the missing WLs needed to be predicted. The two models, which are discussed later, were tested at two sites: 17 and 32. Information regarding wetland sites and contributing watersheds are provided in Barksdale (2013) and detailed briefly here. Sites 17 and 32 were both small wetlands (<1.0 ha) located in the southern portion of Baldwin County, Alabama (Figure 2.1). Wetlands typically occupied gradual slopes eventually draining to first order streams. Sweet bay (*Magnolia virginiana*) was the most common canopy tree species in these wetlands with other common species included red maple (*Acer rubrum*) and swamp tupleo (*Nyssa biflora*). Site 17 was located in the Fish River drainage basin in the southwest portion of the county. Watershed size draining to the wetland was 78 ha with mixed land use. Over half of watershed cover (54.7%) consisted of pine and mixed forest. Site 32 was located in the southeast portion of the county draining to Perdido Bay. Contributing watershed for this wetland was 128 ha in size and also had mixed land use with 41.2% in forest and 27.3% in agriculture. These sites had no long period of missing data, thus provided a good opportunity to test the proposed models.

Hourly prediction of WL data in headwater wetlands is a challenging task. Since the studied wetland systems respond quickly to rainfall events (see Figure 2.2 as an example), shorter duration (compared to the previous studies), i.e. hourly data was considered in this study.

Figure 2.2 clearly shows the instantaneous response of the WL at site 17 to a typical rainfall event that occurred on 07/22/2011.

## 3. Model Development

As mentioned in the study objectives, two distinct models were developed for hourly WL predictions in headwater wetlands. Both models rely on ANN. Below we first provide a brief background about ANNs and then describe the two models. The models are applied to sites 17 and 32 to demonstrate their usefulness.

### 3.1 Artificial Neural Networks

An artificial neural network is made up of a number of interconnected nodes (called neurons) arranged into three basic layers (input, hidden and output). The input nodes represent no computations but distribute the inputs to the network. This kind of network is called multilayer feed forward, which is the most common ANN network, since the information passes one way through the network from the input layer to hidden and finally to the output layers (Dawson and Wilby, 1998). Mathematically, an ANN can be represented as:

$$y = f\left(\sum_{i=1}^{n} w_i p_i + b_i\right) \quad (1)$$

where, $w_i$ represents the weight vector; $p_i$ is the input vector (i=1,…, $n$); $b$ is the bias, $f$ is the transfer function; and $y$ is the output. By developing a multilayer feed forward back-propagation network, the network's weights are modified by minimizing the error between the simulated output and the target. As described in the following sections, two different models were used in this study. For each model and depending on the site where the models were applied, inputs and

outputs varied. In general inputs were some combinations of water levels from nearby sites, antecedent water level and hourly precipitation. Model outputs were always the water levels at different lead times. A simple trial and error procedure was carried out to test tangent sigmoid and logistic sigmoid transfer functions for hidden layer. The tangent sigmoid transfer function performed better and thus was implemented for training and testing of the proposed networks. Other studies (e.g. Rezaeian Zadeh et al. 2010, Yonaba et al. 2010) also found similar results. The same procedure was carried out to find the best training algorithm and finally scaled conjugate gradient (*scg*) training algorithm was chosen (Rezaeian-Zadeh et al. 2013c). Readers are referred to Rezaeian Zadeh et al. (2010), Rezaeianzadeh et al. (2013a, b) and Rezaeian-Zadeh et al. (2012) for details about artificial neural networks (ANNs), transfer functions and scaled conjugate gradient (*scg*) training algorithm. A three-layered network was developed and considered to best fit the data. Before applying the ANN models, the data were normalized to [0.05, 0.95] using a linear transformation (Rezaeian Zadeh et al. (2010); Rezaeianzadeh et al. (2013a, b) :

$$X_n = 0.05 + 0.9\frac{X_r - X_{\min}}{X_{\max} - X_{\min}} \quad (2)$$

where, $X_n$ and $X_r$ are the normalized and the original inputs and $X_{min}$ and $X_{max}$ are the minimum and maximum of input data, respectively.

One of the steps in finding the best network architecture is determining the optimum number of neurons in the hidden layer. The networks resulting in the smallest error were selected for WL prediction. One neuron in the output layer was selected. The target error for the training of networks was set to $10^{-4}$ (dimensionless). The training of networks was stopped when their performances reached the target error. *Tansig* (i.e., tangent sigmoid) and *purelin* (linear) transfer functions were used in the hidden and output layers, respectively. The normalized data were

employed to train each of the models, all of which being three-layered networks. The model outputs were then transformed back to the original scale and then the root mean square error (*RMSE*), coefficient of determination ($R^2$), Nash-Sutcliffe coefficient (*NS*) (Nash and Sutcliffe, 1970) and Akaike's information criterion (*AIC*) (Qi and Zhang 2001; Kalin et al. 2010) performance indices were computed for the training and test data sets. Program codes were written in MATLAB language for the ANN simulations (MathWork, Inc. 2010).

Depending on the availability of data (length or number of data) and the scales (hourly, daily, monthly, etc.) of modeling, various types of splitting the whole dataset have been considered in training and testing phases of ANN models by different researchers. To the best of our knowledge, there are no precise guidelines for splitting the dataset into training and testing phases. For instance, Kisi (2009) used 80% of the whole data for training and the remaining 20% for testing in monthly scale and Isik et al. (2013) used 60% of data for training and the rest (40% of data) for testing and validation phases in daily scale. Generally, 50% to 50% (Kisi 2007), 60% to 40% (Sarangi and Bhattacharya 2005), 70% to 30% (Mutlu et al. 2008) and 80% to 20% (Kisi 2011; Kisi 2009 ) are the most common splitting portions in the application of ANN models in hydrology when the aim is to divide the dataset into two parts. In this study, roughly 70% of the data was used for training and the remaining 30% was used for testing.

### 3.1.1 Continuous Simulation Model (CSM)

In this model, nearby sites having WLs highly-correlated with those from the target site are selected and WL data from those sites are considered as inputs to the ANN model along with hourly precipitation data from target site at various lags. Spearman's rank correlation ($r_s$) was used to decide on the inputs to construct the ANN models, which is given by (Press et al. 1996):

$$r_s = 1 - \frac{6\sum_{i=1}^{n} d_i^{\,2}}{n(n^2 - 1)} \qquad (3)$$

where, $d_i$ is the difference between each rank of corresponding values of WL at each site and those values of target site and *n* is the number of observations. The value of $r_s$ lies between –1 and +1. Values closer to ±1 indicate close association between two variables. A negative sign indicates inverse association. In this study, sites having $r_s$ >0.9 were subjectively assumed to be highly-correlated sites. Anything with $r_s$ below 0.7 would explain no more than 50% ($r_s^2$ of 0.7 → 0.49) of the variation in data. Thus, those sites were deemed not highly-correlated. Accordingly, an ANN-based prediction model was developed that utilize precipitation of the target site and WL data from two to three nearest sites whose WLs are highly-correlated with the target site's WLs.

### 3.1.2 Event-based Model (EBM)

Sometimes there are no nearby sites or WLs of the existing ones are weakly correlated with the target site's WLs. In those cases, an alternative method is needed. For this purpose, the hydrographs of the WLs are first split into high and low frequency (quick and delayed response) components using a digital filter. Quick response component only exists during rain events. An ANN model was then developed based on antecedent WLs and hourly precipitation data to predict the WLs (high+low frequency) for the high frequency periods. The WLs during rainless periods were estimated using the recession curve method.

### 3.1.2.1 Recursive Digital Filter

Despite the importance of groundwater flows in the budget of many wetlands, there is a poor understanding of groundwater hydraulics in wetlands, particularly in those that have organic soils (Mitsch and Gosselink, 2000), meaning that distinguishing between surface and groundwater is not a simple task. In this study, the recursive digital filter technique was used to 1) separate the high and low frequency components of WLs, which are sometime only groundwater, sometime groundwater + surface water; and 2) to help estimate the recession constant ($K_r$) needed for the recession curve method (see below) in estimating low frequency components. It should be mentioned that this technique is commonly used in separating streamflow hydrographs into baseflow and direct runoff components, while its application for WL data will be discussed here. This procedure is based upon a recursive digital filter commonly used in signal analysis and processing (Lyne and Hollick, 1979; Nathan and McMahon, 1990). The filter is of the simple form:

$$f_k = \alpha f_{k-1} + \frac{(1+\alpha)}{2}(y_k - y_{k-1}) \qquad (4)$$

where, $f_k$ is the filtered quick response at the $k^{th}$ sampling instant, $y_k$ is the original data, and $\alpha$ is the filter parameter. The filtered slow response component is thus $s_k = y_k - f_k$. Nathan and McMahon (1990) suggested that $\alpha$ typically varies from 0.90 to 0.95. In this study the filter was applied to site 32 using various filter parameter values within and outside this proposed range. The optimum value for $\alpha$ was determined by trial and error. As a starting point, the WL time series and the corresponding low frequency component time series generated with $\alpha$=0.90 were plotted on the same graph. At the optimal value of $\alpha$, the inflection points on the WL time series should correspond to the separation points of the two time series. The $\alpha$ parameter was

progressively updated so that most inflection points coincided with the separation points. The point of inflection is located where the curvature vanishes. This point is the onset of a linear line on the recession limb of WL hydrograph in semi-logarithmic scale.

#### 3.1.2.2 Recession Curve Method

The recursive digital filter method is only useful in separating the WL time series into high and low frequency components. It cannot be used for predictive purposes. Therefore, the recession curve method, which is another technique normally used with streamflows, was adopted to predict the WLs during no-rain periods (i.e. no high frequency component). Recession curve, which is part of the hydrograph that gradually decays during rainless periods, can be estimated by streamflow recession analysis of historic streamflow measurements (Linsley et al., 1958; Burnash et al., 1973; Leavesley et al., 1983). The recession curve is described by:

$$q_t = q_O * K_r^t \qquad (5)$$

where, $q_t$ = flow at time $t$ with respect to an initial flow $q_o$ and $K_r$ is the recession constant. It's not feasible to have individual $K_r$ values for the recession constant for each storm event. An optimal, representative $K_r$ value is needed to predict WLs. This value was obtained again by trial and error so that most inflection points coincided with the separation points obtained from the recursive digital filter. In this study, WLs replaced flow. Equation (5) is then used to estimate the recession limbs (periods with no high frequency component) of the WL time series.

## 4. Results and Discussion

The CSM and EBM were evaluated at sites 17 and 32, respectively. Recall that CSM requires nearby sites where there is a strong correlation between their WL data and the modeled

site's WL data, while EBM does not have such a requirement and as a matter of fact does not use any WL data from other sites. Site 17 was selected to test the CSM because it meets the condition of having highly correlated nearby sites. Site 32 was selected to test the EBM, because the correlation between its WLs and nearby site's WLs are not too strong. However, CSM was applied to site 32 too to demonstrate the need for EMB model when the nearby site's WLs are not highly correlated to the target site's WLs.

### 4.1 Continuous Simulation Model (CSM)

The Spearman's rank correlation (which does not assume any relationship between variables) of WL values of site 17 with those values from site 26 and 9 were equal to 0.93 and 0.90, respectively, which indicates a very strong correlation. The correlation of WL from site 17 with hourly precipitation values with one- and two-hour lag ($P_{17}(t\text{-}1)$, $P_{17}(t\text{-}2)$) were equal to 0.10 and 0.11 respectively. Table 2.1 summarizes the input combinations used in Eq. (1) and the model performances with the train and test data. The best model (#4 in Table 2.1) has *RMSE*=2.92 cm, *NS*=0.98, and $R^2$=0.99 in test phase. It also has the lowest *AIC*, confirming that it is also the most parsimonious model for site 17. Although there is very small correlation between WL values of site 17 and hourly precipitation values, according to the results of developed models from Table 2.1, it is obvious that addition of precipitation values appreciably reduced the *RMSE*. The time series and WL exceedance curve (similar to flow duration curve) of simulated and observed WL data in the testing phase for site 17 is shown in Figure 2.3 for the best model. It is apparent that the proposed model is very effective when there are nearby sites with highly correlated WL data. Note that addition of more sites, which had lower correlations than 26 and 9, did not improve the model performance any further.

The model was also tested at site 32, the WLs of which do not have very high correlations with the WLs of nearby sites. The results of Spearman's rank correlation for WL of site 32 with those values from site 40, 9 and 17 were equal to 0.51, 0.45 and 0.54, respectively. The correlation of WL data from site 32 with hourly precipitation values of site 32 with one- and two-hour lags ($P_{32}(t\text{-}1)$, $P_{32}(t\text{-}2)$) were almost the same, equal to 0.13. Table 2.2 presents the various input combinations and the corresponding model performances. Although model performances shown in Table 2.2 are good (*RMSE*=3.34 cm, *NS*=0.80), the simulated versus observed time series and the WL exceedance curve have periods with large errors (Figure 2.4). The WL exceedance curve also shows consistent overestimation, especially during low WL conditions (Figure 2.4). Systematic errors most of the time are easier to fix. These types of errors are related to model structure and could be stemming from ignoring some of the processes or due to use of some redundant variables [Kalin et al. 2010]. The overestimation (systematic) error here may have originated from lack of information regarding having no site highly-correlated with site 32.

To check if the proposed methodology (CSM) works well with site 32, comparison of the flashiness may also be useful. A modified version of the Richard-Baker flashiness index (*RB*) (Baker et al. 2004) proposed by Barksdale et al. (2014) is as follows:

$$RB = \left( \frac{\sum_{i=1}^{n} \left| y_i - y_{i-1} \right|}{\sum_{i=0}^{n} y_i} \right) * 1000 \qquad (6)$$

The *RB* values for simulated and observed WLs were 11.63 and 7.80, respectively. The model predicts a 50% more flashy system. In spite of the differences in *RB* and discrepancies

between observed and simulated times series as well as WL exceedance curves (Figure 2.4), depending on the expectations, CSMs can still be a viable option. The maximum error in the predicted WL was never higher than 10.0 cm in Figure 2.4. Further, as long as highly correlated neighboring sites have long records, CSM can be used to generate more accurate time series compared to EBM.

### 4.2 Event-based Model

This model was tested at site 32, the WLs of which have low correlations with the WLs of its nearby sites. The optimal values of the filter parameter $\alpha$ and the recession constant $K_r$ were both 0.97 at this site. One needs to be careful in this model when the data is split into training and testing datasets. After separating the WL hydrograph into high and low frequency components, there will be far less data in the former category. Therefore, it may not be wise to select for example the first 70% of data for training and the rest for testing phases. Further, when there are distinct dry and wet periods, the trained network may not capture both wet and dry conditions, and thus cannot be considered as an optimally trained network. Note that existence of long dry and/or wet periods is not an issue with CSM, because nearby sites providing WL data into the model will have signatures of those climatic conditions.

To remedy this problem, Bartlett's test and t-test (Rezaeian-Zadeh et al. 2010) were used to obtain the optimal datasets for training and testing phases of high frequency components. The homogeneity of variances for two populations can be determined by using Bartlett's (or Levene's) test. According to the results of Bartlett's test ($p$-value = 0.42), the t-test must be performed based on the equal variances assumption. The $p$-value for t-test was equal to 0.12, which is higher than $\alpha$=5% meaning there is no statistically significant difference between

training and testing datasets, and both include high, mean and low values of data. Figure 2.5 shows the boxplots for training and testing datasets.

Twelve separate event-based ANN models were developed to predict one- to six-hour ahead WLs (i.e. $WL\ (t+1)$, $WL\ (t+2)$,…, $WL\ (t+6)$) during periods when there is a rain event. In each model only precipitation and the WL corresponding to the time of rainfall onset were used as inputs to the Eq. (1). The only differences were time lags. Table 2.3 presents the input combinations of these twelve event-based models (EBMs). Models are divided into two sets. The first set uses hourly precipitation values, whereas the second set relies on aggregate precipitation values from the onset to the prediction time step (Table 2.3). The ANN models were trained and tested using those optimally split datasets. Figure 2.6 shows the scatter plots of observed and simulated WLs using EBMs with the first set of inputs. The *RMSE*, *NS* and $R^2$ values for the one-hour ahead WL prediction are 1.4 cm, 0.98 and 0.98, respectively. For 6 hour ahead predictions, those values are 2.7 cm, 0.92 and 0.92, respectively. Figure 2.6 and the performance metrics clearly indicate the ability of EBMs with separately-included precipitation data in predicting WLs up to six hours lead time during rain events. As expected, the skill of the model diminishes gradually from one- to six-hour lead time.

Note that the discussed event-based ANN models were trained and tested based on the inclusion of precipitation values separately. The other version of event-based ANN models (using the second set of inputs) were developed to see how accurate they can work in comparison to the aforementioned version (see Table 2.3). In this version, in addition to WL data, a summation of precipitation values up to the target time step was imported into the model as input, meaning that there is only one precipitation value imported to this version of EBMs. This exercise could be helpful in cases only total rainfall depth is available. Figure 2.7 displays the

scatter plots of observed and simulated WLs for these six event-based ANN models. It is evident that this version works well up to three hours ahead WL prediction compared to the previous version of the EBMs (see Figure 2.6). On the other hand, the differences in model performances are quite discernable from four to six-hour ahead WL prediction. The EBMs with hourly precipitation data inputs outperformed the other one. A comparison of AIC values from Figure 2.6 and Figure 2.7 for each time step demonstrates this fact. Roughly, all six models that rely on hourly precipitation data are the more parsimonious compared to their counterparts, which use cumulative precipitation.

For estimating the recession limb of WL hydrographs, the recession curve method was used with $K_r$ = 0.97. Recession parts of eight WL hydrographs were randomly selected from site 32 (based on the inflection points of WL hydrograph on semi-logarithmic plot). The results of the proposed method for recession hydrographs are presented in Table 2.4. According to this table, the maximum and the average of error for these randomly selected recession hydrographs were 7.2 % and 2.7 %, respectively. This shows that the proposed method can be efficient when splitting the hydrograph into two high and low frequency components. Two recession hydrographs among those randomly selected recession limbs are displayed in Figure 2.8 for demonstration purposes.

## 5. Summary and Conclusions

In this study two different methodologies were proposed for hourly WL prediction in headwater wetlands and applied to wetlands in south Alabama. A correlation analysis was employed to find the associations between/among the target wetland site and nearby site(s). In the case of having high correlation between WLs of target and nearby sites, CSM (used WL data

from nearby sites and hourly precipitation data as input) is advised. Otherwise, EBM is recommended which require partitioning of the WL hydrographs into high and low frequency components. One of the advantages of CSM is that it does not require any antecedent WL data from the target site while almost all the previous studies relied upon antecedent WL data in developing their models. Twelve separate event-based ANN models were developed to predict one- to six-hour ahead WLs using antecedent WL and precipitation as inputs. In six out of the twelve models, hourly precipitation values were used and the rest used cumulative precipitation. Note that in CSMs, WL data from neighboring wetland sites were imported to the ANN models, while in EBMs antecedent WLs were one of the drivers of the developed ANN models. Eventually, a combination of recursive digital filter (to separate the high and low frequency components and to find the optimal recession constant) and the recession curve methods was employed to estimate the low frequency components.

Water level in wetlands, which is one of the most important hydrologic indices, can be simulated through physically-based models or empirical methods (black-box models). Physically-based models consider the ground/surface water interactions and doing so requires proper characterization and synthesis of the surficial aquifer parameters to describe the spatial variability of the subsurface hydrogeology and soil. For instance, groundwater flow patterns and their interactions with surface water at the watershed scale are influenced by topography, geology, and the climate of the region. Furthermore, physically-based watershed models vary in complexity in handling the surface water groundwater interactions (Hantush et al. 2011). Such interactions in wetlands are complex and an understanding of basic principles and physical laws governing exchange between groundwater and surface water is needed for modeling the interactions at multiple scales (Hantush et al. 2011). In this study, accurate prediction was more

important than understanding the physical processes. In the first method, CSM tried to continuously capture water level fluctuations without paying attention to the surface water groundwater interaction. The second method, which is a combination of EBM, recursive digital filter and recession curve methods, distinguishes between high and low frequency components of water level hydrograph and provides some level of understanding about the groundwater contribution (low frequency component) to the wetland system. Since the headwater wetland systems studied in this paper are naturally groundwater driven, recursive digital filter and the recession curve analyses reveal the groundwater contribution to these headwater wetlands. On the other hand, EBM captures the contribution of both surface water and groundwater components.

The following conclusions can be drawn from this study:

1. The use of WL data from nearby sites highly correlated with those from the target site can help prediction of hourly WL fluctuations with high accuracy (CSM).
2. Although Spearman's rank can be employed to find the sites with high level of correlation, those results cannot be considered as the ultimate input combinations. For example, adding hourly precipitation data having low correlation with WLs considerably improved the accuracy of the CSM.
3. In cases with low to no correlation between WL data from target site and those from nearby sites, partitioning the WL hydrograph into two high and low frequency components is proposed. Application of recursive digital filter can be an effective method in separating continuous hydrographs and finding the optimal recession constant.
4. Bartlett’s test and t-test are prominent tools for finding the optimal training and testing datasets in the cases of developing event-based ANN model.

5. EBMs showed the ability to accurately predict WLs up to six hours lead time during rain events.

This study showed that ANN models can effectively be used to predict WL data in headwater wetlands that respond quickly to rainfall events. The results showed that the methodologies introduced in this study are capable of capturing the oscillations in WL at hourly resolution especially in the headwater sites located in southeastern US. Having the ability to predict WL in the headwater wetlands with flashy behavior, the proposed methods in this study should be applicable to other systems/locations with various (low to high) oscillations. The results of this study and the proposed methods can be useful to eco-hydrologists, wetland researchers as well as decision makers to fill the missing data and/or predict WL several steps ahead of time.

**Acknowledgment**: This study was partially funded by Mississippi-Alabama Sea Grant Consortium (MASGC), U.S. Environmental Protection Agency (EPA) and Auburn University Center for Environmental Studies at the Urban-Rural interface (CESURI).

Table 2.1: Performances of continuous simulation model (CSM) with various input combinations for predicting water levels (WL) at site 17.

| | | | Training phase | | | | Testing phase | | | |
|---|---|---|---|---|---|---|---|---|---|---|
| Model no. | Input combinations | ANN ($\alpha$, $\beta$, $\gamma$) | *RMSE* (cm) | *NS* | $R^2$ | *AIC* | *RMSE* (cm) | *NS* | $R^2$ | *AIC* |
| 1 | $WL_{ST\text{-}26}$ | (1,8,1) | 8.12 | 0.93 | 0.93 | 1.820 | 4.96 | 0.96 | 0.97 | 1.392 |
| 2 | $WL_{ST\text{-}26}$, $WL_{ST\text{-}9}$ | (2,8,1) | 8.15 | 0.93 | 0.93 | 1.823 | 3.70 | 0.98 | 0.98 | 1.139 |
| 3 | $WL_{ST\text{-}26}$, $WL_{ST\text{-}9}$, $P_{17}(t\text{-}1)$ | (3,8,1) | 7.53 | 0.94 | 0.94 | 1.755 | 3.96 | 0.97 | 0.98 | 1.199 |
| 4 | $WL_{ST\text{-}26}$, $WL_{ST\text{-}9}$, $P_{17}(t\text{-}1)$, $P_{17}(t\text{-}2)$ | (4,8,1) | 6.88 | 0.95 | 0.95 | 1.676 | 2.92 | 0.98 | 0.99 | 0.932 |

Note: ANN ($\alpha$, $\beta$, $\gamma$): $\alpha$= number of inputs; $\beta$ and $\gamma$ are the number of neurons in the hidden and output layers of ANNs, respectively. ST=site; WL= water level,

Table 2.2: Performances of continuous simulation model (CSM) with various input combinations for predicting water levels (WL) at site 32.

| | | | Training phase | | | | Testing phase | | | |
|---|---|---|---|---|---|---|---|---|---|---|
| Model no. | Input combinations | ANN ($\alpha$, $\beta$, $\gamma$) | *RMSE* (cm) | *NS* | $R^2$ | *AIC* | *RMSE* (cm) | *NS* | $R^2$ | *AIC* |
| 1 | $WL_{ST\text{-}40}$ | (1,8,1) | 6.96 | 0.60 | 0.60 | 1.686 | 7.42 | 0.54 | 0.56 | 1.742 |
| 2 | $WL_{ST\text{-}40}$, $WL_{ST\text{-}9}$ | (2,8,1) | 6.88 | 0.61 | 0.61 | 1.676 | 5.91 | 0.72 | 0.72 | 1.545 |
| 3 | $WL_{ST\text{-}40}$, $WL_{ST\text{-}9}$, $WL_{ST\text{-}17}$ | (3,8,1) | 6.40 | 0.66 | 0.66 | 1.614 | 3.66 | 0.85 | 0.89 | 1.130 |
| 4 | $WL_{ST\text{-}40}$, $WL_{ST\text{-}9}$, $WL_{ST\text{-}17}$, $P_{32}(t\text{-}1)$ | (4,8,1) | 5.41 | 0.76 | 0.76 | 1.468 | 3.34 | 0.80 | 0.91 | 1.052 |
| 5 | $WL_{ST\text{-}40}$, $WL_{ST\text{-}9}$, $WL_{ST\text{-}17}$, $P_{32}(t\text{-}1)$, $P_{32}(t\text{-}2)$ | (5,8,1) | 5.48 | 0.75 | 0.75 | 1.480 | 3.36 | 0.72 | 0.91 | 1.058 |

Note: ANN ($\alpha$, $\beta$, $\gamma$): $\alpha$= number of inputs; $\beta$ and $\gamma$ are the number of neurons in the hidden and output layers of ANNs, respectively. ST=site; WL= water level.

Table 2.3: Input combinations of event-based ANN models to predict one- to six-hour ahead WLs at site 32.

| Prediction lead time | Models that use hourly precipitation | Models that use cumulative precipitation |
|---|---|---|
| $WL$ ($t$+1) | $WL(t)$, $P(t)$, $P(t+1)$ | $WL(t)$, $P_{sum}(t: t+1)$ |
| $WL$ ($t$+2) | $WL(t)$, $P(t)$, $P(t+1)$, $P(t+2)$ | $WL(t)$, $P_{sum}(t: t+2)$ |
| $WL$ ($t$+3) | $WL(t)$, $P(t)$, $P(t+1)$, $P(t+2)$, $P(t+3)$ | $WL(t)$,$^{*}P_{sum}(t: t+3)$ |
| $WL$ ($t$+4) | $WL(t)$, $P(t)$, $P(t+1)$, $P(t+2)$, $P(t+3)$, $P(t+4)$ | $WL(t)$, $P_{sum}(t: t+4)$ |
| $WL$ ($t$+5) | $WL(t)$, $P(t)$, $P(t+1)$, $P(t+2)$, $P(t+3)$, $P(t+4)$, $P(t+5)$ | $WL(t)$, $P_{sum}(t: t+5)$ |
| $WL$ ($t$+6) | $WL(t)$, $P(t)$, $P(t+1)$, $P(t+2)$, $P(t+3)$, $P(t+4)$, $P(t+5)$, $P(t+6)$ | $WL(t)$, $P_{sum}(t: t+6)$ |

$^{*}P_{sum}(t: t+3) = P(t) + P(t+1) + P(t+2) + P(t+3)$

Table 2.4: Performances of the recession curve method for predicting the recession limb of WL hydrograph.

| Start date | Initial WL (cm) | Ending WL (cm) | Estimated ending WL (cm) | Error (%) |
|---|---|---|---|---|
| 03/06/2011 | 26.08 | 24.72 | 25.04 | 1.30 |
| 03/11/2011 | 26.30 | 24.28 | 25.35 | 2.18 |
| 03/20/2011 | 18.89 | 18.52 | 18.79 | 1.49 |
| 07/24/2011 | 31.01 | 30.24 | 30.38 | 0.47 |
| 09/04/2011 | 47.65 | 44.46 | 46.81 | 5.29 |
| 12/07/2011 | 11.89 | 11.19 | 11.33 | 1.25 |
| 02/25/2012 | 41.38 | 40.95 | 41.01 | 0.15 |
| 03/18/2012 | 32.32 | 28.16 | 30.17 | 7.17 |

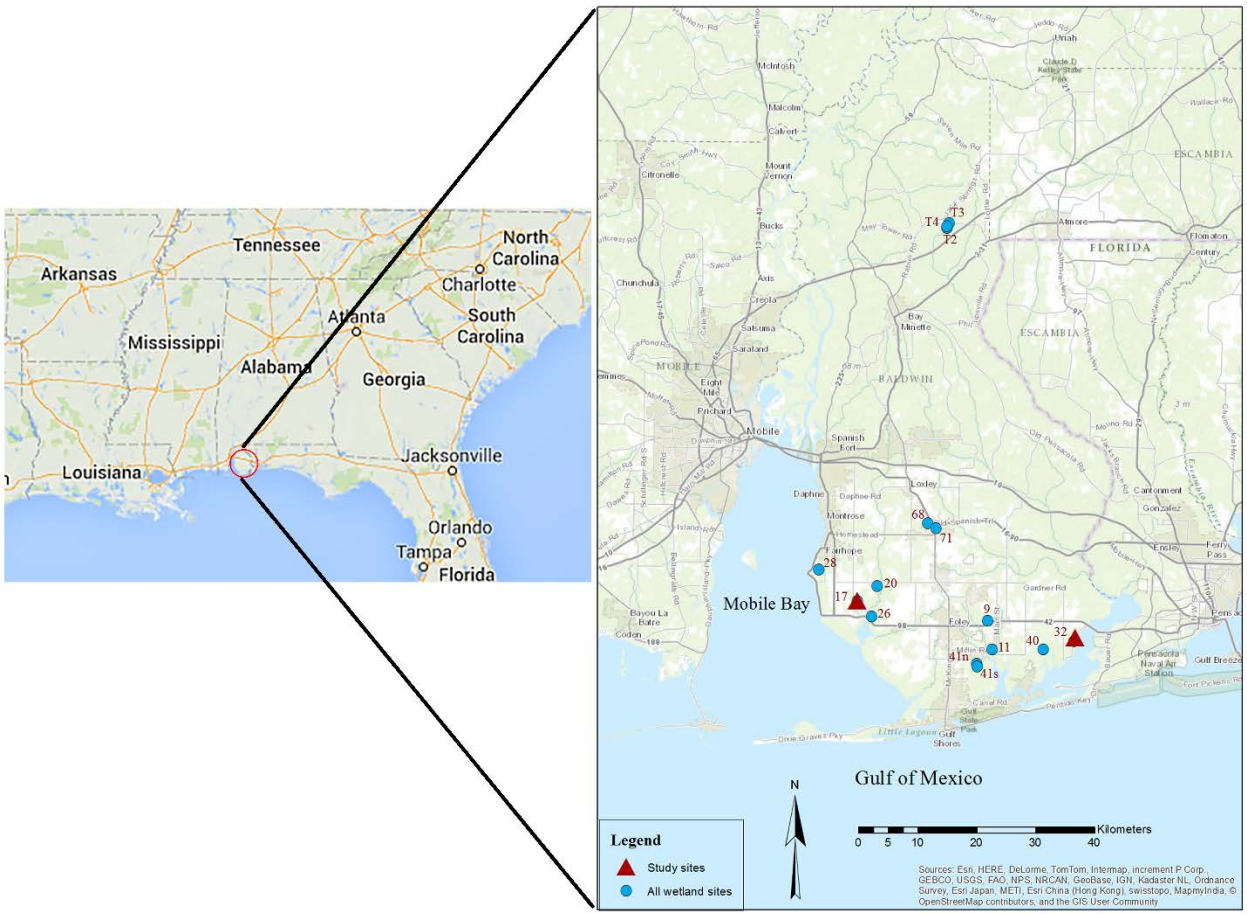


Figure 2.1: Location of study sites (data from Esri, HERE, DeLorme, TomTom, Intermap, increment P Corp., GEBCO, USGS, FAO, NPS, NRCAN, GeoBase, IGN, Kadaster NL, Ordnance Survey, Esri Japan, METI, Esri China (Hong Kong), swisstopo, MapmyIndia, OpenStreetMap contributors, and the GIS User Community)

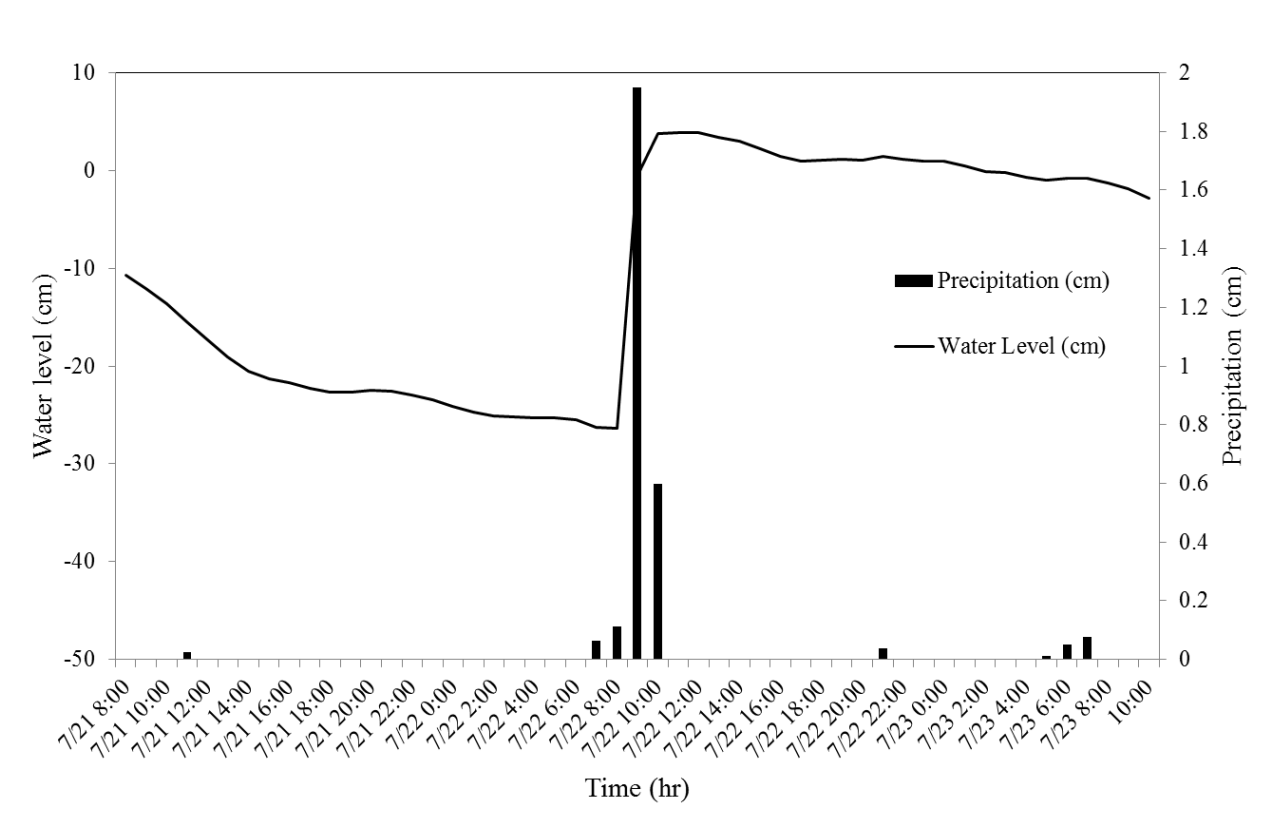


Figure 2.2: Observed water level (WL) response to a rainfall event on 07/22/2011 at site 17 as an example to the flashy behavior of headwater wetland systems.

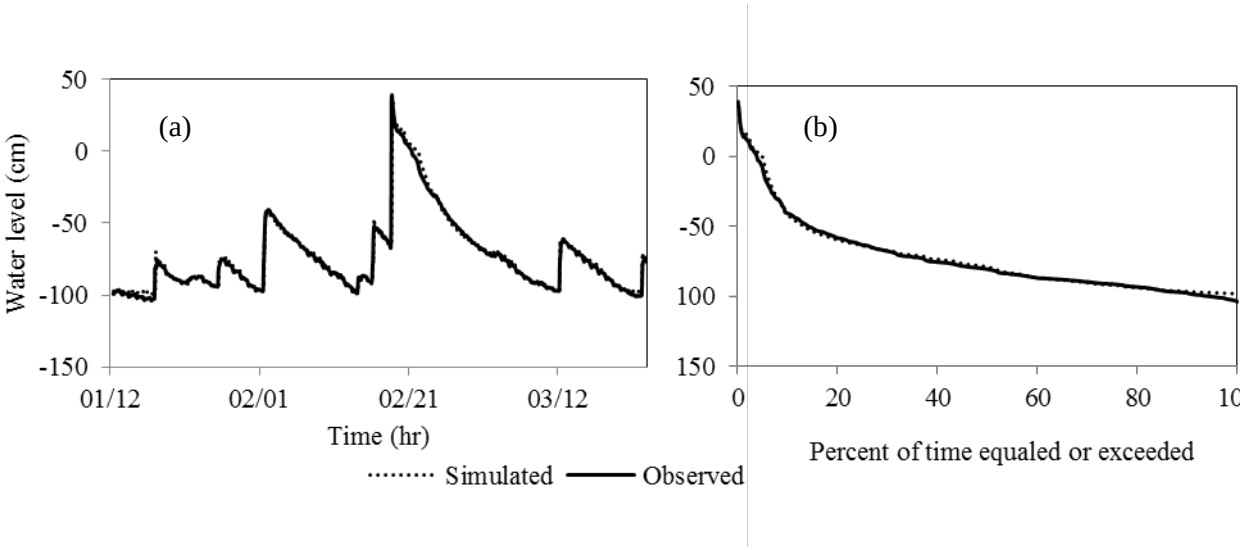


Figure 2.3: (a) Time series of simulated and observed WLs in the testing phase of site 17 with the Continuous Simulation Model (CSM) in 2012; (b) corresponding WL exceedance curves

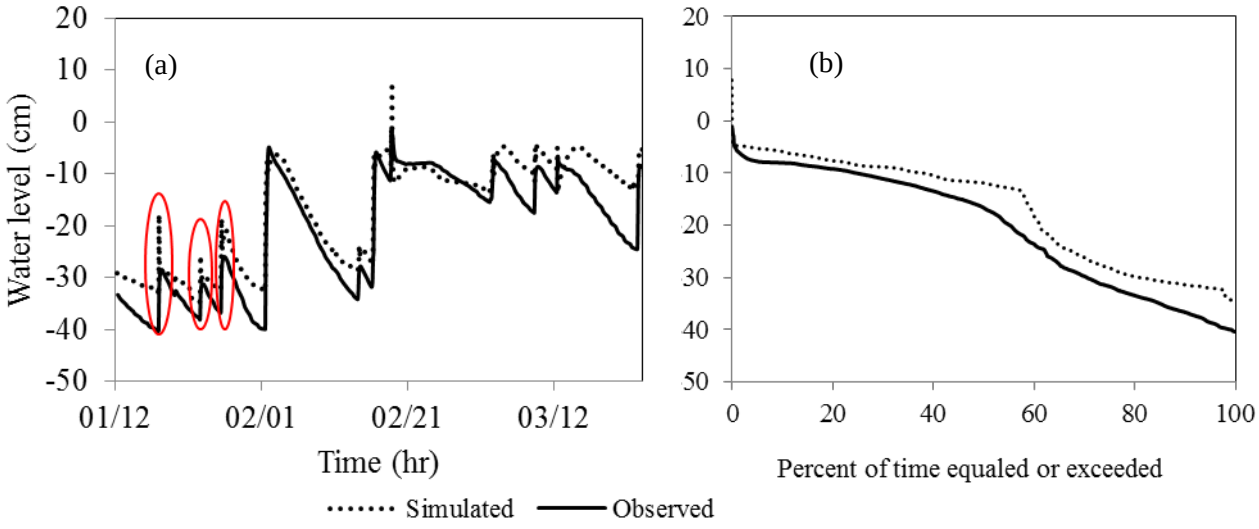


Figure 2.4: (a) Time series of simulated and observed WLs of site 32 in the testing phase using the Continuous Simulation Model (CSM) in 2012, (b) corresponding WL exceedance curves.

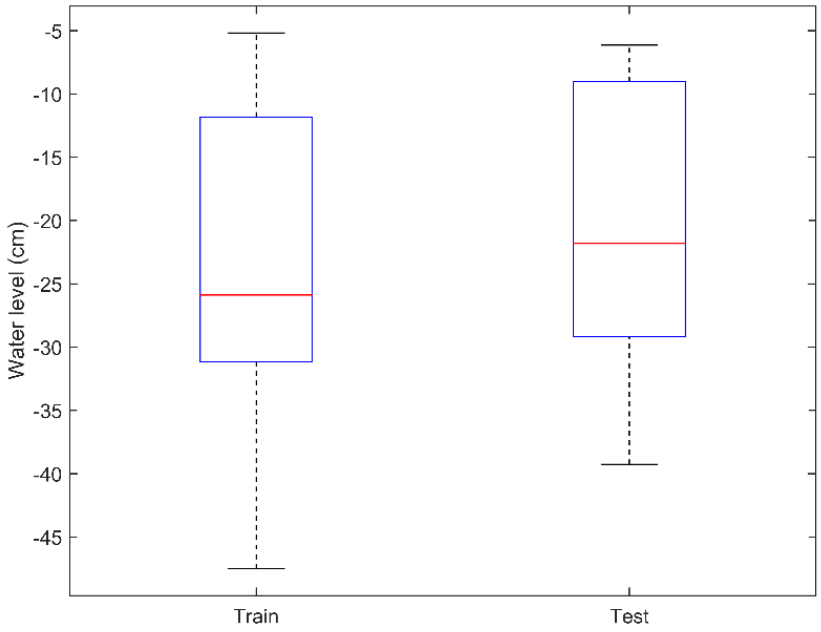


Figure 2.5: Boxplot for optimal training and testing datasets of WLs from the periods with rain events (i.e., they have high frequency components).

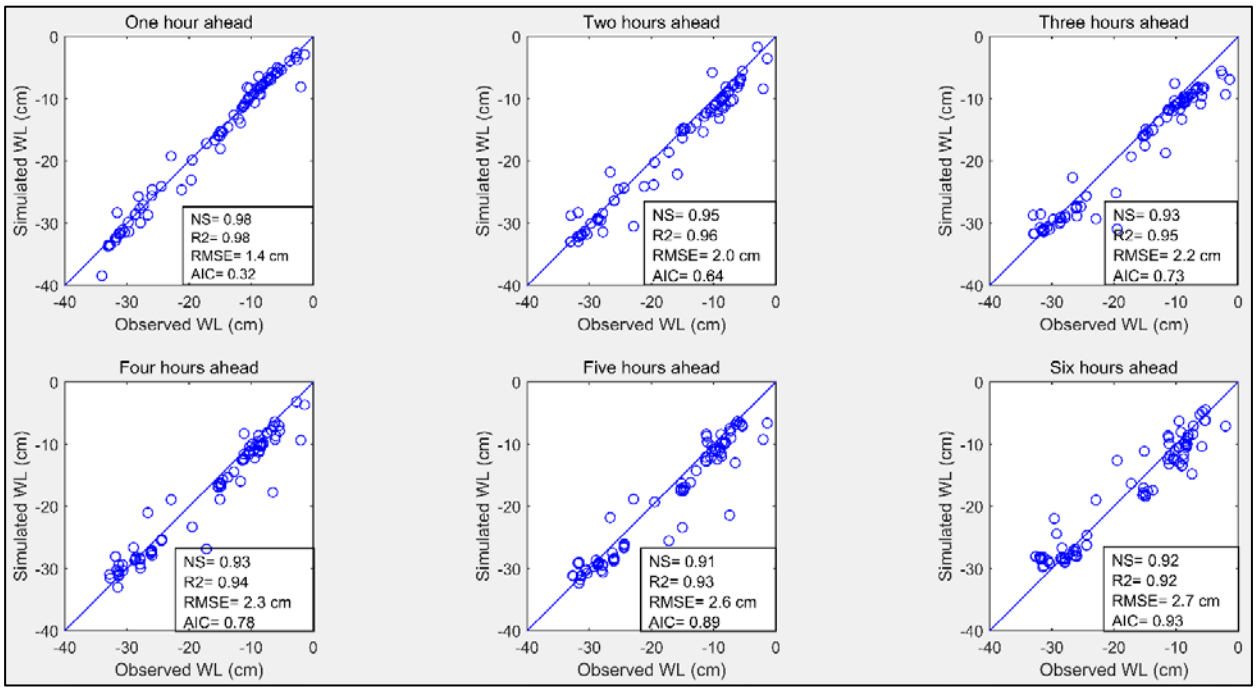


Figure 2.6: Scatter plots for predicted WLs of site 32 in testing phase using the Event Based Model (EBM); this model uses hourly precipitation values as opposed to cumulative precipitation values (see Figure 2.7).

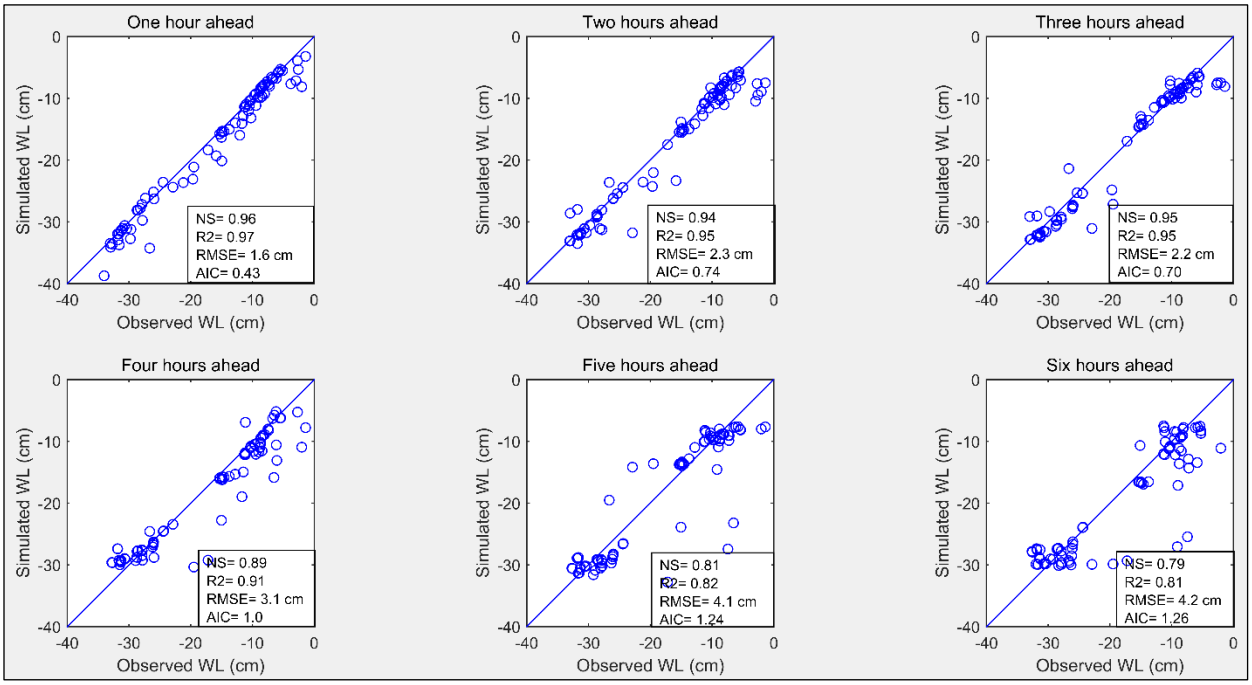


Figure 2.7: Scatter plots for predicted WLs of site 32 in testing phase using the Event Based Model (EBM); the summation of precipitation values up to target time step was considered in this model.

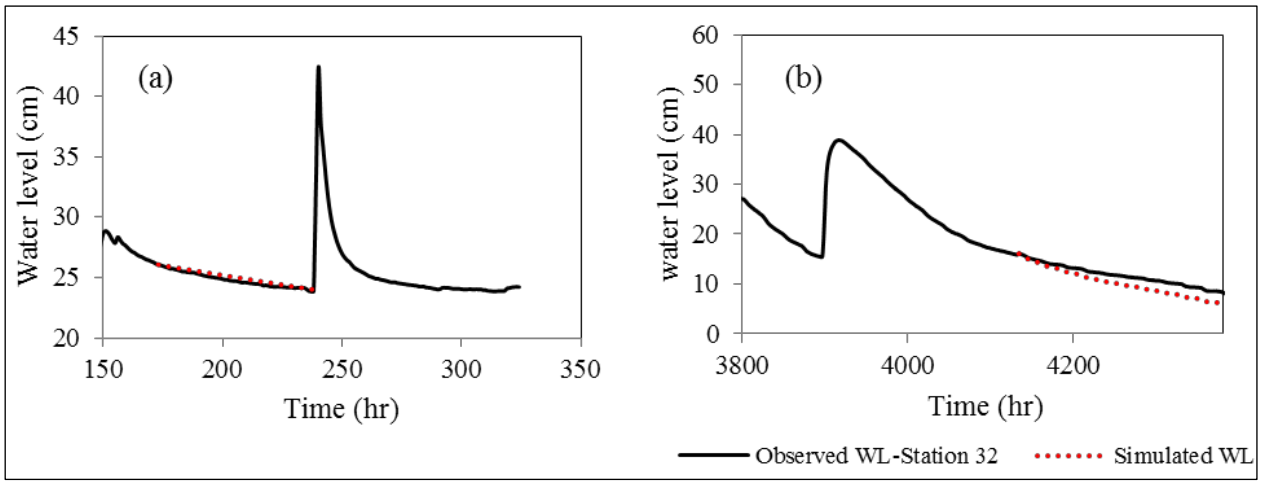


Figure 2.8: Recession WL hydrograph estimation using recession curve method from (a) March 6, 2011; to March 7, 2011; (b) from December 7, 2011; to December 17, 2011, at site 32.

# Chapter 3 : An Integrated Approach for Modeling Wetland Water Level Prediction: Application to Headwater Wetlands in Coastal Alabama


## Abstract

A hybrid modeling approach was developed in this paper for improved water level (WL) predictions in wetlands, by coupling a watershed model with artificial neural networks (ANNs). In this approach, baseflow and stormflow estimates from the watershed draining to a wetland are first estimated using an uncalibrated Soil and Water Assessment Tool (SWAT). These estimates are then combined with meteorological variables and utilized as inputs to an ANN model for predicting daily WLs in wetlands. Application of the developed methodology to a typical headwater wetland in coastal Alabama, USA, showed great promise. To demonstrate the utility of this approach, the developed model was used to assess the potential impacts of climate change on WL fluctuation in this headwater wetland. Historical observations (1951-2005, representing baseline period) and future projections from 11 downscaled, and bias-corrected global climate model (GCM) outputs of precipitation and temperature (2006-2060, representing future period) were used to predict WLs over 1951-2060. Trend analysis shows both increasing and decreasing trends in the predicted WLs for the future period compared to the baseline period. The decreasing trends are dominant particularly in low and high WLs whereas the medium WLs show increasing trends. Water levels predicted with this hybrid model were also used to explore possible teleconnections between El Niño Southern Oscillation (ENSO) and WLs in the study wetland. Results show that both precipitation and the variations in WLs were partially affected by ENSO. The findings suggest wetter conditions in winter regarding precipitation during El Niño in Coastal Alabama. However, WL reduction in spring during El Niño is expected. Precipitation and WLs are also correlated to ENSO with up to two-month lag time. The findings

of this study and the developed methodology/tools are useful to predict long-term WLs in wetlands, identify the probable future trends of wetlands' hydro-climatic components and eventually construct more accurate restoration plans under climate change.

## 1. Introduction

Headwater wetlands are among one of the most important types of wetlands located in coastal plains of southeastern U.S. Since they are often the source of first and second order perennial streams, they act as natural filters for water quality improvements and therefore are crucial in protecting downstream aquatic systems (Savage and Baker 2007). Headwater wetlands are characterized by water tables at or near the surface that respond rapidly to rainfall events (Noble et al. 2007). Driven by both groundwater and surface water inputs, water levels (WLs) can be above or below the ground at any given time depending on the season and climatic conditions (Rezaeianzadeh et al. 2015); this dynamic behavior creates a complex ecosystem. The seasonal patterns of WL in a wetland (i.e., hydroperiod) exhibit annual variation in response to climatic and antecedent conditions (Mitsch and Gosselink, 2015). Hence, long-term WL predictions can be a valuable source for evaluating these year to year variabilities. Furthermore, WL prediction and assessment are of great importance especially in headwater wetlands since changing climate and land use/cover in watersheds draining to the wetlands affect WLs.

It is now widely accepted that climate is changing and by the end of this century temperature and precipitation patterns will be altered (Acreman et al. 2009), which can have considerable implications for all ecosystems, especially wetlands, whose ecological characters are highly dependent on their hydrological regime. Changes in wetland water balance due to

climate change could alter wetland extent or cause wetland loss (Records et al. 2014). For instance, van der Valk et al. (2015) reported that a 25–30 cm increase or decrease in inter-annual WLs of Florida Everglades can lead to changes in the number and composition of vegetation communities. Wetlands are responsible for 20 to 25 percent of global methane emissions to the Earth's atmosphere, yet they also have the best capacity of any ecosystem to retain carbon through permanent burial (sequestration); both processes have implications for climate change (Mitsch and Gosselink 2015). Among all eco-hydrologic indices, WL plays a key role in controlling $CH_4$ emissions by determining the interface between aerobic and anaerobic processes (above- vs. below-ground, respectively) (Kang et al. 2012). WL also determines the degree of $CO_2$ production (Daulat and Clymo 1998; Chimner and Cooper 2003). Hence, having knowledge about WL changes under the future projected climate can provide the researchers with valuable insight into the probable $CH_4$ and $CO_2$ dynamics in wetlands.

All wetlands have both intra-annual (i.e., seasonal) and inter-annual (i.e., variation from year to year) WL fluctuations (McVoy et al. 2011). Such WL fluctuations have direct control on the composition of plants and animal communities/assemblages in wetlands (van der Valk et al. 2015). Hodson et al. (2011) demonstrated that climate variability has a significant impact on wetland $CH_4$ emissions. Studies have shown that rainfall and streamflow in the southeastern US are influenced by El Niño Southern Oscillation (ENSO). ENSO is a periodic fluctuation in sea surface temperature (El Niño) and the air pressure of the overlying atmosphere (Southern Oscillation) across the equatorial Pacific Ocean. In the Southeast US, large seasonal to interannual climate variability results in frequent droughts and is majorly influenced by ENSO. These ENSO-induced droughts cause severe water shortages that get exacerbated by increased urbanization and irrigation (Singh et al. 2015). Headwater wetlands provide many benefits to

Coastal Alabama and it is highly likely that their functioning (i.e., pollution reduction/ water quality improvement, water storage and providing habitat to many animals and plants) are impacted by ENSO, which has not been investigated before. Thus, the potential impacts of climate change and variability on wetlands and their eco-hydrological characters are of great importance. Utilizing the entire WL dataset from 15 headwater wetlands of coastal Alabama, Barksdale et al. 2014 observed that WLs were normally several decimeters below the ground surface.

WL in wetlands can be simulated by physically-based models (e.g., FEUWAnet by Dall'O' et al. 2001; SWATRE by Spieksma and Schouwenaars, 1997; MIKE SHE by House et al. 2016) or empirical methods (e.g. Rezaeianzadeh et al. 2015). While the former need information regarding soil, geomorphology, and hydrogeology of the system (draining watershed and wetland), which makes their development and application difficult particularly in data-scarce watersheds, the latter rely heavily on the hydro-climatic forcing (and their fluctuations) to the system. Artificial intelligence-based models such as artificial neural networks (ANNs) can be viable options where observed hydro-climatic data (e.g. inflow, outflow, water depth, precipitation, and temperature, etc.) exists but there is a lack of information on soil and hydrogeology of the system. Two examples of ANN applications in wetland hydrology studies predicting WLs are Dadaser-Celik and Cengiz (2013) and Rezaeianzadeh et al. (2015).

Transition in a watershed's land use and land cover (LULC) can alter groundwater recharge and surface runoff regimes. If the abutting uplands drain to a wetland, which is the case in headwater wetlands, these changes can adversely impact wetland's hydrology (Barksdale et al. 2014). Because of the land-use developments and increases in imperviousness in the watersheds draining to wetlands, headwater wetlands in time can become more of a flow-through system.

Consequently, the retention time and the performance of the wetland in filtering pollutants can be altered. Evidence of such impacts and alterations of wetland hydrology have been reported by Barksdale (2013) and Barksdale et al. (2014) in headwater wetlands of coastal Alabama. Nilsson et al. (2013) pointed out that understanding the cumulative effects of wetlands at the watershed scale needs a good understanding of WL fluctuations. The need for incorporating groundwater/surface water components from contributing watersheds in wetland WL prediction studies is very clear.

To build a predictive model capable of capturing physical processes to some extent, coupling a watershed model with ANN would be useful. By running a watershed model, the hydrologic inputs from the contributing watershed to the wetland (i.e., slow and quick flow components) can be simulated. Input combinations to ANN play a crucial role in developing a robust model. In that sense, importing the baseflow and stormflow simulated by a watershed model as inputs to ANN can improve the accuracy of ANNs. To the best of authors' knowledge, no study has considered combining a watershed model with ANN to predict wetland WL, although there are studies that coupled watershed models and ANNs for streamflow prediction. For instance, Loukas and Vasiliades (2014) coupled the University of British Columbia (UBC) watershed model with ANN to predict streamflow. Noori and Kalin (2016) showed that combining ANN and watershed models can help overcome the limitations of each model and result in a stronger model for streamflow prediction.

I developed a coupled SWAT-ANN model in this paper to predict WLs in headwater wetlands. I then apply the model to a headwater wetland in coastal Alabama, USA to predict the WL at the deepest point of the wetland. The study wetland is a typical headwater wetland in coastal Alabama and is representative of many in the region since this wetland is one of those 15

selected by Barksdale et al. (2014) to properly represent the surrounding LULC of the region. Also, groundwater discharge (from surrounding uplands) is a major hydrologic input to these headwater wetlands (Noble et al. 2007). Baseflow and stormflow estimates from the SWAT model are fed into the ANN model as forcing data to capture slow and quick flow components from the contributing watershed to the study wetland. Observed WL data are then used to train and test the ANN model. The coupled model of this paper overcomes some of the limitations of the two previously developed WL prediction models by Rezaeianzadeh et al. (2015), which either required WL data from nearby wetlands (continuous model) or antecedent WL data from the target wetland itself (event based model) as input. None of those models are suited for long term predictions, which is needed to explore impacts of climate change and variability on wetland hydrology. The utility of the developed model is demonstrated with two applications. In the first application, potential impacts of future climate change on WLs are assessed. The second application is related to climate variability rather than change where we explore the potential teleconnections between El Niño Southern Oscillation (ENSO) and WL fluctuations in the study wetland. This study is the first attempt to the best of our knowledge looking at the hydrologic function of a headwater wetland in coastal Alabama under varying ENSO conditions.

## 2. Study Area and Data Sets

The study wetland is located in Baldwin County, Alabama, USA (Figure 3.1). Mild winters and hot and humid summers are the main climatic characteristics of the region. Mean annual temperature and precipitation are 19.5˚C and 1650 mm, respectively. Headwater wetlands in coastal Alabama are groundwater driven and are usually located in the headwater reaches of first order streams (Noble et al. 2007). Hummock/hollow microtopography and gradual slopes

are the terrain characteristics. The soils of these wetlands are classified as “wet loamy alluvial lands” (McBride and Burgess 1964). The study wetland is a representative of the headwater wetlands throughout the southern Alabama. Figure 3.1a shows the 15 headwater wetlands that have been originally studied by Barksdale et al. (2014). The minimum and maximum elevation of the study wetland is 7.12 m and 10.24 m, respectively. Those values are 7.12 and 24.84 m for the contributing watershed. The study wetland is located within the Fish River watershed in the southwest portion of the county, which drains into Weeks Bay, a sub-estuary of Mobile Bay. The delineated watershed area (based on the outlet of the wetland) draining to the wetland is 83.57 ha with a mixed land use/cover (Figure 3.1b). Pasture/hay and evergreen forests are the dominant land uses in the watershed (Figure 3.1c). The dominant hydrologic soil groups are C (i.e., slow infiltration rate covering 41.3% of the area) and A (with high infiltration rate and 40% of the area), respectively. According to the information derived from National Wetlands Inventory (NWI), the study wetland is comprised of three sections which includes PFO1C (0.737 ha), PFO4C (0.485 ha) and PFO1C (0.314 ha) classification codes. These three sections are called Freshwater Forested/Shrub Wetland types by NWI which are classified as *inland* wetlands. Precipitation, minimum and maximum temperature data were obtained from the NOAA Robertsdale (USC00016988) climatic station. Wetland WLs (relative to the ground surface) were monitored at hourly time scale at the deepest point of the wetland in shallow wells using In-Situ Mini-Troll 500 pressure transducers from February 2011 to March 2012 (see Barksdale et al. 2014).

## 3. Methodology

### 3.1 Soil and Water Assessment Tool (SWAT)

SWAT is a semi-distributed, process-based watershed model that operates on a daily basis (Arnold et al. 1998). Division of a watershed into a number of subbasins is needed and done when different parts of the watershed are dominated by land uses or soils dissimilar enough to impact hydrology (Neitsch et al. 2011). Hydrologic response units (HRUs) are lumped land areas within the subbasin that consist of unique land cover, soil and management combinations (Neitsch et al. 2011). In this study, the thresholds for land use, soil and slope overlay, were all set to 10%, and the number of subbasins and HRUs were 5 and 74, respectively. Soil data from SURRGO, and land use/cover data from 2011 NLCD were used. Lu et al. (2005) recommended Hamon method (Hamon 1961) for regional applications of potential evapotranspiration (PET) estimations in the southeastern United States. This method was used for PET calculation, which utilizes the daily mean air temperature. Daily average temperatures were obtained by simply averaging daily minimum and maximum temperatures. A three-year warm-up period was considered for SWAT run, and the baseflow and stormflow estimates generated from SWAT (no calibration) were regarded as two hydrologic inputs to the ANN model. Observed flow data (outflow from the watershed or inflow to the wetland) were not available for model calibration, which is the case for many natural wetlands. Natural headwater wetlands may not have surface inflow.

### 3.2 Artificial Neural Networks (ANNs)

An ANN consists of a number of neurons organized into three basic layers (input, hidden and output). Multilayer feed forward is one of the most common ANN which is utilized in this study. Input combinations, the number of neurons in the hidden layer, transfer function and training algorithms are the most important components of an ANN structure. Input combinations and transfer function are discussed in the following sections. For this study, with the available hourly WL data from February 2011 to March 2012, we obtained the best architecture to be (8, 6, 1) where those values refer to the number of inputs, and the number of neurons in hidden and output layers, respectively. A simple trial and error procedure was carried out to find the best training algorithm and Levenberg–Marquardt training algorithm was chosen for this study. Before applying the ANN models, the observed data were normalized to [0.05, 0.95] using a linear transformation (Rezaeian Zadeh et al. 2010; Rezaeianzadeh et al. 2015):

$$X_n = 0.05 + 0.9\frac{X - X_{\min}}{X_{\max} - X_{\min}} \quad (1)$$

where, $X_n$ and $X$ are the normalized and original inputs and $X_{min}$ and $X_{max}$ are the minimum and maximum values of the original data, respectively.

The normalized data were employed to train the ANN model. The model outputs were then transformed back to the original scale and then the performance indices were computed for the training and test data sets. In this study, roughly 70% of the data was used for training and the remaining 30% was used for testing. To distribute the high, mean and low WL values into both training and testing datasets, the data were randomly selected (Rezaeianzadeh et al. 2015). This randomization eliminates potential biases that may arise when there are distinct dry and wet periods. The randomization is done by randomly distributing the data into training and testing datasets until the *p*-value in t-test is above 5%, i.e. there is no statistically significant difference

between the means from the training and testing datasets. Note that the t-test is performed based on the equal variances assumption by conducting a Levene's test. The methodology is described in detail in Rezaeianzadeh et al. (2015), therefore it is not repeated here. Previous exercises by Rezaeian-Zadeh et al. (2010) and Rezaeianzadeh et al. (2015) showed the efficiency of this method to optimally train the ANNs. Codes were written in MATLAB for the ANN simulation (MathWork, Inc. 2010).

### 3.3 SWAT-ANN coupling

To enhance WL predictions by the ANN model, a coupled SWAT-ANN model was developed. To that end, baseflow and stormflow components of streamflow are first simulated at the watershed outlet by the SWAT model without calibration (i.e., default SWAT parameter values were used). This is achieved by picking the outlet of the wetland and delineating the watershed draining to that point as if there is no wetland there. Then, we generated streamflow at that point with SWAT using default model parameters. No calibration was carried out because streamflow data was not available. In addition to streamflow, SWAT also provides model outputs to help partition the streamflow into stormflow and baseflow components. We note that in many instances the wetland WLs are below the ground surface whereby groundwater bypasses the wetland surface and discharges directly to the main channel as baseflow. The simulated values for baseflow and stormflow at day *t* are then fed into ANN to predict WL on day *t*. A trial and error procedure was utilized to examine various input combinations, and their accuracies were evaluated with the Nash-Sutcliffe ($E_{NS}$) and root mean square error (*RMSE*) performance metrics. Eventually, to predict WL on day *t*, this combination was identified:

$$WL(t) = f\{Q_b(t), Q_b(t-1), Q_s(t), Q_s(t-1), P(t), P(t-1), PET(t), PET(t-1)\} \quad (2)$$

where, $WL(t)$ is water depth at deepest point in the wetland at time $t$; and $Q_b, Q_s, P$ and $PET$ denote baseflow (i.e., groundwater contribution to streamflow), stormflow (or quick flow, i.e., surface runoff+interflow), precipitation and potential evapotranspiration, respectively. These variables were found to serve as the best input combinations and were imported into ANN to predict WLs at deepest point in the wetland for baseline and future periods. Figure 3.2 shows a flowchart describing the developed methodology of this study.

### 3.4 Climate Change Application: WL prediction for baseline and future periods

Because long-term observations are not available to study the impacts of climate change and variability, the developed SWAT-ANN model was used to generate WLs in the study wetland. Historical observations (1951-2005, representing baseline period) and future projections from 11 downscaled, and bias-corrected global climate model (GCM) outputs of precipitation and temperature (2006-2060, representing future period) were used to predict WLs over 1951-2060. By predicting WLs for the baseline period, a benchmark is created, first, to evaluate any probable trends in future WL (compared to the baseline period) and, second, to explore any teleconnections between WLs and ENSO phases. To predict WL for the baseline period, observed data from Fairhope 2 station (USC00012813) which is the nearest climatic station (<10 Km) with long-term historical data from 1948 to 2005 were used to run the SWAT model. SWAT model was run with a three-year warm-up period (1948-1950) from 1951 to 2005 to prepare the input data required for the trained ANN model. By importing baseflow and stormflow from the SWAT model, as well as precipitation and potential evapotranspiration to the trained ANN, WLs were predicted for the baseline period (i.e., 1951-2005).

To predict WLs for the future period, downscaled Coupled Model Intercomparison Project Phase 5 (CMIP5) climate projections were used for daily precipitation and max/min temperature data (downloaded and accessed on 04/24/2015 from http://gdo-dcp.ucllnl.org/downscaled_cmip_projections/dcpInterface.html). For this study, data from 11 climate models with 4 emission scenarios (Representative Concentration Pathways; RCPs 2.6, 4.5, 6.0, 8.5) were gathered from the website mentioned above (total 44 ensembles). The GCM models used in this study are: *bcc-csm1.1*, *ccsm4*, *gfdl-esm2g*, *gfdl-esm2m*, *ipsl-cm5a-lr*, *ipsl-cm5a-mr*, *miroc-esm*, *miroc-esm-chem*, *miroc5*, *mri-cgcm3* and *noresm1-m*. This corresponds to 44 SWAT runs for the bias-corrected future projections, and they were performed for the period 2000-2060 with the first five years being warm-up period.

### 3.4.1. Bias correction using Quantile Mapping technique

Comparison of simulated historic climate data by GCMs to observed data (i.e., daily precipitation, minimum and maximum air temperatures) often shows that simulations tend to be biased: wetter, drier, cooler, and/or warmer, with biases varying by locations, season and variables (Reclamation 2013). Hence, to extend the WL prediction for the future period (2006-2060 as explained above), there was a need to correct the biases on the GCM outputs. To enable an efficient application of methodology, downscaled climate models with the finest resolutions available, which is 1/8 degree (12 Km), were selected. Bias-correction using Quantile Mapping technique is explained below. Altogether, three major datasets were gathered and prepared for bias correction through quantile mapping technique: (1) observed historical data (i.e., daily precipitation, minimum and maximum air temperatures) from Fairhope 2 station (USC00012813) from 1950 to 1999; (2) simulated historical conditions from each GCM, which

comes under the name “1/8 degree Observed data (1950-1999)”; (3) the GCM’s simulated future projections. The next step was to identify biases. To that end, a bias-identification period of common overlap in datasets (1) and (2) was adopted. In CMIP5 applications, this period is usually chosen to be 1950-1999 (Reclamation, 2013). Quantile mapping technique was used for bias correction of daily precipitation, and maximum and minimum temperature values (Reclamation, 2013). For a given variable, all the daily observations in month *m* over the 50-year period are lumped into one pool and a cumulative distribution function (CDF) is created for that month. The same is done for all historical values simulated by GCMs (dataset 2). The paired CDFs combine to form a “quantile map” where at each rank probability one can assess the bias between dataset (1) and (2) (observations minus historical GCM values). By fitting a 3$^{rd}$ order polynomial function between the historical GCM data (as $x$) and the biases (as $y$), GCM simulated daily values are bias corrected. By providing any new $x$ (which could be either historical GCM values or GCM’s simulated future projections, regardless of their order) for a particular month and a specific variable, the corresponding correction value ($y$) is achieved. Then, the returned value ($y$) of the polynomial fit is added to the historical GCM data (or GCM’s simulated future projections) to construct the bias corrected GCM data. Readers are referred to Drusch et al. (2005) and Maurer et al. (2010) to find more about the details of bias correction.

In the next step, dataset (3) were adjusted based on the quantile maps produced in the previous step. For bias correction of future projections of GCMs, two assumptions are considered: (i) bias structure for future simulations are same as historical ones, and (ii) bias in future projections should be corrected for future trends. To fulfill the second assumption, for minimum and maximum air temperatures, the linear trend is removed before bias correction and

added back afterward. Readers are referred to Thrasher et al. (2012) for more information regarding the bias correction of minimum and maximum air temperatures.

To identify the probable long-term changes in the calculated WLs under climate change, the 1951-2005 was selected as the baseline period to compare with the 2006-2060 period. The most commonly used trend identification techniques, such as Mann-Kendall (MK) and Spearman's rho (SR) tests are valid under a set of restrictive assumptions. Those assumptions include independency of the structure of time series (refers to auto- or serial correlation), normality of distribution of the variable, and rather long data sets. Although the Mann-Kendall trend test does not require normality assumption, the time series should be independent without any serial correlation (Şen, 2012). To overcome all those restrictions, the trend analysis introduced by Şen (2012) was applied in this study. The basis of the approach rests on the fact that if two time series are identical to each other, their plots against each other should show scatter of points along the 1:1 line on the Cartesian coordinate system (Şen, 2012). Depending on the fall of scatter points onto the upper or lower triangular area of the scatter region, there is a monotonic increasing or decreasing trend. In the case of the composition of various trends in the time series (non-monotonic trends), the scatter points fall on a curve.

### 3.5. Climate Variability Application: El Niño Southern Oscillation (ENSO) Effects on WL variations

Since rainfall and streamflow are influenced by ENSO in the southeastern US (Singh et al. 2015), one can also expect ENSO affecting WLs in wetlands. The WLs predicted by the SWAT-ANN model over the period 1951-2005 were associated with ENSO indices to explore the existence of such a teleconnection at the study wetland. Several correlation methods are

available to assess the strength of the relationship between large-scale atmospheric circulation patterns (such as ENSO) and hydro-climatic variables, but the two most commonly applied ones are Pearson's correlation and Spearman's rank correlation. Pearson's correlation needs both variables to be normally distributed while no such assumption is necessary for the application of Spearman's rank correlation (Hosseinzadeh Talaee et al. 2014). For this study, Spearman's correlation coefficient between the Niño 3.4 index (as an indicator of ENSO strength) and the hydro-climatic variables precipitation and WL were examined. The Niño 3.4 index represents the sea-surface temperature (SST) anomalies in the Niño 3.4 region (5˚N–5˚S, 120–170˚W) and is based on a 3-month running average (Singh et al. 2015). The Niño 3.4 indices for the period 1951 to 2005 (to capture approximately 10 ENSO cycles) were obtained from the National Weather Service Climate Prediction Center:

(http://www.cpc.ncep.noaa.gov/products/analysis_monitoring/ensostuff/ensoyears.shtml).

When Niño 3.4 index is between -0.5 ˚C and 0.5 ˚C, it is considered to be Neutral phase, and indices above 0.5 ˚C and below -0.5 ˚C are listed as El Niño and La Niña phases of ENSO, respectively.

## 4. Results and Discussion

### 4.1 SWAT-ANN Model Performance

Figure 3.3 displays the simulated and observed WLs for the training and testing phases in scatter plots and exceedance curve (i.e., probability of exceedance of "depth below ground surface") formats. According to the training results of Figure 3.3, except for a few extreme high WLs the model has captured the observed WL fluctuations. Despite model's poor estimations of some extreme high WLs, the testing phase of Figure 3.3 also confirms the ability of the model to

predict WLs accurately. WL exceedance curve in Figure 3.3 regarding training phase illustrates that in general model slightly overestimated WLs below -70 cm. On the contrary, it slightly underestimated WLs above -60 cm. Despite the results of the model in the training phase, the model in testing phase overestimated the extreme high WLs. Similar to the training phase, WLs below -70 cm were overestimated in the testing phase, too. $E_{NS}$ and *RMSE* values were equal to 0.73, 14.5 cm, and 0.52, 17.8 cm, respectively, for the training and testing phases. Both performance indices showed better results in training phase compared to the testing phase. Better results regarding performance metrics were achieved too, but taking into the consideration of the generalization and overfitting problems, the reported performances and the related model was the best and the most reliable.

To utilize the developed model for the climate change application, we elaborate on the generalization ability of the model. In making future projections, some extreme values may be observed beyond the range of available time series used for model training, which would require paying attention to the generalization ability of the ANNs. The generalization ability including both interpolations and extrapolations is defined as the model's skill to perform well on a dataset that is not utilized for its calibration (Cheng and Titterington, 1994). Although it is generally accepted that the ANNs cannot extrapolate beyond the range of the training data (Maier and Dandy, 2000), utilization of sigmoidal-type and linear transfer functions in hidden and output layers, respectively has been recommended for extrapolation purposes (see Kaastra and Boyd, 1995; Karunanithi et al., 1994). For instance, Rezaeian-Zadeh et al. (2012) successfully tested the generalization ability of ANNs to predict hourly air temperatures by using the same type of transfer functions. The other successful example of the extrapolation ability of ANNs (compared to multi non-linear regression) was reported by Cigizoglu (2003) on daily river flow data. Hence,

in the current study, logistic sigmoid and linear transfer functions were utilized in hidden and output layers, respectively. Logistic sigmoid transfer function is defined for a variable *s* as:

$$logsig(s) = \frac{1}{(1+e^{-s})} \quad (3)$$

Generalization ability is also defined as a function of the ratio of the number of training samples to the number of connection weights. If this ratio is too small, continued training can result in overfitting of the training data (Maier and Dandy, 2000). Overfitting (i.e., having high variance) can happen when there are too many features (i.e., inputs) but insufficient amount of observed data; in which case the learned hypothesis may fit the training set very well, but fail to generalize to new datasets. For this study, we obtained the best architecture to be (8, 6, 1) where those values refer to the number of inputs, and the number of neurons in hidden and output layers, respectively. Hence, we had 8× 195 (=1560) training patterns (samples), 54 weights and (6+1=7) "bias" weights which constitute a total of 61 connection weights (i.e., free model parameters). The ratio for the developed model in this study was >25 which confirms a reliable ANN with regard to generalization ability and overfitting problem. To ensure a good generalization ability, various ratios have been suggested by researchers such as 2 to 1 (Masters, 1993) or 10 to 1 (e.g. Weigend et al., 1990). Amari et al. (1997) suggested that overfitting does not occur if the above ratio exceeds 30.

### 4.2. Climate Change Application Results

Before simulating the WLs for the baseline and future periods, bias corrections were performed for all 44 GCM datasets using the quantile mapping technique explained earlier. To demonstrate how bias corrections improved the GCM outputs (i.e., precipitation and temperature data), one out of 44 ensembles was selected as an example and the results are displayed in Figure

3.4a (for precipitation) and Figure 3.4b (for maximum temperature) for two selected months. As can be seen in both figures, the bias corrected CDFs of GCM outputs closely follow the observed CDFs.

Figure 3.5a shows the annual precipitation time series for the baseline period and the future period based on bias corrected GCM outputs. No clear increasing or decreasing trend in the future is distinguishable according to this figure. Figure 3.5b displays Sen's trend analysis for annual precipitation to provide a better insight to the potential trend. As can be seen from the figure, no considerable change in annual precipitation is expected during dry and normal precipitation years (P<1650 mm). However, wet years are clearly expected to get wetter. Figure 3.5c shows the mean annual temperature time series for the baseline period and the future period based on bias corrected GCM outputs. There is a clear warming trend in the future (about 0.021 °C/year). Figure 3.5d also indicates a clear increasing trend in the future temperature suggested by various GCMs.

### *4.2.1 Baseline vs Future WLs*

Baseline and future WLs were predicted by utilizing the hybrid SWAT-ANN model. Predicted WLs for the baseline and future periods were compared by employing trend analysis and WL exceedance curves. Note that WL exceedance curve refers to the probability of exceedance of "depth below ground surface". Figure 3.6 displays the trend analysis of annual mean WLs and WL exceedance curves at daily scale. Trend analysis shows both increasing and decreasing trends projected by various GCMs. In terms of ensemble median of annual mean WL, which represents the median of future projections, increasing trends are dominant in medium WLs while decreasing trends are dominant in low and high WLs. WL exceedance curve gives us

an insight into the probable future changes in various WL clusters (i.e., low, medium and high WLs) and it has a high degree of uncertainty. This uncertainty is in its highest degree for the calculated WLs ranging from 100 to 300 cm below the ground (about 40% of the time). According to the ensemble median of WL exceedance curve, future daily WLs are predicted to be deeper than 100 cm below the ground for ~55% of the time. This was 59% for the baseline period. Furthermore, future ensemble median depicts that about 7.8% of the time, daily WLs will be above the ground surface (i.e., where ponding starts) while this was about 9.4% for the baseline period. WLs were calculated higher than 100 cm above the ground for about 1.5% and 2% of the time, respectively, regarding future ensemble median and baseline period.

From the WL exceedance curve in Figure 3.6, although it does not seem to be a considerable difference between the calculated WL for baseline period and the ensemble median of future scenarios, a two-sample t-test (at the 5% significance level) declared that there is a statistically significant difference between the means ($p<0.05$) of those two ordered-values intervals. To provide more insights on various parts of the daily WL exceedance curve, both baseline and future ensemble median ordered-values intervals were split into different parts based on quantiles. We compared the ordered-values intervals for $0^{th}$-$10^{th}$, $10^{th}$-$20^{th}$, $80^{th}$-$90^{th}$ and $90^{th}$-$100^{th}$ percentiles (e.g., the $10^{th}$ percentile refers to WLs which is exceeded 90% of the time). Two-sample t-test was performed for these partial ordered-values intervals. Results showed that there is a statistically significant difference between the means (-360.7 cm and -369.7 cm, respectively for baseline and future ensemble median) of the $0^{th}$-$10^{th}$ percentile. The same analysis resulted in a significant difference between means (-342.6 cm and -349.0 cm, respectively, for baseline and ensemble median) for $10^{th}$-$20^{th}$ percentile. Significant differences between the means of $80^{th}$-$90^{th}$ percentile and $90^{th}$-$100^{th}$ percentile ordered-values intervals were

also obtained. 12.0 cm versus 3.4 cm, and 61.7 cm versus 46.2 cm correspond to the means of $80^{th}$-$90^{th}$ percentile and $90^{th}$-$100^{th}$ percentile ordered-values intervals, respectively, for baseline and future ensemble median. Hence, at least 40 percent of the time, representing low and high daily WLs are expected to have a statistically significant reduction. WL fluctuations can impact biodiversity and vegetation communities of these flashy systems which are altered by any major future declines in extreme WLs.

### 4.3. Climate Variability Results

Figure 3.7 displays the Spearman's correlation coefficient between Niño 3.4 index (as an indicator of ENSO strength) and monthly precipitation and WLs from 1951 to 2005. In August, September and October, monthly precipitations are negatively correlated with Niño 3.4 index in all three phases, but not at a statistically significant level ($\alpha$=5%). From November to July, the correlations between monthly precipitations and Niño 3.4 index are positive for almost all months and phases. However, only January in neutral phase ($p$-value=0.036) and February in La Niña phase ($p$-value=0.030) had statistically significant correlations (approximately $r$=0.28 for both cases). Average monthly WLs in March and April have a statistically significant negative correlation with Niño index in both El Niño and La Niña phases, with a stronger correlation with the former. WLs in May also showed significant negative correlation with Niño index in El Niño phase. There are no statistically significant correlations between monthly WLs and Niño index during the neutral phase.

Figure 3.8 displays Spearman correlation coefficients between Niño index and precipitation/WL at seasonal level. Correlations between Niño index representing various ENSO phases and seasonal precipitations are non-significant except for a positive correlation in winter

during El Niño phase. This also aligns with what others reported (e.g. Sharda et al. 2012; Mo and Schemm 2008). Correlations between Niño index and seasonal WLs are non-significant except for spring during El Niño phase, which has a negative correlation. Hence, lower WLs can be expected during El Niño phase in spring. In late spring, Alabama is anomalously dry during the resurgence phase of El Niño. In late spring of a developing El Niño, low-level winds that bring moist air from the Gulf of Mexico to the U.S. shift westward (Lee et al. 2014) which again confirms having less precipitation (than normal). Mearns et al. (2003) found that precipitation over the southeastern U.S. shows different seasonality over the region.

Having statistically significant positive correlation between Niño index and precipitation in winter and negative correlation with WLs in spring (Figure 3.8), although appears to be contradicting at the first glance, is a potential sign for lag effect. To explore this, sample cross-correlation between monthly precipitation and ENSO and monthly WLs and ENSO were evaluated. Determining significant lag correlations can be useful in forecasting. Lags up to 12 months were evaluated. Figure 3.9 displays the cross-correlation graphs between Niño 3.4 Index and precipitation and WL. There are statistically significant positive correlations (at 95% confidence level) between monthly precipitation and zero, one- and two-month lag ENSO index time series. Cross-correlation between WL time series and ENSO index time series showed significant negative correlations at zero-month and one-month time lags. Furthermore, Figure 3.10 displays cross-correlations between monthly WLs and precipitations with time lags. The graph confirms the existence of a significant negative correlation between WL and one-month lag time in precipitation. It also shows a positive correlation between WLs and five- to seven-month lag precipitation time series. Note that the statistically significant positive correlation was observed with 6-month lag in precipitation which was the peak of the correlations. The negative

correlation between Niño index and precipitation in the months of August, September, and October during El Niño phase (Figure 3.7) along with the significant 6-month lag positive correlation between WLs and precipitation imply that on average WLs in the wetland would respond by decreasing around March to May during this phase of ENSO. The peak value in the cross-correlation at time lag 6 months (Figure 3.10) may be attributed to the typical lagged response of subsurface hydrology and groundwater recharge to precipitation (McCuen, 2002). All the aforementioned results guide us to the dominant contribution of groundwater in the study wetland. To elaborate more on this, spring precipitation and WL can be a typical example of the situation. There is a (low) positive correlation between spring precipitation and Niño index in El Niño phase and while one can expect to see an increase (although insignificant) in the spring WLs, this is not the case here. Headwater wetlands of coastal Alabama have two distinct aspects which can shed light on this subject: *i*) they respond quickly to rainfall events which represent the stormflow component and *ii*) they are groundwater driven in which this component apparently plays a crucial rule in these ecosystems. Figure 3.6b in WL exceedance curve shows that WLs are below the ground surface more than 80% of the time (~90%) for this study wetland; hence groundwater component dominates the hydrology. Altogether, spring WLs have been probably affected more by the lagged response of subsurface hydrology and groundwater recharge to decreased precipitation at the end of summer during El Niño phase and early autumn than spring precipitation. Time-lagged correlation between ENSO index, precipitation and WLs confirmed that ENSO indicators can be used to predict precipitation and WLs with some success in headwater wetlands of coastal Alabama. This result is in good agreement with findings of Lù et al. (2011).

### 4.5 Potential Implications of WL Alteration

The hydrology of wetlands is affected by climate change mostly through changes in precipitation and temperature regimes with significant global variability (Erwin 2009). Even slight changes in wetland hydrologic conditions can affect soil biogeochemistry and consequently nutrient cycles; biota may respond with considerable changes in species composition and richness and in ecosystem productivity (Mitsch and Gosselink, 2015). In forested wetlands, hydrologic changes can also have substantial effects on forest productivity and carbon cycling (Barksdale et al. 2014) directly through duration and intensity of flooding, and through changes in vegetation (Majidzadeh et al. 2015). Barksdale et al. (2014) found a strong correlation between WL and total carbon content at the soil surface using data from 15 headwater wetlands (which included the wetland studied in this paper). According to their findings, wetlands with lower median groundwater levels showed surface soils with less organic matter and reduced carbon storage. High and low WLs are expected to drop in the study wetland and this will potentially lead to reduced organic material and carbon stock and the same impacts could be expected in the other headwater wetlands of Baldwin County, Alabama. Reduction in WLs could also result in changes in the vegetation communities since the depth and percentage of time a location remains inundated has been shown to have a direct influence on the vegetative communities (Todd et al. 2012). This could cause the establishment of invasive plant species which are major threats to local diversity and other ecosystem functions (Barksdale and Anderson, 2014). With lowered WLs and the consequent increase in oxygen availability, a reduction in $CH_4$ emission and an increase in $CO_2$ production will be the most probable scenarios expected. Hydrologic alteration of headwater wetlands has the potential to impact

some wildlife species, but the most severe impacts would be to amphibians since they are highly vulnerable to wetland drainage (Noble 2007).

In this study, the potential impacts of climate change and variability on wetlands through alteration in one of the hydrologic indices (i.e., wetland water level) were discussed only. Other climate-related variables could have noticeable impacts such as increased temperature and altered evapotranspiration, altered biogeochemistry, altered amount and patterns of suspended sediment loadings and fire (Erwin, 2009). Note that the impact of altered temperature and consequently evapotranspiration were indirectly considered by importing potential evapotranspiration as an input to the developed model in this study. Also, human-induced alterations (which were beyond the scope of this study) including wetland drainage, filling/dredging, water diversions, introducing pollutants and unsustainable developments need to be taken into account in the evaluation of potential impacts on wetlands and to avoid the detrimental impacts of these significant stressors. An assessment of coastal LULC change from 1974 to 2008 in southern Alabama showed that the expansion of urban landscape, especially in Baldwin County, is expected given the most recent population statistics that suggest future population growth. 34% of upland forest were converted to urbanized landscapes for Mobile and Baldwin counties over the studied period (Ellis et al. 2011). Considering the effects of LULC changes in wetland WL prediction studies is suggested for the future studies.

## 5. Summary and Conclusions

Acquiring knowledge about the probable changes in long-term WL fluctuations in wetlands and identifying their trends are challenging tasks because of the complexity of hydrological processes in these ecosystems. Rezaeianzadeh et al. (2015) developed two ANN-

based methodologies by utilizing precipitation and WL values from the nearby sites as inputs to predict hourly WLs in headwater wetlands. In this study, we built upon the previous study by eliminating the need for WL data from nearby wetlands as inputs to the model. The new modeling approach couples SWAT and ANN by using baseflow and stormflow components simulated from SWAT as inputs to ANN. Although coupling data-driven models with semi-distributed hydrologic models (such as SWAT) is not new, to the best of authors' knowledge, the developed model for the prediction of daily WLs is a novel approach in wetland hydrology studies. The model requires only WL measurements over a period of time to train the ANN.

The model was applied to a headwater wetland in coastal Alabama. After constructing the hybrid SWAT-ANN model, WLs were predicted for both long-term baseline (1951-2005) and future (2006-2060) periods. Regarding future projections, GCM outputs of precipitation and min/max air temperatures were bias corrected by using the quantile mapping technique prior to their utilizations into the model. The bias correction procedure was an important step in this study because finding the right distribution and variations in precipitation and temperature is very crucial in studying climate change impacts on wetlands. A recently introduced trend analysis having no restrictive assumption was utilized and the trends in WL dynamics were assessed. Finally, the teleconnection between ENSO and precipitation/WLs in the study wetland were also explored by using Spearman's rank correlation and cross-correlation analyses. In summary, the following conclusions can be drawn from this study:

1. Climate projections show a noticeable increase in temperature from 2006 to 2100. Furthermore, no considerable change in annual precipitation is expected during dry and normal precipitation years. However, wet years are clearly expected to get wetter.

2. Coupled SWAT-ANN model could be a viable tool to simulate WLs for wetlands at a daily scale. To develop this model, availability of at least yearlong WL data plays a crucial role.
3. Simulated future WLs by utilizing different GCM ensembles showed both decreasing and increasing trends. However, the increasing trend was dominant in medium WLs and the decreasing trend was dominant in low and high WLs.
4. The findings show that winter gets wetter in terms of precipitation and spring gets drier regarding the WLs over El Niño phase.
5. Analyses on daily WLs demonstrated that at least 40 percent of the time indicating extreme low and high daily WLs are expected to have a drop.
6. The results of this study suggested that expected climate change and variability could have a significant impact on the overall vegetation of the study wetland.

The methodology proposed in this paper should be transferable to other wetlands and their draining watersheds within different geographic and climatic regions to evaluate probable WL fluctuations based on future climate projections or shorter term climatic variations. Studies, such as the one presented in this paper, are important in order to understand the potential hydrological changes associated with climate change and variability. Acreman et al. (2009) point out that a full assessment of the potential impacts of climate change on a specific wetland should assess the uncertainties in climate change projections by comparing various scenarios from a number of global or regional climate models. In the current study, although we did not directly discuss the uncertainty issue, by considering various GCM outputs as well as various emission scenarios, we provide a valuable insight on the potential impacts of climate change and also

climate variability on the study wetland. These findings are of interest to wetland scientists, eco-hydrologist, wetlands managers as well as domestic/international policy makers.

**Acknowledgment**: This study was partially funded by Auburn University Center for Environmental Studies at the Urban-Rural interface (CESURI). The authors would like to thank Dr. Christopher J. Anderson and W. Flynt Barksdale for providing us with water level data. It has not been subject to the U.S. EPA review and therefore does not necessarily reflect the views of the Agency, and no official endorsement should be inferred.

(a) (b) (c)

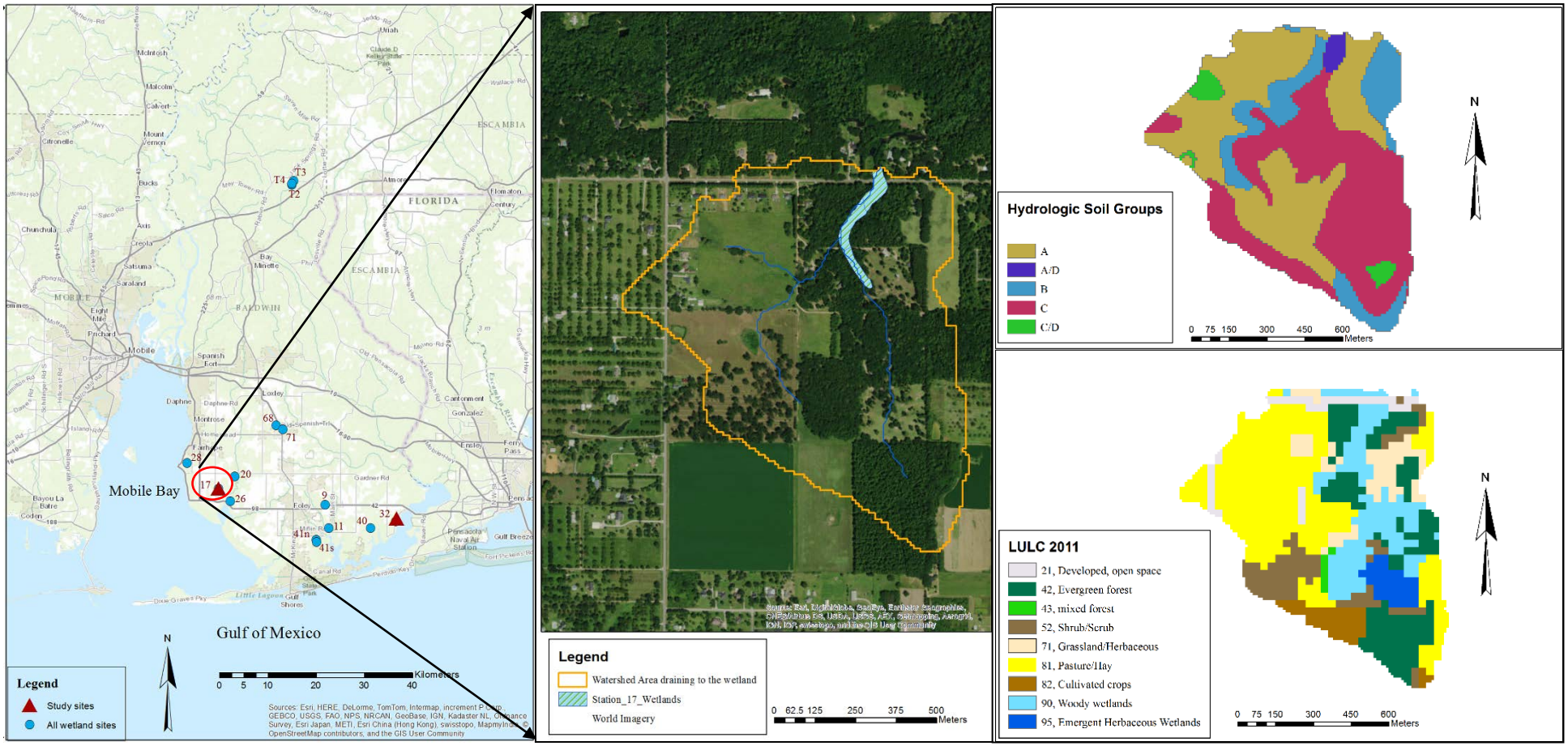


Figure 3.1: Station 17 wetland with the delineated contributing watershed (a, b), and Hydrologic soil groups map and the land use/cover map based on 2011 NLCD for the study watershed (c)

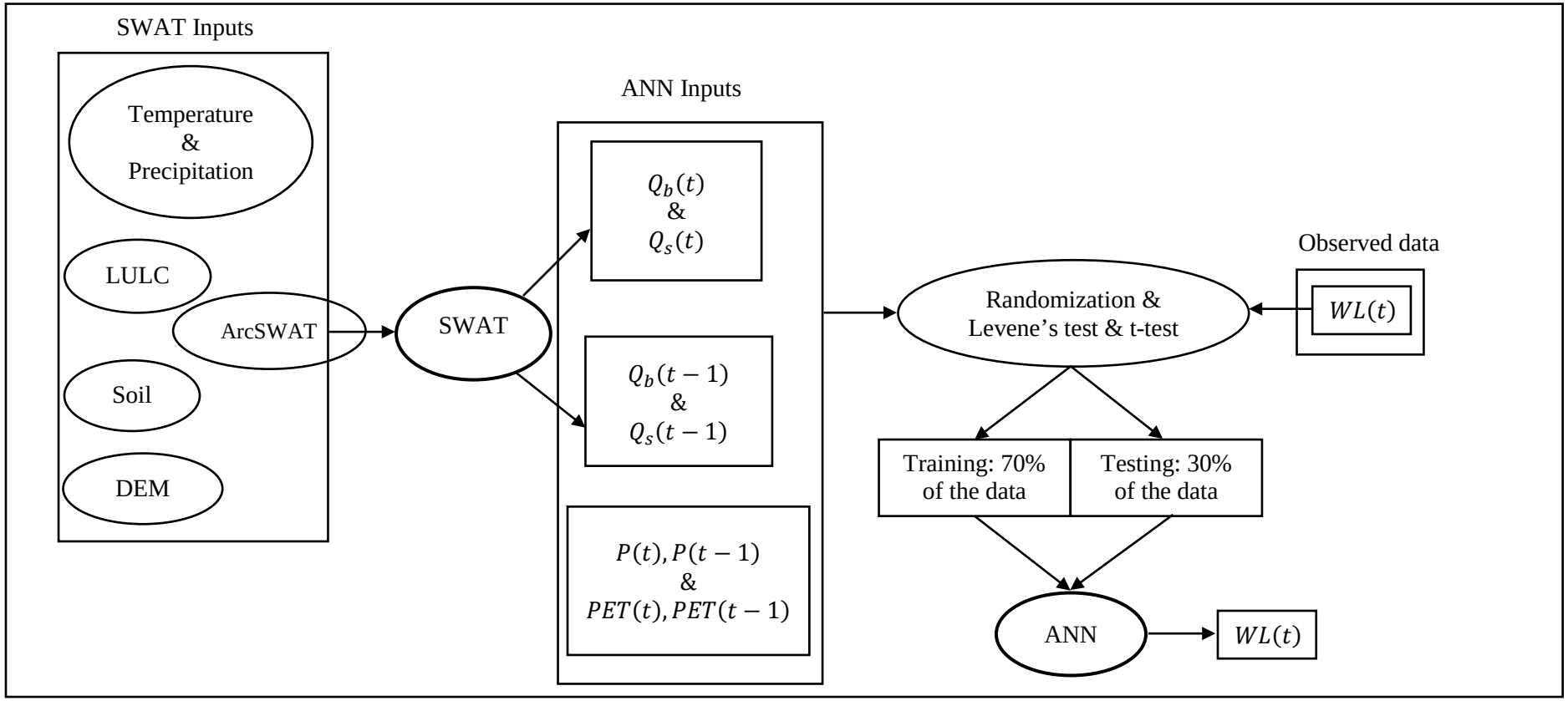


Figure 3.2: Model development flowchart. $Q_b, Q_s,$ $P$ and $PET$ denote baseflow, stormflow, precipitation and potential evapotranspiration, respectively. Data were randomly selected in which Levene's test and t-test (Rezaeianzadeh et al. 2015) were used to obtain the optimal datasets for training and testing phases.

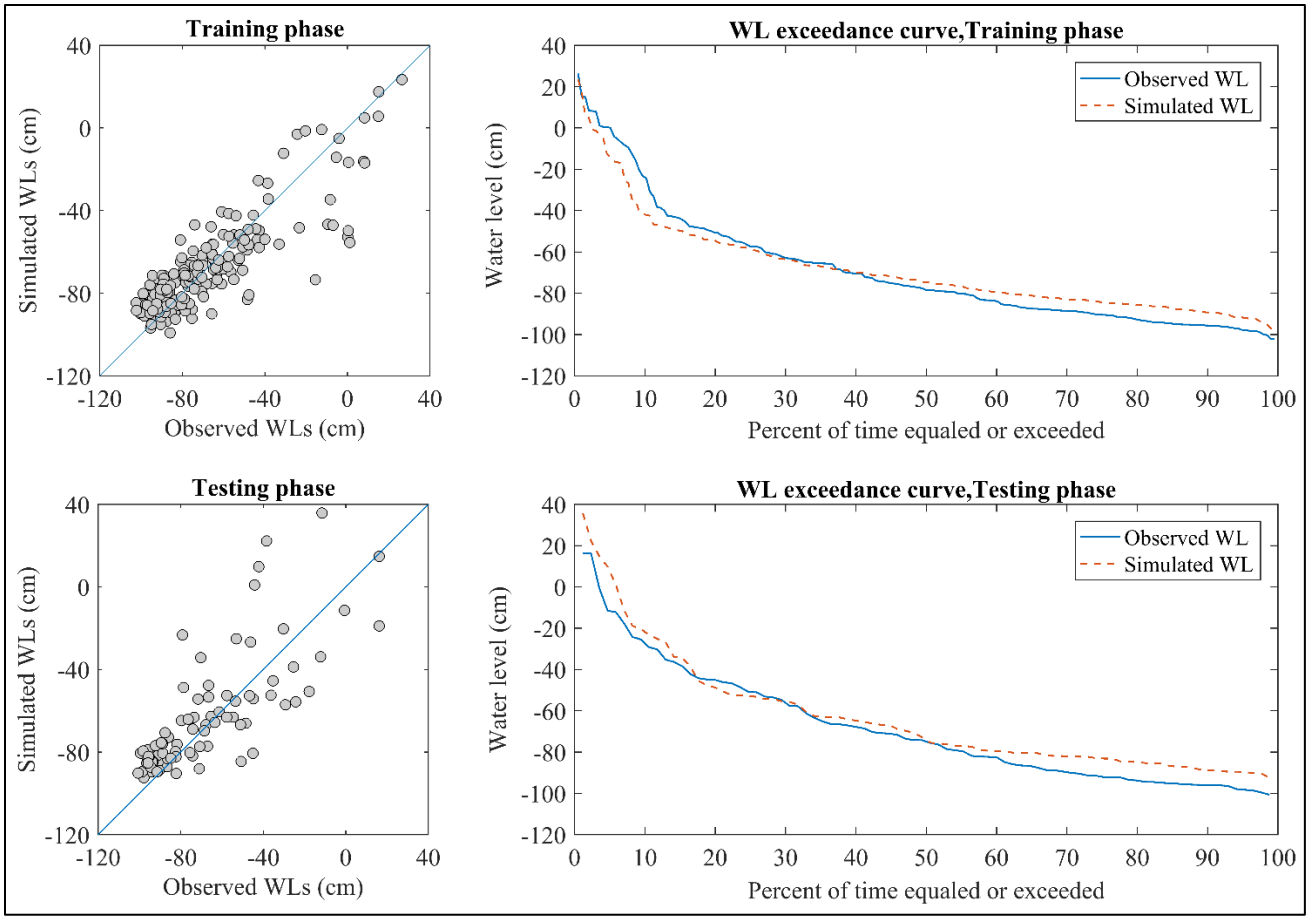


Figure 3.3: Scatter plots and exceedance curves for training and testing phases

(a) (b)

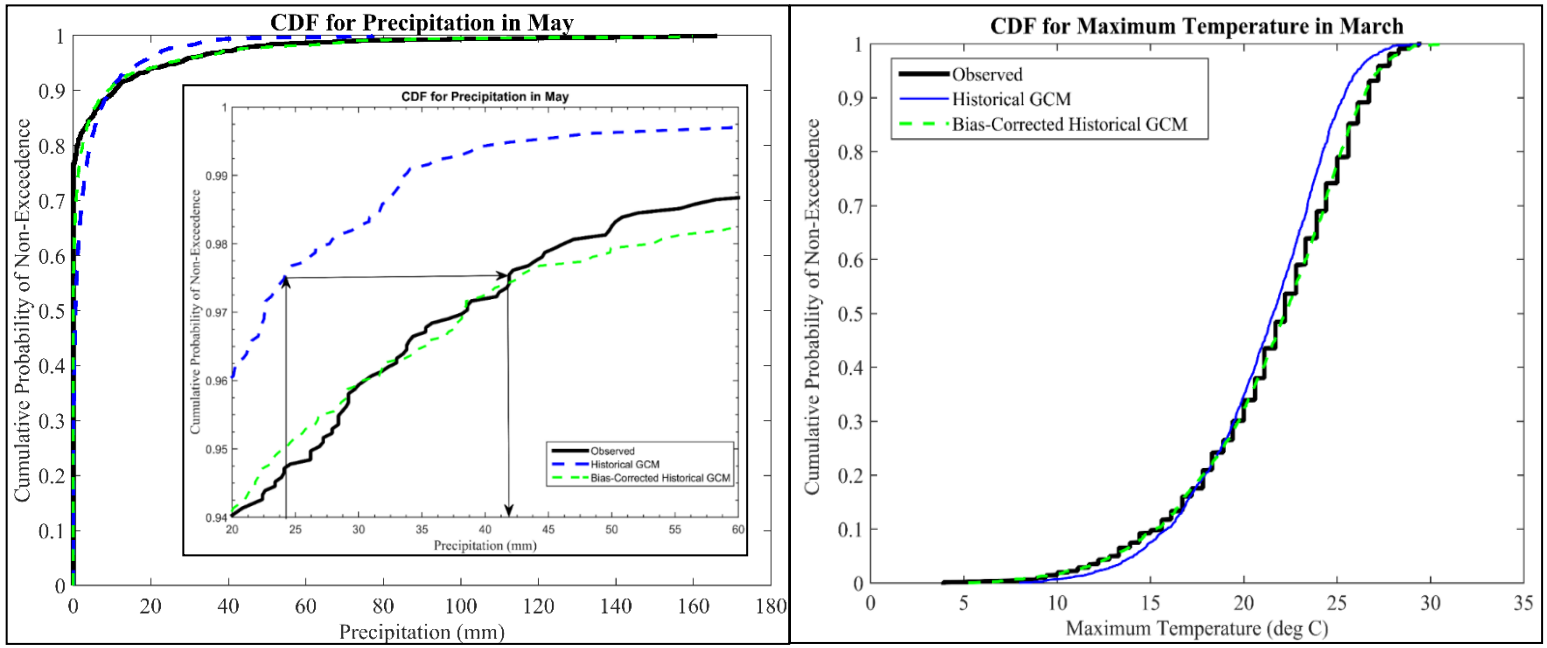


Figure 3.4: (a) Example Cumulative distribution functions (CDFs) for historical (observed) precipitation data, historical conditions of a GCM and the bias-corrected historical *bcc-csm1.1* RCP 4.5. Note that this graph displays pool of daily precipitation values for May from 1950 to 1999; A closer look at the CDFs. The arrows illustrate how the historical GCM are bias corrected. (b) Cumulative distribution functions (CDFs) for historical (observed) maximum temperature data, historical conditions of *bcc-csm1.1*, RCP 4.5 and the bias-corrected historical GCM. Note that this graph displays pool of daily maximum temperature values for March from 1950 to 1999.

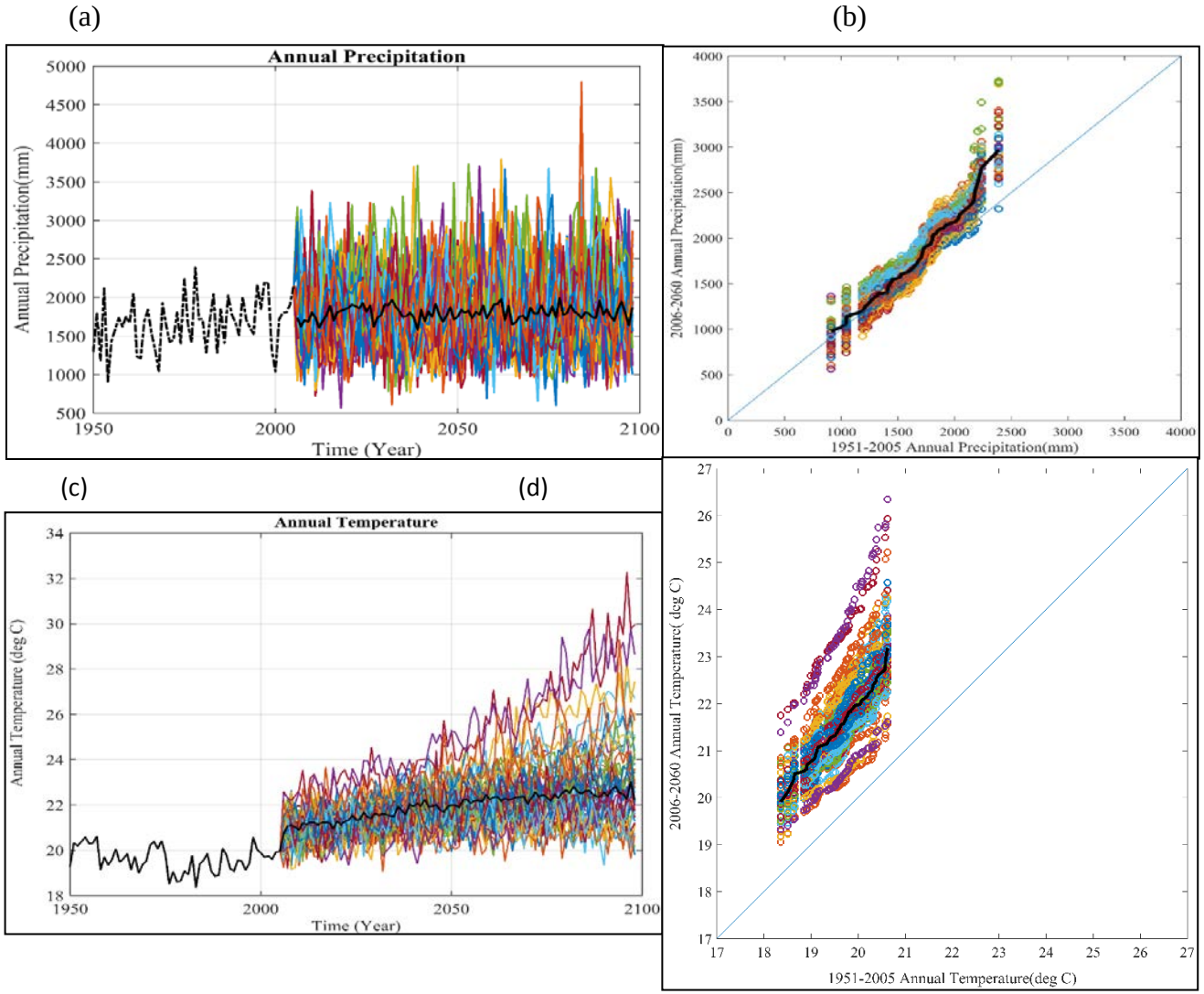


Figure 3.5: (a) Annual precipitation time series for the baseline period (dashed line) and the future period based on bias corrected GCM outputs for all 44 ensembles; bold black line corresponds to the ensemble median. (b) Trend analysis of annual precipitation; Black line depicts the median. (c) Annual temperature time series for the baseline period and the future period based on bias corrected GCM outputs for all 44 ensembles. (d) Trend analysis of annual mean temperature; Black line depicts the median.

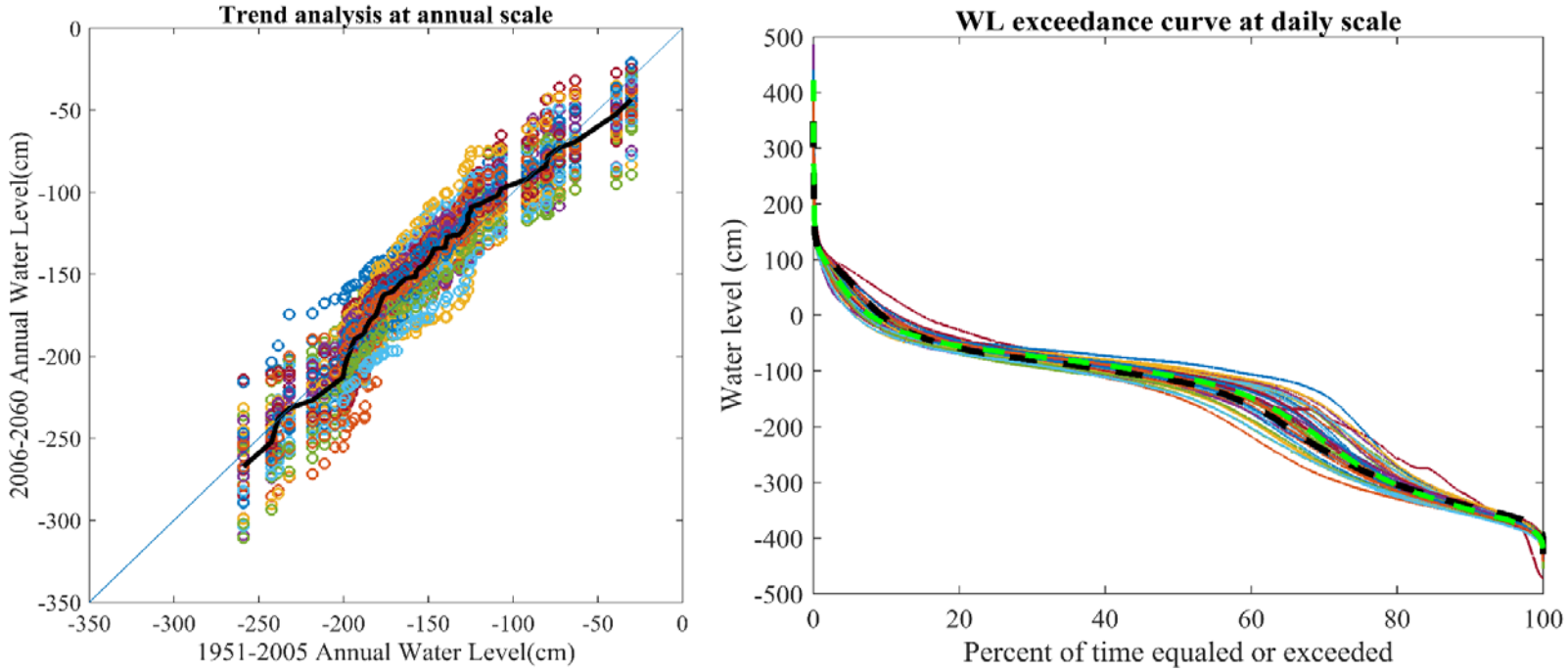


Figure 3.6: (Left) Trend analysis of annual mean WLs in which black line corresponds to ensemble median; (Right) WL exceedance curve at daily scale. Note that WL exceedance curve refer to the probability of exceedance of "depth below ground surface". Black and green dashed lines depict WL calculated for baseline period and ensemble median, respectively.

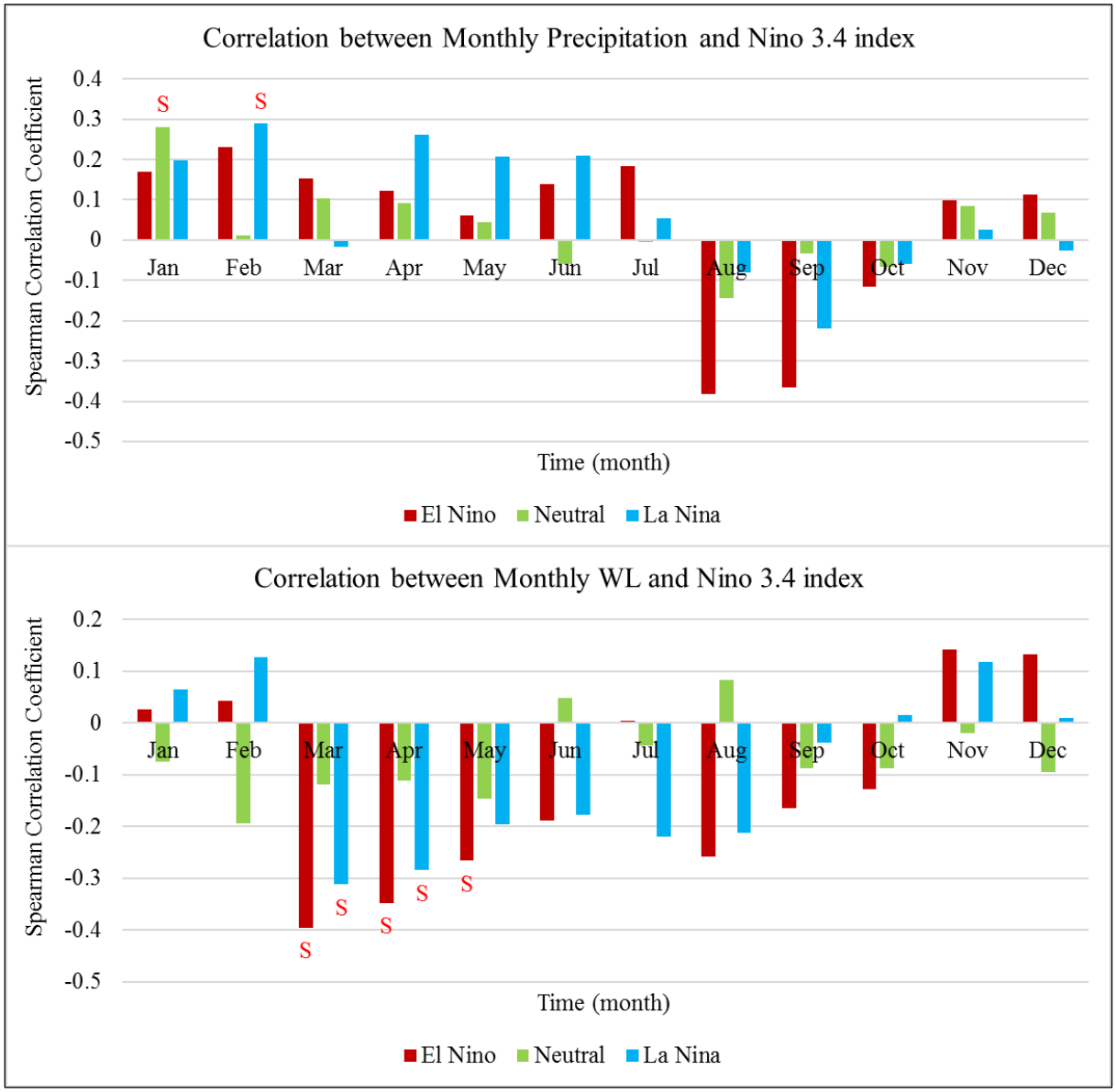


Figure 3.7: Spearman's correlation coefficient between Niño 3.4 index and precipitation (top figure) and WL (bottom figure) in monthly scale. *S* indicates the significant correlations at 95% confidence level.

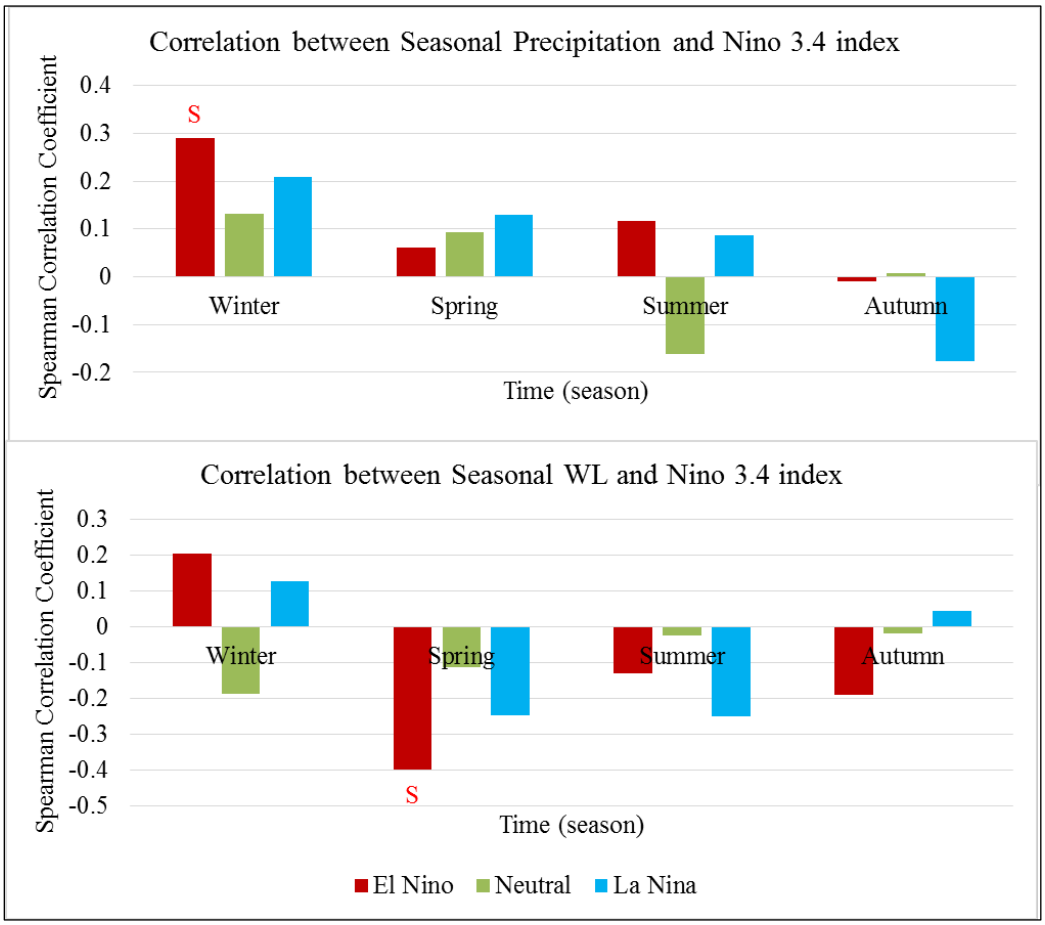


Figure 3.8: Spearman correlation coefficients between ENSO phases and precipitation/WL at seasonal scale

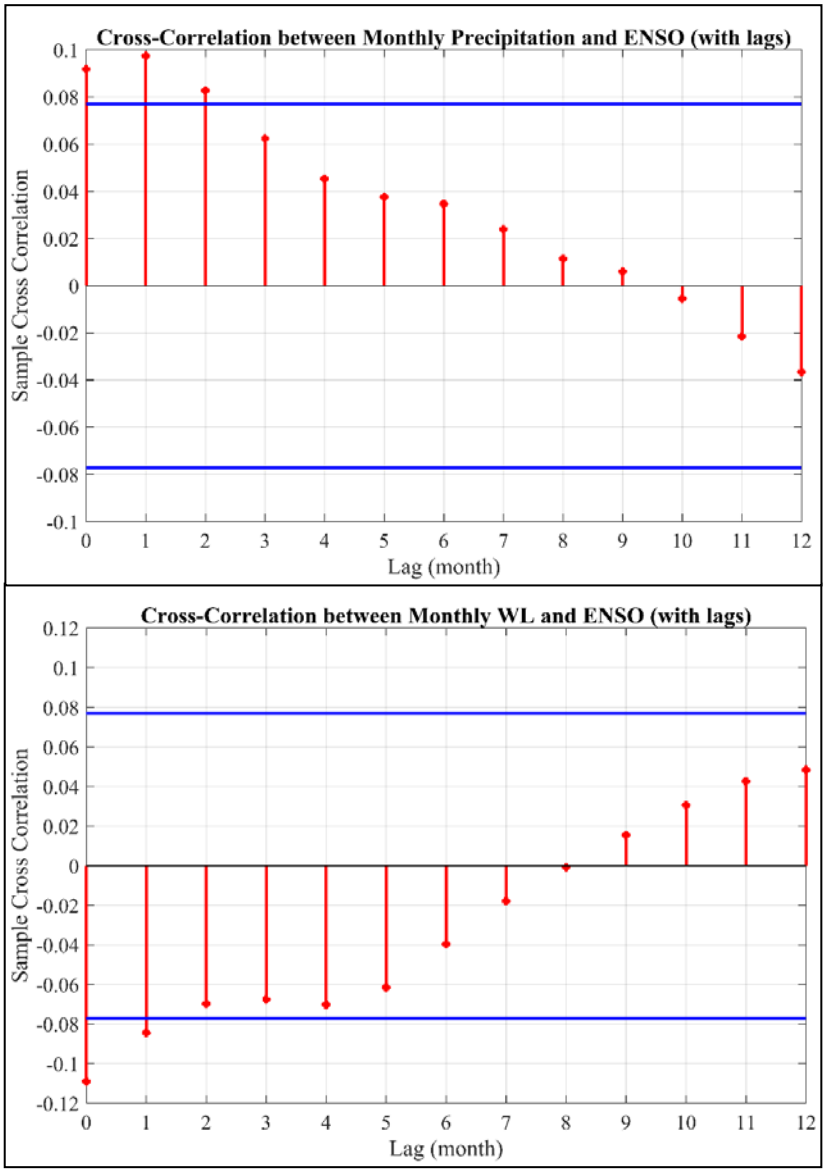


Figure 3.9: Cross-correlation between precipitation/WL time series and lag time of ENSO time series; blue lines represent 95% confidence levels.

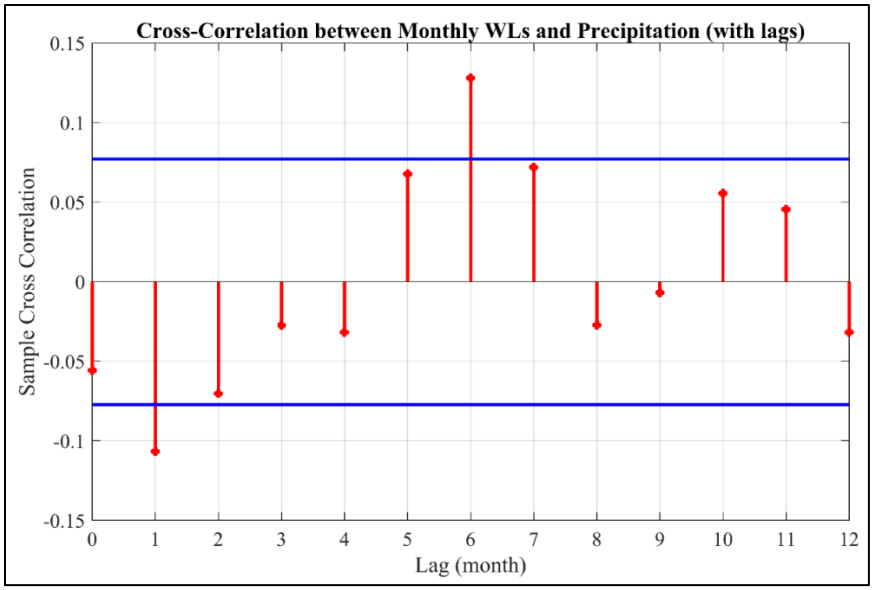


Figure 3.10: Cross-correlation between WL and lag time of precipitation time series; blue lines represent 95% confidence levels.

# Chapter 4 : A Physically-based Model for Predicting Soil Moisture Dynamics in Wetlands


## Abstract

A depth-averaged version of the one-dimensional Richard's equation (RE) was developed to predict the temporal variation of the average moisture content of the root zone and the layer below it in unsaturated parts of wetlands. This simplified solution for predicting average moisture content converts the partial differential equations (PDE) of the RE into ordinary differential equations (ODEs), thus computationally it is much more efficient. This method takes into account the plant uptake and groundwater table fluctuations, which are commonly overlooked in hydrologic models dealing with wetlands undergoing wetting and drying cycles. The Heun's predictor-corrector method was adopted to discretize and solve the equations numerically. For verification purposes, the developed depth-averaged solutions were compared to Hydrus-1D model, which uses full RE, under gravity drainage only assumption and under full-term equations. Model verifications were carried out under various top boundary conditions: no ponding at all, ponding at some point, and no rain. Results are presented in time series of soil water contents in each layer. Through hypothetical scenarios and actual atmospheric and groundwater level data from a field in the Hupselse Beek watershed in the Netherlands, the utility of the developed depth-averaged RE was demonstrated. Gravity drainage version of the depth-averaged model worked well in comparison to Hydrus-1D, under all the assigned atmospheric boundary conditions of varying fluxes for all examined soil types including sandy loam, loam, sandy clay loam, and sand. The full-term depth-averaged RE method offers reasonable accuracy compared to the full RE solutions from Hydrus-1D, with a significant reduction in computational time. The full-term version of the depth-averaged RE model

estimated the moisture content with better accuracy for the root zone by considering zero pressure head at a fixed groundwater depth as the bottom boundary condition. The accuracy of this model is lower for the second layer. The developed/evaluated model of this study for moisture accounting at the vadose zone not only applies to non-flooded wetlands but also is suitable for application to watersheds and can be utilized in watershed hydrology models.

## 1. Introduction

Hydrology is the main driving force for many physical, chemical and biological processes in wetlands. To account for biogeochemical processes and their cycling in wetlands, two aspects of wetland hydrology should be considered; *i*) the effects of groundwater fluctuations on wetland soil moisture and *ii*) the effects of seasonal water level patterns in wetlands and the rise and fall of wetland surface and subsurface water (Sharifi, 2013). Regarding the former, many wetland hydrology models use a simple water balance equation to simulate groundwater levels based on precipitation and ET loses (Sharifi et al. 2017). In other words, wetlands are considered to be wetted only from above in many large-scale models while the hydrologic representation of groundwater-fed wetlands (i.e., wetted from below by groundwater upwelling) is inadequate (Fan and Miguez-Macho, 2011). In the latter, wetland soil transitions between saturated and unsaturated conditions, which requires consideration of soil moisture dynamics to capture the effects of unsaturated zones on the wetland hydrology and eventually wetland biogeochemistry. Figure 4.1 displays a hypothetical seasonally flooded wetland which is flooded for extended periods. When water level falls and rises, the flooded section of the wetland shrinks and expands, respectively.

The *WetQual* model (Hantush et al. 2013; Kalin et al. 2013, Sharifi et al. 2013) and several other wetland models (e.g. Martin and Reddy 1997; van Dam et al. 2007) are unable to track the dynamics of geochemical reactions in the unsaturated sections of the wetland. Sharifi et al. (2017) recently extended the wetland water quality model, *WetQual* to account for the nutrient cycling in both ponded and unsaturated section of wetlands, however, as discussed in detail later, the hydrology component of their model is too complex causing numerical issues. Consequently, the applications of these models to simulate nutrient dynamics in wetlands going through wetting and drying cycles are limited.

Wetlands are low-lying, regularly inundated ecosystems that can affect local/regional hydrology and the fate and transport of various water quality constituents (e.g., sediment and nutrients) (Wang et al. 2010). In a watershed with a considerable number of wetlands, their cumulative influences can strongly affect the magnitude, frequency, and duration of hydrologic and biogeochemical fluxes or transfers of water and materials to downstream aquatic systems (Kalin et al. 2017). Wetlands are usually connected to local and regional water bodies where wetland-groundwater interactions are important. Wetlands can recharge the groundwater, receive inflow from groundwater, or do both. In fact, considering wetland and groundwater connectivity is essential to understand the hydrological processes beyond the site scale at the broader watershed scale (Kalin et al. 2017). The soil moisture condition may vary from fully saturated, where wetland free water may or may not be hydraulically connected to the underlying aquifer, to partially saturated soil (Kalin et al. 2017). If the water table falls deep below the soil surface, or if the ponded water starts receding, unsaturated soil conditions will start developing (Kalin et al. 2017). Under such conditions, a variably saturated model such as the matric potential form of the RE is commonly used. The RE is the most complete equation to quantify movement of soil

moisture in the unsaturated soil. In the multidimensional WETLANDS model developed by Mansell et al. (2000), RE was coupled to a lumped pond water budget equation to model local hydrology for an individual cypress pond wetland system by considering the effects of plant uptake. However, the fact that RE is highly non-linear makes it very difficult to solve and computationally demanding, compared to other simpler equations such as Darcy's equation. Solving RE for every node in a wetland hydrology model domain can be quite time-consuming and computationally demanding when performing long-term simulations.

To address wetland soil heterogeneity, the nonlinearity of soil hydraulic characteristics, vertical variation of physical properties in the soil profile, and non-uniform root water uptake, a numerical solution of RE was found to be useful Sharifi et al. (2017). One-dimensional (1D) RE was then utilized to simulate soil moisture contents in the unsaturated zone of wetlands in *WetQual* model. Thompson et al. (2004) had reported the utilization of 1D RE for unsaturated flow, and 3D saturated subsurface flows using the Boussinesq equation in a wet grassland, the Elmley Marshes in southeast England, by a coupled MIKE SHE/MIKE 11 modeling system. These two studies, in theory, are superior to those that utilized Darcy's law in their 1D mass balance equations (Hammer and Kadlec 1986; Kazezyilmaz-Alhan et al. 2007) because of the better representation of the physics. However, Sharifi et al. (2017) considered a head-controlled boundary condition (BC) for the bottom node, assuming the existence of a non-fluctuating perched water table at the bottom of the soil column. A key component, plant uptake effects on soil moisture redistribution, is missing in Thompson et al. (2004).

One of the appreciable efforts related to simulating soil moisture dynamics in the unsaturated section of wetland soils was recently made by Sharifi et al. (2017). They adapted and slightly modified the van Dam and Feddes (2000) finite difference solution to solve 1D RE.

Following van Dam and Feddes (2000), for an implicit backward finite difference solution to RE, the active soil layer was divided into compartments with a thickness of $\Delta z$ with each compartment containing a node in the middle. The variably saturated compartment-averaged volumetric moisture content is obtained by depth-averaging of the solution of Richard's equation over each of the unsaturated layer. Once the daily soil moisture profile of wetland soil was attained, *WetQual* model relationships were updated to simulate geochemical reactions and track concentrations of N and C related constituents in wetland soil. They reported frequent crashes in the numerical solution, specifically when a soil is close to saturation due to the hyperbolic nature of RE and high non-linearity of soil hydraulic functions. Multiple crashes of the numerical model forced them to run the soil moisture model deterministically. Hence, the numerical solution of RE for the infiltration-redistribution cycle is complicated and is not recommended for wetland hydrology modeling in the vadose zone. For a proper application of *WetQual* model, a Monte Carlo (MC) simulation of 50,000 or 100,000 runs are usually suggested. This is computationally demanding and solving RE can be quite challenging for the application of *WetQual* to non-flooded wetlands. Since there is no guarantee that the numerical solutions of RE will converge, there is a risk in conducting MC simulations that a small percentage of RE solutions jeopardize the stability of the entire *WetQual* simulation. Furthermore, *WetQual* is a lumped model in need of average moisture content only. There is no reason to calculate moisture contents at multiple points in wetland soils.

In this chapter, we aim to address the explained drawback of available wetland models by developing a depth-averaged solution to the RE for one-dimensional vertical unsaturated flow in *WetQual* model. This model will extend the *WetQual* model to unsaturated wetland soil and is a reliable replacement for extended *WetQual* model for the vadose zone developed by Sharifi et al.

(2017). To achieve this goal, a two-layer depth-averaged solution to RE was utilized and examined in this study. This method considers the effect of plant uptake and takes into account the groundwater level fluctuations. Because of a simpler mathematical representation of the depth-averaged RE (DARE) through defining ordinary differential equations (ODEs) instead of Richards' partial differential equation (PDE), the problem of crashing model in the unsaturated flow calculation is no longer an issue with the application of *WetQual* to non-flooded wetlands. To that end, the gravity drainage condition, which assumes a uniform, vertical unit-gradient and ignores suction forces was first considered for numerical development and verification of DARE. In the next step of developing numerical solution/code, negative pressure head component was taken into consideration which resulted in the full-term version of the DARE. The two layers include root zone and the zone between roots and the water table. In DARE, groundwater table is assumed to be always below the root zone. We also assume that the unsaturated aerobic section of active sediment layer is the same as the depth to groundwater table. The methodology and verification of the model through a case study are presented in this chapter.

## 2. Model Development

### 2.1 WetQual Model

The process-based *WetQual* model simulates hydrology and water quality of wetlands (Hantush et al. 2013; Kalin et al. 2013, Sharifi et al. 2013). Nutrient cycling in *WetQual* accounts for nitrogen (N), phosphorus (P), total suspended sediment (TSS) and carbon (C) cycles and their dynamics in wetlands. The model partitions a wetland into three basic compartments: (1) (free) water column, (2) wetland soil layer, which is further portioned into aerobic and anaerobic zones, and (3) plant biomass (Hantush et al., 2013). Processes in surface water and the bottom-

active soil layer are described by a system of coupled ordinary differential equations (Hantush et al. 2013). The model runs on a daily time scale, while it internally divides the one-day time interval into a smaller time interval for numerical integration. Earlier versions of the model were applicable to permanently ponded wetlands (Hantush et al. 2013; Kalin et al. 2013, Sharifi et al. 2013). Sharifi et al. (2017) extended the model to account for the variably saturated areas surrounding ponded soil using the 1D RE. The model lumps the mass of nutrients and tracks the biogeochemical transformation/exchanges within the ponded part of the wetland and the surrounding unsaturated soil (Sharifi et al. 2017). In this study, a new soil moisture accounting method was developed as a simpler but robust alternative to the unsaturated flow component of *WetQual* developed by Sharifi et al. (2017).

## 2.2 Conceptualization of Ponded and Variably Saturated Compartments

In the extended *WetQual* model, the wetland is divided into ponded and variably saturated compartments. The ponded compartment consists of a pool of standing water (W) at the top, a thin layer of aerobic soil in the middle ($S_1$), and a relatively thick column of anaerobic soil at the bottom ($S_2$) (Figure 4.2) (Sharifi et al. 2017). The variably saturated compartment has three layers of soil standing on top of each other (Figure 4.2). There is a column of unsaturated soil at the top extended from the soil surface down to the top of water table ($S_0$ in Figure 4.2), which is assumed to be entirely aerobic. Extending from the water table to some depth below represents a thin aerobic layer ($S_1$). Below this depth, where oxygen is practically negligible, the soil is saturated but anaerobic, with a thickness extending from the depth of zero oxygen concentration to the depth of the active sediment layer ($S_2$) (Sharifi et al. 2017). The model is fully mixed in each layer, where constituent concentrations are represented with average values

for each layer. Layer $S_0$, which is the focus of this study, is further divided into two layers (i.e., root zone and the zone between roots and the water table) and soil moisture estimations are calculated for each of those layers. To track the mass exchange between the two compartments, a transitional compartment was introduced. At each time step, the transitional compartment will form and will adopt the concentrations of either ponded or variably saturated compartment (depending on whether water level is falling or rising) (Sharifi et al. 2017).

### 2.3 Modeling Moisture Redistribution in Wetland Soil

Wetland soil heterogeneity, the nonlinearity of physical properties in wetland soil and non-uniform root water uptake of wetland plants make the simulation of soil moisture dynamics a challenging endeavor. The key to a successful water quality model in wetlands with varying degree of saturation is an accurate simulation of soil moisture content. A proper soil moisture accounting model should consider the different sources of water to wetland soil (precipitation, groundwater upwelling, etc.) and sinks of water from the wetland soil (soil evaporation, plant water uptake, percolation, etc.). A robust soil moisture accounting model needs to handle different boundary conditions at the top and bottom of a soil column. To this end, a depth-averaged version of RE was developed, and numerically solved for estimating average moisture content in the variably saturated zone of wetlands.

### 2.4 Richards' Equation

1D RE for water movement in unsaturated non-swelling soil can be obtained by applying Buckingham's continuity equation to Darcy's law (Richards 1931):

$$\frac{\partial \theta}{\partial t} = C(\psi)\frac{\partial \psi}{\partial t} = \frac{\partial}{\partial z}\left[K(\psi)\left(\frac{\partial \psi}{\partial z} + 1\right)\right] - S(z) \quad (1)$$

where, $\theta$ is volumetric moisture content (dimensionless); $K$ is soil hydraulic conductivity ($LT^{-1}$); $\psi$ is soil water pressure head (L); $t$ is time (T); $S$ is plant transpiration rate per unit depth ($T^{-1}$); $z$ is depth below the soil surface (L, positive downward); $C$ ($=\frac{\partial\theta}{\partial\psi}$) is specific water content capacity ($L^{-1}$). The development of two-layer DARE is explained below. Dr. Mohamed Hantush derived the gravity drainage and full-term depth-averaged forms of the Richard Equation and contributed to Heun's method numerical scheme. I developed the dimensionless forms of the equations, the numerical discretization, and the coding. I also performed the model verification of the two-layer DARE.

**2.5 Two-layer Depth-Averaged Solution to Richards' Equation**

Continuity Equation:

$$\frac{\partial\theta}{\partial t} = -\frac{\partial q}{\partial z} - S(z,t) \tag{2}$$

Darcy's Equation:

$$q = K(\psi)\frac{\partial\psi}{\partial z} + K(\psi)$$

where, $\theta$ is volumetric moisture content (dimensionless); $K$ is hydraulic conductivity ($LT^{-1}$) under unsaturated flow condition; $\psi$ is soil water pressure head (L); $t$ is time (T); $S$ is plant transpiration rate per unit depth ($T^{-1}$); $z$ is depth below the soil surface (L, positive downward); $\psi$ is soil water pressure head (L); $K$ is hydraulic conductivity ($LT^{-1}$) and $q$ ($LT^{-1}$) is Darcy's flow.

Let's define $\bar{\theta}_1(t)$ and $\bar{\theta}_2(t)$ as

$$\bar{\theta}_1(t) = \frac{1}{h}\int_0^h \theta(z,t)\,dz$$

$$\bar{\theta}_2(t) = \frac{1}{H-h}\int_h^H \theta(z,t)\, dz$$

where, $h$ is the depth of root zone, and $H$ is the depth of the top of capillary fringe (saturated water at air-entry pressure). Figure 4.3 displays the schematic of soil profile for the two-layer depth-averaged solutions to Richards (1931).

Integrating Eq. (2) from z = 0 to z = h

$$\int_0^h \frac{\partial \theta}{\partial t} dz = -\int_0^h \frac{\partial q}{\partial z} dz - \int_0^h S(z,t)\, dz$$

yields

$$h\frac{d\bar{\theta}_1}{dt} = -q|_{z=h} + q|_{z=0} - h\bar{S} \tag{3}$$

where,

$$\bar{S} = \frac{1}{h}\int_0^h S(z,t)\, dz$$

Integrating Eq. (2) from $z = h$ to $z = H(t)$ and dropping the $S$ term

$$\int_h^{H(t)} \frac{\partial \theta}{\partial t} dz = -\int_h^{H(t)} \frac{\partial q}{\partial z} dz$$

Thus,

$$\frac{d}{dt}\int_h^{H(t)} \theta(z,t)dz - \theta(H,t)\frac{dH}{dt} = -q|_{z=H} + q|_{z=h}$$

or

$$\frac{d}{dt}[(H(t)-h)\bar{\theta}_2(t)] - \theta_s\frac{dH}{dt} = q|_{z=h} \tag{4}$$

Note that $\theta(H,t) = \theta_s$, and $q|_{z=H} = 0$. Adding Eq. (3) to (4) yields

$$h\frac{d\bar{\theta}_1}{dt}+\frac{d}{dt}[(H(t)-h)\bar{\theta}_2(t)]-\theta_s\frac{dH}{dt}=q|_{z=0}-h\bar{S} \quad (5)$$

The solution of Eqs (3) and (5) should be exactly that of (3) and (4). Either way, an expression for $q|_{z=h}$ is needed. We make the following approximation:

$$q|_{z=h}\cong\bar{q}=\frac{1}{h}\int_0^h q(z,t)\,dz$$

Thus,

$$q|_{z=h}\cong\frac{1}{h}\int_0^h\left\{K(\psi)\frac{\partial\psi}{\partial z}+K(\psi)\right\}dz$$

The integral can be approximated to yield

$$q|_{z=h}\cong\frac{1}{h}\overline{K(\psi)}\int_0^h\frac{\partial\psi}{\partial z}\,dz+\overline{K(\psi)}$$

$$q|_{z=h}\cong\frac{1}{h}\overline{K(\psi)}(\psi(h,t)-\psi(0,t))+\overline{K(\psi)} \quad (6)$$

Taylor expansion of $K(\psi)$ around $\bar{\psi}$ is

$$K(\psi)=\mathrm{K}(\bar{\psi})+\left.\frac{\partial K}{\partial\psi}\right|_{\psi=\bar{\psi}}(\psi-\bar{\psi})+\frac{1}{2}\left.\frac{\partial^2K}{\partial\psi^2}\right|_{\psi=\bar{\psi}}(\psi-\bar{\psi})^2+\cdots$$

To the first order, the integration of the R.H.S. from $z$ = 0 to $z$ = $h$ and dividing by $h$ can be approximated as:

$$\overline{\mathrm{K}(\psi)}\cong\mathrm{K}(\bar{\psi})$$

Assuming $\psi(h,t)\cong\bar{\psi}_1$, equation (6) becomes:

$$q|_{z=h}\cong\frac{1}{h}\mathrm{K}(\bar{\psi}_1)(\bar{\psi}_1-\psi(0,t))+\mathrm{K}(\bar{\psi}_1)$$

The remaining challenge is computing $\psi(0,t)$ and $q$(0,t). First, we expand $\psi(z,t)$ around $z$ = 0 using Taylor series:

$$\psi(\mathrm{z},\mathrm{t}) = \psi(0,\mathrm{t}) + \left.\frac{\partial\psi}{\partial z}\right|_{z=0} z + \frac{1}{2}\left.\frac{\partial^2\psi}{\partial z^2}\right|_{z=0} z^2 + \cdots$$

Integrating from $z = 0$ to $z = h$ and dividing by $h$

$$\bar{\psi} = \psi(0,\mathrm{t}) + \frac{1}{2}\left.\frac{\partial\psi}{\partial z}\right|_{z=0} h + \cdots$$

yields

$$\left.\frac{\partial\psi}{\partial z}\right|_{z=0} = 2\,\frac{\bar{\psi} - \psi_0}{h}$$

Thus,

$$q(0,t) = 2K(\psi_0)\frac{\bar{\psi}_1 - \psi_0}{h} + K(\psi_0) \tag{7}$$

in which $\psi_0 \equiv \psi(0,t)$. Before incipient ponding, $q(0,t) = i$ and Eq. (7) becomes

$$i = 2K(\psi_0)\frac{\bar{\psi}_1 - \psi_0}{h} + K(\psi_0) \tag{8}$$

This boundary condition couples $\psi_0$ with $\bar{\psi}_1$. An iterative numerical scheme (Picard iteration) would be needed to solve Eqs. (3) and (5) subject to (8). Assuming gravity drainage (i.e., zero pressure gradient at the surface), a simpler, decoupled equation using any of the formulas for unsaturated $K$ can be solved for $\psi_0$:

$$K(\psi_0) = i$$

Either way, Eqs. (3) and (5) become

$$h\frac{d\bar{\theta}_1}{dt} = -\frac{1}{h}\mathrm{K}(\alpha\,\bar{\psi}_1 + (1-\alpha)\,\bar{\psi}_2 - \psi_0) - \mathrm{K}(\bar{\psi}_1) + i - h\bar{S}$$

by ignoring $\alpha$ (which is defined later):

$$h\frac{d\bar{\theta}_1}{dt} = -\frac{1}{h}\mathrm{K}(\bar{\psi}_1)(\bar{\psi}_1 - \psi_0) - \mathrm{K}(\bar{\psi}_1) + i - h\bar{S} \tag{9}$$

$$h\frac{d\bar{\theta}_1}{dt} + \frac{d}{dt}[(H(t) - h)\bar{\theta}_2] - \theta_s\frac{dH}{dt} = i - h\bar{S} \tag{10}$$

With Eq. (8), we have three equations with three unknowns, $\bar{\theta}_1$, $\bar{\theta}_2$, and $\psi_0$. If ponding occurs at depth *d*, we have $\psi_0 = -d$ and

$$q(0,t) = 2K(\theta_s)\frac{\bar{\psi}_1 + d}{h} + K(\theta_s) \tag{11}$$

This equation and that for $q|_{z=h}$ can be substituted into Eq. (3) and (5) to yield

$$h\frac{d\bar{\theta}_1}{dt} = -\frac{1}{h}\mathrm{K}(\bar{\psi}_1)(d + \bar{\psi}_1) - \mathrm{K}(\bar{\psi}_1) + 2K(\theta_s)\frac{\bar{\psi}_1 + d}{h} + K(\theta_s) - h\bar{S} \tag{12}$$

$$h\frac{d\bar{\theta}_1}{dt} + \frac{d}{dt}[(H(t) - h)\bar{\theta}_2(t)] - \theta_s\frac{dH}{dt} = 2K(\theta_s)\frac{\bar{\psi}_1 + d}{h} + K(\theta_s) - h\bar{S} \tag{13}$$

Note that $\bar{\theta}_1$ and $\bar{\psi}_1$ are related using any of soil moisture characteristic curves. Also, note that Equations (12) and (13) assume that flow in the root zone is independent of that in the lower layer. The assumption of $\psi(h,t) \cong \bar{\psi}_1$ made above is, therefore, a limiting one. A more general approach is to assume $\psi(h,t)$ equal to some weighted average of $\bar{\psi}_1$ and $\bar{\psi}_2$:

$$\psi(h,t) = \alpha\,\bar{\psi}_1 + (1-\alpha)\,\bar{\psi}_2$$

For example, an approach is assuming $\alpha = \frac{h}{H}$ and 1- $\alpha$ = (*H*-*h*)/*H*. Alternatively, $\alpha$ can be determined by calibration or comparison with full RE. In this case, Eq. (6) and (12) become:

$$q|_{z=h} \cong \frac{1}{h}\mathrm{K}(\bar{\psi}_1)(\alpha\,\bar{\psi}_1 + (1-\alpha)\,\bar{\psi}_2 - \psi_0) + \mathrm{K}(\bar{\psi}_1)$$

$$h\frac{d\bar{\theta}_1}{dt} = -\frac{1}{h}\mathrm{K}(\bar{\psi}_1)(\alpha\,\bar{\psi}_1 + (1-\alpha)\,\bar{\psi}_2 + d) - \mathrm{K}(\bar{\psi}_1) + 2K(\theta_s)\frac{\bar{\psi}_1 + d}{h} + K(\theta_s) - h\bar{S} \tag{14}$$

Equation (4) becomes:

$$h\frac{d\bar{\theta}_1}{dt} + \frac{d}{dt}[(H(t) - h)\bar{\theta}_2(t)] - \theta_s\frac{dH}{dt} = 2K(\theta_s)\frac{\bar{\psi}_1 + d}{h} + K(\theta_s) - h\bar{S} \tag{15}$$

If there is no rain, a proper boundary condition would be $q(0,t) = -e_v$; in which case, Eqs. (3) and (5) become:

$$h\frac{d\bar{\theta}_1}{dt} = -\frac{1}{h}\mathrm{K}(\bar{\psi}_1)(\alpha\,\bar{\psi}_1 + (1-\alpha)\,\bar{\psi}_2 - \psi_0) - \mathrm{K}(\bar{\psi}_1) - e_v - h\bar{S} \tag{16}$$

$$h\frac{d\bar{\theta}_1}{dt} + \frac{d}{dt}[(H(t)-h)\bar{\theta}_2(t)] - \theta_s\frac{dH}{dt} = -e_v - h\bar{S} \tag{17}$$

Equations (16) and (17) require additional information for $\psi_0$:

$$e_v = -2K(\psi_0)\frac{\bar{\psi}_1 - \psi_0}{h} - K(\psi_0) \tag{18}$$

We implement the soil hydraulic functions of van Genuchten (1980) who used the statistical pore-size distribution model of Mualem (1976) to obtain a predictive equation for the unsaturated hydraulic conductivity function in terms of soil water retention parameters (Šimůnek et al. 2013). Soil hydraulic functions of $\theta(\psi)$, $K(\psi)$ and $K(\theta)$ could be described by the van Genuchten- Mualem model Genuchten (1980):

$$\theta(\psi) = \theta_{res} + \frac{\theta_{sat} - \theta_{res}}{[1 + |\alpha\psi|^n]^m} \tag{19}$$

$$K(\psi) = \frac{\{(1-(\alpha\psi)^{n-1})[1+(\alpha\psi)^n]^{-m}\}^2}{[1+|\alpha\psi|^n]^{m/2}} \tag{20}$$

$$K(\theta) = K_{sat}{S_e}^l\left[1-(1-{S_e}^{1/m})^m\right]^2 \tag{21}$$

$$S_e = \frac{\theta - \theta_{res}}{\theta_{sat} - \theta_{res}} \tag{22}$$

$$m = 1 - \frac{1}{n} \tag{23}$$

where, $\theta_{res}$ and $\theta_{sat}$ are, respectively, residual and saturated water content (dimensionless), $K_{sat}$ is the saturated hydraulic conductivity ($LT^{-1}$), and $\psi$is the soil water pressure head (L). A pore-size distribution index $n$ (dimensionless), a pore connectivity parameter $\lambda$ (dimensionless) and $\alpha$ ($L^{-1}$) are fitting parameters, which can be extracted from soil databases (e.g., Kroes et al. 2008). The pore connectivity parameter $\lambda$ in the hydraulic conductivity function was estimated (Mualem, 1976) to be about 0.5 as an average for many soils (Šimůnek et al. 2013).

**2.6 Dimensionless Equations and Numerical Solutions for Specific Cases**

The developed two-layer DARE was first evaluated under gravity drainage condition, which assumes a uniform, vertical unit-gradient and ignores negative pressure head (i.e., $\frac{\partial \psi}{\partial z} = 0$). Hydrus-1D which solves the full-term RE was chosen to serve as the benchmark in this study. Its merits are explained in "Model Assessment" section. Lower boundary condition of "Free Drainage" was considered in the Hydrus-1D model to keep these two models consistent as much as possible for verification purposes. The next two upcoming sections present the equations for gravity drainage condition. Development of the gravity drainage condition is required for wetlands where there is no groundwater table or groundwater table is very deep. Following the evaluation of the gravity drainage condition, the more complete version of the equations was evaluated. Numerical solutions were performed for gravity drainage condition using explicit scheme of finite difference and Heun's method, and the results from these two numerical methods were compared. The solutions were compared for one scenario, i.e., "no rainfall and no ET" as the top BC. We found that there is no considerable difference between the results from explicit finite difference and those from Heun's method. Calculated moisture contents by the two

approaches have negligible differences (~1/10,000). Although there are certain cases where easily programmable techniques, such as Euler's method, can be applied to advantage, the Heun and midpoint methods are superior and should be implemented if the problem objectives can be achieved (Chapra and Canale, 2010). We decided to continue with the Heun's method to develop the numerical solutions for dimensionless depth-averaged equations for both gravity drainage conditions and full-term equations (i.e., by considering negative pressure head component). Heun's method solutions to gravity drainage and full-term versions of DARE are explained following the development of dimensionless equations. Dimensionless forms of equations were developed to help generate monographs in the future, applicable to any geometry, soil and hydroclimate parameters. Although I did not have the time to fully benefit from these dimensionless equations in this dissertation, it will help future studies especially in developing monographs. To that end, we first came up with several dimensionless variables that best represent the gravity drainage version of DARE. The same procedure was followed for the full-term DARE.

### 2.6.1 Dimensionless Equations for Gravity Drainage Condition

In the development of full-term DARE and accordingly the gravity drainage condition, the following three top boundary conditions were considered: "no ponding at all" ($i<fc$), "ponding at some point" ($i>fc$), and "no rain" ($i=0$), where $i$ and $fc$ are rainfall intensity and infiltration capacity, respectively. The infiltration rate at the soil surface $q(0,t)$ is given by equation (7). This equation can be used to calculate $\psi_0$ and accordingly $\theta_0$ is obtained from equation (19). By comparing moisture content at the soil surface $\theta_0$ with the saturated moisture content $\theta_s$ at each time step, we can determine if there is ponding during that time step.

However, a simplification was considered in this study in which the soil infiltration capacity (*fc*) was assumed to be equal to the saturated hydraulic conductivity ($K_s$) of the soil. This actually comes from the assumption of $\bar{\psi}_1 = \psi_0$, with which equation (7) becomes $q(0,t) = K(\psi_0)$. Since $K(\psi_0) = K_s$ during ponding, this leads to $q(0,t) = K_s$. By doing so, we have increased consistency between DARE and Hydrus-1D for the verification purposes of this study. More information about the Hydrus-1D model comes later in this chapter. Dimensionless variables for gravity drainage conditions are defined as:

$$t^* = \frac{t * K_s}{h}, \quad H^* = \frac{H}{h}, \quad K^*(\bar{\theta}_1) = \frac{K(\bar{\theta}_1)}{K_s}, K^*(\bar{\theta}_2) = \frac{K(\bar{\theta}_2)}{K_s}, \quad S^* = \frac{(h\bar{S})}{K_s} = \frac{(S)}{K_s},$$
$$ET^* = \frac{(ev + h\bar{S})}{K_s}, i^* = \frac{i}{K_s}$$

where $t^*$, $H^*$, $K^*(\bar{\theta}_1)$, $K^*(\bar{\theta}_2)$, $S^*$, $ET^*$ and $i^*$ are dimensionless forms of $t$=time (T), $H$=depth to groundwater table (L), $K(\bar{\theta}_1)$=hydraulic conductivity for the 1st layer (i.e., root zone) ($LT^{-1}$), $K(\bar{\theta}_2)$=hydraulic conductivity for the 2nd layer (i.e., depth below root zone to groundwater table) ($LT^{-1}$), $\bar{S}$ = average plant transpiration per unit depth ($T^{-1}$), $S$=plant transpiration rate ($LT^{-1}$), $ET$=evapotranspiration ($LT^{-1}$) and $i$= rainfall intensity ($LT^{-1}$), respectively. Note that $h$ and $ev$ are defined as depth of root zone (L) and soil evaporation ($LT^{-1}$), respectively. We assume that soil evaporation is negligible during a rainfall event. Hence, evapotranspiration ($ET = e_v + h\bar{S}$) is just defined for "no rain" boundary condition. Gravity drainage equations and their dimensionless forms for various top boundary conditions are given below:

***i)*** $\boldsymbol{i < f_c}$

1st layer:

$$h\frac{d\bar{\theta}_1}{dt} = -\mathrm{K}(\bar{\theta}_1) + i - h\bar{S}$$

$$\frac{d\bar{\theta}_1}{dt^*} = -K^*(\bar{\theta}_1) + i^* - S^*$$

$$2^{nd}\text{ layer:}\quad \begin{cases} h\dfrac{d\bar{\theta}_1}{dt} + (H-h)\dfrac{d\bar{\theta}_2}{dt} = -K(\bar{\theta}_2) + i - h\bar{S} \\ \dfrac{d\bar{\theta}_1}{dt^*} + (H^*-1)\dfrac{d\bar{\theta}_2}{dt^*} = -K^*(\bar{\theta}_2) + i^* - S^* \end{cases}$$

***ii*) $i > f_c$**

$$1^{st}\text{ layer:}\quad \begin{cases} h\dfrac{d\bar{\theta}_1}{dt} = K(\theta_s) - \mathrm{K}\left(\bar{\theta}_1\right) - h\bar{S} \\ \dfrac{d\bar{\theta}_1}{dt^*} = 1 - K^*(\bar{\theta}_1) - S^* \end{cases}$$

$$2^{nd}\text{ layer:}\quad \begin{cases} h\dfrac{d\bar{\theta}_1}{dt} + (H-h)\dfrac{d\bar{\theta}_2}{dt} = -K(\bar{\theta}_2) + K(\theta_s) - h\bar{S} \\ \dfrac{d\bar{\theta}_1}{dt^*} + (H^*-1)\dfrac{d\bar{\theta}_2}{dt^*} = -K^*(\bar{\theta}_2) + 1 - S^* \end{cases}$$

***iii*) $i = 0$**

$$1^{st}\text{ layer:}\quad \begin{cases} h\dfrac{d\bar{\theta}_1}{dt} = -\mathrm{K}\left(\bar{\theta}_1\right) - e_v - h\bar{S} \\ \dfrac{d\bar{\theta}_1}{dt^*} = -K^*(\bar{\theta}_1) - ET^* \end{cases}$$

$$2^{nd}\text{ layer:}\quad \begin{cases} h\dfrac{d\bar{\theta}_1}{dt} + (H-h)\dfrac{d\bar{\theta}_2}{dt} = -K(\bar{\theta}_2) - e_v - h\bar{S} \\ \dfrac{d\bar{\theta}_1}{dt^*} + (H^*-1)\dfrac{d\bar{\theta}_2}{dt^*} = -K^*(\bar{\theta}_2) - ET^* \end{cases}$$

### 2.6.2 Numerical Solutions of Dimensionless Gravity Drainage Equations by Heun's Method

***i*) $i < f_c$**

$$1^{st}\text{ layer:}\quad \begin{cases} \boldsymbol{\dfrac{d\bar{\theta}_1}{dt^*} = -K^*(\bar{\theta}_1) + i^* - S^*} \end{cases}$$

For simplification purposes, $\theta_1$ *and* $\theta_2$ are used below for $\bar{\theta}_1$ *and* $\bar{\theta}_2$, respectively.

The slope or time derivative of the function $\theta(t)$ at the beginning of the time interval:

$$\frac{d\theta_{1_i}}{dt^*} = f\left(t_i^*, \theta_{1_i}\right) = -K^*\left(\theta_{1_i}\right) + i_i^* - S_i^*$$

$$\theta^0{}_{1_{i+1}} = \theta_{1_i} + f\left(t_i^*, \theta_{1_i}\right) * (\Delta t^*)$$

where, subscript $i$=time step and $\Delta t^*$ is the dimensionless form of $\Delta t$=length of each time step. $\theta^0{}_{1_{i+1}}$refers to the standard Euler method (predictor equation). The slope at the end of the time interval:

$$\frac{d\theta_{1_{i+1}}}{dt^*} = f\left(t_{i+1}^*, \theta^0{}_{1_{i+1}}\right) = (-\mathrm{K}\left(\theta^0{}_{1_{i+1}}\right)^* + i_{i+1}^* - S_{i+1}^*)$$

Eventually,

$$\theta_{1_{i+1}} = \theta_{1_i} + \frac{f\left(t_i^*, \theta_{1_i}\right) + f\left(t_{i+1}^*, \theta^0{}_{1_{i+1}}\right)}{2} * (\Delta t^*)$$

which is the corrector equation.

2nd layer: $\left\{ \quad \boldsymbol{\frac{d\bar{\theta}_1}{dt^*} + (H^* - 1)\frac{d\bar{\theta}_2}{dt^*} = -K^*(\bar{\theta}_2) + i^* - S^*} \right.$

The slope at the beginning of the time interval:

$$\frac{d\theta_{2_i}}{dt^*} = f\left(t_i^*, \theta_{1_i}, \theta_{2_i}\right) = \frac{(-f\left(t_i^*, \theta_{1_i}\right) - \mathrm{K}\left(\theta_{2_i}\right)^* + i_i^* - S_i^*)}{H_i^* - 1}$$

$$\theta^0{}_{2_{i+1}} = \theta_{2_i} + f\left(t_i^*, \theta_{1_i}, \theta_{2_i}\right) * (\Delta t^*)$$

The slope at the end of the time interval:

$$\frac{d\theta_{2_{i+1}}}{dt^*} = f\left(t_{i+1}^*, \theta^0{}_{1_{i+1}}, \theta^0{}_{2_{i+1}}\right) = \frac{(-f\left(t_{i+1}^*, \theta^0{}_{1_{i+1}}\right) - \mathrm{K}\left(\theta^0{}_{2_{i+1}}\right)^* + i_{i+1}^* - S_{i+1}^*)}{H_{i+1}^* - 1}$$

Eventually,

$$\theta_{2_{i+1}} = \theta_{2_i} + \frac{f\left(t_i^*, \theta_{1_i}, \theta_{2_i}\right) + f\left(t_{i+1}^*, \theta^0{}_{1_{i+1}}, \theta^0{}_{2_{i+1}}\right)}{2} * (\Delta t^*)$$

***ii)*** $\boldsymbol{i > f_c}$

1st layer: $\boldsymbol{\frac{d\bar{\theta}_1}{dt^*} = 1 - K^*(\bar{\theta}_1) - S^*}$

The slope at the beginning of the time interval:

$$\frac{d\theta_{1_i}}{dt^*} = f\left(t_i^*, \theta_{1_i}\right) = \left(-\mathrm{K}\left(\theta_{1_i}\right)^* + 1 - S_i^*\right)$$

$$\theta^0{}_{1_{i+1}} = \theta_{1_i} + f\left(t_i^*, \theta_{1_i}\right) * (\Delta t^*)$$

The slope at the end of the time interval:

$$\frac{d\theta_{1_{i+1}}}{dt^*} = f\left(t_{i+1}^*, \theta^0{}_{1_{i+1}}\right) = \left(-\mathrm{K}\left(\theta_{1_{i+1}}\right)^* + 1 - S_{i+1}^*\right)$$

Eventually,

$$\theta_{1_{i+1}} = \theta_{1_i} + \frac{f\left(t_i^*, \theta_{1_i}\right) + f\left(t_{i+1}^*, \theta^0{}_{1_{i+1}}\right)}{2} * (\Delta t^*)$$

which is the corrector equation.

2nd layer: $\boldsymbol{\frac{d\bar{\theta}_1}{dt^*} + (H^* - 1)\frac{d\bar{\theta}_2}{dt^*} = -K^*(\bar{\theta}_2) + 1 - S^*}$

The slope at the beginning of the time interval:

$$\frac{d\theta_{2_i}}{dt^*} = f\left(t_i^*, \theta_{1_i}, \theta_{2_i}\right) = \frac{\left(-f\left(t_i^*, \theta_{1_i}\right) - \mathrm{K}\left(\theta_{2_i}\right)^* + 1 - S_i^*\right)}{H_i^* - 1}$$

$$\theta^0{}_{2_{i+1}} = \theta_{2_i} + f\left(t_i^*, \theta_{1_i}, \theta_{2_i}\right) * (\Delta t^*)$$

The slope at the end of the time interval:

$$\frac{d\theta_{2_{i+1}}}{dt^*} = f\left(t^*_{i+1}, {\theta^0}_{1_{i+1}}, {\theta^0}_{2_{i+1}}\right) = \frac{\left(-f\left(t^*_{i+1}, {\theta^0}_{1_{i+1}}\right) - \mathrm{K}\left({\theta^0}_{2_{i+1}}\right)^* + 1 - S^*_{i+1}\right)}{H^*_{i+1} - 1}$$

Eventually,

$$\theta_{2_{i+1}} = \theta_{2_i} + \frac{f\left(t^*_i, \theta_{1_i}, \theta_{2_i}\right) + f\left(t^*_{i+1}, {\theta^0}_{1_{i+1}}, {\theta^0}_{2_{i+1}}\right)}{2} * (\Delta t^*)$$

***iii)*** $\boldsymbol{i = 0}$

1st layer: $\frac{d\bar{\theta}_1}{dt^*} = -\boldsymbol{K}^*(\bar{\boldsymbol{\theta}}_1) - \boldsymbol{ET}^*$

The slope at the beginning of the time interval:

$$\frac{d\theta_{1_i}}{dt^*} = f\left(t^*_i, \theta_{1_i}\right) = \left(-\mathrm{K}\left(\theta_{1_i}\right)^* - ET^*_i\right)$$

$${\theta^0}_{1_{i+1}} = \theta_{1_i} + f\left(t^*_i, \theta_{1_i}\right) * (\Delta t^*)$$

The slope at the end of the time interval:

$$\frac{d\theta_{1_{i+1}}}{dt^*} = f\left(t^*_{i+1}, {\theta^0}_{1_{i+1}}\right) = \left(-\mathrm{K}\left({\theta^0}_{1_{i+1}}\right)^* - ET^*_{i+1}\right)$$

Eventually,

$$\theta_{1_{i+1}} = \theta_{1_i} + \frac{f\left(t^*_i, \theta_{1_i}\right) + f\left(t^*_{i+1}, {\theta^0}_{1_{i+1}}\right)}{2} * (\Delta t^*)$$

which is the corrector equation.

2nd layer: $\frac{d\bar{\theta}_1}{dt^*} + (\boldsymbol{H}^* - \boldsymbol{1})\frac{d\bar{\theta}_2}{dt^*} = -\boldsymbol{K}^*(\bar{\boldsymbol{\theta}}_2) - \boldsymbol{ET}^*$

The slope at the beginning of the time interval:

$$\frac{d\theta_{2_i}}{dt^*} = f\left(t_i^*, \theta_{1_i}, \theta_{2_i}\right) = \frac{\left(-f\left(t_i^*, \theta_{1_i}\right) - \mathrm{K}\left(\theta_{2_i}\right)^* - ET_i^*\right)}{H_i^* - 1}$$

$$\theta^0{}_{2_{i+1}} = \theta_{2_i} + f\left(t_i^*, \theta_{1_i}, \theta_{2_i}\right) * (\Delta t^*)$$

The slope at the end of the time interval:

$$\frac{d\theta_{2_{i+1}}}{dt^*} = f\left(t_{i+1}^*, \theta^0{}_{1_{i+1}}, \theta^0{}_{2_{i+1}}\right) = \frac{\left(-f\left(t_{i+1}^*, \theta^0{}_{1_{i+1}}\right) - \mathrm{K}\left(\theta^0{}_{2_{i+1}}\right)^* - ET_{i+1}^*\right)}{H_{i+1}^* - 1}$$

Eventually,

$$\theta_{2_{i+1}} = \theta_{2_i} + \frac{f\left(t_i^*, \theta_{1_i}, \theta_{2_i}\right) + f\left(t_{i+1}^*, \theta^0{}_{1_{i+1}}, \theta^0{}_{2_{i+1}}\right)}{2} * (\Delta t^*)$$

The next section explains the development of dimensionless form of full-term DARE. Following that, the numerical solutions by Heun's method are presented for the developed dimensionless form of equations.

### 2.6.3 Dimensionless Equations for the Full-term DARE

Earlier we had the assumption of $\psi(h,t) \cong \bar{\psi}_1$ for the matric suction at the interface of the two layers in the full-term depth-averaged equations. This assumption was later removed to have a better approximation of matric suction at the interface by considering depth-weighted average of matric suctions from both layers as follows:

$$\psi_h = \psi(h,t) \cong \frac{H-h}{H} * \bar{\psi}_1 + \frac{h}{H} * \bar{\psi}_2$$

Another assumption that was made in the original derivation of equations, besides that on the interfacial suction head, was that the flux from the first layer to the second one at the interface

($z=h$) is equal to average flux in the first layer. This assumption about the interfacial flux was also modified as a weighted average of fluxes in both layers.

The modified versions of equations are:

$$\bar{q}_1 = \frac{1}{h}\mathrm{K}(\bar{\psi}_1)(\alpha\bar{\psi}_1 + (1-\alpha)\bar{\psi}_2 - \psi_0) + \mathrm{K}(\bar{\psi}_1)$$

$$\alpha = \frac{H-h}{H} \qquad 1-\alpha = \frac{h}{H}$$

$$\bar{q}_2 = \frac{1}{H-h}\mathrm{K}(\bar{\psi}_2)(-\alpha\bar{\psi}_1 - (1-\alpha)\bar{\psi}_2 + \psi_b) + \mathrm{K}(\bar{\psi}_2)$$

where, $\psi_b$ is the critical bubbling suction (i.e., air-bubbling capillary pressure) of the soils. Hence, for the first layer we eventually have:

***i)*** $\boldsymbol{i < f_c}$

$$h\frac{d\bar{\theta}_1}{dt} = -\alpha\bar{q}_1 - (1-\alpha)\bar{q}_2 + i - h\bar{S}$$

***ii)*** $\boldsymbol{i > f_c}$

$$h\frac{d\bar{\theta}_1}{dt} = -\alpha\bar{q}_1 - (1-\alpha)\bar{q}_2 + 2K(\theta_s)\frac{\bar{\psi}_1 + d}{h} + K(\theta_s) - h\bar{S}$$

***iii)*** $\boldsymbol{i = 0}$

$$h\frac{d\bar{\theta}_1}{dt} = -\alpha\bar{q}_1 - (1-\alpha)\bar{q}_2 - e_v - h\bar{S}$$

The equations for the second layer were further modified to allow for upward flow from the capillary zone to the second layer. We had initially considered zero flux at $z=H$. The modified full-term depth-averaged equations for the second layer follow as:

***i)*** $\boldsymbol{i < f_c}$

$$h\frac{d\bar{\theta}_1}{dt} + \frac{d}{dt}[(H-h)\bar{\theta}_2(t)] - \theta_s\frac{dH}{dt} = i - h\bar{S} - 2\frac{K(\theta_s)}{H-h}(\psi_b - \bar{\psi}_2) - K(\theta_s)$$

***ii)*** $\boldsymbol{i > f_c}$

$$h\frac{d\bar{\theta}_1}{dt}+\frac{d}{dt}[(H-h)\bar{\theta}_2(t)]-\theta_s\frac{dH}{dt}=2K(\theta_s)\frac{\bar{\psi}_1+d}{h}-2\frac{K(\theta_s)}{H-h}(\psi_b-\bar{\psi}_2)-K(\theta_s)-h\bar{S}$$

***iii*) $i=0$**

$$h\frac{d\bar{\theta}_1}{dt}+\frac{d}{dt}[(H-h)\bar{\theta}_2(t)]-\theta_s\frac{dH}{dt}=-e_v-h\bar{S}-2\frac{K(\theta_s)}{H-h}(\psi_b-\bar{\psi}_2)-K(\theta_s)$$

Note that H was considered to be the depth to water table, not the depth to the top of capillary fringe. Hence, $\psi_b$ was replaced with 0.

Dimensionless variables are defined as:

$$t^*=\frac{t*K_s}{h},\quad H^*=\frac{H}{h},\quad K^*(\bar{\theta}_2)=\frac{K(\bar{\theta}_2)}{K_s},K^*(\bar{\theta}_1)=\frac{K(\bar{\theta}_1)}{K_s},\quad S^*=\frac{(h\bar{S})}{K_s},i^*=\frac{i}{K_s}$$

$$ET^*=\frac{(e_v+h\bar{S})}{K_s},\bar{\psi}_1{}^*=\frac{\bar{\psi}_1}{h},\bar{\psi}_2{}^*=\frac{\bar{\psi}_2}{h},\bar{\psi}_0{}^*=\frac{\bar{\psi}_0}{h},\mathrm{d}^*=\frac{\mathrm{d}}{h},\bar{q}_1^*=\frac{\bar{q}_1}{K_s},\bar{q}_2^*=\frac{\bar{q}_2}{K_s}$$

$$\psi^*{}_h=\frac{\psi_h}{h}$$

where $t^*$, $H^*$, $K^*(\bar{\psi}_0)$, $K^*(\bar{\psi}_1)$, $S^*$, $ET^*$, $i^*$, $\bar{\psi}_0{}^*$, $\bar{\psi}_1{}^*$, $\mathrm{d}^*$, $\bar{q}_1^*$, $\bar{q}_2^*$ and $\psi^*{}_h$ are dimensionless forms of $t$=time (T), $H$=depth to groundwater table (L), $K(\bar{\psi}_0)$=hydraulic conductivity which corresponds to soil water pressure head at the soil surface ($LT^{-1}$), $K(\bar{\psi}_1)$=hydraulic conductivity which corresponds to soil water pressure head in the 1st layer (i.e., root zone) ($LT^{-1}$), $S$=plant transpiration ($LT^{-1}$), $ET$=evapotranspiration ($LT^{-1}$), $i$= rainfall intensity ($LT^{-1}$), $\bar{\psi}_0$= soil water pressure head at the soil surface (i.e., $z=0$) (L), $\bar{\psi}_1$ = soil water pressure head in the 1st layer (L), d = ponding depth (L), $\bar{q}_1$ = average flux in the 1st layer ($LT^{-1}$), $\bar{q}_2$ = average flux in the 2nd layer ($LT^{-1}$), and $\psi_h$= soil water pressure head at the interface of two layers (L). Note that $h$ and $e_v$ are defined as depth of root zone (L) and soil evaporation ($LT^{-1}$), respectively.

***i)*** $\boldsymbol{i < f_c}$

$$\text{1st layer:}\begin{cases} h\dfrac{d\bar{\theta}_1}{dt} = -\alpha\bar{q}_1 - (1-\alpha)\bar{q}_2 + i - h\bar{S} \\ \dfrac{d\bar{\theta}_1}{dt^*} = -\alpha\bar{q}_1^* - (1-\alpha)\bar{q}_2^* + i^* - S^* \end{cases}$$

Prior ponding, $\psi_0$ is obtained by solving:

$$i^* = 2K^*(\psi_0)(\bar{\psi}^*{}_1 - \psi^*_{0_i}) + K^*(\psi_0)$$

$$\text{2nd layer:}\begin{cases} h\dfrac{d\bar{\theta}_1}{dt} + \dfrac{d}{dt}[(H-h)\bar{\theta}_2(t)] - \theta_s\dfrac{dH}{dt} = i - h\bar{S} - 2\dfrac{K(\theta_s)}{H-h}(-\bar{\psi}_2) - K(\theta_s) \\ \dfrac{d\bar{\theta}_1}{dt^*} + \bar{\theta}_2\dfrac{dH^*}{dt^*} + (H^*-1)\dfrac{d\bar{\theta}_2}{dt^*} - \theta_s\dfrac{dH^*}{dt^*} = i^* - S^* + \left(\dfrac{2\,\bar{\psi}_2{}^*}{H^*-1}\right) - 1 \end{cases}$$

***ii)*** $\boldsymbol{i > f_c}$

$$\text{1st layer:}\begin{cases} h\dfrac{d\bar{\theta}_1}{dt} = -\alpha\bar{q}_1 - (1-\alpha)\bar{q}_2 + 2K(\theta_s)\dfrac{\bar{\psi}_1 + d}{h} + K(\theta_s) - h\bar{S} \\ \dfrac{d\bar{\theta}_1}{dt^*} = -\alpha\bar{q}_1^* - (1-\alpha)\bar{q}_2^* + 2*(\bar{\psi}_1{}^* + \mathrm{d}^*) + 1 - S^* \end{cases}$$

$$\text{2nd layer:}\begin{cases} h\dfrac{d\bar{\theta}_1}{dt} + \dfrac{d}{dt}[(H-h)\bar{\theta}_2(t)] - \theta_s\dfrac{dH}{dt} = 2K(\theta_s)\dfrac{\bar{\psi}_1 + d}{h} - 2\dfrac{K(\theta_s)}{H-h}(-\bar{\psi}_2) - K(\theta_s) - h\bar{S} \\ \dfrac{d\bar{\theta}_1}{dt^*} + \bar{\theta}_2\dfrac{dH^*}{dt^*} + (H^*-1)\dfrac{d\bar{\theta}_2}{dt^*} - \theta_s\dfrac{dH^*}{dt^*} = 2\left(\bar{\psi}_1{}^* + \mathrm{d}^*\right) + \left(\dfrac{2\,\bar{\psi}_2{}^*}{H^*-1}\right) - 1 - S^* \end{cases}$$

***iii)*** $\boldsymbol{i = 0}$

$$\text{1st layer:}\begin{cases} h\dfrac{d\bar{\theta}_1}{dt} = -\alpha\bar{q}_1 - (1-\alpha)\bar{q}_2 - e_v - h\bar{S} \\ \dfrac{d\bar{\theta}_1}{dt^*} = -\alpha\bar{q}_1^* - (1-\alpha)\bar{q}_2^* - ET^* \end{cases}$$

During evaporation, $\psi_0$ is obtained by solving:

$$-e_v{}^* = 2K^*(\psi_0)(\bar{\psi}^*{}_1 - \psi^*_{0_i}) + K^*(\psi_0)$$

$$2^{\text{nd}}\text{ layer:}\begin{cases} h\dfrac{d\bar{\theta}_1}{dt} + \dfrac{d}{dt}[(H-h)\bar{\theta}_2(t)] - \theta_s\dfrac{dH}{dt} = -e_v - h\bar{S} + 2\dfrac{K(\theta_s)}{H-h}(\bar{\psi}_2 - \psi_b) - K(\theta_s) \\ \dfrac{d\bar{\theta}_1}{dt^*} + \bar{\theta}_2\dfrac{dH^*}{dt^*} + (H^*-1)\dfrac{d\bar{\theta}_2}{dt^*} - \theta_s\dfrac{dH^*}{dt^*} = -ET^* + \dfrac{2}{H^*-1}(\bar{\psi}_2{}^* - \psi_b^*) - 1 \end{cases}$$

### 2.6.4 Numerical Solutions of Dimensionless Full-term DARE by Heun's Method

***i)*** $\boldsymbol{i < f_c}$

$$1^{\text{st}}\text{ layer:}\begin{cases} \dfrac{d\bar{\theta}_1}{dt^*} = -\alpha\bar{q}_1{}^* - (1-\alpha)\bar{q}_2{}^* + i^* - S^* \end{cases}$$

For simplification purposes, Let $\theta_1, \theta_2\ and\ \psi_1$ denote $\bar{\theta}_1, \bar{\theta}_2\ and\ \bar{\psi}_1$, respectively. The slope at the beginning of the time interval is written as:

$$\frac{d\theta_{1_i}}{dt^*} = f\left(t_i^*, \theta_{1_i}, \psi_{1i}^*, \psi_{2i}^*, \psi_{0i}^*\right) = -\alpha\bar{q}_{1_i}^* - (1-\alpha)\bar{q}_{2_i}^* + i_i^* - S_i^*$$

$$\theta^0{}_{1_{i+1}} = \theta_{1_i} + f\left(t_i^*, \theta_{1_i}, \psi_{1i}^*, \psi_{2i}^*, \psi_{0i}^*\right) * (\Delta t^*)$$

$\theta^0{}_{1_{i+1}}$refers to the standard Euler method (predictor equation). Next, we need to compute $\psi^*{}_{1_{i+1}}{}^0$ and $\psi^*{}_{0_{i+1}}{}^0$. $\psi^*{}_{0_{i+1}}{}^0$ and $\psi^*_{0_i}$ can be computed from the boundary algebraic equation given $\psi^*{}_{1_{i+1}}{}^0$and $\psi^*_{1_i}$, respectively, using any root finding method such as the Bisection Method. The equation follows as:

$$i^* = 2K^*(\psi_0)(\bar{\psi}^*{}_1 - \psi^*_{0_i}) + K^*(\psi_0)$$

The slope at the end of the time interval is given by:

$$\frac{d\theta_{1_{i+1}}}{dt^*} = f\left(t_{i+1}^*, \theta_{1_{i+1}}{}^0, \psi^*{}_{1_{i+1}}{}^0, \psi^*{}_{2_{i+1}}{}^0, \psi^*{}_{0_{i+1}}{}^0\right) = -\alpha\bar{q}^*{}_{1_{i+1}}{}^0 - (1-\alpha)\bar{q}^*{}_{2_{i+1}}{}^0 + i_{i+1}^* - S_{i+1}^*$$

Eventually,

$$\theta_{1_{i+1}} = \theta_{1_i} + \frac{f\left(t_i^*, \theta_{1_i}, \psi_{1i}^*, \psi_{2i}^*, \psi_{0i}^*\right) + f\left(t_{i+1}^*, {\theta_{1_{i+1}}}^0, {\psi_{1_{i+1}}^*}^0, {\psi_{2_{i+1}}^*}^0, {\psi_{0_{i+1}}^*}^0\right)}{2} * (\Delta t^*)$$

which, is the corrector equation.

2nd layer: $\frac{d\bar{\theta}_1}{dt^*} + \bar{\theta}_2 \frac{dH^*}{dt^*} + (H^* - 1)\frac{d\bar{\theta}_2}{dt^*} - \theta_s \frac{dH^*}{dt^*} = i^* - S^* + (\frac{2\,{\bar{\psi}_2}^*}{H^* - 1}) - 1$

The slope at the beginning of the time interval is written as:

$$\frac{d\theta_{2_i}}{dt^*} = g\left(\theta_{1_i}, \theta_{2_i}, \psi_{1i}^*, \psi_{2i}^*, \psi_{0_i}^*\right)$$

$$= \frac{\left(-f\left(\theta_{1_i}, \psi_{1i}^*, \psi_{2i}^*, \psi_{0_i}^*\right) + \left(\theta_s - \theta_{2_i}\right) * \left(\frac{H_{i+1}^* - H_i^*}{\Delta t^*}\right) + i_i^* - S_i^* + (\frac{2\,{\bar{\psi}_{2_i}}^*}{H_i^* - 1}) - 1\right)}{H_i^* - 1}$$

$${\theta^0}_{2_{i+1}} = \theta_{2_i} + g\left(\theta_{1_i}, \theta_{2_i}, \psi_{1i}^*, \psi_{2i}^*, \psi_{0_i}^*\right) * (\Delta t^*)$$

The slope at the end of the time interval is given by:

$$\frac{d\theta_{2_{i+1}}}{dt^*} = g\left({\theta_{1_{i+1}}}^0, {\theta_{2_{i+1}}}^0, {\psi_{1i+1}^*}^0, {\psi_{0i+1}^*}^0, \bar{\psi}_{2_{i+1}}^*\right)$$

$$= \frac{\left(-f\left({\theta_{1_{i+1}}}^0, {\psi_{1_{i+1}}^*}^0, {\psi_{0_{i+1}}^*}^0\right) + \left(\theta_s - {\theta_{2_{i+1}}}^0\right) * \left((H_{i+1}^* - H_i^*)/\Delta t^*\right) + i_{i+1}^* - S_{i+1}^* + (\frac{2\,{\psi_{2_{i+1}}^*}^0}{H_{i+1}^* - 1}) - 1\right)}{H_{i+1}^* - 1}$$

Eventually,

$$\theta_{2_{i+1}} = \frac{g\left(\theta_{1_i}, \theta_{2_i}, \psi_{1i}^*, \psi_{2i}^*, \psi_{0_i}^*\right) + g\left({\theta_{1_{i+1}}}^0, {\theta_{2_{i+1}}}^0, {\psi_{1i+1}^*}^0, {\psi_{0i+1}^*}^0, \bar{\psi}_{2_{i+1}}^*\right)}{2} * \Delta t^*$$

***ii)*** $\boldsymbol{i > f_c}$

1st layer: $\dfrac{d\bar{\theta}_1}{dt^*} = -\alpha\bar{q}_1^* - (1-\alpha)\bar{q}_2^* + 2 * (\bar{\psi}_1{}^* + \mathrm{d}^*) + 1 - S^*$

The slope at the beginning of the time interval is given by:

$$\frac{d\theta_{1_i}}{dt^*} = f\left(t_i^*, \theta_{1_i}, \psi_{1i}^*, \psi_{2i}^*\right) = -\alpha\bar{q}_{1_i}^* - (1-\alpha)\bar{q}_{2_i}^* + 2\left(\psi_{1_i}^* + \mathrm{d}^*\right) + 1 - S_i^*$$

$$\theta^0{}_{1_{i+1}} = \theta_{1_i} + f\left(t_i^*, \theta_{1_i}, \psi_{1i}^*, \psi_{2i}^*\right) * (\Delta t^*)$$

The slope at the end of the time interval is written as:

$$\frac{d\theta_{1_{i+1}}}{dt^*} = f\left(t_{i+1}^*, \theta_{1_{i+1}}{}^0, \psi_{1_{i+1}}^*, \psi_{2_{i+1}}^*\right) = -\alpha\bar{q}_{1_{i+1}}^*{}^0 - (1-\alpha)\bar{q}_{2_{i+1}}^*{}^0 + 2\left(\psi_{1_{i+1}}^* + \mathrm{d}^*\right) + 1 - S_{i+1}^*$$

Eventually,

$$\theta_{1_{i+1}} = \theta_{1_i} + \frac{f\left(t_i^*, \theta_{1_i}, \psi_{1i}^*, \psi_{2i}^*\right) + f\left(t_{i+1}^*, \theta_{1_{i+1}}{}^0, \psi_{1_{i+1}}^*, \psi_{2_{i+1}}^*\right)}{2} * (\Delta t^*)$$

which, is the corrector equation.

During ponding $\psi_0 = -d$. To calculate depth of ponding ($d$), for each time step, the calculated average moisture content of first layer at time $t$ ($\bar{\theta}_{1_t}$) is compared to saturated moisture content ($\theta_s$) and when $\bar{\theta}_{1_t}$ is higher than $\theta_s$, the difference is added up to obtain $d$ by d=$(\bar{\theta}_{1_t} - \theta_s) * h$.

2nd layer: $\dfrac{d\bar{\theta}_1}{dt^*} + \bar{\theta}_2\dfrac{dH^*}{dt^*} + (H^* - 1)\dfrac{d\bar{\theta}_2}{dt^*} - \theta_s\dfrac{dH^*}{dt^*} = 2\left(\bar{\psi}_1{}^* + \mathrm{d}^*\right) + \left(\dfrac{2\,\bar{\psi}_2{}^*}{H^* - 1}\right) - 1 - S^*$

The slope at the beginning of the time interval is given by:

$$\frac{d\theta_{2_i}}{dt^*} = g\left(\theta_{1_i}, \theta_{2_i}, \psi_{1_i}^*, \psi_{2i}^*\right)$$

$$= \frac{\left(-f\left(t_i^*, \theta_{1_i}, \psi_{1i}^*\right) + \left(\theta_s - \theta_{2_i}\right) * \left(\frac{H_{i+1}^* - H_i^*}{\Delta t^*}\right) + 2\left(\psi_{1_i}^* + \mathrm{d}^*\right) + \left(\frac{2\,\psi_{2_i}^*}{H_i^* - 1}\right) - 1 - S_i^*\right)}{H_i^* - 1}$$

$$\theta^0{}_{2_{i+1}} = \theta_{2_i} + g\left(\theta_{1_i}, \theta_{2_i}, \psi_{1_i}^*, \psi_{2i}^*\right) * (\Delta t^*)$$

The slope at the end of the time interval is given by:

$$\frac{d\theta_{2_{i+1}}}{dt^*} = g\left(\theta_{1_{i+1}}{}^0, \theta_{2_{i+1}}{}^0, \psi_{1_{i+1}}^*{}^0, \psi_{2_{i+1}}^*{}^0\right)$$

$$= \frac{\left(-f\left(\theta_{1_{i+1}}{}^0, \psi_{1_{i+1}}^*{}^0\right) + \left(\theta_s - \theta_{2_{i+1}}{}^0\right) * \left(\frac{H_{i+1}^* - H_i^*}{\Delta t^*}\right) + 2\left(\psi_{1_{i+1}}^*{}^0 + \mathrm{d}^*\right) + \left(\frac{2\,\psi_{2_{i+1}}^*{}^0}{H_{i+1}^* - 1}\right) - 1 - S_{i+1}^*\right)}{H_{i+1}^* - 1}$$

Eventually,

$$\theta_{2_{i+1}} = \frac{g\left(\theta_{1_i}, \theta_{2_i}, \psi_{1_i}^*, \psi_{2i}^*\right) + g\left(\theta^0{}_{1_{i+1}}, \theta^0{}_{2_{i+1}}, \psi_{1_{i+1}}^*{}^0, \psi_{2_{i+1}}^*{}^0\right)}{2} * \Delta t^*$$

***iii)*** $\boldsymbol{i = 0}$

1st layer: $\frac{d\bar{\theta}_1}{dt^*} = -\alpha\bar{q}_1^* - (1-\alpha)\bar{q}_2^* - ET^*$

The slope at the beginning of the time interval is given by:

$$\frac{d\theta_{1_i}}{dt^*} = f\left(t_i^*, \theta_{1_i}, \psi_{1i}^*, \psi_{2i}^*, \psi_{0i}^*\right) = -\alpha\bar{q}_{1_i}^* - (1-\alpha)\bar{q}_{2_i}^* - ET_i^*$$

$$\theta^0{}_{1_{i+1}} = \theta_{1_i} + f\left(t_i^*, \theta_{1_i}, \psi_{1_i}^*, \psi_{0_i}^*\right) * (\Delta t^*)$$

Then, we need to compute $\psi_{1_{i+1}}^*{}^0$ and $\psi_{0_{i+1}}^*{}^0$. $\psi_{0_{i+1}}^*{}^0$ and $\psi_{0_i}^*$ are computed using the Bisection method, from the boundary algebraic equation given $\psi_{1_{i+1}}^*{}^0$and $\psi_{1_i}^*$, respectively. The equation follows as:

$$-ev^* = 2K^*(\psi_0)(\bar{\psi}^*{}_1 - \psi^*_{0_i}) + K^*(\psi_0)$$

The slope at the end of the time interval:

$$\frac{d\theta_{1_{i+1}}}{dt^*} = f\left(\theta_{1_{i+1}}{}^0, \psi^*_{1_{i+1}}{}^0, \psi^*_{0_{i+1}}{}^0\right) = -K^*\left(\theta_{1_{i+1}}{}^0\right)\left(\psi^*_{1_{i+1}}{}^0 - \psi^*_{0_{i+1}}{}^0\right) - K^*\left(\theta_{1_{i+1}}{}^0\right) - ET^*_{i+1}$$

$$\frac{d\theta_{1_{i+1}}}{dt^*} = f\left(t^*_{i+1}, \theta_{1_{i+1}}{}^0, \psi^*_{1_{i+1}}{}^0, \psi^*_{2_{i+1}}{}^0, \psi^*_{0_{i+1}}{}^0\right) = -\alpha\bar{q}^*_{1_{i+1}}{}^0 - (1-\alpha)\bar{q}^*_{2_{i+1}}{}^0 - ET^*_{i+1}$$

Eventually,

$$\theta_{1_{i+1}} = \theta_{1_i} + \frac{f\left(t^*_i, \theta_{1_i}, \psi^*_{1i}, \psi^*_{2i}, \psi^*_{0i}\right) + f\left(t^*_{i+1}, \theta_{1_{i+1}}{}^0, \psi^*_{1_{i+1}}{}^0, \psi^*_{2_{i+1}}{}^0, \psi^*_{0_{i+1}}{}^0\right)}{2} * (\Delta t^*)$$

which is the corrector equation.

2nd layer:
$$\frac{d\bar{\theta}_1}{dt^*} + \bar{\theta}_2\frac{dH^*}{dt^*} + (H^* - 1)\frac{d\bar{\theta}_2}{dt^*} - \theta_s\frac{dH^*}{dt^*} = -ET^* + \frac{2}{H^* - 1}(\bar{\psi}_2{}^*) - 1$$

The slope at the beginning of the time interval given by:

$$\frac{d\theta_{2_i}}{dt^*} = g\left(\theta_{1_i}, \theta_{2_i}, \psi^*_{1_i}, \psi^*_{2_i}, \psi^*_{0_i}\right)$$

$$= \frac{\left(-f\left(\theta_{1_i}, \psi^*_{1_i}, \psi^*_{0_i}\right) + (\theta_s - \theta_{2_i}) * \left(\frac{H^*_{i+1} - H^*_i}{\Delta t^*}\right) - ET^*_i + \left(\frac{2\,\psi_{2_i}{}^*}{H^*_i - 1}\right) - 1\right)}{H^*_i - 1}$$

$$\theta^0{}_{2_{i+1}} = \theta_{2_i} + g\left(\theta_{1_i}, \theta_{2_i}, \psi^*_{1_i}, \psi^*_{2_i}, \psi^*_{0_i}\right) * (\Delta t^*)$$

The slope at the end of the time interval is written as:

$$\frac{d\theta_{2_{i+1}}}{dt^*} = g\left(\theta_{1_{i+1}}{}^0, \theta_{2_{i+1}}{}^0, \psi^*_{1_{i+1}}{}^0, \psi^*_{0_{i+1}}{}^0, \psi^*_{2_{i+1}}{}^0\right)$$

$$= \frac{\left(-f\left(\theta_{1_{i+1}}{}^0, \psi^*_{1_{i+1}}{}^0, \psi^*_{0_{i+1}}{}^0\right) + (\theta_s - \theta_{2_{i+1}}{}^0) * ((H^*_{i+1} - H^*_i)/\Delta t^*) - ET^*_{i+1} + \left(\frac{2\,\psi^*_{2_{i+1}}{}^0}{H^*_{i+1} - 1}\right) - 1\right)}{H^*_{i+1} - 1}$$

Eventually,

$$\theta_{2_{i+1}} = \theta_{2_i} + \frac{g\left(\theta_{1_i}, \theta_{2_i}, \psi^*_{1_i}, \psi^*_{2_i}, \psi^*_{0_i}\right) + g\left({\theta_{1_{i+1}}}^0, {\theta_{2_{i+1}}}^0, {\psi^*_{1_{i+1}}}^0, {\psi^*_{0_{i+1}}}^0, {\psi^*_{2_{i+1}}}^0\right)}{2} * \Delta t^*$$

**3. Model Assessment**

To test the developed model in this study, Hydrus-1D was selected as the benchmark. HYDRUS-1D is a well-established model for the solution of RE. A mass-lumped linear finite elements scheme has been used in HYDRUS-1D for discretization of the mixed form of the RE which results in an equivalent and somewhat standard finite difference scheme (e.g., Vogel et al., 1996). Comparison of RE-based models or simplified versions of RE to Hydrus-1D is a common practice in the literature (e.g., Zhu et al. 2012; Carbone et al. 2015; Ogden et al. 2015). Among Hydrus-1D's example projects, one (i.e., "Water Flow in a Field Soil Profile under Grass") appears to be suitable for model verification purposes. Hence, atmospheric data and observed groundwater levels from a field in the Hupselse Beek watershed in the Netherland were considered which provided the required BCs for the numerical model (Šimůnek et al. 2013). The depth of the root zone was 30 cm. Calculations and model verifications were performed for the period of April 1 to September 30 of the year 1982 (=183 days). Soil moisture contents obtained by DARE were compared with those generated by Hydrus-1D. Note that in this study, and for model verification purposes, a uniform soil for the entire depth was used.

The soil surface (i.e., top) BC involved actual precipitation and potential evapotranspiration rates for a grass cover (Figure 4.4). However, to evaluate the performance of the developed model, other hypothetical scenarios were considered which are discussed in the next section. Model verification is more concerned with identifying and removing errors in the

model formulation that is typically achieved by comparing the numerical output from the model to analytical or other accurate benchmark solutions. The surface fluxes including rainfall and evapotranspiration rates were incorporated into both DARE and Hydrus-1D models by using average daily rates distributed uniformly over each day. The bottom BC consisted of a prescribed groundwater level (initially set at 55 cm below the soil surface). However, we started evaluating the developed model with a fixed groundwater level of $H$=2$h$ where $h$ refers to the depth of root zone, and $H$ is the depth of groundwater table.

Calculated moisture contents by DARE for various (top) BCs were compared to those calculated by Hydrus-1D for four different soil textures: sandy loam, loam, sandy clay loam, and sand. Table 4.1 represents the soil hydraulic parameters for these four soils, derived from Hydrus-1D's "Water Flow – Soil Hydraulic Parameters" window. The source for this information is Carsel and Parrish (1988).

The developed code for DARE generates both sub-daily and average daily moisture contents for each layer. We compared the results of average daily moisture contents in each layer. A number of performance indices including coefficient of determination ($R^2$), Nash-Sutcliffe efficiency ($E_{ns}$), root mean square error (*RMSE*), and normalized *RMSE* (*NRMSE*) were considered for quantitative comparison of DARE to Hydrus-1D. The equations of the performance indices are given below:

$$\mathrm{R}^2 = \frac{\left[\sum_{\mathrm{i}=1}^{\mathrm{m}}(\theta_{hyd,i} - \bar{\theta}_{hyd})(\theta_{da,i} - \bar{\theta}_{da})\right]^2}{\left[\sum_{\mathrm{i}=1}^{\mathrm{m}}(\theta_{hyd,i} - \bar{\theta}_{hyd})^2\right]\left[\sum_{\mathrm{i}=1}^{\mathrm{m}}(\theta_{da,i} - \bar{\theta}_{da})^2\right]} \tag{24}$$

$$E_{NS} = 1 - \left[\frac{\sum_{i=1}^{m}(\theta_{hyd,i} - \theta_{da,i})^2}{\sum_{i=1}^{m}(\theta_{hyd,i} - \bar{\theta}_{hyd})^2}\right] \tag{25}$$

$$\text{NRMSE} = \frac{RMSE}{\bar{\theta}_{hyd}} = \frac{\sqrt{\frac{1}{m}\sum_{i=1}^{m}(\theta_{hyd,i} - \theta_{da,i})^2}}{\bar{\theta}_{hyd}} \quad (26)$$

where, $\theta_{hyd,i}$, $\theta_{da,i}$ denote calculated moisture contents by Hydrus-1D and DARE at the $i^{th}$ day, respectively. $\bar{\theta}_{hyd}$ and $\bar{\theta}_{da}$ refer to the average of moisture contents calculated by Hydrus-1D and DARE, respectively, and *m* represents the number of days of simulation.

## 4. Results

### 4.1 Gravity Drainage Condition

***Results for "no rain/ET" top boundary condition; $i, ET = 0$***

We started evaluating the gravity drainage condition with a simple "no rainfall, no ET" top BC. Figure 4.5 displays the comparison graphs for various soil types for "no rainfall, no ET" BC. Results show high agreement between the calculated moisture contents from DARE and those from Hydrus-1D. The best and worst performances were related to sandy clay loam and sandy soils in the first layer where the calculated values for $R^2$, $E_{NS}$, *RMSE*, and *NRMSE* were equal to 1.0 (for sandy clay loam) and 0.97 (for sand), 0.98 and 0.95, 0 and 0.01, and 0.02 and 0.09, respectively; all of which confirm a good performance of the developed model for this top BC in the root zone. In the figure, DARE captures the reduction rate in moisture content in time equally well. The rate of reductions are higher in earlier time periods and diminish gradually. As expected, sand is drying very fast, and sandy-clay-loam is drying much slower, and DARE captures these behaviors well in both soil layers.

***Results for "no ponding at all"; $i < f_c$***

Various scenarios for the top boundary condition in which rainfall intensity is less than soil infiltration capacity (i.e., "no ponding at all"; $i < f_c$) were evaluated including "constant rainfall and constant ET", "variable rainfall, variable ET", "low initial moisture content with increasing (variable) rainfall and variable ET", and "high-intensity variable rain and variable ET". Figure 4.6 shows the results of comparison for the top BC of "constant rainfall and constant ET". The assigned values of this scenario for rainfall intensity and evapotranspiration rates were: $i$=0.5 (cm/day), and $ET$=0.4 (cm/day). The comparison results illustrate that the calculated moisture contents by DARE for sandy loam and sandy soils are in great agreement with those calculated by Hydrus-1D. With the $E_{ns}$ values of 0.97 obtained for both layers, calculated moisture contents by DARE for sandy soils have the best match with those generated by Hydrus-1D. Although the performance of the model for sandy clay loam soils is the worst regarding $E_{ns}$ values (=0.23, and 0.53, for the first and second layers, respectively), its performance is comparable to other soil types regarding other performance indices. DARE showed a high performance in comparison to the Hydrus's output for the assigned scenario i.e., "constant rainfall and constant ET". DARE and Hydrus-1D have shown the similar behavior in terms of the rate of reduction in soil moisture content. Note that eventually, they all have reached to a steady state condition.

Figure 4.7 displays the results for the top BC of "variable rain and variable ET". Figure 4.4 illustrates the daily rainfall intensity and ET rates applied for evaluating this scenario which are the actual observed data from the study area. The performance of DARE for sandy soil was shown to be superior compared to other soil types. Calculated values for $R^2$, $E_{NS}$, *RMSE*, and *NRMSE* for sandy soil were almost the same for both layers, and those values for the 2$^{nd}$ layer

were equal to 0.89, 0.86, 0.01, and 0.09, respectively. Although the performances of the calculated moisture contents by DARE for sandy loam, loam and sandy clay loam are not very good just in terms of $E_{ns}$ values, *i*) they have captured the general trends of fluctuations in the calculated moisture contents by Hydrus-1D, and *ii*) have obtained very good results in terms of other performance indices. DARE and Hydrus-1D have shown an approximately same rate of reduction in the soil moisture contents in earlier time periods and this behaviour is more evident for sand.

Up to this point, all the hypothesized scenarios had high initial moisture contents. To evaluate the performance of the developed model under low antecedent moisture contents, top BC of "low initial moisture content with increasing (variable) rainfall and variable ET" was considered (it can also be called, "Buildup" scenario). Figure 4.8 shows the rainfall intensity assigned for this hypothesized scenario. Figure 4.9 illustrates the comparison results for the Buildup scenario. Loam and sandy clay loam soils have shown to be superior in terms of both $R^2$ and $E_{ns}$ values. Sandy loam has the 3$^{rd}$ rank in the model performance among all evaluated soil types while the calculated moisture content for the sandy soil showed the highest difference with those calculated by Hydrus-1D. The calculated moisture contents by the DARE have followed the same trends as those calculated by Hydrus-1D.

Another hypothesized scenario considered to evaluate the performance of the model in capturing the moisture content fluctuations was the top BC of "high-intensity variable rain and variable ET". Figure 4.10 depicts the rainfall pattern utilized for this scenario. Figure 4.11 shows the comparison results for this scenario. Similar to the findings of "variable rain, variable ET" scenario, sandy soil achieved the best performance in the comparison results for calculated moisture contents for this scenario. Despite the fact that all other three soil types have shown

acceptable results regarding $R^2$, *RMSE*, and *NRMSE*, they all have negative $E_{ns}$ values. However, the overall performance of the model is acceptable because DARE has captured the general trends and fluctuations observed in Hydrus-1D outputs.

***Results for "Ponding at Some Point" (i.e., $i > f_c$)***

To evaluate the performance of the developed DARE under "Ponding at some point" (i.e., $i > f_c$) conditions, two scenarios were developed. Figure 4.12 displays the comparison results for the top BC of "low initial moisture and high rainfall intensity to reach ponding". For the purpose of this top BC, various constant rainfall intensities were considered for different soil types. There is a high agreement between the calculated moisture contents from both DARE and Hydrus-1D.

In the second scenario for the evaluation of "Ponding at some point" where we started with a high initial moisture content, and a high constant rainfall intensity to keep saturation and then decrease the rainfall intensity. Figure 4.13 shows the rainfall intensity considered for constructing this scenario. Calculated moisture contents by DARE for various soil types are presented in Figure 4.14. Moisture contents simulated by the DARE for all soil types have proved to be close to those simulated by Hydrus-1D. Loam and sandy clay loam soils have had an increase in soil moisture, and they have reached saturation; then by a drop in rainfall intensity, there are reductions in the simulated moisture contents. In contrast, sandy loam and sandy soils have exhibited step-wise reductions in the simulated moisture content without reaching to a full saturation at the commencement of the simulations. The saturated hydraulic conductivity ($K_s$) for loam and sandy clay loam are 24.96 (cm/day), and 31.44 (cm/day), respectively; both of which are less than or very close to the starting (constant) rainfall intensity of 30 (cm/day). The DARE

has underestimated the moisture contents compared to Hydrus-1D's simulated values. However, simulated moisture contents by the DARE have been consistent in general trend with Hydrus-1D. In Figure 4.14, for loamy soil simulated moisture contents by DARE starts dropping sharply at 50 days following the sudden drop in rainfall intensity. However, HYDRUS-1D has a 10-day lag. These differences are not unexpected, because DARE was purely based on gravity drainage, and thus had omitted terms. Regardless of the bottom boundary condition of "Free Drainage" assigned in Hydrus-1D, Hydrus-1D solves RE for all the internal nodes. We ignored the negative pressure head effects in the development of gravity drainage version of DARE.

## 4.2 Full-term DARE

### *Results for "no rain" top boundary condition; $i = 0$*

To evaluate the full-term RE, the same scenarios used in assessing gravity drainage version of DARE were utilized. Bottom BC of zero pressure head at a fixed groundwater depth (i.e., $H$=2$h$=60 cm) was assumed for the evaluation of various scenarios performed in this study. The simple condition of "no rainfall, no ET" top BC was first examined. Figure 4.15 illustrates the comparison graphs for various soil types for the "no rainfall, no ET" top BC. Simulated soil moisture contents from the full-term DARE have a good agreement with those calculated by the Hydrus-1D. Results for sandy soil in the second layer display the highest discrepancies (*NRMSE* =0.23).

### *Results for "no ponding at all"; $i < f_c$*

To evaluate the full-term DARE for the top boundary condition in which rainfall intensity is less than soil infiltration capacity (i.e., "no ponding at all"; $i < f_c$), a number of scenarios were

considered which include: “constant rainfall and constant ET”, “variable rainfall, variable ET”, “low initial moisture content with increasing (variable) rainfall and variable ET”, and “high-intensity variable rain and variable ET”.

Figure 4.16 shows the comparison results for the top BC of “constant rainfall and constant ET”. $i$ = 0.5 (cm/day) and $ET$ = 0.4 (cm/day) were, respectively, the assigned gain and loss fluxes to/from the soil surface for this scenario. The comparison results illustrate that the calculated moisture contents from the two models are in great agreement. The results for loam and sandy loam soils derived from the full-term DARE are very close to those calculated by Hydrus-1D. The discrepancy between two model results is higher for sandy clay loam, and it is at its highest value for sandy soil. However, the highest difference in the calculated moisture contents from two methods is slightly below 0.05 for the second layer in the sandy soil. Performance indices also confirm these findings; *NRMSE* equals zero for loam in both soil layers, and it has the worst values (=0.40 and 0.21) for sandy soil in the first and second layers, respectively.

Results for the top BC of “variable rain and variable ET” are displayed in Figure 4.17. Figure 4.4 illustrates the observed rainfall intensity and ET rates applied to this scenario too. The full-term DARE has captured soil moisture fluctuations in the first layer except for sandy soil. Results for the second layer are also close to those obtained by Hydrus-1D, however, DARE shows fewer fluctuations compared to Hydrus-1D.

DARE exhibited a poor performance for simulating moisture content in sand. *NRMSE* values of 0.37 and 0.23, respectively for the first and second soil layers, show the weakness of full-term version of DARE for accurately simulating moisture content for sandy soil. Despite the other soil textures evaluated in this study, DARE has presented inconsistent fluctuations in

calculated moisture contents compared to those calculated by Hydrus-1D for sand. The DARE model has done a better job in predicting soil moisture contents for loamy soil in both layers compared to the other soil types.

Figure 4.18 displays the comparison results for the top BC of "high-intensity variable rain and variable ET". The rainfall intensity illustrated in Figure 4.10 was used for the evaluation of this top BC. As can be seen from the Figure 4.18, the simulated moisture contents from the full-term DARE for the root zone closely match those predicted by Hydrus-1D. For example, $R^2$, $E_{ns}$, *RMSE*, and *NRMSE* values are equal to 0.74, 0.61, 0.02, and 0.10, respectively for sandy loam soil in the first layer. The calculated moisture contents from DARE for the second layer, although were close to those simulated by Hydrus-1D, the DARE model shows less accurate simulations in capturing soil moisture fluctuations. However, the DARE model has partially captured fluctuations in the loamy soil in the second later. The full-term DARE has shown a poor performance in calculating mositure contents for sand compared to those calculated by hydrus-1D. For instance, the *NRMSE* values for the first and the second soil layers are equal to 0.54 and 0.17, respectively, confirming the inability of DARE for simulating mositure content in sandy soil.

To evaluate the performance of the full-term DARE for starting points with low moisture contents, a top BC of "low initial moisture content with increasing (variable) rainfall and variable ET" was considered. This scenario is also called the "Buildup" scenario. Figure 4.8 shows the daily rainfall intensity used in order to establish this scenario. Figure 4.19 depicts the comparison results for "Buildup" scenario. Results obtained from the full-term DARE show good agreement with those calculated by Hydrus-1D for all the evaluated soil textures except sandy soil. The DARE has calculated moisture contents for both layers for loam soil with the

highest performance indices. As an example, $R^2$, $E_{NS}$, *RMSE* and *NRMSE* values for the simulated moisture content for the loam soil in the root zone are 0.88, 0.65, 0.02, and 0.06, respectively. DARE has shown poor performance in calculating moisture contents for sandy soil particularly for the first layer with *NRMSE* value equal to 0.65.

***Results for "Ponding at Some Point" ($i > f_c$)***

Two different top BCs establishing two scenarios were considered to evaluate the performance of the full-term DARE model for "ponding at some point" condition (i.e., $i > f_c$). Figure 4.20 displays the results for the top BC of "low initial moisture and high rainfall intensity to reach ponding". To establish this top BC, various constant rainfall intensities were considered for various soil types. The assigned values for rainfall intensities were $i_p = 50\left(\frac{cm}{day}\right)$, $i_p = 30\left(\frac{cm}{day}\right)$, $i_p = 35\left(\frac{cm}{day}\right)$, and $i_p = 500\left(\frac{cm}{day}\right)$, respectively, for sandy loam, loam, sandy clay loam, and sandy soil. Results show that the calculated moisture contents from the DARE model for the first layer almost exactly match with those calculated by Hydrus-1D, except for sandy soil. Although the DARE-calculated moisture contents for the second layer are close to those calculated by Hydrus-1D (except for sandy soil), the DARE model has underestimated moisture contents for the second layer, with the highest difference between model results in sand with a *NRMSE* value of 0.42. The simulated moisture content by the DARE for the second layer in loam has the lowest *NRMSE* value of 0.06. DARE exhibits poor performances with large underestimations for sandy soil in both soil layers.

To evaluate the "Ponding at some point" condition, another top BC was developed where we started with a high initial moisture content, and a high constant rainfall intensity to keep saturation and then decrease the rainfall intensity. Figure 4.13 displays the rainfall intensity

considered for establishing this scenario. Figure 4.21 shows the comparison results for this top boundary condition. Moisture contents simulated for the root zone by the full-term DARE model for all four soil types, except sandy soil, are in good agreement with those calculated by Hydrus-1D. For instance, $R^2$, $E_{NS}$, *RMSE* and *NRMSE* values for sandy clay loam soil in the root zone are equal to 0.99, 0.90, 0.02 and 0.05, respectively. The accuracy of the calculated moisture contents in the second layer by the full-term DARE model are lower. The developed model was not able to accurately capture the average moisture contents in the second layer. However, in terms of *NRMSE*, the worst value was achieved for the second layer of sandy soil which was equal to 0.15. This is a prediction error of about 15%. According to the results obtained by Hydrus-1D, loam and sandy clay loam have shown an increase in the soil moisture contents in both layers and have reached saturation. The full-term DARE has shown the same behavior in the root zone. However, we see a small reduction in soil moisture contents of the second layer calculated by the DARE model at the commencement of the simulation for loam and sandy clay loam. Sandy loam soil has shown a step-wise decrease in the moisture contents without reaching the saturation at the initial part of the simulation. The saturated hydraulic conductivity ($K_s$) for sandy loam, loam, sandy clay loam, and sand are 106.1 (cm/day), 24.96 (cm/day), 31.44 (cm/day), and 712.8 (cm/day), respectively; the starting (constant) rainfall intensity of 30 (cm/day) was considered for this scenario. The full-term DARE has underestimated the moisture contents compared to Hydrus-1D's simulated values. DARE has shown poor performance for simulating soil moisture content in sandy soil with this scenario, too.

Table 4.2 to Table 4.5 summarize the performance metrics for the calculated moisture contents by DARE for sandy loam, loam, sandy clay loam and sand, respectively. In the evaluation of gravity drainage version of DARE, we reported a 10-day lag generated by Hydrus-

1D in response to reduction in rainfall intensity (Figure 4.14). On the same figure, DARE had no such lag. However, as can be seen in Figure 4.21, the full-term DARE and Hydrus-1D have shown similar behavior in with no lag.

## 5. Discussion

Based on the developed scenarios in this study and the analyzed soil types, DARE for gravity flow condition showed excellent agreements with Hydrus-1D's outputs for both soil layers. The full-term version of DARE was tested for zero pressure head at a fixed groundwater depth bottom boundary condition. Although same scenarios were considered for verification purposes, due to the differences in the assigned bottom boundary conditions, comparing the performance of the gravity drainage version of the DARE to the performance of the full-term version of DARE is not recommended. Therefore, one cannot reach to the conclusion that gravity drainage version of DARE is superior to the full-term version of DARE based on their performances. The full-term DARE proved to generate accurate estimations of soil moisture contents for the first soil layer (i.e., root zone) in comparison to calculated moisture contents by Hydrus-1D. However, there were some discrepancies between the calculated moisture contents from the full-term DARE with those calculated by Hydrus-1D for the second soil layer. DARE has shown poor performances in calculating soil moisture contents in sandy soil under some of assigned scenarios in this study. Although the performance of the full-term version of DARE was not acceptable under all scenarios for sandy soil, having wetlands in areas with sandy soil texture is not common. Hence, the application of full-term version of DARE in calculating moisture contents in unsaturated section of wetlands is not limited because of its weakness in sandy soil. However, in case of having wetlands with sandy soil, the gravity drainage version of DARE works well. We must bear in mind that each model comes with some assumptions and

limitations in application. The DARE has been an ongoing development/project, and as discussed earlier, we had a couple of revisions on the derived equations where we recently removed some initial simplifying assumptions. The challenge has been keeping the introduced model less computationally intensive by solving ODEs compared to the RE in PDE.

In this study, the bottom boundary condition of zero pressure head (at a fixed groundwater depth) were considered for evaluating full-term DARE versus Hydrus-1D. Four different soil types including sandy loam, loam, sandy clay loam, and sand were examined. However, we tried to run Hydrus-1D with the same bottom boundary condition of zero pressure head for clay soil to have a quick understanding of the probable convergence issue of solving RE. We faced non-convergence issue for running Hydrus-1D for clay. Ogden et al. (2015) used a hodograph transformation, finite water-content discretization, and the method of lines to produce a set of three ODEs to calculate one-dimensional vertical flow in an unsaturated porous medium. The same issue was reported by Ogden et al. (2015) where they excluded clay and the other two fine soils (sandy clay and silty clay) from comparison because Hydrus-1D failed to converge on those soils unless they set the air entry pressure to be -2 cm in Hydrus-1D, a physically unrealistic value for those soils. Our solution to RE does not suffer from this problem (i.e., non-convergence). Further analyses are needed to verify the application of the full-term DARE for other soil textures which have not been taken into consideration in this study.

Although we did have the opportunity to take full advantage of the dimensionless forms of the equations developed in this dissertation. Those dimensionless equations can be utilized for further and future analyses. The developed dimensionless forms of equations and the related developed code have made the model ready for generating monographs during future studies,

where many more soil texture, rainfall/groundwater table/ET patterns, etc. can tested and under what soil, climatic and hydrologic patterns DARE works can be tabulated.

### 5.1 Computational Efficiency

To provide the readers with an idea about the computational efficiency of the developed model, the run times of the full-term DARE and Hydrus-1D for the "Ponding at some point" top boundary condition for sandy clay loam were compared (see Figure 4.21). The former took less than 2 seconds and the latter took about 644 seconds. However, this was not the case for all the scenarios. Any further modifications could impact this computational efficiency.

## 6. Summary and Conclusions

In this chapter, a new methodology was introduced, numerically solved and verified versus Hydrus-1D model which solves a highly nonlinear RE for soil moisture accounting in the vadose zone. The developed/evaluated model in this study is a two-layer depth-averaged solution (i.e., ODEs) to RE's which is a PDE. Some hypothetical scenarios along with at least one scenario utilizing actual observed atmospheric fluxes were considered for the evaluation of DARE in both gravity drainage condition and full-term equations (i.e., by taking into account the negative pressure head). Dimensionless forms of equations were developed, and Heun's method (with a comparison to explicit finite difference method) was utilized to discretize the solutions numerically. The following conclusions can be drawn from this study:

1. Gravity drainage condition of the two-layer DARE showed great performance for all the assigned scenarios and all evaluated soil types in comparison to Hydrus-1D with "Free Drainage" bottom BC.

2. The full-term version of DARE performed well for the root zone with three soil types which include sandy loam, loam and sandy clay loam soil types. The full-term DARE showed a poor performance in simulating moisture contents in sandy soil. The full-term DARE for the second layer, although has calculated soil moisture contents close to those calculated by Hydrus-1D, it was not able to capture the fluctuations fully in the second layer, except for loam. Loam soil had the best results for the second soil layer with the full-term equations.

The DARE proved to be less computationally intensive, and it does not suffer from the non-convergence problem, which is one of the most significant issues with the application of RE in fine textured soils. Ogden et al. (2015) also did not compare their results with Hydrus-1D for sandy clay, silty clay, and clay because Hydrus-1D utilizing RE failed to converge on those three soil textures. Model comparison results showed that DARE is a reasonable approximation to full RE for estimating average moisture contents. However, further analyses on additional soil types, considering variable pressure heads for bottom boundary condition and variable groundwater table heights are needed to ensure the generalization of the developed model under any possible natural and real-world scenarios. Although the primary purpose of developing DARE for soil moisture accounting in unsaturated zone was to extend the *WetQual* model for the unsaturated section of wetlands, the developed model can be utilized in watershed-scale hydrologic models to serve as a robust solution to RE especially for cases when there is significant groundwater-surface water interaction.

Table 4.1: Soil hydraulic parameters for various soil types evaluated in this study; $\theta_{res}$ and $\theta_{sat}$ are, respectively, residual and saturated water content (dimensionless), and $K_{sat}$ is the saturated hydraulic conductivity (cm/day); $n$ (dimensionless; a pore-size distribution index), $\lambda$ (dimensionless; a pore connectivity parameter) and $\alpha$ ($L^{-1}$) are fitting parameters, which can be extracted from soil databases.

| Soil type | $\theta_{res}$ | $\theta_{sat}$ | $\alpha$ (1/cm) | $n$ | $K_{sat}$ (cm/day) | $\lambda$ |
|---|---|---|---|---|---|---|
| Sandy loam | 0.065 | 0.41 | 0.075 | 1.89 | 106.1 | 0.5 |
| Loam | 0.078 | 0.43 | 0.036 | 1.56 | 24.96 | 0.5 |
| Sandy clay loam | 0.100 | 0.39 | 0.059 | 1.48 | 31.44 | 0.5 |
| Sand | 0.045 | 0.43 | 0.145 | 2.68 | 712.8 | 0.5 |

Table 4.2: Performance indices for the calculated moisture contents by DARE for sandy loam

| Scenarios | First soil layer | | | | Second soil layer | | | |
|---|---|---|---|---|---|---|---|---|
| | $R^2$ | $E_{NS}$ | *RMSE* | *NRMSE* | $R^2$ | $E_{NS}$ | *RMSE* | *NRMSE* |
| GD-1st | 0.98 | 0.97 | 0.00 | 0.04 | 0.99 | 0.97 | 0.01 | 0.04 |
| GD-2nd | 0.95 | 0.90 | 0.01 | 0.03 | 0.96 | 0.92 | 0.00 | 0.02 |
| GD-3rd | 0.81 | 0.02 | 0.02 | 0.10 | 0.81 | 0.21 | 0.02 | 0.09 |
| GD-4th | 0.97 | 0.52 | 0.03 | 0.12 | 0.91 | 0.61 | 0.04 | 0.13 |
| GD-5th | 0.71 | -0.20 | 0.03 | 0.13 | 0.66 | -0.48 | 0.03 | 0.12 |
| GD-6th | 1.00 | 0.66 | 0.01 | 0.03 | 0.99 | 0.83 | 0.01 | 0.02 |
| GD-7th | 0.99 | 0.66 | 0.04 | 0.14 | 0.99 | 0.80 | 0.03 | 0.12 |
| FT-1st | 0.99 | 0.70 | 0.01 | 0.05 | 0.98 | -0.93 | 0.01 | 0.03 |
| FT-2nd | 0.99 | 0.57 | 0.01 | 0.05 | 0.98 | -1.24 | 0.01 | 0.04 |
| FT-3rd | 0.65 | 0.06 | 0.02 | 0.11 | 0.92 | -0.61 | 0.01 | 0.03 |
| FT-4th | 0.91 | 0.63 | 0.03 | 0.12 | 0.80 | -3.48 | 0.03 | 0.10 |
| FT-5th | 0.74 | 0.61 | 0.02 | 0.10 | 0.50 | -4.54 | 0.02 | 0.05 |
| FT-6th | 1.00 | 0.98 | 0.00 | 0.01 | 1.00 | -3.21 | 0.04 | 0.1 |
| FT-7th | 0.99 | 0.93 | 0.02 | 0.09 | 0.89 | -2.63 | 0.03 | 0.09 |

GD and FT denote gravity drainage and full-term versions of DARE, respectively.1st = no rainfall, no ET; 2nd = constant rainfall and constant ET; 3rd = variable rain and variable ET; 4th = low initial moisture content with increasing (variable) rainfall and variable ET; 5th = high intensity variable rain and variable ET; 6th = low initial moisture and high rainfall intensity to reach ponding; 7th = scenario of "Ponding at some point" where we started with a high initial moisture content, and a high constant rainfall intensity to keep saturation and then decrease the rainfall intensity.

Table 4.3: Performance indices for the calculated moisture contents by DARE for loam

| Scenarios | First soil layer | | | | Second soil layer | | | |
|---|---|---|---|---|---|---|---|---|
| | $R^2$ | $E_{NS}$ | *RMSE* | *NRMSE* | $R^2$ | $E_{NS}$ | *RMSE* | *NRMSE* |
| GD-1st | 1.00 | 0.96 | 0.01 | 0.03 | 1.00 | 0.98 | 0.00 | 0.02 |
| GD-2nd | 0.97 | 0.52 | 0.01 | 0.02 | 0.98 | 0.70 | 0.01 | 0.02 |
| GD-3rd | 0.84 | 0.22 | 0.02 | 0.07 | 0.69 | 0.21 | 0.02 | 0.07 |
| GD-4th | 0.95 | 0.72 | 0.03 | 0.09 | 0.84 | 0.69 | 0.05 | 0.12 |
| GD-5th | 0.74 | -0.65 | 0.03 | 0.10 | 0.58 | -1.74 | 0.03 | 0.09 |
| GD-6th | 0.98 | 0.98 | 0.00 | 0.01 | 0.80 | 0.78 | 0.01 | 0.03 |
| GD-7th | 0.96 | 0.64 | 0.04 | 0.11 | 0.96 | 0.66 | 0.04 | 0.10 |
| FT-1st | 0.98 | -4.06 | 0.02 | 0.06 | 0.63 | -0.32 | 0.00 | 0.00 |
| FT-2nd | 0.99 | 0.98 | 0.00 | 0.00 | 0.60 | -1.73 | 0.00 | 0.00 |
| FT-3rd | 0.84 | 0.14 | 0.01 | 0.05 | 0.53 | -3.78 | 0.00 | 0.00 |
| FT-4th | 0.88 | 0.65 | 0.02 | 0.06 | 0.92 | 0.48 | 0.01 | 0.03 |
| FT-5th | 0.67 | 0.61 | 0.02 | 0.06 | 0.67 | -14.42 | 0.01 | 0.02 |
| FT-6th | 1.00 | 1.00 | 0.00 | 0.00 | 1.00 | -0.76 | 0.03 | 0.06 |
| FT-7th | 1.00 | 0.87 | 0.02 | 0.05 | 0.93 | -6.06 | 0.01 | 0.04 |

GD and FT denote gravity drainage and full-term versions of DARE, respectively.1st = no rainfall, no ET; 2nd = constant rainfall and constant ET; 3rd = variable rain and variable ET; 4th = low initial moisture content with increasing (variable) rainfall and variable ET; 5th = high intensity variable rain and variable ET; 6th = low initial moisture and high rainfall intensity to reach ponding; 7th = scenario of "Ponding at some point" where we started with a high initial moisture content, and a high constant rainfall intensity to keep saturation and then decrease the rainfall intensity.

Table 4.4: Performance indices for the calculated moisture contents by DARE for sandy clay loam

| Scenarios | First soil layer | | | | Second soil layer | | | |
|---|---|---|---|---|---|---|---|---|
| | $R^2$ | $E_{NS}$ | *RMSE* | *NRMSE* | $R^2$ | $E_{NS}$ | *RMSE* | *NRMSE* |
| GD-1st | 1.00 | 0.98 | 0.00 | 0.02 | 1.00 | 0.98 | 0.00 | 0.02 |
| GD-2nd | 0.94 | 0.23 | 0.01 | 0.02 | 0.97 | 0.53 | 0.00 | 0.02 |
| GD-3rd | 0.81 | 0.22 | 0.02 | 0.06 | 0.64 | 0.04 | 0.02 | 0.06 |
| GD-4th | 0.93 | 0.72 | 0.03 | 0.08 | 0.82 | 0.70 | 0.04 | 0.11 |
| GD-5th | 0.70 | -0.43 | 0.03 | 0.08 | 0.63 | -1.29 | 0.02 | 0.08 |
| GD-6th | 0.99 | 0.99 | 0.00 | 0.00 | 0.89 | 0.85 | 0.01 | 0.02 |
| GD-7th | 0.99 | 0.67 | 0.03 | 0.09 | 0.99 | 0.68 | 0.03 | 0.08 |
| FT-1st | 0.99 | -1.04 | 0.01 | 0.04 | 0.32 | -18.53 | 0.00 | 0.01 |
| FT-2nd | 0.95 | -3.13 | 0.01 | 0.03 | 0.26 | -35.80 | 0.01 | 0.01 |
| FT-3rd | 0.69 | -0.32 | 0.02 | 0.08 | 0.24 | -11.64 | 0.00 | 0.01 |
| FT-4th | 0.83 | 0.08 | 0.03 | 0.08 | 0.79 | -1.91 | 0.03 | 0.07 |
| FT-5th | 0.70 | 0.70 | 0.02 | 0.06 | 0.46 | -73.00 | 0.01 | 0.04 |
| FT-6th | 1.00 | 0.99 | 0.00 | 0.00 | 1.00 | -7.20 | 0.04 | 0.11 |
| FT-7th | 0.99 | 0.90 | 0.02 | 0.05 | 0.85 | -0.02 | 0.02 | 0.04 |

GD and FT denote gravity drainage and full-term versions of DARE, respectively.1st = no rainfall, no ET; 2nd = constant rainfall and constant ET; 3rd = variable rain and variable ET; 4th = low initial moisture content with increasing (variable) rainfall and variable ET; 5th = high intensity variable rain and variable ET; 6th = low initial moisture and high rainfall intensity to reach ponding; 7th = scenario of "Ponding at some point" where we started with a high initial moisture content, and a high constant rainfall intensity to keep saturation and then decrease the rainfall intensity.

Table 4.5: Performance indices for the calculated moisture contents by DARE for sand

| Scenarios | First soil layer | | | | Second soil layer | | | |
|---|---|---|---|---|---|---|---|---|
| | $R^2$ | $E_{ns}$ | *RMSE* | *NRMSE* | $R^2$ | $E_{ns}$ | *RMSE* | *NRMSE* |
| GD-1st | 0.97 | 0.95 | 0.01 | 0.09 | 0.98 | 0.96 | 0.00 | 0.07 |
| GD-2nd | 0.97 | 0.97 | 0.00 | 0.03 | 0.97 | 0.97 | 0.00 | 0.03 |
| GD-3rd | 0.89 | 0.85 | 0.01 | 0.10 | 0.89 | 0.86 | 0.01 | 0.09 |
| GD-4th | 0.99 | -0.03 | 0.02 | 0.13 | 0.99 | 0.22 | 0.02 | 0.12 |
| GD-5th | 0.73 | 0.36 | 0.02 | 0.17 | 0.78 | 0.37 | 0.02 | 0.15 |
| GD-6th | 1.00 | 0.74 | 0.01 | 0.03 | 1.00 | 0.98 | 0.00 | 0.01 |
| GD-7th | 0.98 | 0.64 | 0.03 | 0.19 | 0.99 | 0.84 | 0.02 | 0.14 |
| FT-1st | 0.95 | 0.72 | 0.01 | 0.17 | 0.99 | -31.23 | 0.05 | 0.23 |
| FT-2nd | 1.00 | -5.17 | 0.04 | 0.40 | 0.99 | -26.50 | 0.04 | 0.21 |
| FT-3rd | 0.40 | 0.17 | 0.02 | 0.37 | 0.94 | -31.67 | 0.05 | 0.23 |
| FT-4th | 0.05 | -94.55 | 0.10 | 0.65 | 0.34 | -1.94 | 0.02 | 0.08 |
| FT-5th | 0.18 | -4.52 | 0.06 | 0.54 | 0.50 | -19.59 | 0.04 | 0.17 |
| FT-6th | 1.00 | -81.77 | 0.13 | 0.31 | 1.00 | -281.84 | 0.18 | 0.42 |
| FT-7th | 0.02 | -9.15 | 0.10 | 0.64 | 0.15 | -6.30 | 0.04 | 0.15 |

GD and FT denote gravity drainage and full-term versions of DARE, respectively.1st = no rainfall, no ET; 2nd = constant rainfall and constant ET; 3rd = variable rain and variable ET; 4th = low initial moisture content with increasing (variable) rainfall and variable ET; 5th = high intensity variable rain and variable ET; 6th = low initial moisture and high rainfall intensity to reach ponding; 7th = scenario of "Ponding at some point" where we started with a high initial moisture content, and a high constant rainfall intensity to keep saturation and then decrease the rainfall intensity.

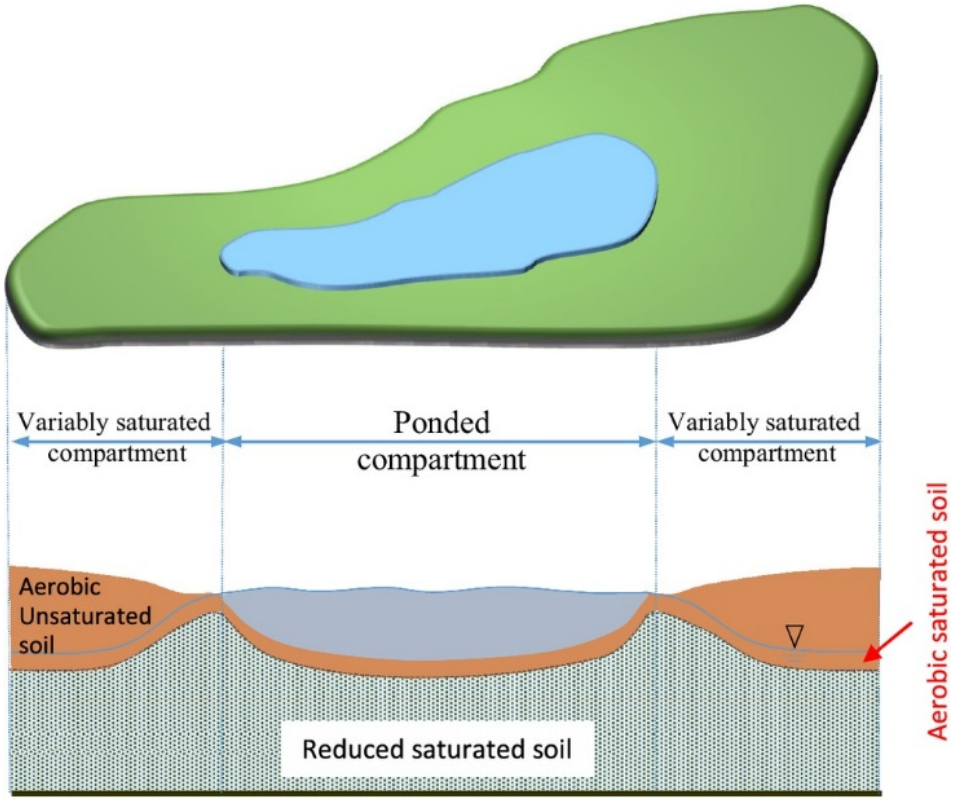


Figure 4.1: Schematics of a hypothetical seasonally flooded wetland (Sharifi et al. 2017; reprinted "With permission from ASCE")

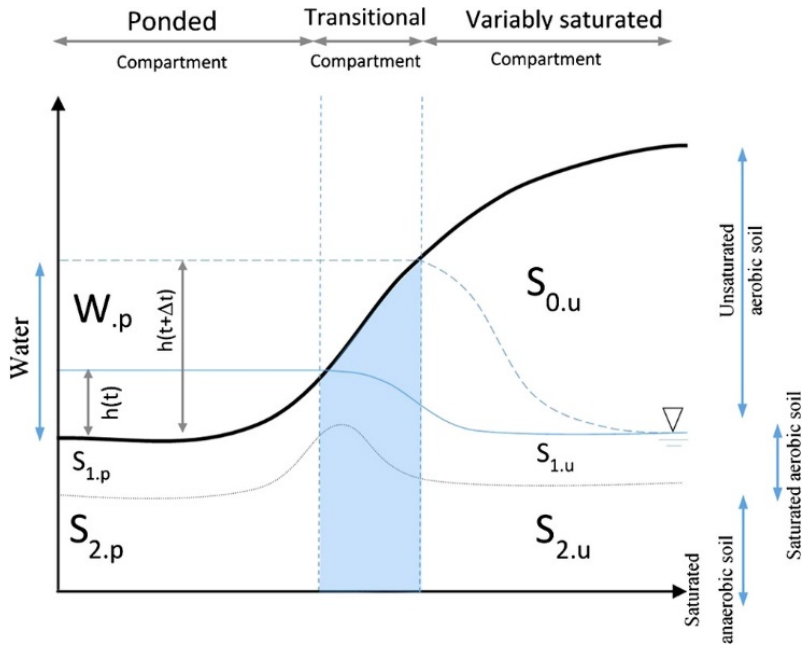


Figure 4.2: Schematic representation of the wetland compartmentalization into ponded and variably saturated compartments; subscripts p and u refer to ponded and variably saturated compartments, respectively; $h(t)$ and $h(t+\Delta t)$, respectively, represent water level in the ponded compartment at times $t$ and $t+\Delta t$ (Sharifi et al. 2017; reprinted "With permission from ASCE")

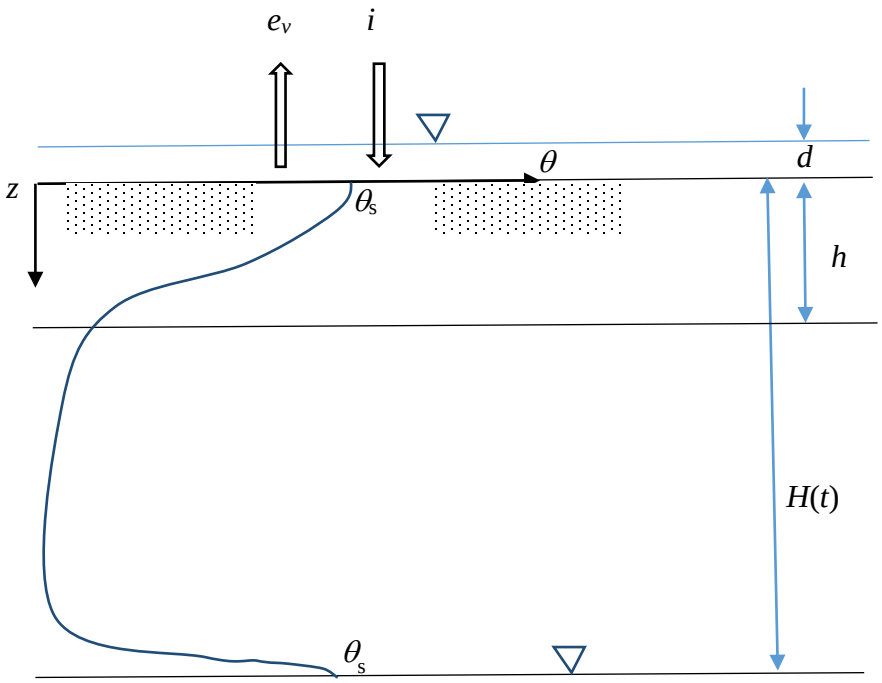


Figure 4.3: Schematic of soil profile for the two-layer depth-averaged solutions to Richards (1931)

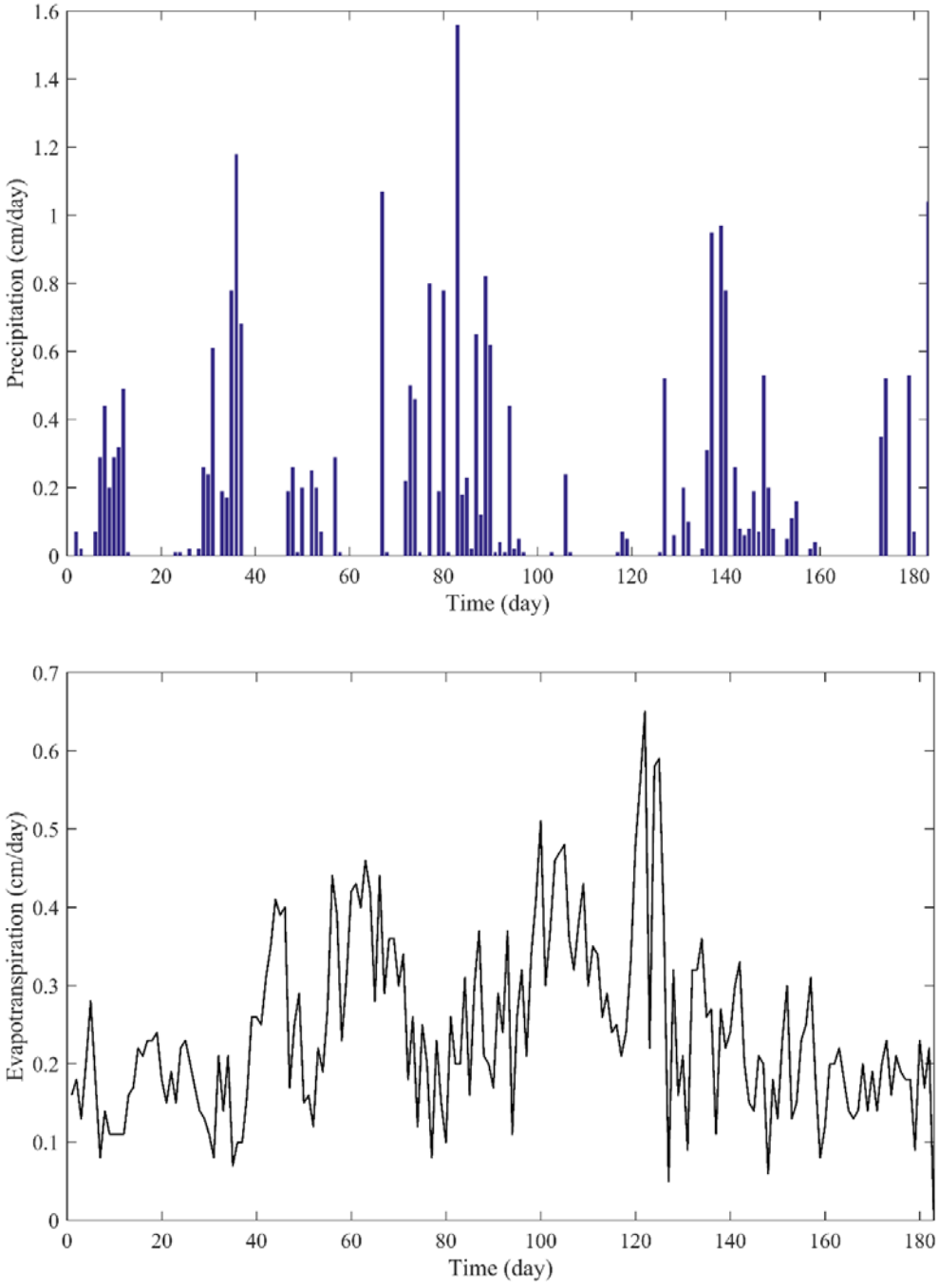


Figure 4.4: Daily precipitation (top) and evapotranspiration (bottom) in the study area

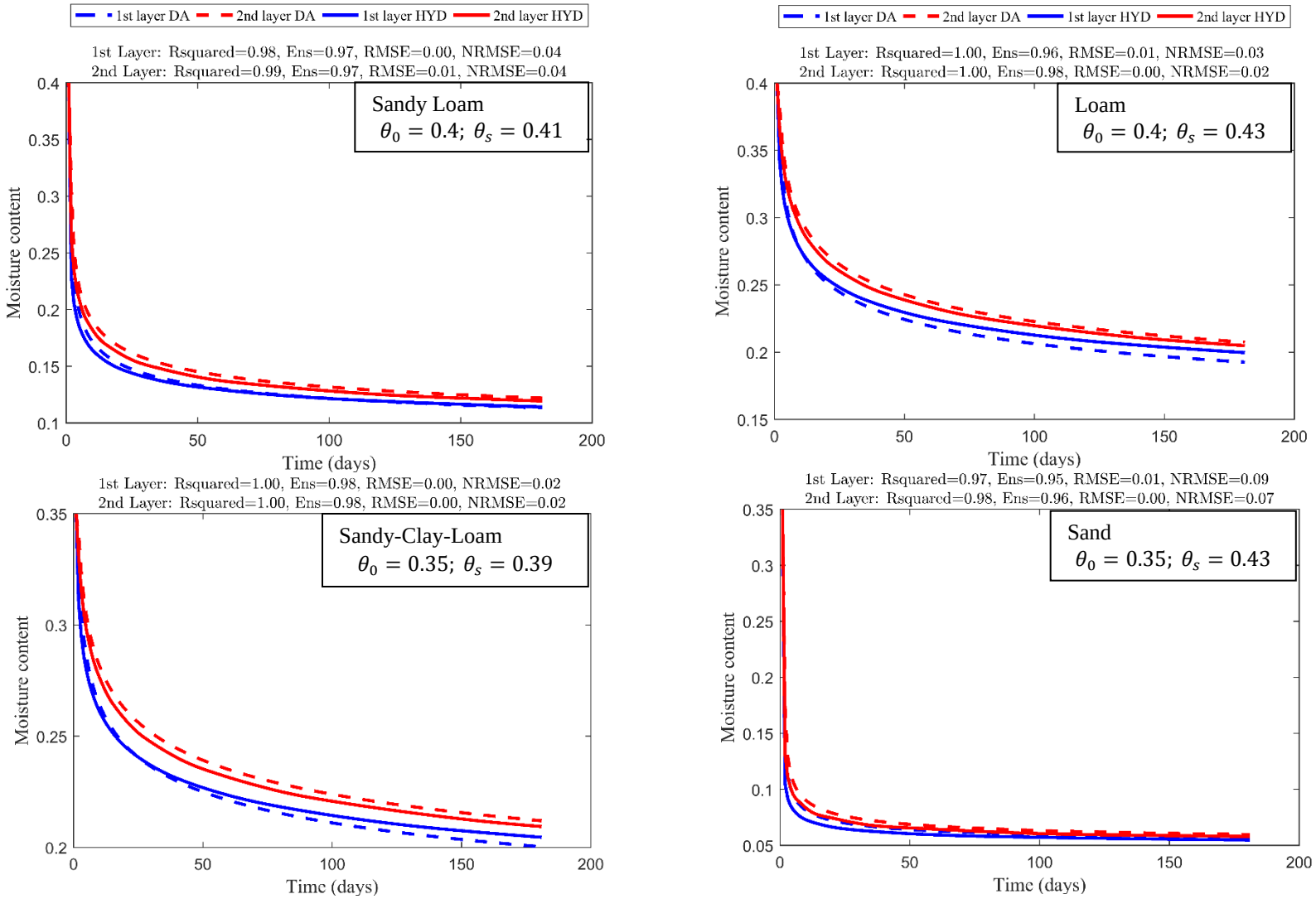


Figure 4.5: Comparison of calculated soil moisture contents for the first and second layers by DARE and Hydrus-1D for gravity drainage (bottom boundary) conditions; top boundary condition of “no rainfall and no ET” was considered.

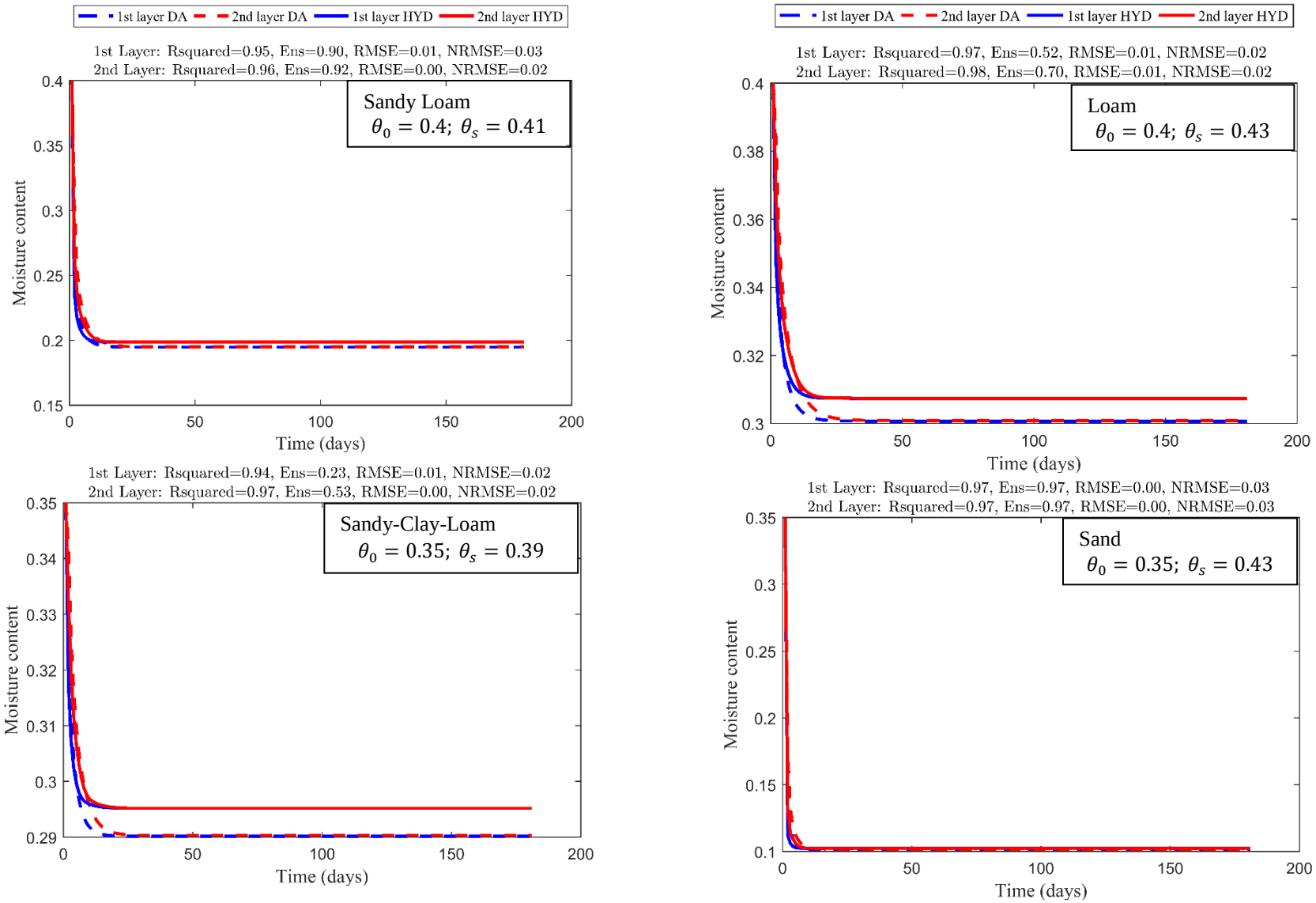


Figure 4.6: Comparison of calculated soil moisture contents for the first and second layers by DARE and Hydrus-1D for gravity drainage (bottom boundary) conditions; top boundary condition of "constant rainfall and constant ET" was considered.

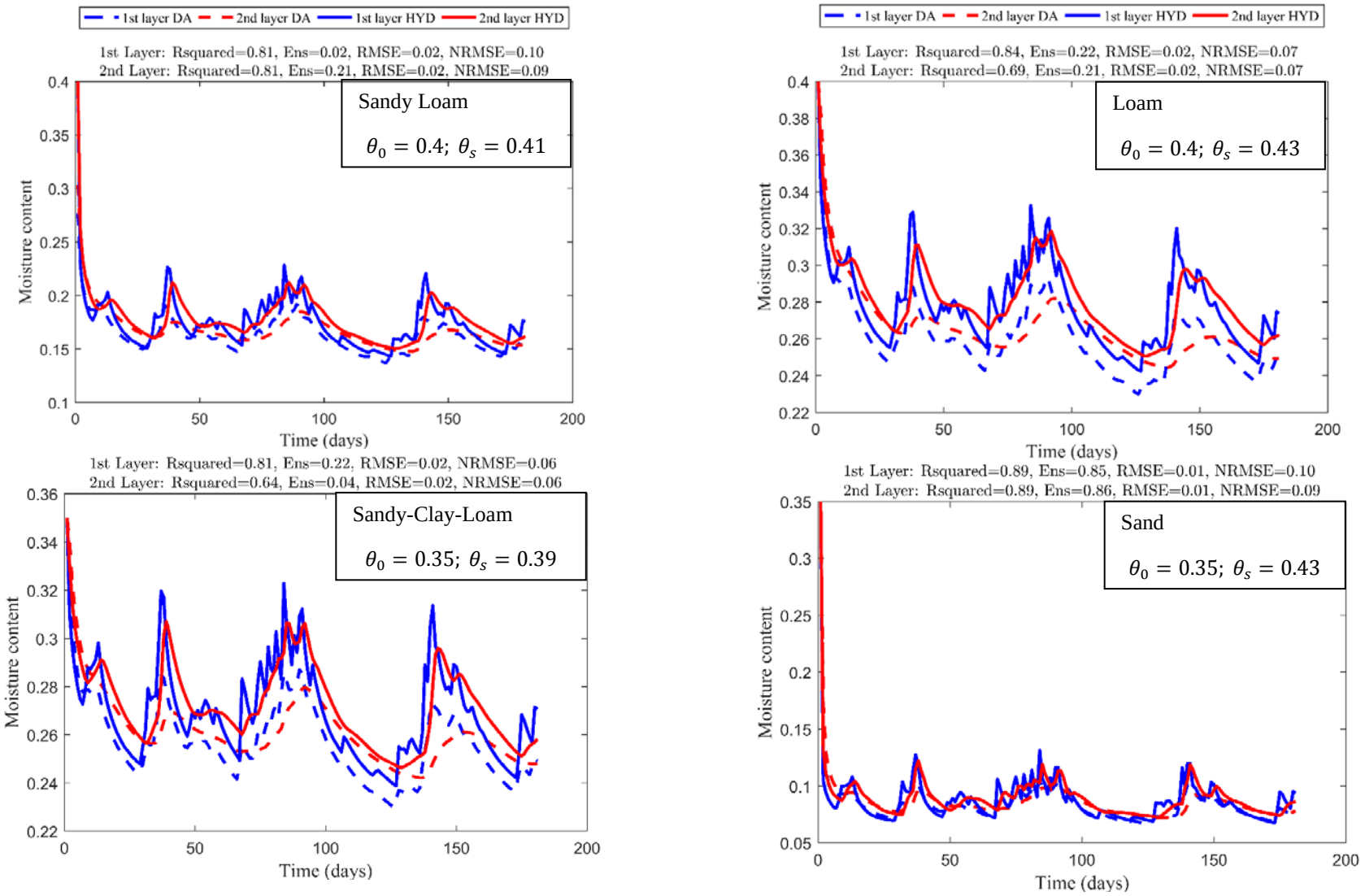


Figure 4.7: Comparison of calculated soil moisture contents for the first and second layers by DARE and Hydrus-1D for gravity drainage (bottom boundary) conditions; top boundary condition of "variable rain and variable ET" was considered.

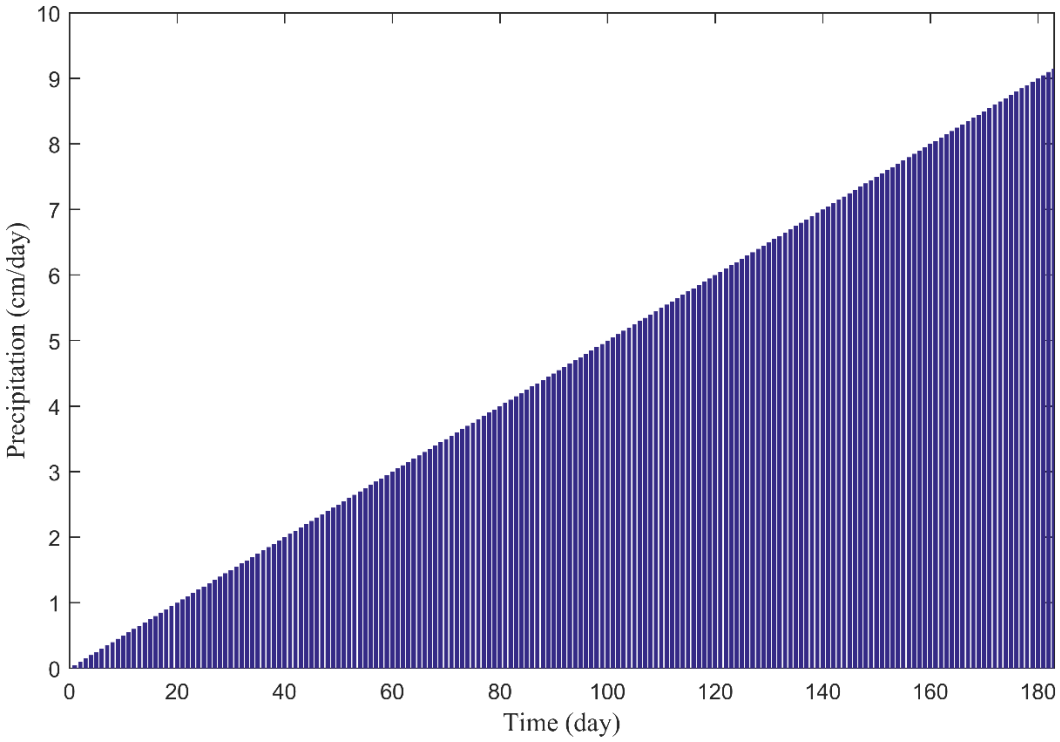


Figure 4.8: Daily rainfall intensity used for the top boundary condition of “low initial moisture content with increasing (variable) rainfall and variable ET”. (Buildup Scenario)

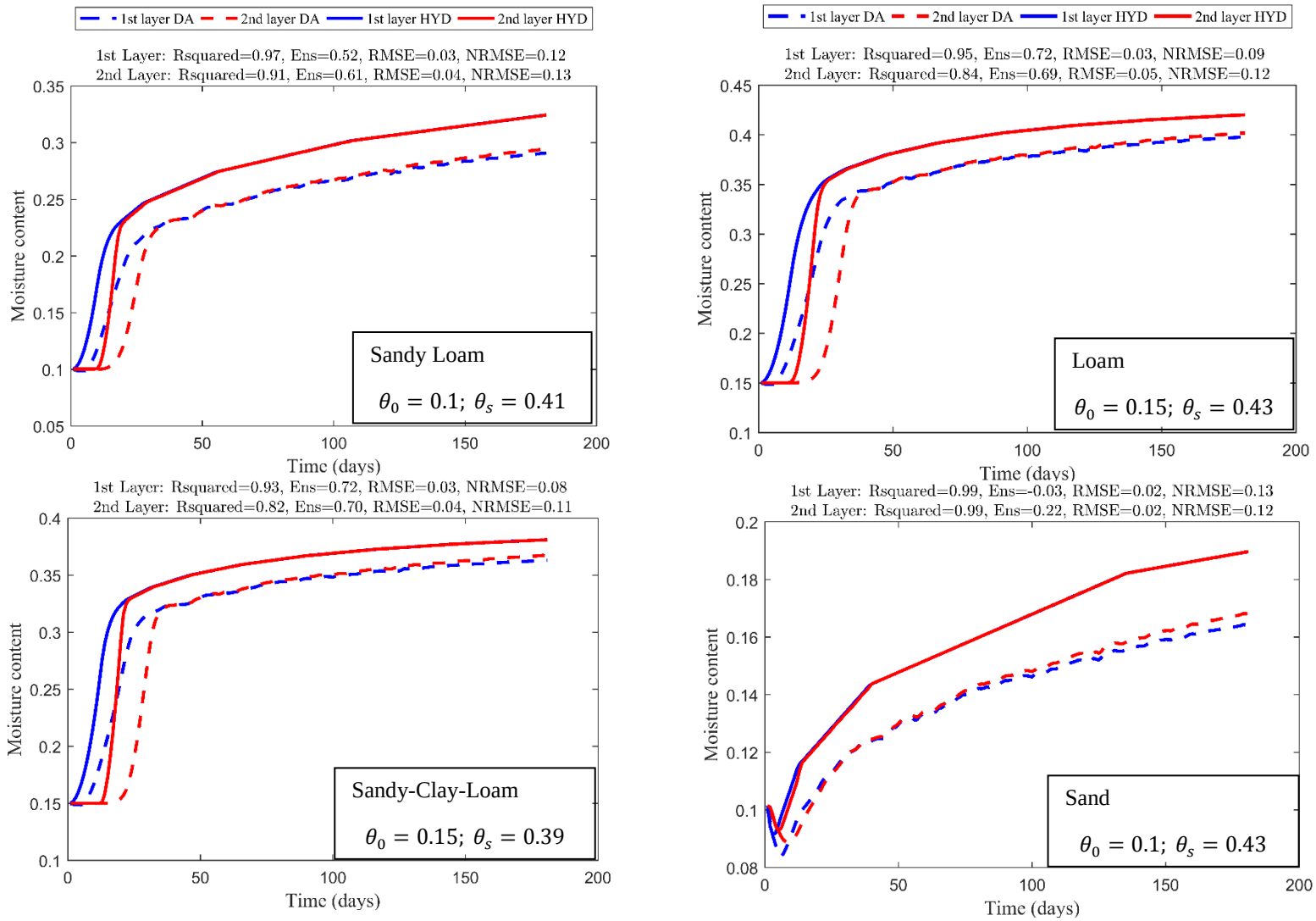


Figure 4.9: Comparison of calculated soil moisture contents for the first and second layers by DARE and Hydrus-1D for gravity drainage (bottom boundary) conditions. For this scenario, "low initial moisture content with increasing (variable) rainfall and variable ET" was considered. ("Buildup" scenario)

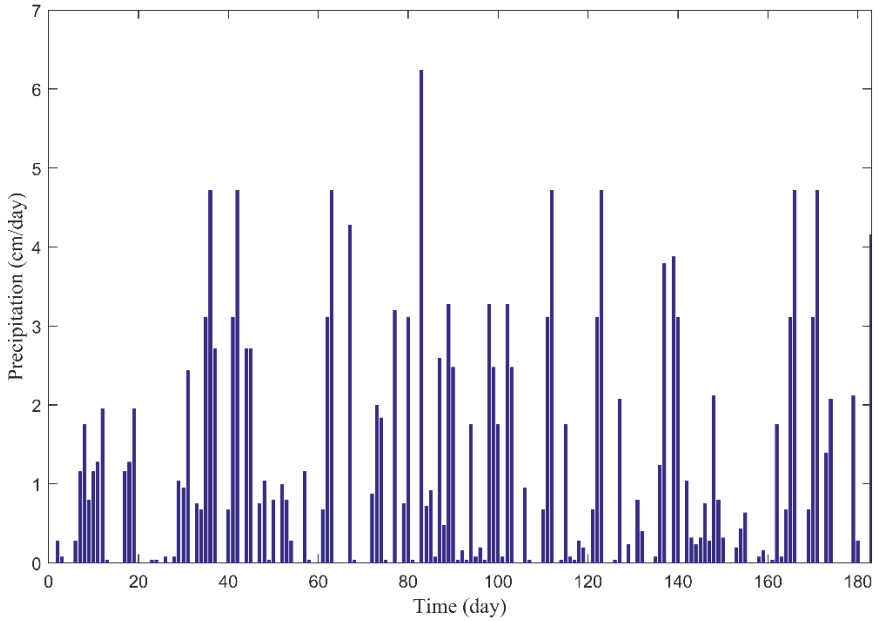


Figure 4.10: Daily rainfall intensity used for the top boundary condition of “high-intensity variable rain and variable ET”

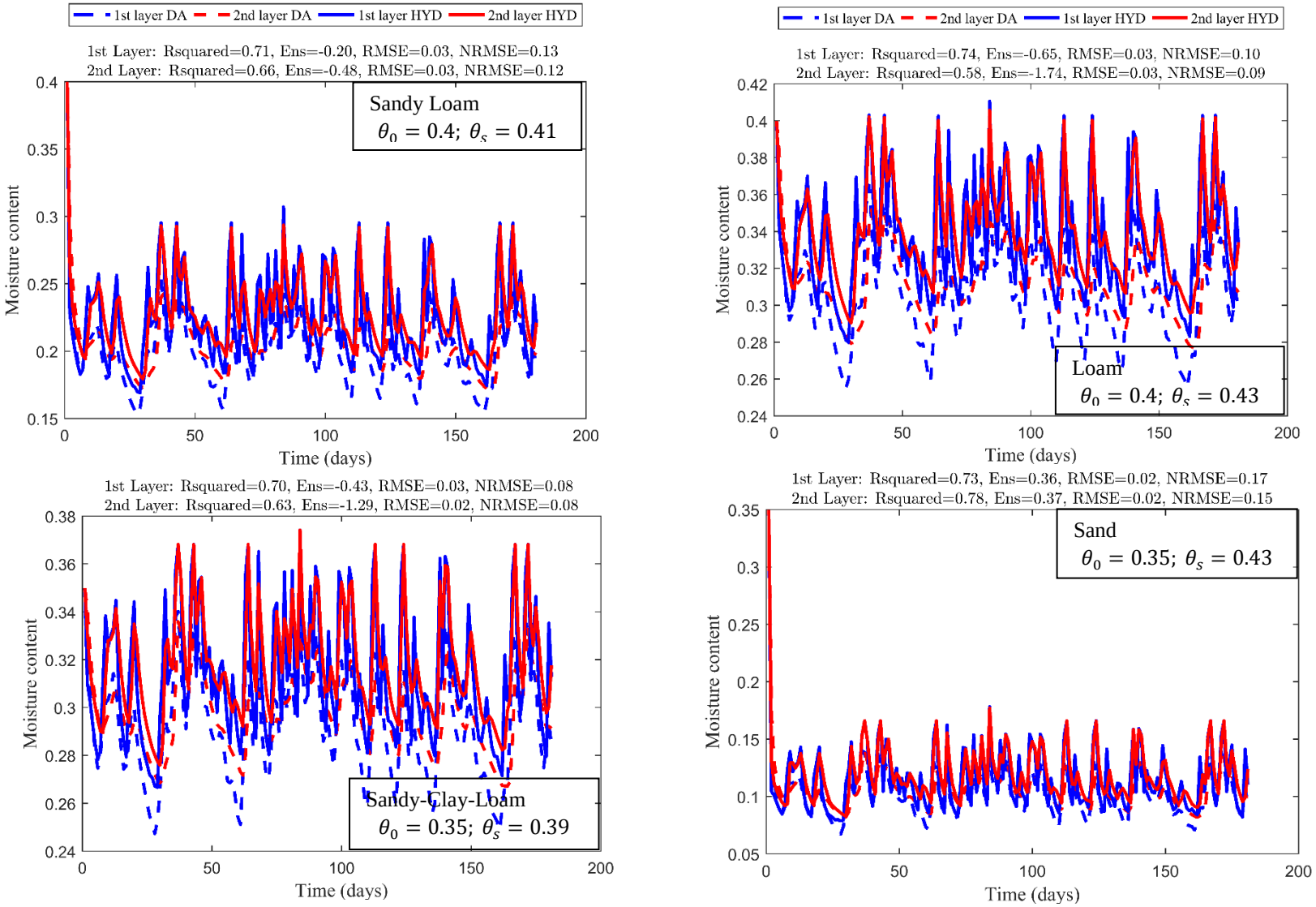


Figure 4.11: Comparison of calculated soil moisture contents for the first and second layers by DARE and Hydrus-1D for gravity drainage (bottom boundary) conditions; top boundary condition of “high intensity variable rain and variable ET” was considered.

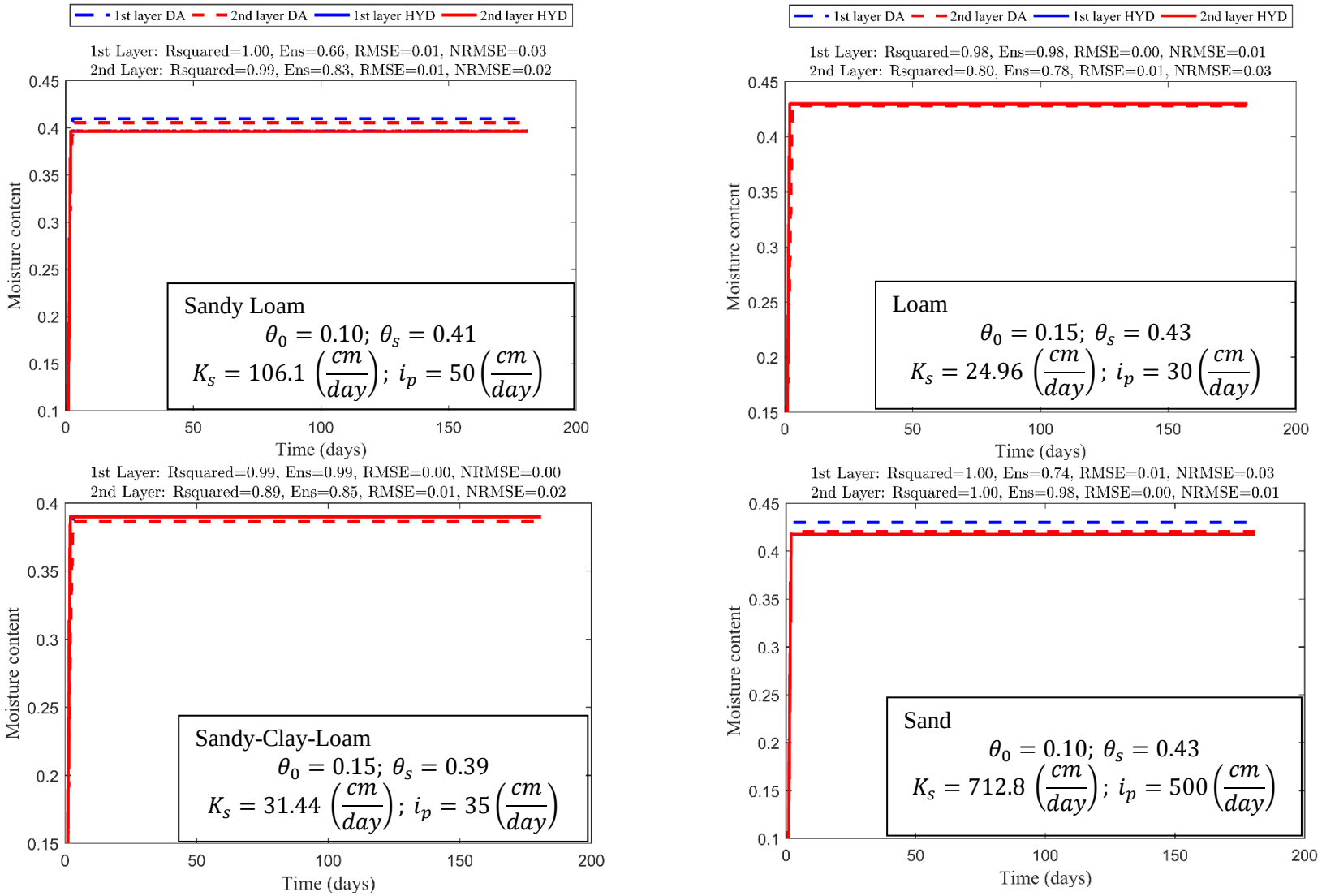


Figure 4.12: Comparison of calculated soil moisture contents for the first and second layers by DARE and Hydrus-1D for gravity drainage (bottom boundary) conditions; top boundary condition of "low initial moisture and high rainfall intensity to reach ponding" was considered; $i_p$ and ($K_s$) denotes rainfall intensity and soil saturated hydraulic conductivity.

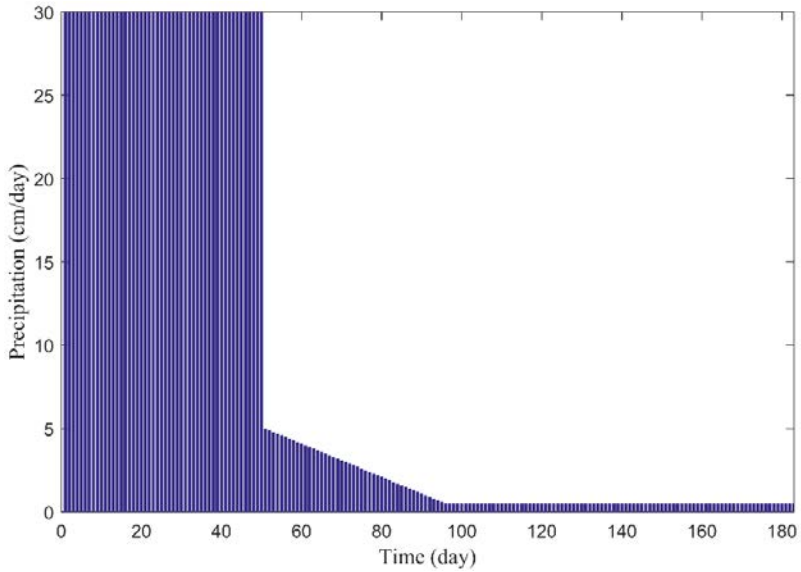


Figure 4.13: Daily rainfall intensity used to establish the scenario of “Ponding at some point” where we started with a high initial moisture content, and a high constant rainfall intensity to keep saturation and then decrease the rainfall intensity.

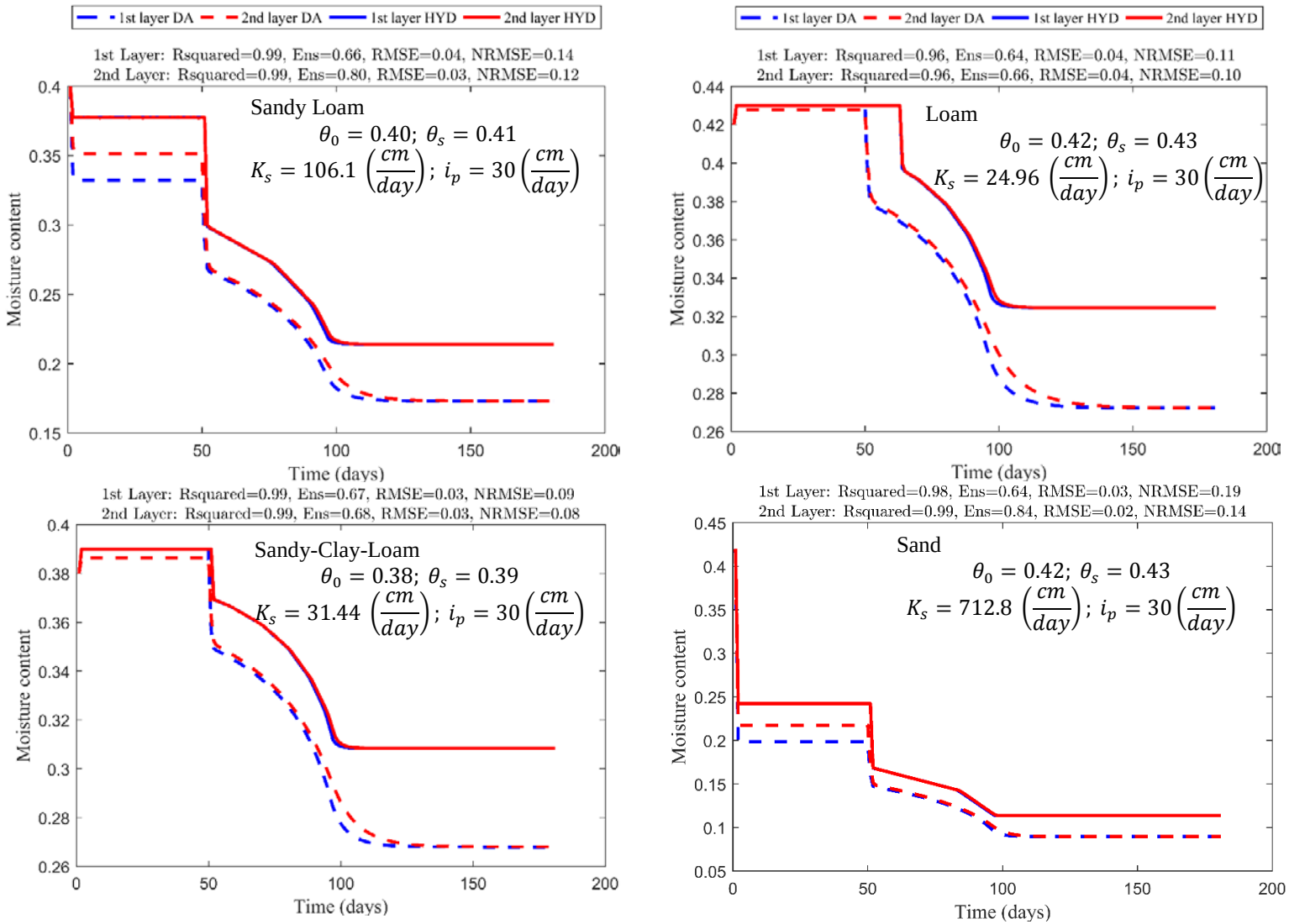


Figure 4.14: Comparison of calculated soil moisture contents for the first and second layers by DARE and Hydrus-1D for gravity drainage (bottom boundary) conditions; scenario of "Ponding at some point" where we started with a high initial moisture content, and a high constant rainfall intensity to keep saturation and then decrease the rainfall intensity.; Figure 4.13 represents the rainfall intensity applied for establishing this scenario; $i_p$ and ($K_s$) denote rainfall intensity and soil saturated hydraulic conductivity, respectively.

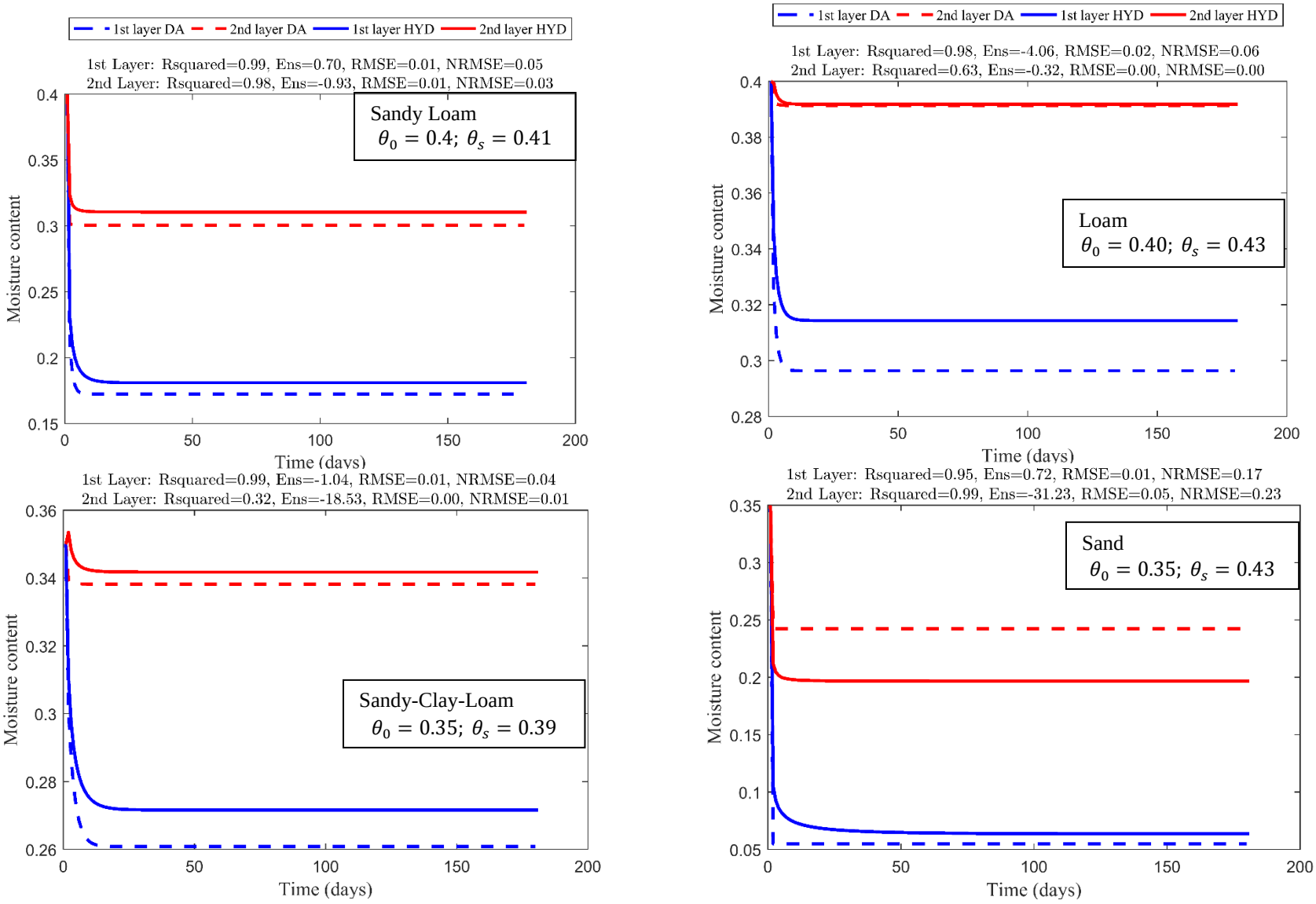


Figure 4.15: Comparison of calculated soil moisture contents for the first and second layers by the full-term DARE and Hydrus-1D; bottom BC of “zero pressure head at a fixed groundwater depth” and top BC of “no rainfall and no ET” were considered.

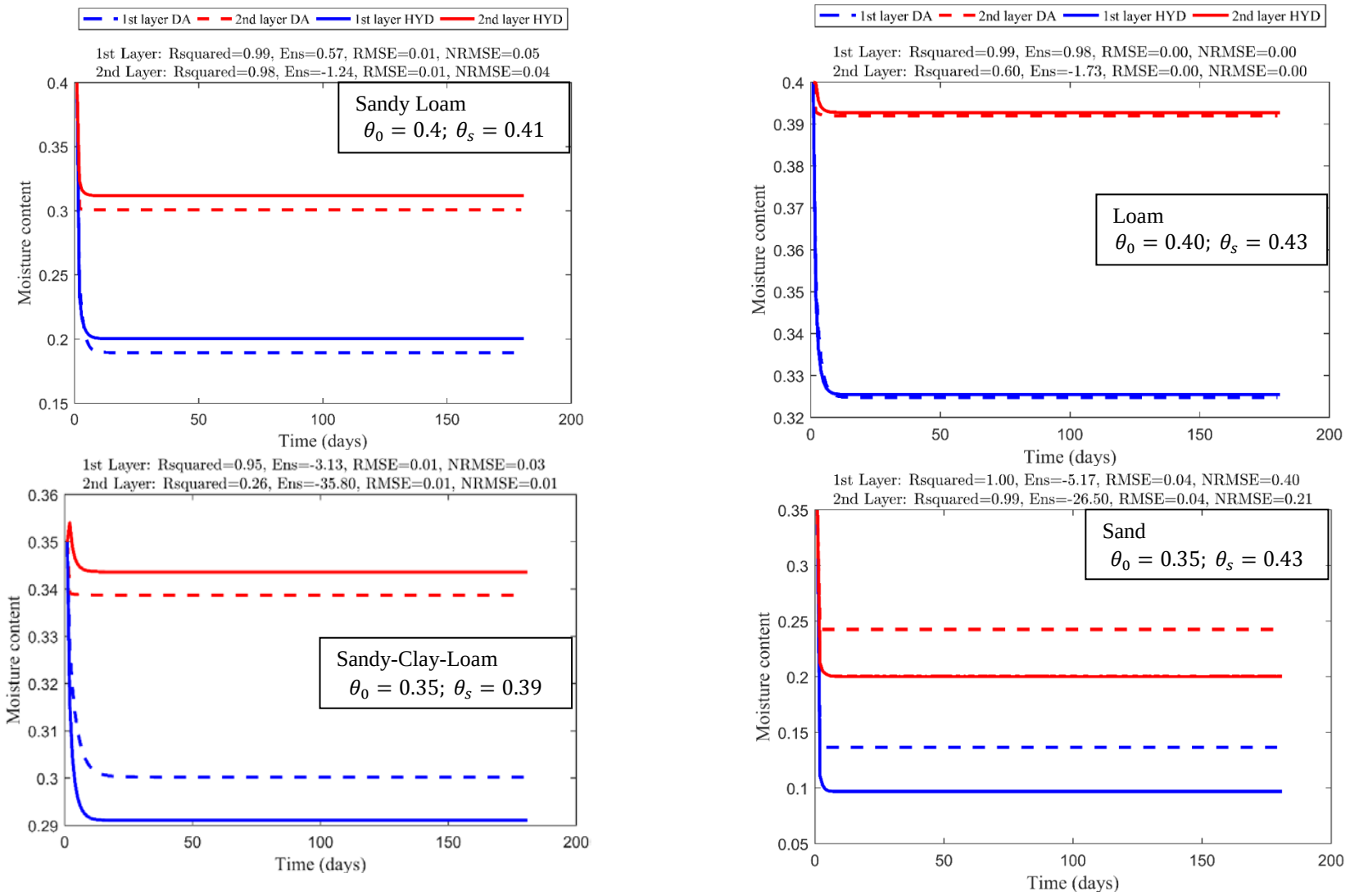


Figure 4.16: Comparison of calculated soil moisture contents for the first and second layers by the full-term DARE and Hydrus-1D; bottom BC of “zero pressure head at a fixed groundwater depth” and top BC of “constant rainfall and constant ET” were considered.

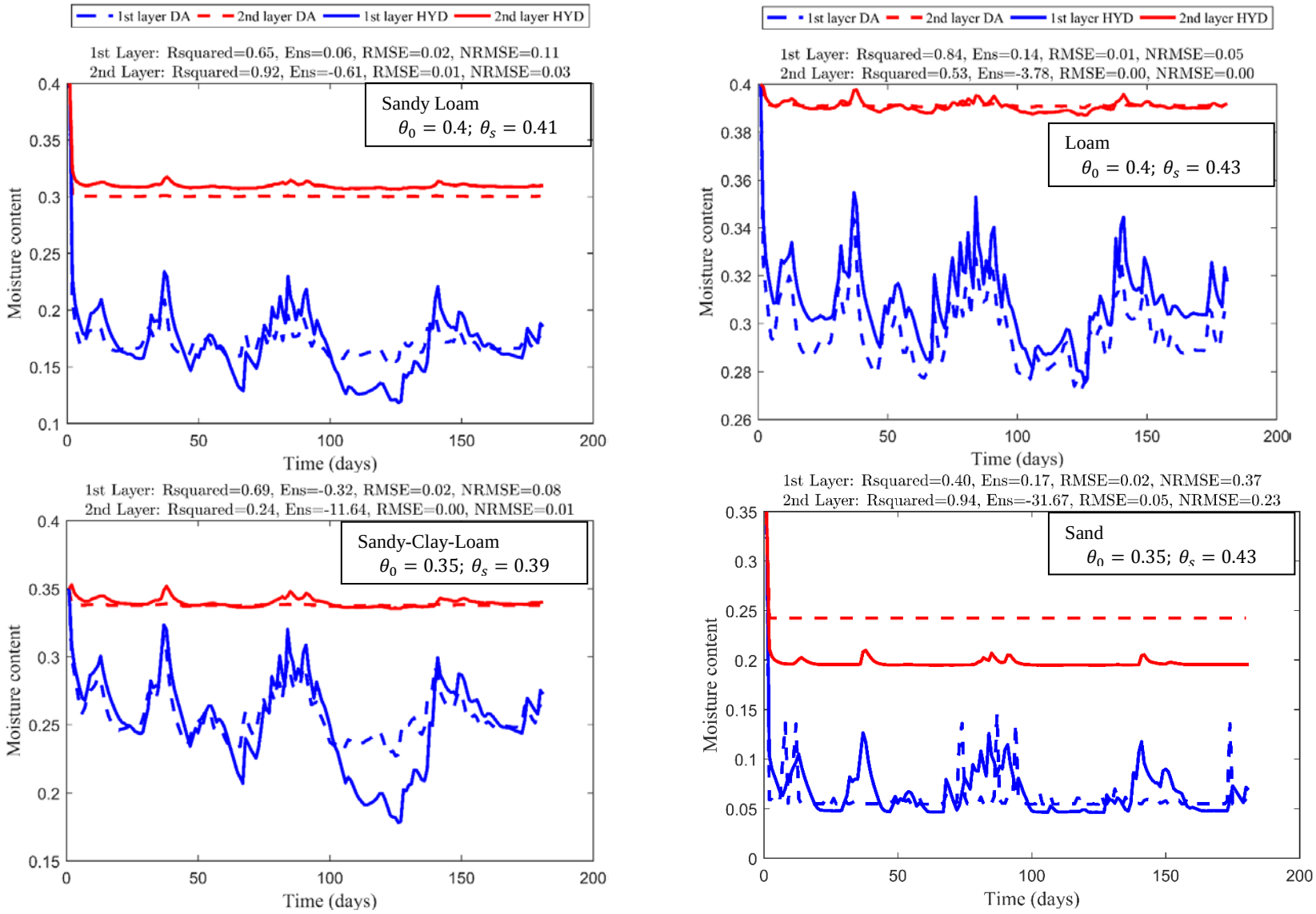


Figure 4.17: Comparison of calculated soil moisture contents for the first and second layers by the full-term DARE and Hydrus-1D; bottom BC of “zero pressure head at a fixed groundwater depth” and top BC of “Variable rainfall and variable ET” were considered.

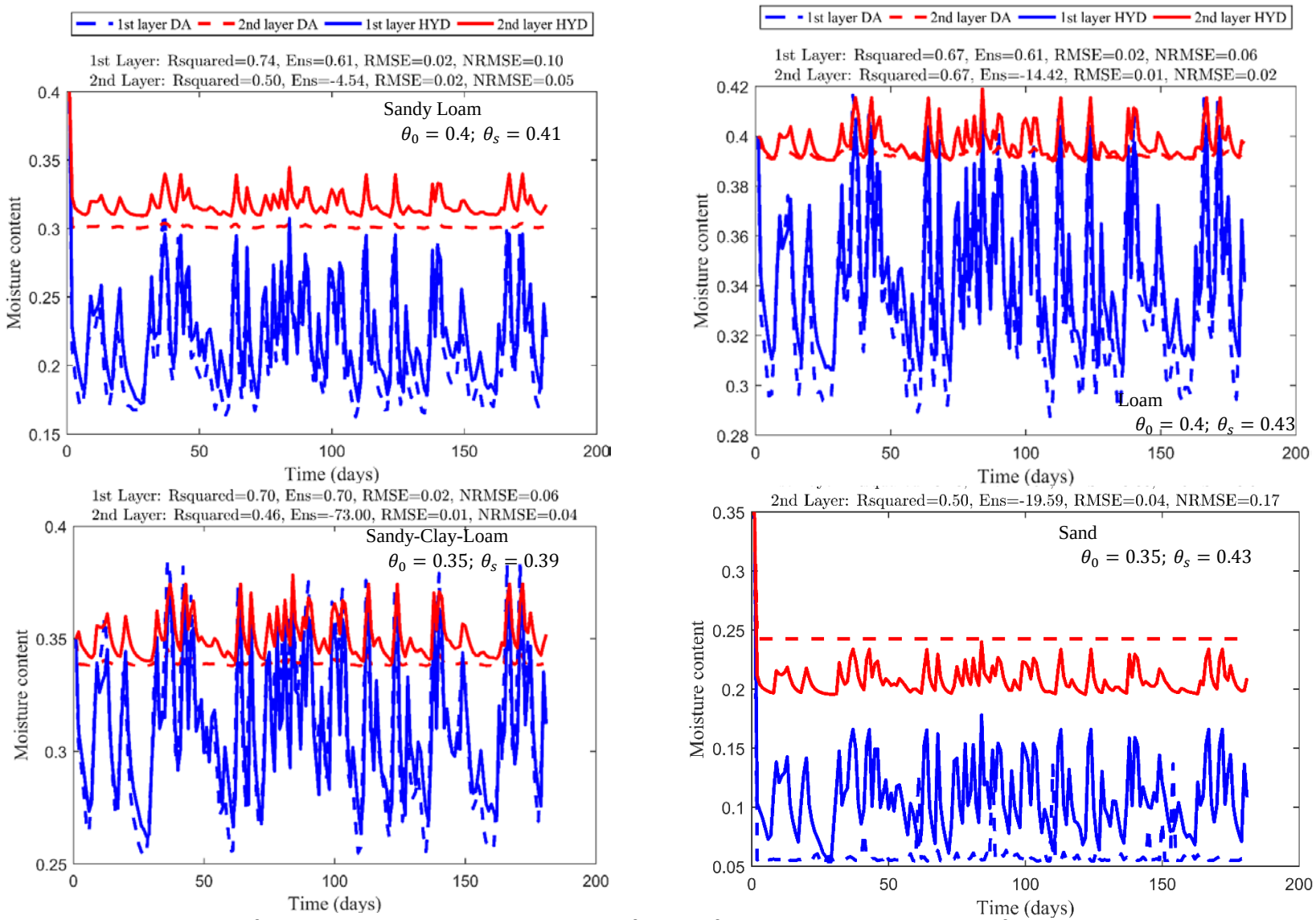


Figure 4.18: Comparison of calculated soil moisture contents for the first and second layers by full-term DARE and Hydrus-1D; bottom BC of "zero pressure head at a fixed groundwater depth" and top BC of "High intensity variable rain and variable ET" were considered.

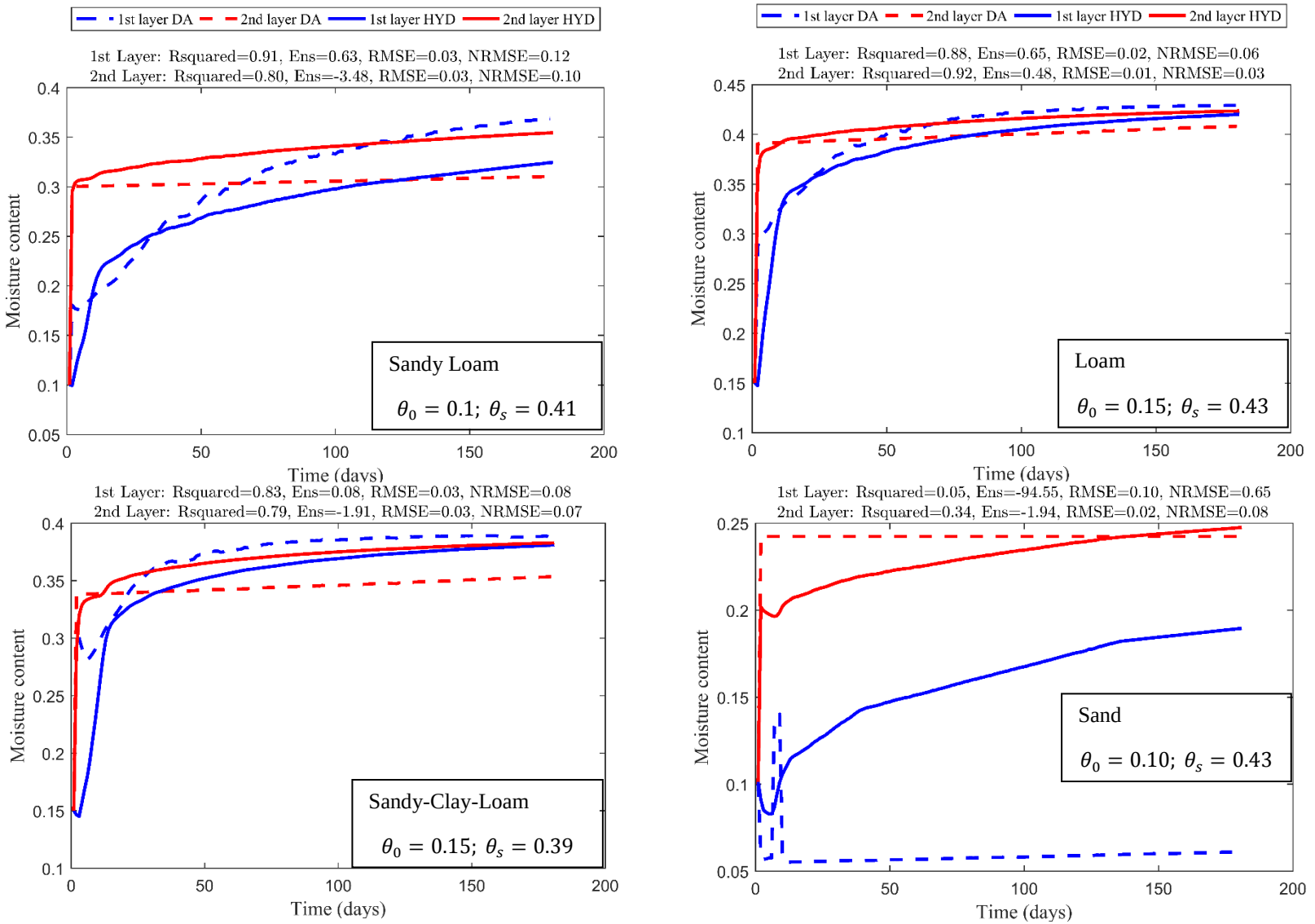


Figure 4.19: Comparison of calculated soil moisture contents for the first and second layers by the full-term DARE and Hydrus-1D; bottom BC of "zero pressure head at a fixed groundwater depth" and top BC of "low initial moisture content with increasing (variable) rainfall and variable ET" was considered. ("Buildup" scenario)

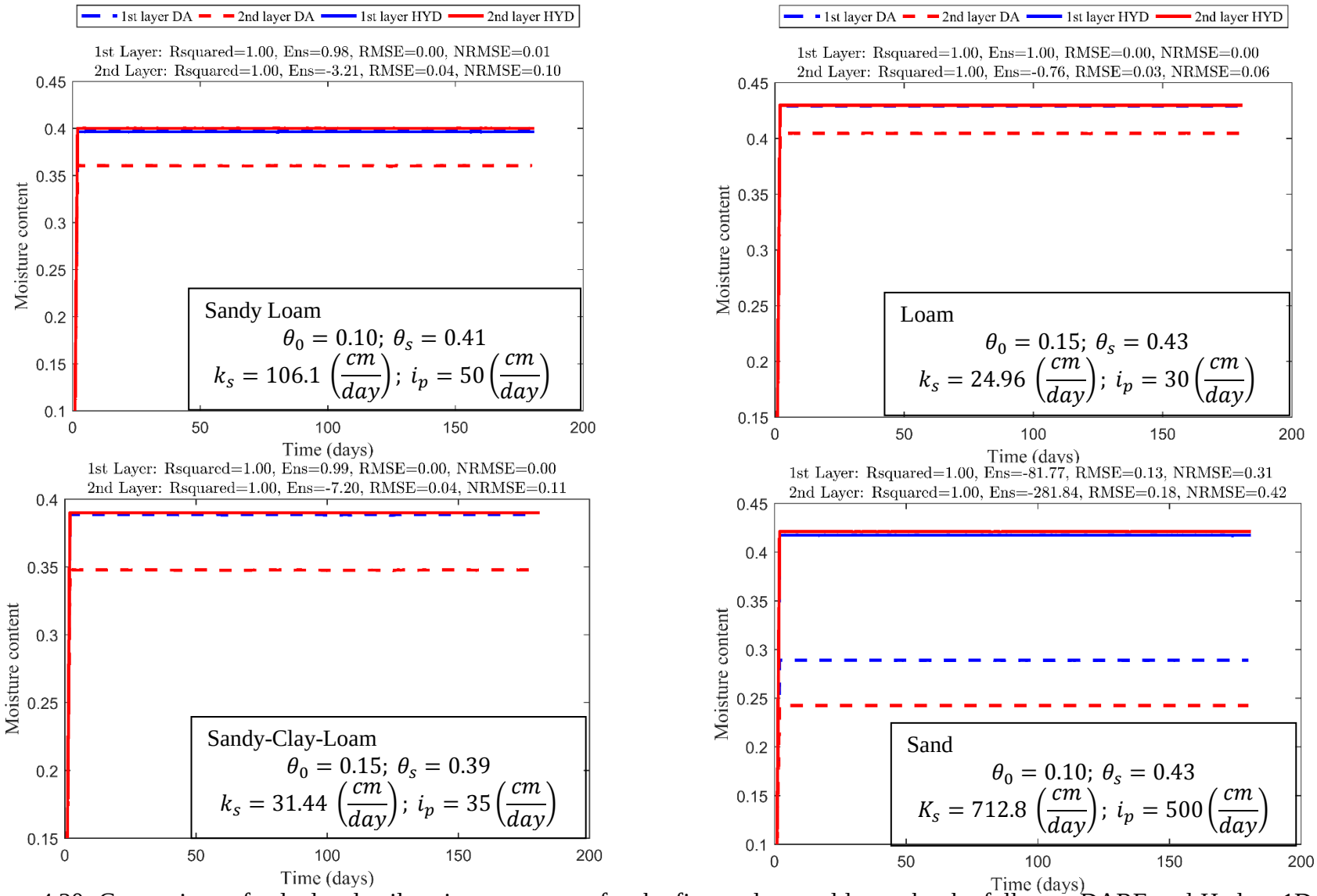


Figure 4.20: Comparison of calculated soil moisture contents for the first and second layers by the full-term DARE and Hydrus-1D; bottom BC of "zero pressure head at a fixed groundwater depth"; top BC of "low initial moisture and high rainfall intensity to reach ponding" were considered; $i_p$ and ($K_s$) denotes rainfall intensity and soil saturated hydraulic conductivity.

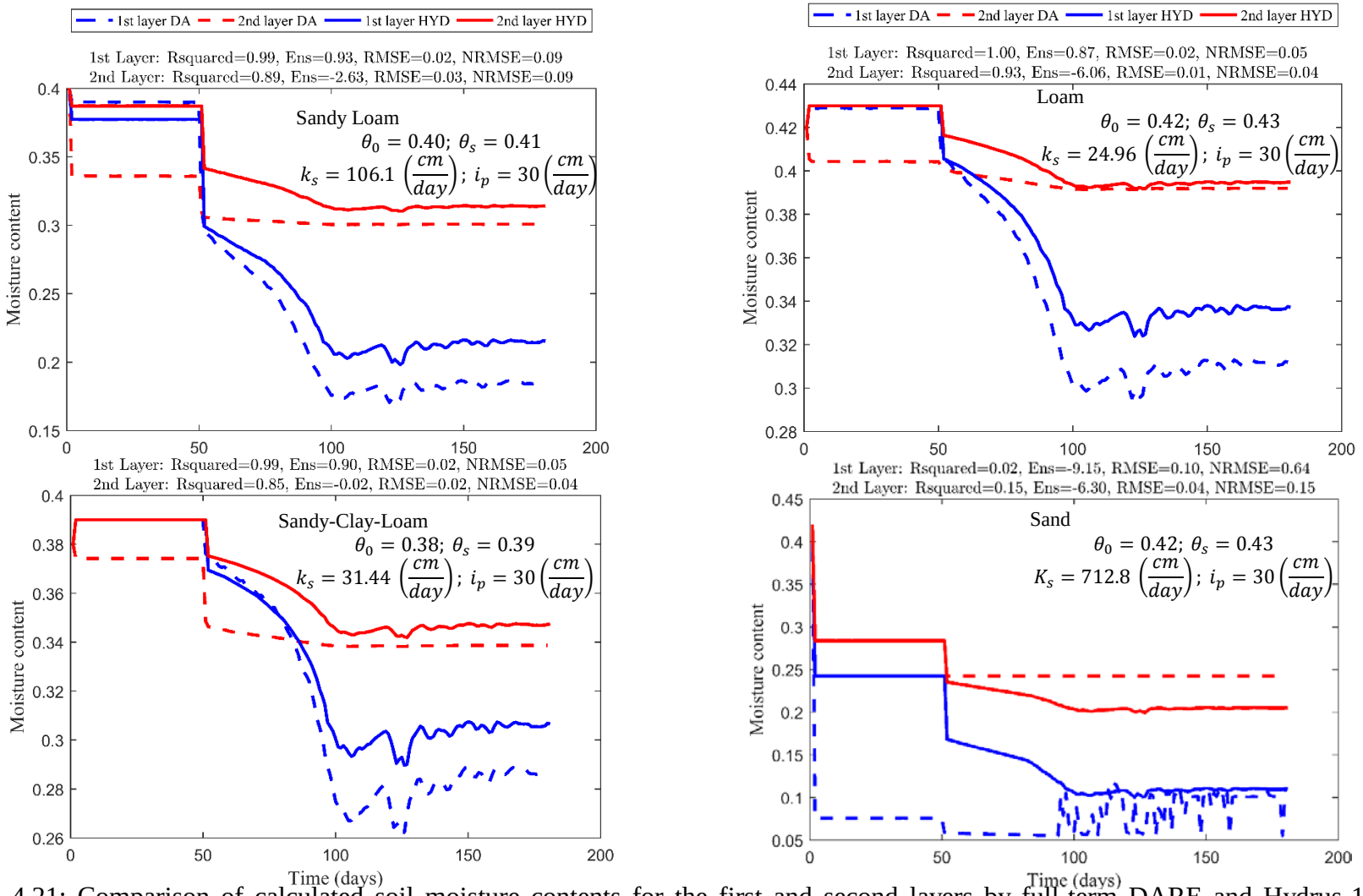


Figure 4.21: Comparison of calculated soil moisture contents for the first and second layers by full-term DARE and Hydrus-1D; bottom BC of "zero pressure head at a fixed groundwater depth"; scenario of "Ponding at some point" where we started with a high initial moisture content, and a high constant rainfall intensity to keep saturation and then decrease the rainfall intensity.; $i_p$ and ($K_s$) denotes rainfall intensity and soil saturated hydraulic conductivity.

# Chapter 5 : Graphical User Interface for the Wetland Water Quality Model, *WetQual*


## Abstract

A Graphical User Interface (GUI) was developed for the Wetland Water Quality Model, *WetQual* which enables users with a basic knowledge of hydrology and water quality to easily apply the *WetQual* model to their wetland sites. The processes-based *WetQual* model can simulate the water quality including nitrogen, phosphorous, carbon and sediment cycles in natural and constructed wetlands. *WetQual* can be used in continuously flooded environments or wetlands going through wetting and drying cycles. This GUI has been developed to handle continuously ponded wetlands. The ponded version of *WetQual* does not include a hydrology component which limits its application. By solving the continuity equation through a flow routing module, a hydrology component was added to calculate the times series of outflow, wetland water level, surface area, and volume. The added hydrology component is useful in case users do not have the pre-defined/measured hydrologic inputs. The GUI allows the *WetQual* model to be run either in a deterministic or stochastic mode. In the stochastic model, users need to select the probability distributions (uniform, log-normal or triangular) and relevant statistics for model parameters. The GUI generates random parameter sets and performs Monte Carlo simulations to produce an ensemble of outputs. It provides an opportunity to visualize both deterministic and stochastic model outputs through series of graphs. With the latter, users can visualize the time series of various *WetQual* outputs for a particular parameter set. Alternatively, GUI can summarize the ensemble of model runs through prediction intervals. The GUI can perform Generalized Likelihood Uncertainty Estimation (GLUE) and Bayesian Monte Carlo simulation and Maximum Likelihood estimation (BMCML) analyses for uncertainty analyses.

The utility of the GUI was demonstrated through a case study in a small restored wetland called Barnstable wetland, located in Kent Island, Maryland. This GUI presents a tool to help wetland scientists, managers and water quality professionals have a better understanding of nutrient cycling/removal in the flooded wetlands. Hence, it can also help for better wetland restoration, enhancement, planning, and management.

## 1. Introduction

Most of the commonly used hydrology and water quality models have some types of graphical interfaces to provide the users with a user-friendly environment for visualization/interpretation of inputs/outputs and post processing of model outputs. Visualizing inputs/outputs, importing and exporting the data from/to other platforms, which include the outputs from other models to be used in the target model or vice versa, are some of the capabilities of the user interfaces developed for those models. A Graphical User Interface (GUI) can facilitate the application of vital hydrology and water quality models. GUIs provide an interactive and easy-to-use control of software application. A primary objective of GUIs is to present the modeling environment as transparent as possible to the user (Tim, 1995). Over the years, with the emerging of object-oriented languages (such as C++ and C#), user-friendly versions of hydrology and water quality models have been developed. Table 5.1 provides a summary of some of the hydrology and water quality models in this regard. Two well-known watershed hydrology and water quality models, Storm Water Management Model (SWMM) and Hydrological Simulation Program-Fortran (HSPF) were initially formulated in the FORTRAN environment, but they also have Windows-based (written in C/C++ languages, called WinHSPF)

versions, developed over the last two decades which give the users greater flexibility and more advanced interactive capabilities. The Windows interface to HSPF, known as WinHSPF (Duda et al., 2001), was created for BASINS and works with the USEPA-supported HSPF model (Duda et al. 2012). Olivera et al. (2004) developed a Geographic Information System (GIS) interface in Visual Basic (VB) for the Soil and Water Assessment Tool (SWAT; which is written originally in FORTRAN) called ArcSWAT (or ArcGIS-SWAT). The distributed Kinematic Runoff and Erosion model, KINEROS2, written originally in FORTRAN, has a GUI developed within Microsoft .NET framework within Visual Studio 2003, called Automated Geospatial Watershed Assessment (AGWA 2.x), which is an ArcView GIS extension (Goodrich et al. 2006; Burns et al. 2007). Recently, Dile et al. (2016) developed an open source GIS (QGIS) user interface (UI), called QSWAT, which performs similar functions as ArcSWAT, but with additional enhanced features such as merging small subbasins. Another watershed hydrology model, MIKE SHE was first written in FORTRAN, and then the related GUI was developed in C++ (Christensen 2004). GUIs can also be used for training and educational purposes. For example, AghaKouchak et al. (2013) developed a MATLAB GUI for ensemble streamflow simulation through which the user can get an insight into how hydrological processes are interconnected. These practical tools are needed to help the uptake of the advanced hydrology/water quality models for non-scientists.

The Wetland Water Quality Model, *WetQual* (Hantush et al. 2013; Kalin et al. 2013; Sharifi et al. 2013) has been developed in FORTRAN language, and the new modules will also be written in this environment. The ponded version of *WetQual* does not include a hydrology component which limits its application. Hydrologic information (flow in and out of the wetland, depth-area-volume time series, etc.) needs to be provided as an input, which could be observed data or modeled externally. Adding a hydrology component is required in case users do not have

the pre-defined/measured hydrologic inputs for the wetland which is mostly the case. By solving continuity equation through a flow routing module, a hydrology component should read in the hydrologic forcing time series (i.e., inflow, evapotranspiration (ET), precipitation and subsurface/groundwater flow), and geometry table (i.e., depth-area-volume-outflow relationship), to calculate the times series of outflow, wetland water level, surface area, and volume. An inclusion of the hydrology component in the *WetQual* will help conduct a smoother water quality modeling by providing the users with a better understanding of hydrologic processes in the study wetland. Furthermore, the users do not need to perform wetland hydrologic modeling individually outside the *WetQual*.

For a proper application of *WetQual* model, a Monte Carlo (MC) simulation of 50,000 or 100,000 runs are highly recommended. Generating an ensemble of *WetQual* outputs by conducting MC simulations is the first step in conducting uncertainty analyses. With the current format, the users have to do uncertainty and sensitivity analyses outside of the *WetQual* in other software, such as Excel. They also need to transfer model outputs to other platforms to visually assess their results, which would be challenging when they set the model for high number of simulations, in which case the output files would be very big in size. The *WetQual* model has text-based input/output interactions with no visualization interface. A GUI would help extend the model's accessibility for public use. A GUI can be an invaluable platform ready to employ other fundamental functionalities such as uncertainty and sensitivity analysis which are essential for any reliable hydrologic/water quality studies.

Improved understanding of the physics and dynamics of hydrologic systems, and considerable growth in the computational power have considerably improved the hydrologic modeling (Liu and Gupta, 2007). This has resulted in the establishment of higher levels of

complexity into the hydrologic models and reflects our improved understanding. However, they have increased the need for robust methods to encounter the increased uncertainty associated with these models and the observations required for the development and evaluation of the models (Liu and Gupta, 2007). The same but important issue comes with the development and evaluation of process-based/physically-based water quality models. Uncertainty originates from various sources including the structure of the model, estimation of model parameter values, input forcing and boundary condition and errors in measurements (i.e., field observations) (Beven and Binley, 2014). A sufficient understanding of uncertainty sources is needed to reduce the total predictive uncertainty (Renard 2010); an estimation of model predictive uncertainty can establish a basis for environmental decision makers to select among alternative actions (Reckhow and Qian 1994). *WetQual* as a process-based model includes a large number of parameters that have to be estimated from a limited information or data available from wetland hydrology and water quality measurements. Table 5.2 represents some of *WetQual* model's parameters used in the calculation of nitrogen (N), phosphorus (P) and total suspended sediment (TSS) cycles. For brevity, C parameters are not listed in the table. Readers are referred to Sharifi et al. (2013) regarding the carbon cycle and the related parameters in *WetQual*.

A better representation of physics and natural processes comes with a higher complexity in the model and consequently more uncertainties, and that is why a robust wetland water quality model can benefit from post-processing and sensitivity analyses embedded into its graphical interface. The generalized likelihood uncertainty estimation (GLUE) (Beven and Freer, 2001) has been extensively used in water quality modeling and management studies (e.g., Zheng and Keller, 2007; Freni et al., 2008; Mannina, 2011; Zhang et al., 2015). The GLUE methodology rejects the concept of an optimum parameter set for a model and instead promotes the concept of

"equifinality" of different parameter sets and/or model structures (Kalin et al. 2013). The intention of equifinality thesis is to bring attention to the fact that there are many acceptable representations that cannot be easily rejected and that should be considered in assessing the uncertainty associated with predictions (Beven, 2006). Wagener et al. (2001) developed a Monte-Carlo Analysis Toolbox (MCAT) for regional sensitivity analysis which also performs GLUE analysis. The philosophy behind GLUE is to avoid a difficult full probabilistic model specification but to instead search regions in the parameter space where the model predictions are consistent with the observations (Nott et al. 2012). Huang et al. (2014) developed CV-GLUE uncertainty estimation tool for wetland water quality models which provides predictive uncertainty estimation in terms of a characteristic coefficient of variation (CV). Characteristic CV is a simple measure of uncertainty that can be used to represent the uncertainty within local data or the values of local parameters (Hakanson, 2000). The applied likelihood function in their tool is equivalent to a coefficient of determination or the Nash-Sutcliffe efficiency ($E_{NS}$) (Nash and Sutcliffe, 1970) criterion. GLUE lacks rigorous statistical assumptions and uncertainty, and therefore is no longer expressed in terms of probabilities (Chaudhary and Hantush 2017).

As emphasized by Chaudhary and Hantush (2017), Bayesian frameworks have been recently utilized to link model calibration and uncertainty estimation to water quality risk assessment. In addition to the GLUE method and to obtain relatively more accurate probabilistic inferences, the wetland water quality model of this study (i.e., *WetQual*) was equipped with a novel approach presented by Hantush and Chaudhary (2014). This approach combines the Bayesian Monte Carlo (BMC) simulation (e.g., Dilks et al. 1992) with the maximum likelihood estimation, called BMCML, and borrows the concept of "equifinality" from the GLUE methodology, i.e. the emphasis is placed on the generated parameter sets (Hantush and

Chaudhary, 2014). BMCML method is inherently computationally intensive especially in highly parameterized hydrology and water quality models (Chaudhary and Hantush, 2017).

The objective of this study was adding a flow routing module to the ponded version of *WetQual* and creating a GUI that bring the hydrologic and water quality modeling under one umbrella. The developed *WetQual* GUI has a hydrologic component that can calculate wetland outflow, depth, area and volume time series through flow routing. The GUI also simplifies the input/output transfer and provides users with a powerful visualization and post processing tool which include uncertainty and sensitivity analyses. By utilizing this GUI, users can perform the GLUE and BMCML analyses. GUI in its post processing module provides a tool for model predictive uncertainty analysis. By conducting GLUE, it provides estimate for the 95% prediction interval. Through BMCML it can provide 95% confidence limits. Sensitivity analysss based on Kolmogorov-Smirnov (K-S) test and dotty plots are also available in the GUI. The utility of the GUI is demonstrated through its application to Barnstable wetland, located in Kent Island, Maryland.

## 2. WetQual GUI development

### 2.1. WetQual Model

The process-based *WetQual* model simulates nitrogen (N), phosphorus (P), total suspended sediment (TSS) and carbon (C) cycles and their dynamics in wetlands. The model partitions a wetland into three basic compartments: (1) (free) water column, (2) wetland soil layer (which is further portioned into aerobic and anaerobic zones), and (3) plant biomass (Hantush et al., 2013). Processes in surface water and the bottom-active soil layer are described by a system of coupled ordinary differential equations. Figure 5.1 explains the internal

structures/steps and processes of *WetQual* model using a flowchart. The model runs on daily time scale, while it internally divides the one-day time interval into a smaller time interval for numerical integration.

## 2.2. Design

The GUI was written in the C#.NET environment within Visual Studio (VS) 2015. “C# is an elegant and type-safe, object-oriented language that enables developers to build a variety of secure and robust applications that run on the Microsoft .NET Framework” (MSDN 2015). Type-safe code accesses only the memory locations it is authorized to access. For example, type-safe code cannot read values from another object's private fields (MSDN 2017). To that end, XAML language is employed by the Windows Presentation Foundation (WPF) to define the linkage of various interface elements. WPF graphic subsystem is used to build the UI of a window (like basic layout, data binding, and basic UI components). Note that NET Framework 4.5.2 or higher version is required to install *WetQual* which comes with the install package. To better understand the development of *WetQual* GUI, the conceptual structure is shown in Figure 5.2.

*WetQual* GUI uses a suite of multiple modules to perform a successful visualization of inputs/outputs of *WetQual* accompanied with uncertainty and sensitivity analyses. Those modules include *WetQual* with Windows graphics, random parameter generation, post-processing by likelihood calculations through GLUE and BMCML methods, and sensitivity analysis using Kolmogorov-Smirnov (K-S) test and dotty plots. Table 5.3 to Table 5.5 represent hydro-climate inputs, input concentrations, and the outputs of *WetQual* GUI, respectively. All

the parameters of the model are too many to be listed here, and readers are referred to Hantush et al. (2013), Kalin et al. (2013), and Sharifi et al. (2013)..

*WetQual* GUI accepts TEXT files in “space delimited” format, visualizes inputs/outputs and gives editing capability for model inputs. Once the user provided the required data for *WetQual* GUI, they can view the time series of data in tables and graphs where they can edit and save any required (future) changes/revisions. The user needs to assign a starting date of simulation, hydro-climate data, fixed parameters, initial and input concentrations of constituents of interest for the project. “Save as” option gives the user the flexibility to move their project to another location, including other computers, without affecting their original project, and without its input files being lost. Note that the GUI has an option of opening an existing project. All these, along with the interactive and user-friendly windows for various inputs under “Input Files” header of the GUI, meet the objective of the smooth moving, copying and archiving the projects within and between computers. A project consists of *i*) a project file which controls the state of the UI and its functions and *ii*) the project directory where the project input/output files are stored. Main *WetQual* GUI components are 1) input files, 2) model parameters, 3) running and visualizing the results, 4) post-processing and sensitivity analyses which are explained in the following sections. Figure 5.3 shows the main headers and menus embedded in *WetQual* GUI.

**2.3. Input files**

*WetQual* GUI requires several level of inputs from the user. Assigning a start date for the project is the first step. *WetQual* needs the day number within a year (Julian days) for the equation governing rooted/benthic plant growth/death. Hence, having a starting day of simulation helps keep track of the Julian days for the plant-related calculations in the model. The

"Hydro-Climate Parameters" menu is either to upload "Pre-existing Data" or to run "Flow Routing" module to simulate the hydrologic data (i.e., times series of outflow, wetland water depth, area, and volume). Hydro-climate data includes 10 parameters which are inflow rate ($Q_{in,}$ $m^3$/day), outflow rates ($Q_{out,}$ $m^3$/day), volume of wetland ($V_{w,}$ $m^3$), wetland surface area ($A$, $m^2$), Evapotranspiration rate ($ET$, cm/day), precipitation rate ($ip$, cm/day), reference depth of water ($H$, m), groundwater discharge ($Q_{g,}$ $m^3$/day; negative for infiltration/recharge), wind speed ($U_{w,}$ m/s) and daily water temperature ($T_{water}$, °C), respectively. More details about the definitions, symbols, and units are given in Table 5.3. The user has the option to select between pre-defined (measured/calculated) hydrologic data and "Flow Routing" module. The "Flow Routing" module works as an individual routing module that can be used in case the users do not have the pre-defined/measured hydrologic inputs for the wetland which is mostly the case. The continuity equation is solved using the third-order scheme of Runge-Kutta method in the "Flow Routing" module of the *WetQual* GUI. Overall water budget for a wetland is defined as:

$$\phi_w \frac{dV}{dt} = Q_i \pm Q_g - AE_T + Ai_P \pm Q_T - Q_o \qquad (1)$$

where, $V$ is the water volume of wetland surface water ($L^3$); $A$ is the wetland surface area ($L^2$); $Q_i$ is the volumetric inflow rate (including flooding streams) ($L^3T^{-1}$), $Q_g$ is groundwater discharge or recharge ($L^3T^{-1}$), $Q_o$ is wetland discharge (outflow) rate ($L^3T^{-1}$), $i_p$ is precipitation rate ($LT^{-1}$), $E_T$ is evapotranspiration rate ($LT^{-1}$), $Q_T$ is tidal inflow or outflow and $\phi_w$ is effective porosity of wetland surface water (since biomass occupies a part of the submerged wetland volume). The terms in the equation vary in importance depending on the type of wetland. Furthermore, not all the terms in the above hydrologic budget equation apply to all wetlands.

The third-order scheme of Runge-Kutta involves breaking each time interval into three increments and calculating successive values of water surface elevation and wetland discharge for each increment. The continuity equation can also be described as:

$$\phi_w \frac{dV}{dt} = I(t) - Q(H) \tag{2}$$

where

$$I(t) = Q_i(t) \pm Q_g(t) - AE_T(t) + Ai_P(t) \pm Q_T(t) \tag{3}$$

where $V$ is the volume of water in storage in the wetland; $I(t)$ is the inflow into the wetland as a function of time; $Q(H)$ is the outflow from the wetland, which is determined by elevation i.e., wetland water level ($H$). The change in volume, $dV$, due to the change in elevation, $dH$, can be expressed as (Chow et al. 1988):

$$dV = A(H)dH \tag{4}$$

where $A(H)$ is the water surface area at elevation $H$. The continuity equation is then rewritten as:

$$\frac{dH}{dt} = \frac{I(t) - Q(H)}{\phi_w A(H)} \tag{5}$$

For third-order scheme, the slope, $\frac{dH}{dt}$, approximated by $\frac{\Delta H}{\Delta t}$ is first evaluated at $(H_j, t_j)$, then at $(H_j + \frac{\Delta H_1}{3}, t_j + \frac{\Delta t}{3})$, and finally at $(H_j + \frac{2\Delta H_2}{3}, t_j + \frac{2\Delta t}{3})$. In equations, $\Delta H_1$, $\Delta H_2$, and $\Delta H_3$ are defined for the $j$-th interval as:

$$\Delta H_1 = \frac{I(t_j) - Q(H_j)}{\phi_w A(H_j)} \Delta t \tag{6}$$

$$\Delta H_2 = \frac{I\left(t_j + \frac{\Delta t}{3}\right) - Q(H_j + \frac{\Delta H_1}{3})}{\phi_w A(H_j + \frac{\Delta H_1}{3})} \Delta t \tag{7}$$

$$\Delta H_3 = \frac{I\left(t_j + \frac{2\Delta t}{3}\right) - Q(H_j + \frac{2\Delta H_2}{3})}{\phi_w A(H_j + \frac{2\Delta H_2}{3})}\Delta t \quad (8)$$

The value of $H_{j+1}$ is given by:

$$H_{j+1} = H_j + \Delta H \quad (9)$$

where

$$\Delta H = \frac{\Delta H_1}{4} + \frac{3\Delta H_3}{4} \quad (10)$$

This module reads in the incoming time series (i.e., inflow, evapotranspiration (ET), precipitation and groundwater inflow/outflow which constituete the $I(t)$), geometry table (i.e., depth-area-volume-outflow relationship; *h-A-V-Q*), and temperature (for ET calculations through "ET" module if necessary) to calculate the times series of outflow, reference depth of water in wetland, wetland surface area and volume of wetland surface water. Not that users have an option for ET calculations based on Hamon method (Hamon 1961). In case the inflow to wetland is not measured, running a watershed model such as SWAT is a practical option. Groundwater inflow/outflow can be externally calculated using any of the groundwater flow models such as *MODFLOW*. In case the wetland surface water is hydraulically connected to subsurface water table, gravity drainage may be assumed and seepage from the flooded wetland area can be estimated as $Q_g = K_s A_w$, where $K_s$ is saturated hydraulic conductivity ($LT^{-1}$) and $A_w$ is daily inundated area ($L^2$) (Sharifi et al. 2017). To obtain *h-A-V* relationship, using high-resolution Digital Elevation Model (DEM) generated from Light Detection and Ranging (LIDAR) data is suggested. Spatial Analyst Supplemental Toolbox in ArcGIS version 10.4 can also be utilized to establish *h-A-V* relationship. Wetlands usually do not have an outlet structures to have *h-Q* relationship, especially natural wetlands. By developing *h-A-V* relationship and knowing the volume at which the wetland can hold the maximum amount of water ($V_{max}$), for $V > V_{max}$, the

$Q_{out} = \frac{V - V_{max}}{t}$ can be used to establish the $h$-$Q$ relationship. $V \leq V_{max}$ means no outflow from the wetland.

The "Fixed Parameters" menu is used to assign the time-independent model parameters. It includes parameters like fraction of mineral nitrogen plant uptake in water column, soil aerobic and anaerobic layers, and some other control parameters such as the time step of simulations, number of simulations (for stochastic run), etc. The "Water Quality" menu is used to import "Initial Concentration" of N, P, TSS, and C, and to import and view "Input Concentrations" which is the time series of water quality constituents.

**2.4. Model parameters**

In this step, some of the *WetQual* parameters which are considered to be stochastic (some biogeochemical parameters and reaction rates) are introduced. They are called random parameters because we generate a set of random parameters for a stochastic run of the model. As can be seen from Figure 5.3, the GUI allows *WetQual* to be run either in deterministic or stochastic mode. The selected ranges (Min, Max) and distributions for the listed parameters/coefficients were extracted from literature and expert knowledge (e.g. Schnoor, 1996; Chapra, 1997; Di Toro, 2001; Reddy and Delaune, 2008; Cerco and Cole, 1995, and Ji, 2008). See Hantush et al. (2013), Kalin et al. (2013) and Sharifi et al. (2013) to find details about *WetQual* parameters. For Deterministic mode, the median of the selected range for each model parameter was chosen to serve as the default value. Users can change them.

Regarding the "Stochastic Model", the user needs to choose the distribution type and relevant statistics. The default (probability) distribution types suggested from the literature are uniform, log-normal or triangular. Minimum and maximum range of parameters are required for

uniform distribution. In the case of log-normal distribution, min/max and ($X_{0.1\%}$, $X_{99.9\%}$), where $X_{0.1\%}$ and $X_{99.9\%}$ denote lower and upper percentiles for log-normal distribution, respectively, or mean ($\mu$) and standard deviation are required. For the triangular distribution, the peak location (i.e., the peak of the data) is required in addition to Min and Max values. To have a *WetQual* run with "Stochastic Model", we consider a Monte Carlo simulation. Monte Carlo type of uncertainty analysis is typically used for quantifying the predictive uncertainty of a model (Siade et al., 2015). The GUI generates random parameter sets and performs Monte Carlo Simulations to produce ensemble of outputs. Figure 5.4 represents the MATLAB scripts for random parameter generation as an example of the codes and the related modules that have been developed and utilized inside the GUI. *WetQual* GUI also summarizes the ensemble of model runs through prediction intervals.

**2.5. Running and visualizing the results**

After all the inputs and parameters have been assigned "Run Simulations" menu is used in which the GUI executes and exports the outputs of *WetQual* model. Since the deterministic model performs only one simulation, running it takes only seconds. However, depending on the number of the simulations assigned for the stochastic model, and the processor, it may take from couple of minutes to a couple of hours to complete and run the stochastic model. Note that having a system equipped with a solid state drive (SSD) could reduce the running time up to 4 times less than the regular time required for a particular run.

The current version of the *WetQual* model (i.e., *WetQual* executable by itself and without graphical user interface) does not include a visualization of the model inputs/outputs. To quickly identify any issues (in the simulation process) in need of further investigation, visualization of

the data through time series graphs and tables is required and is time-saving. “Analyze Output Files” provides an opportunity to visualize both deterministic and stochastic model outputs through series of graphs. The user can select the output of interest (out of 29 *WetQual* outputs for N, P, TSS and C, listed in Table 5.4) to view and evaluate the graphical output (i.e., time series graph). A “Time Series Table” represents the simulated values in time series. Furthermore, the user can print the graphs or save them in *.pdf and *.png formats. For the sake of simplicity and GUI performance efficiency, the *WetQual* outputs (in *.txt format) are stored in the same folder as inputs. Since the stochastic model results in an ensemble of outputs, an option was added to allow the user choose among the number of simulations in “Analyze Output Files”. Users can pick any simulation number and visualize their outputs. The graphs are dynamic, and the user can focus on any parts of the graph. Clicking on the graph will show the date and the value of the parameter.

### 2.6. Post Processing

In “Post Processing” window for deterministic model, the user can select the parameters for which the observations are available to evaluate the performance indices of the simulated versus observed values. On the upper right side of the window, the performance indices in terms of Nash-Sutcliffe efficiency ($E_{\mathrm{NS}}$), Mass Balance Error (*MBE*) and normalized root mean square error (*NRMSE*; *RMSE* values divided by the average of observed values) are presented for the selected output of interest. Furthermore, the simulated versus observed values are depicted in blue dashed line and red dots, respectively. Performance indices are given as:

$$E_{NS} = 1 - \left[\frac{\sum_{i=1}^{m}(y_{obs,i} - y_{sim,i})^2}{\sum_{i=1}^{m}(y_{obs,i} - \bar{y}_{obs})^2}\right] \qquad (11)$$

$$MBE\ (\%) = \left[\frac{\sum_{i=1}^{m}(y_{obs,i} - y_{sim,i})}{\sum_{i=1}^{m}(y_{obs,i})}\right] * 100 \quad (12)$$

$$\text{NRMSE} = \frac{\sqrt{\frac{1}{m}\sum_{i=1}^{m}(y_{obs,i} - y_{sim,i})^2}}{\bar{y}_{obs}} \quad (13)$$

where $y_{obs,i}$ and $y_{sim,i}$ denote observed and simulated values at the $i^{\text{th}}$ observation, respectively. $\bar{y}_{obs}$ refers to the average of observed values and *m* represents the number of observations.

"Post Processing" for stochastic model performs GLUE and BMCML analyses. If observed data is available, GUI can carry out GLUE analysis (Beven and Freer 2001) where users can visualize graphs of behavior and non-behavior datasets, the posterior uncertainty band, and model performance metrics. To establish the GLUE procedure, Beven (1989) starts from the premise that, any model/parameter set combination that predicts the variable(s) of interest, must be considered as equally likely as a simulator of the system. Because all model structures must be in error and that all observations and measurements on which model calibration is based on must also be subject to error, we cannot expect that any one set of parameter values will represent a true parameter set to be found through calibration. Rather, it is suggested that it is only possible to make an assessment of the likelihood or probability of a particular parameter set being an acceptable simulator of the system (Beven and Binley, 1992). To that end, the likelihood function applied in this study uses a combination of $E_{\text{NS}}$ and *MBE* (Kalin and Hantush, 2006; Sharifi et al. 2013) such that:

$$L_k = 0.5 * (E_{NS} + \exp\left(\frac{-|MBE|}{100}\right)) \quad (14)$$

However, in the GLUE page, the user can select either Nash-Sutcliffe efficiency ($E_{\text{NS}}$; "Nash" button) or the likelihood function ("likelihood" button). The user can update the results of likelihood calculations by changing the percentage of their behavioral simulations from 1 to

10. The user needs to select the desired value. In the next step, top (1-10)% of simulations with the highest likelihoods (or $E_{NS}$ values) are separated as behavioral ($B$) and the rest are selected as non-behavioral simulations ($B'$). Following this step, a graph for each model output is depicted which includes observed data, upper and lower limit of behavioral simulations, 95% prediction interval (P.I.) of BUB′, and the median for $B$U$B'$ simulations. The graph in the GLUE page also shows the performance indices (i.e., $E_{NS}$, *MBE*, and NRMSE) for the best simulation which is the top simulation with the highest likelihood/$E_{NS}$. In case there is no observation to calculate likelihoods, the user can see the 95% P.I. for the whole simulations as well as the median of the simulations. In the developed GUI for *WetQual* model, we considered both $E_{NS}$ and a likelihood function which combines Mass Balance Error (*MBE*) and $E_{NS}$ (Kalin and Hantush, 2006; Sharifi et al. 2013).

"Post Processing" for the stochastic model in BMCML page conducts a Bayesian Monte Carlo simulation and maximum likelihood estimation analysis. For BMCML calculations in *WetQual* GUI, the methodology developed in Hantush and Chaudhary (2014) and Chaudhary and Hantush (2017) were utilized. Some useful information and the related important equations are provided here. In the context of the BMCML and according to Bayes theorem (Hantush and Chaudhary, 2014):

$$P(\theta_i|O) = kl(\theta_i)P(\theta_i) \qquad (15)$$

where $P(\theta_i|O)$ is the posterior probability mass of parameter set $\theta_i = (\theta_1^i, \theta_2^i, \dots, \theta_r^i)^T$; $r$ = number of model parameters; $i = 1,2,\dots,n,$ where $n$ is the number of randomly sampled parameter sets; $l(\theta_i)$ is the likelihood of observations given $\theta_i$; $P(\theta_i)$ is the prior probability mass of parameter set $\theta_i$; $k$ is a normalizing factor such that $\sum_{i=1}^{n} P(\theta_i|O) = 1$; that is $k =$

$[\sum_{i=1}^{n} l(\theta_i)P(\theta_i)]^{-1}$. We also assume equally likely parameter sets prior to the introduction of measurements, i.e., $P(\theta_i) = {}^{1}/_{n}$ (Chaudhary and Hantush, 2017).

The model error is:

$$\varepsilon_k = \rho\varepsilon_{k-1} + \mu(1-\rho) + \omega_k = O_k - C_k(\theta_i) \tag{16}$$

where $\varepsilon_k$ (i.e., residual error) is the difference between observed ($O_k$) and model simulated ($C_k(\theta_i)$) values, $\mu$ is bias of overall error, $\rho$ is lag-one autocorrelation of the overall error, $\omega_k$ is zero-mean, independent and normally-distributed residual error ($\omega_k \sim N(0, \sigma_\omega^2)$), and $\sigma_\omega^2$ is variance of residual errors (Hantush and Chaudhary 2014). The log-likelihood function is:

$$ln\, l = -\frac{m}{2} ln(2\pi) - m\, ln\, \sigma_\omega - \frac{1}{2}\sum_{k=1}^{m}\left(\frac{\varepsilon_k - \rho\varepsilon_{k-1} - (1-\rho)\mu}{\sigma_\omega}\right)^2 \tag{17}$$

Minimizing ln *l* with respect to $\sigma_\omega$yields

$$\hat{\sigma}_\omega^2 = \frac{1}{m}\sum_{k=1}^{m}[(\varepsilon_k - \hat{\mu}) - \hat{\rho}(\varepsilon_{k-1} - \hat{\mu})]^2 \tag{18}$$

Minimizing ln *l* is identical to minimizing the sum of squares of residual errors of $y_t = ax_t + b + \omega_t$ where $y_t = \varepsilon_t$, $x_t = \varepsilon_{t-1}$, $a = \rho$, and $b = (1-\rho)\mu$ and therefore the least-square estimates are (Ang and Tang, 2007):

$$(1-\hat{\rho})\hat{\mu} = \frac{1}{m}\sum_{k=1}^{m}\varepsilon_k - \frac{\hat{\rho}}{m}\sum_{k=1}^{m}\varepsilon_{k-1} = \bar{\varepsilon_k} - \hat{\rho}\,\overline{\varepsilon_{k-1}} \tag{19}$$

$$\hat{\rho} = \frac{\sum_{k=1}^{m}(\varepsilon_{k-1} - \overline{\varepsilon_{k-1}})(\varepsilon_k - \bar{\varepsilon_k})}{\sum_{k=1}^{m}(\varepsilon_{k-1} - \overline{\varepsilon_{k-1}})^2} \tag{20}$$

in which $\bar{\varepsilon_k} = \frac{1}{m}\sum_{k=1}^{m}\varepsilon_k$, and $\overline{\varepsilon_{k-1}} = \frac{1}{m}\sum_{k=1}^{m}\varepsilon_{k-1}$.

Evaluating (10) for $\hat{\rho}$, then $\hat{\mu}$ from (9), and finally (8) for $\hat{\sigma}_\omega^2$ gives the residual error estimates. Maximum likelihood value are obtained from $\hat{l}\ (\theta_i) = (2\pi e\hat{\sigma}_{\varepsilon i}^2)^{-\frac{m}{2}}$ where $\hat{\sigma}_{\varepsilon i}^2$ is the

variance of model structural error which is calculated by $\sigma_{\varepsilon}^{2} = \frac{\sigma_{w}^{2}}{1-\rho^{2}}$. Users are referred to Hantush and Chaudhary (2014) and Chaudhary and Hantush (2017) for details about the BMCML method.

Note that BMCML method was applied by sequentially conditioning each output of interest on other *WetQual* outputs based on their dependency in the *WetQual* model. For example, posterior probability mass for total ammonia-nitrogen ($N_{aw}$) with implicit dependence on particulate organic nitrogen ($N_{ow}$), $P(\theta_i|Naw, Now)$ is calculated as:

$$P(\theta_i|Naw, Now) = \frac{l_{Naw}(\theta_i) * P(\theta_i|Now)}{\sum_{i=1}^{n}[P(\theta_i|Now) * l_{Naw}(\theta_i)]} \quad (1)$$

where $P(\theta_i|Now)$ and $l_{Naw}$ refers to posterior probability mass for particulate organic nitrogen ($N_{ow}$) and maximum likelihood value for total ammonia-nitrogen ($N_{aw}$).

The Bayesian estimate of each model output concentration *Y* at any point in time is the conditional mean of *Y* given the observation *O*, $E(Y|O)$, which in discrete form can be approximated (assuming uniformly sampled parameter space) as (Hantush and Chaudhary 2014):

$$E(Y|O) = \sum_{i=1}^{n} E(Y|\theta_i)P(\theta_i|O) = \sum_{i=1}^{n} C(\theta_i)P(\theta_i|O) \quad (22)$$

where $C(\theta_i)$ is model simulated output. The explicit expression for the posterior CDF of the model parameters and the expressions used to construct predictions (i.e., median and confidence limits) for future observed values of *Y* given the observed records, *O*, is (Hantush and Chaudhary 2014):

$$E(Y|O) = \frac{1}{2} + \frac{1}{2}\sum_{i=1}^{n} erf\left(\frac{y - C(\theta_i)}{\sqrt{2}\hat{\sigma}_{\varepsilon}}\right)P(\theta_i|O) \quad (23)$$

## 2.7. Sensitivity Analysis

In "Sensitivity Analysis" of the *WetQual* GUI, global sensitivity analysis (GSA) and dotty plots are considered to evaluate the sensitivity of the *WetQual* outputs to various parameters. By using the $B$ and $B'$ datasets, GUI performs Kolmogorov-Smirnov (K-S) test in "Sensitivity Analysis" window, where the most sensitive parameters of the model are ranked based on their order of sensitivity in terms of maximum deviation ($D_{\max}$) between the cumulative distribution function (CDF) for behavioral and non-behavioral datasets. To that end, CDFs of the $B$ and $B'$ are constructed for each *WetQual* parameter. Then, for each parameter, maximum deviation ($D_{\max}$) between the two CDFs are determined (Kalin et al. 2013):

$$D_{max} = max|CDF_B(x) - CDF_{B'}(x)| \quad (24)$$

For a predetermined significance level of $\alpha$, $D_{\max}$ larger than K-S statistic, $D_\alpha$, or $p$-value$<\alpha$ indicates a sensitive parameter. For the sake of saving space, GUI displays the 20 most sensitive parameters by ranking $D_{\max}$ values from largest to smallest. In addition to the K-S test, dotty plots were added to the "Sensitivity Analysis" window. Dotty plots provide information about sensitive parameters and most importantly depict the range in which the model is most sensitive to a given parameter. They also reveal the optimal ranges of the values of each parameter where the model performs best (Kalin et al. 2013).

*WetQual* GUI has a modular structure and provides a unique advantage. The modular structure makes it easy to add/utilize new codes/modules or functions into the GUI either by utilizing executables developed in other programming environments or by using new modules developed directly in C#.Net. For the purpose of developing *WetQual* GUI, random parameter generation, K-S test, and BMCML methods were initially developed in MATLAB environment as prototype codes, and after evaluating their accuracy, they were transferred to the GUI in

C#.Net. The same procedure was carried out for flow routing and ET modules but by developing them in FORTRAN environment.

## 3. Case Study

### 3.1 Study area and the input data

The *WetQual* GUI was demonstrated in a small restored wetland called Barnstable wetland, located in Kent Island, Maryland. Approximately two years of water flow and water quality data from May 9, 1995, through May 12, 1997, discussed thoroughly by Jordan et al. (2003), were available and were used for *WetQual* GUI demonstration purposes. During the two-year sampling period, the study wetland and the watershed draining to it had an area of 1.3ha and 14ha, respectively. The watershed was mainly covered with farmlands (82%), cultivated primarily for corn and soybean production, and the rest (18%) was covered by forest (Sharifi et al. 2016). Figure 5.5 shows the study wetland and the draining watershed. Weekly flow averaged nitrate-N, total ammonia-N, organic N, inorganic P, total suspended sediment (TSS) and total organic carbon (TOC) were available from Jordan et al. (2003). For the purposes of brevity, this demonstration is focused on the visualization and evaluation of the results for nitrogen constituents which include particulate organic nitrogen concentration in free water $N_{ow}$ (mg/L), Total ammonia-nitrogen ([NH4+] + [NH3]) concentration in free water $N_{aw}$ (mg/L), and Nitrate-nitrogen concentration in free water $N_{nw}$ (mg/L). To obtain daily values from weekly average concentrations provided by Jordan et al. (2013), the concentrations were assumed to be constant over the given weekly period.

### 3.2 Project setup and visualization of input/outputs

A new project was created by assigning a folder as the project directory. The starting date of the project was set to be 05/09/1995 according to data sampling period. By preparing the input data as earlier explained, the GUI reads in the input data and model parameters' information under "Input Files" and "Model Parameters" windows; it gives the users the ability to visualize and modify input data and model parameters efficiently. Figure 5.6 shows an example of visualization tools employed in the GUI. To provide users with some examples, Figure 5.6 (a) displays "Hydro-climate" data table, and graph for volumetric inflow rate ($Q_{in}$; $m^3$/day); Figure 5.6 (b) shows graph for reference depth of water in the wetland (H, m), and Figure 5.6 (c) depicts "Input concentration" data table and the graph of organic nitrogen concentration in incoming flow ($N_{owi}$; mg/L)

## 4. Results

### 4.1 Deterministic model

For demonstration purposes, the default values (i.e., the median of the selected range for each model parameter) of "Model Parameters" for "Deterministic Model" were considered without any changes. The results of post-processing analysis for the calculated $N_{ow}$ (mg/L), $N_{aw}$ and $N_{nw}$ from the deterministic model are illustrated in Figure 5.7. $E_{NS}$, *MBE*, and *NRMSE* values were computed to be -0.20, -5.46%, and 0.48, respectively, for particulate organic nitrogen concentration in free water. Those three performance indices were 0.24 and 0.69, 12.43% and 31.11%, and 0.98 and 1.0, respectively, for $N_{aw}$ and $N_{nw}$ which also depicted in Figure 5.7. *WetQual* has predicted total ammonia and nitrate concentrations (in free water) with higher accuracies compared to particulate organic nitrogen concentration, based on the assigned default

values for model parameters (i.e., median of the selected range for *WetQual* model parameters) in the deterministic model. Users can manually change those values to calibrate the model.

### 4.2 Stochastic model

To demonstrate the performance of *WetQual* GUI for the stochastic model, 50,000 simulations were performed with randomly generated model parameters. The results of post-processing analysis by the GLUE method, for $N_{ow}$, $N_{aw}$, and $N_{nw}$ are displayed in Figure 5.8 (a). The model appears to be doing a satisfactory job in predicting ammonia, and nitrate concentrations while the result was not good for particulate organic nitrogen. $E_{\mathrm{NS}}$, *MBE (%)* and *NRMSE* values of the best model simulation for ammonia and nitrate were equal to 0.52, 10.9, 0.78 and 0.74, 35.9, 0.92, respectively. Those values for particulate organic nitrogen (i.e., $N_{ow}$) were equal to -0.13, -0.91 and 0.47 showing a poor simulation. However, regarding *NRMSE* values, the model in predicting particulate organic nitrogen outperformed both ammonia and nitrate predictions. The wide uncertainty band coincides with the prolonged dry period in the first year. Figure 5.8 (b) illustrates the 95% confidence limits and BMCML estimates by using the BMCML method. $E_{\mathrm{NS}}$, *MBE* (%) and *NRMSE* between observed values of particulate organic nitrogen and BMCML estimates were equal to -0.81, -39.82 and 0.60, respectively. Model predictions of ammonia and nitrate concentrations showed better performances regarding $E_{\mathrm{NS}}$ values with those values reaching to 0.50 and 0.70, respectively. However, *NRMSE* values were higher for ammonia (=0.80) and nitrate (=1.17).

Figure 5.9 shows the sensitivity analysis results regarding $D_{\max}$ versus *p*-values and dotty plots for particulate organic nitrogen concentration. According to $D_{\max}$ values, effective resuspension rate ($v_r$; which is named “a_vr_o” in the GUI) and effective settling velocity

(cm/day) ($v_s$; which is named “vels_o” in the GUI) appear to be the most sensitive parameters for $N_{ow}$. This result is in good agreement with the findings by Kalin et al. (2013). Regarding dotty plots, $E_{NS}$ values are on vertical axes, and the model parameters are shown on horizontal axes. For instance, although it may not be very clear, the optimal range for $v_s$ seems to be in the [1, 5] (cm/day) range for particulate organic nitrogen.

*WetQual* GUI runs only under Windows operating systems at this time. A user manual, which is a step by step guideline to apply the *WetQual* model, was also prepared and is published with the *WetQual* GUI executable (install package). Note that the user manual includes explanations and definitions for various types of inputs (i.e., hydro-climate, input concentrations, etc.) required for a successful run, parameters and outputs of *WetQual* model. It also gives the user the necessary knowledge and background regarding post-processing and sensitivity analyses.

## 5. Conclusions

*WetQual* GUI, a user-friendly graphical user interface for the *WetQual* model, was developed in C#.Net environment inside Visual Studio 2015 to provide users with both water quality as well as hydrology analyses. The ponded version of *WetQual* did not include the hydrology component, and a necessary flow routing tool was added in this study. *WetQual* GUI provides both tabular representations and graphical visualization of *WetQual* inputs/outputs and generates random parameter sets which are needed for a successful application of a process-based wetland water quality model like *WetQual*. Visualization of the *WetQual* outputs is invaluable for interpretation of the large number/size of *WetQual* outputs. GUI simplifies the

input/output transfer. It performs post processing and sensitivity analysis of the model. Post processing option was equipped with two powerful uncertainty analyses of GLUE and BMCML. The GUI was successfully setup and applied to a small restored wetland located in Kent Island, Maryland. The model evaluation indicated a satisfactory performance of the *WetQual* in predicting various nitrogen constituents. Inputs/Outputs visualization, post-processing by conducting GLUE and BMCML analyses and sensitivity analysis helped us have a better understanding of the internal processes in the study wetland. *WetQual* GUI, therefore, is an invaluable tool in working with and applying *WetQual* model. *WetQual* GUI is a very informative source to be utilized as a training tool for hydrology and water quality modeling in wetlands. This GUI is a unique source of essential analyses (including uncertainty and sensitivity analyses) needed for a comprehensive water quality modeling in wetland studies that can be utilized for flooded wetlands in research-based and real-world projects. The GUI has the added advantage of conducting Bayesian probabilistic analysis for model predictive uncertainty estimation and risk assessment. Wetlands scientists and managers, eco-hydrologists and decision makers in water quality field can benefit from this GUI. *WetQual* GUI will be soon available to the public and can be easily applied to hydrology and water quality studies in flooded wetlands and the related projects.

Table 5.1: Some examples of hydrology and water quality models written originally in FORTRAN equipped with GUIs

| Model | Original Programming Environment | Language of GUI | Remarks | Citations |
|---|---|---|---|---|
| SWMM | FORTRAN | C/C++ | SWMM 5 | Shamsi (2005) |
| HSPF | FORTRAN | C/C++ | WinHSPF | Duda et al. (2001) |
| SWAT | FORTRAN | Visual Basic (VB) | GIS interface for the SWAT model; ArcSWAT | Olivera et al. (2004) |
| SWAT | FORTRAN | Python | Open source GIS (QGIS) UI for the SWAT model; QSWAT | Dile et al. (2016) |
| MIKE SHE | FORTRAN | C++ | ----- | Christensen (2004) |
| HEC Software | FORTRAN | C/C++ | HEC-1 ➡ HEC-HMS<br>HEC-2 ➡ HEC-RAS | Charley et al. (1995) |
| KINEROS2 | FORTRAN | Microsoft .NET framework within Visual Studio 2003 | Automated Geospatial Watershed Assessment (AGWA 2.x), an ArcView GIS extension | Goodrich et al. (2006); Burns et al. (2007) |

Table 5.2: Nitrogen (N), phosphorus (P), total suspended sediment (TSS) parameters as examples of *WetQual* model parameters

| Symbol in publications | Symbols in the model files | Definition, Units |
|---|---|---|
| $l_2$ | L2 | Thickness of anaerobic soil layer (cm) |
| θ | theta | Temperature coefficient in Arhenious equation |
| Is | Is | Optimal light level (ly/day), range from about 100 to 400 ly/d (Chapra, 1997, p 611) |
| $f_N$ | fNup | Fraction of total ammonia nitrogen in ionized form |
| $k_d$ | Kd | Ammonium ion distribution coefficient (mL/g) |
| $k_{ga}$ | kga0 | Growth rate of free-floating plant (1/day) |
| $k_{gb}$ | kgb0 | Growth rate of benthic and rooted plant (1/day) |
| $k_{mr}$ | kmin1s | First-order rapid mineralization rate in wetland soil (1/day) |
| $k_{nw}$ | knw | First-order nitrification rate in wetland free water (1/day) |
| $k_{mw}$ | kminw | First-order mineralization rate in wetland free water (1/day) |
| $k_{ns}$ | kns | First-order nitrification rate in aerobic soil layer (1/day) |
| $k_{dn}$ | kden | Denitrification rate in anaerobic soil layer (1/day) |
| ρ*s* | rows | Wetland soil particle density |
| $v_{so}$ | vels_o | Effective settling velocity (cm/day) for organic material |
| $v_{ss}$ | vels_s | Effective settling velocity (cm/day) for sediment |
| $v_b$ | velb | Effective burial velocity (cm/day) |
| $a_{na}$ | ana | Gram of nitrogen per gram of chlorophyll-a in plant/algae (gN/gChl) |
| *rc,chl* | rChl | Ratio of carbon mass to chlorophyll a mass in algae (gC/gChl) |
| *Ss* | Ss | Oxygen removal rate per unit volume of aerobic layer by other processes (g/L/day) |
| $S_w$ | Sw | Volumetric oxygen consumption rate in water by other processes (gr/cm$^3$/day) |
| α | c_uw | Empirical parameter used for calculating volatilization mass transfer velocity ($k_v$) |
| *fr* | frap | Fraction of rapidly mineralizing particulate organic matter |
| c1 | c1 | Used for calculating pK (Keq, equilibrium coefficient) |
| c2 | c2 | Used for calculating pK (Keq, equilibrium coefficient) |
| *pH* | PH | pH |
| S | S | Rate of nitrogen fixation by microorganisms (mg-N/m$^3$/hr) |
| Kw | Kw | Phosphorus sorption coefficient in water (cm$^3$/g) |
| $a_{pa}$ | apa | Ratio of phosphorus to Chlorophyll-a in algae (grP/grChl) |
| Dpw | Dpw | Inorganic phosphorus free-water diffusion coefficient (cm$^2$/day) |
| Ksa | Ksa | Accounts for partitioning to phosphorus sorption site (cm$^3$/g) |
| Ksb | Ksb | Accounts for association with iron hydroxide precipitate (cm3/g) |
| Ran1 | Ran1 | Random number used for calculating soil porosity (φ) and free-water oxygen diffusion coefficient |
| *fw* | fW | Fraction of nitrogen fixation in water |
| $f_{act}$ | fact | Vertical diffusion magnification factor |
| $C_{ro}$ | alfa_velr_o | Coefficient for resuspension/recycling of organic material |
| $C_{rs}$ | alfa_velr_s | Coefficient for resuspension/recycling of sediment |
| φ*w* | porw | Effective porosity of wetland surface water |

Table 5.3: Hydro-Climate Inputs of *WetQual*

| Symbol | Definition, Units |
|---|---|
| $Q_{in}$ | Volumetric inflow rate ($m^3$/day) |
| $Q_{\text{out}}$ | Wetland discharge (outflow) rate ($m^3$/day) |
| $V_w$ | Water volume of wetland surface water ($m^3$) |
| $A$ | Wetland surface area ($m^2$) |
| $E_T$ | Evapotranspiration rate (cm/day) |
| $i_p$ | Precipitation rate (cm/day) |
| $H$ | Reference depth of water in wetland (m) |
| $Q_g$ | Groundwater discharge (negative for infiltration) ($m^3$/day) |
| $U_{\text{w}}$ | Wind speed (m/s) |
| $T_{\text{water}}$ | Daily water temperature (°C) (note that the users have an option to calculate $T_{\text{water}}$ if they have daily air temperature ($T_{\text{air}}$) available) |

Table 5.4: Input Concentrations ("13_input_concentrations.txt" file)

| Symbol | Definition, Units |
|---|---|
| *ONin* | Organic nitrogen concentration in incoming flow (mg/L) |
| *NO3in* | Nitrate-nitrogen concentration in incoming flow (mg/L) |
| *NWin* | Total ammonia-nitrogen ([NH4+] + [NH3]) concentration in incoming flow (mg/L) |
| *NO3g* | Nitrate-nitrogen concentration in groundwater discharge (mg/L) |
| *Ng* | Total ammonia-nitrogen concentration in groundwater discharge (mg/L) |
| *Owin* | Oxygen concentration in incoming flow (mg/L) |
| *PO4in* | Phosphate concentration in incoming flow (mg/L) |
| *Pg* | Total phosphorus concentration in groundwater discharge (mg/L) |
| *mwin* | Sediment concentration in incoming flow (mg/L) |
| *NH4air* | Ammonium concentration in precipitation (mg/L) |
| *NO3air* | Nitrate-nitrogen concentrations in precipitation (mg/L) |
| *Qa* | Dry depositional rates of total ammonia nitrogen ($mg/m^2/day$) |
| *Qn* | Dry depositional rates of total nitrate-nitrogen ($mg/m^2/day$) |
| *LPOCin* | Labile particulate organic carbon concentration in incoming flow (mg/L) |
| *RPOCin* | Refractory particulate organic carbon concentration in incoming flow (mg/L) |
| *DOCin* | Dissolved organic carbon concentration in incoming flow (mg/L) |
| *DOCatm* | Atmospheric deposition for total organic carbon ($mg/m^2/day$) |
| *TOCgw* | Total organic carbon concentration in groundwater discharge (mg/L) |

Table 5.5: Definitions for *WetQual* outputs

| Output file Name | Symbol | Definition, Units |
|---|---|---|
| 102_Onw | *Onw* | Particulate organic nitrogen concentration in free water (mg/L) |
| 104_Onsf | *Onsf* | Concentration of organic nitrogen in in aerobic sediment layer (mg/L) |
| 103_Onss | *Onss* | Concentration of organic nitrogen in in anaerobic sediment layer (mg/L) |
| 105_Nw | *Nw* | Total ammonia-nitrogen ([NH4+] + [NH3]) concentration in free water (mg/L) |
| 106_Ns1 | *Ns1* | Total ammonia-nitrogen pore-water concentration in upper aerobic layer (mg/L) |
| 107_Ns2 | *Ns2* | Total ammonia-nitrogen pore-water concentration in lower anaerobic layer (mg/L) |
| 108_NO3w | *NO3w* | Nitrate-nitrogen concentration in free water (mg/L) |
| 109_NO3s1 | *NO3s1* | Nitrate-nitrogen pore-water concentration in upper aerobic layer (mg/L) |
| 110_NO3s2 | *NO3s2* | Nitrate-nitrogen pore-water concentration in lower anaerobic layer (mg/L) |
| 111_Ow | *Ow* | Oxygen concentration in free water (mg/L) |
| 112_a | *a* | Mass of free floating plant (gr chlorophyll a) |
| 113_b | *b* | Mass of rooted plants (gr chlorophyll a) |
| 114_Pw | *Pw* | Total inorganic phosphorus concentration in free water (mg/L) |
| 115_Ps1 | *Ps1* | Total phosphorus concentration in aerobic layer (mg/L) |
| 116_Ps2 | *Ps2* | Total phosphorus concentration in anaerobic layer (mg/L) |
| 118_mw | *mw* | Sediment concentration in free water (mg/L) |
| 150_DOCw | *DOCw* | Concentrations of dissolved organic C in free water (mg/L) |
| 151_LPOCw | *LPOCw* | Concentrations of labile (fast reacting) particulate organic C in free water (mg/L) |
| 152_RPOCw | *RPOCw* | Concentrations of refractory (slow reacting) particulate organic C in free water (mg/L) |
| 153_DOCs1 | *DOCs1* | Pore water concentrations of DOC in aerobic sediment layer (mg/L) |
| 154_LPOCs1 | *LPOCs1* | Pore water concentrations of LPOC in aerobic sediment layer (mg/L) |
| 155_RPOCs1 | *RPOCs1* | Pore water concentrations of RPOC in aerobic sediment layer (mg/L) |
| 156_DOCs2 | *DOCs2* | Pore water concentrations of DOC in lower anaerobic sediment layer (mg/L) |
| 157_LPOCs2 | *LPOCs2* | Pore water concentrations of LPOC in lower anaerobic sediment layer (mg/L) |
| 158_RPOCs2 | *RPOCs2* | Pore water concentrations of RPOC in lower anaerobic sediment layer (mg/L) |
| 159_TOCw | *TOCw* | Concentrations of total organic C in free water (mg/L) |
| 160_CH4w | *CH4w* | Methane concentration in free water (mg/L) |
| 161_CH4s1 | *CH4s1* | Methane concentration in aerobic sediment layer (mg/L) |
| 162_CH4s2 | *CH4s2* | Methane concentration in anaerobic sediment layer (mg/L) |

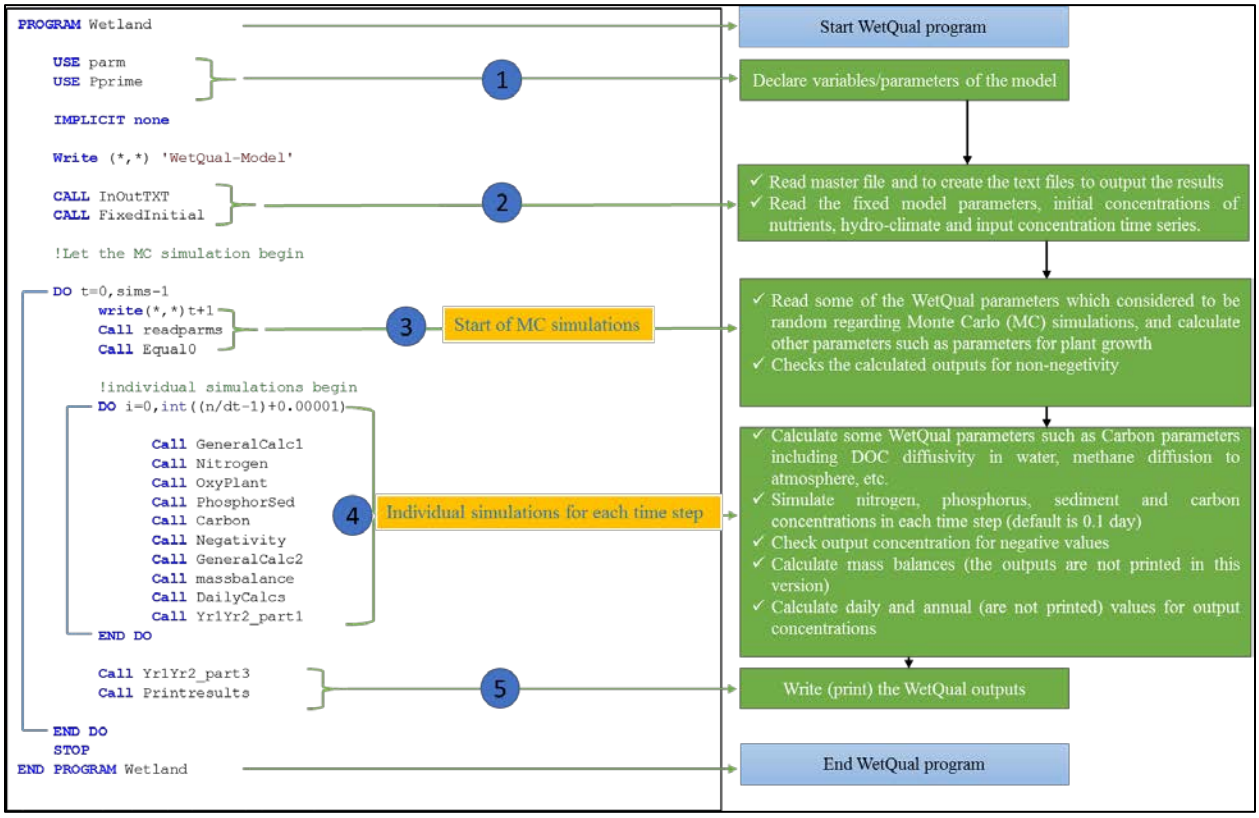


Figure 5.1: A flowchart representing the internal structure and processes of *WetQual*

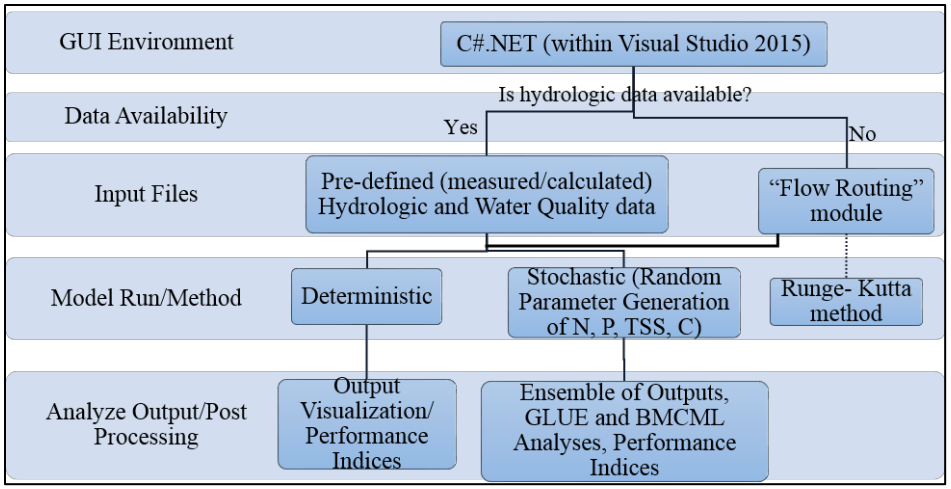


Figure 5.2: Structure, flow of information and basic steps in developing the *WetQual* GUI

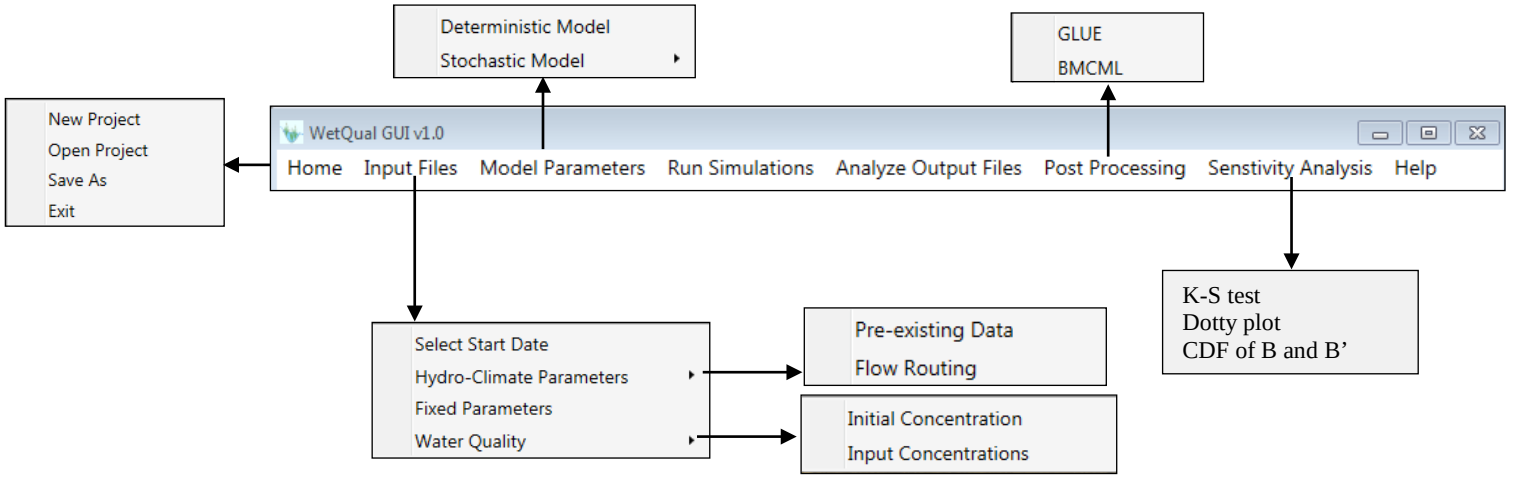


Figure 5.3: Main *WetQual* GUI headers and menus; CDF refers to the cumulative distribution functions for behavioral (*B*) and non-behavioral datasets (*B'*)

```
% Random Parameter Generation (Uniform Distribution, Log Normal Distribution Triangular Distribution)
 [m,n,k] = textread('input_control.txt','m=%f n=%f k=%f %*[^\n]',1,'whitespace','\n')
%m=input('m= Enter a number from 1 to 3 to choose among "Uniform=1", "Log Normal=2", "Triangular=3"
%Distributions:'), %n=input('n= The number of random variables:')
switch m
   case 1  %Random data generation based on "Uniform Distribution"
%        Xl=input('Min of the parameter range for Uniform Distribution:')
%        Xu=input('Max of the parameter range for Uniform Distribution:')
      [Xl,Xu] = textread('input_uniform_dist.txt','Xl=%f Xu=%f %*[^\n]',1, ...
                         'whitespace','\n')
      r_uniform= (Xu-Xl).*rand(n,1) + Xl;

   case 2  %Random data generation based on "Log Normal Distribution"
%        Xl=input('Min of the parameter range for Log Normal Distribution:')
%        Xu=input('Max of the parameter range for Log Normal Distribution:')
%        Rl=input('Lower percentile for Log Normal Distribution:')
%        Ru=input('Upper percentile for Log Normal Distribution:')
       switch k % to select between two scenarios of having "mu" and "sigma" or not
          case 1
             [mu,sigma] = textread('input_lognorm_dist_mu.txt','mu=%f sigma=%f %*[^\n]',1, ...
                          'whitespace','\n')
             r_lognorm= logninv(rand(n,1),mu,sigma);  %Lognormal inverse cumulative distribution function

          case 2
             [Xl,Xu,Rl,Ru] = textread('input_lognorm_dist.txt','Xl=%f Xu=%f Rl=%f Ru=%f %*[^\n]',1, ...
                          'whitespace','\n')
             Finv_Rl=norminv(Rl/100,0,1)%Normal inverse cumulative distribution function
             Finv_Ru=norminv(Ru/100,0,1)
             mu=(log(Xu)*Finv_Rl-log(Xl)*Finv_Ru)/(Finv_Rl-Finv_Ru)% Mean calculation
             sigma=log(Xu/Xl)/(Finv_Ru-Finv_Rl)% StD calculation
             r_lognorm= logninv(rand(n,1),mu,sigma);  %Lognormal inverse cumulative distribution function
       end;
   case 3 %Random data generation based on "Triangular Distribution"
%        a=input('input "a" as lower limit:');%lower limit
%        c=input('input "c" as Peak Location:');%Peak Location
%        b=input('input "b" as Upper limit:');%Upper limit
      [a,c,b] = textread('input_triangular_dist.txt','a=%f c=%f b=%f %*[^\n]',1, ...
                         'whitespace','\n')
      U=rand(n,1);
      Fc=(c-a)/(b-a);
      for i=1:length(U)
         if U(i,1)<Fc
           r_triangular(i,1)=a+sqrt(U(i,1)*(b-a)*(c-a));
         else
           r_triangular(i,1)=b-sqrt((1-U(i,1))*(b-a)*(b-c));
         end;
      end;
end;
```

Figure 5.4: An example of source codes developed for various functionalities of the GUI: MATLAB code for Random Parameter generation which was transferred to C#.Net inside Visual Studio 2015

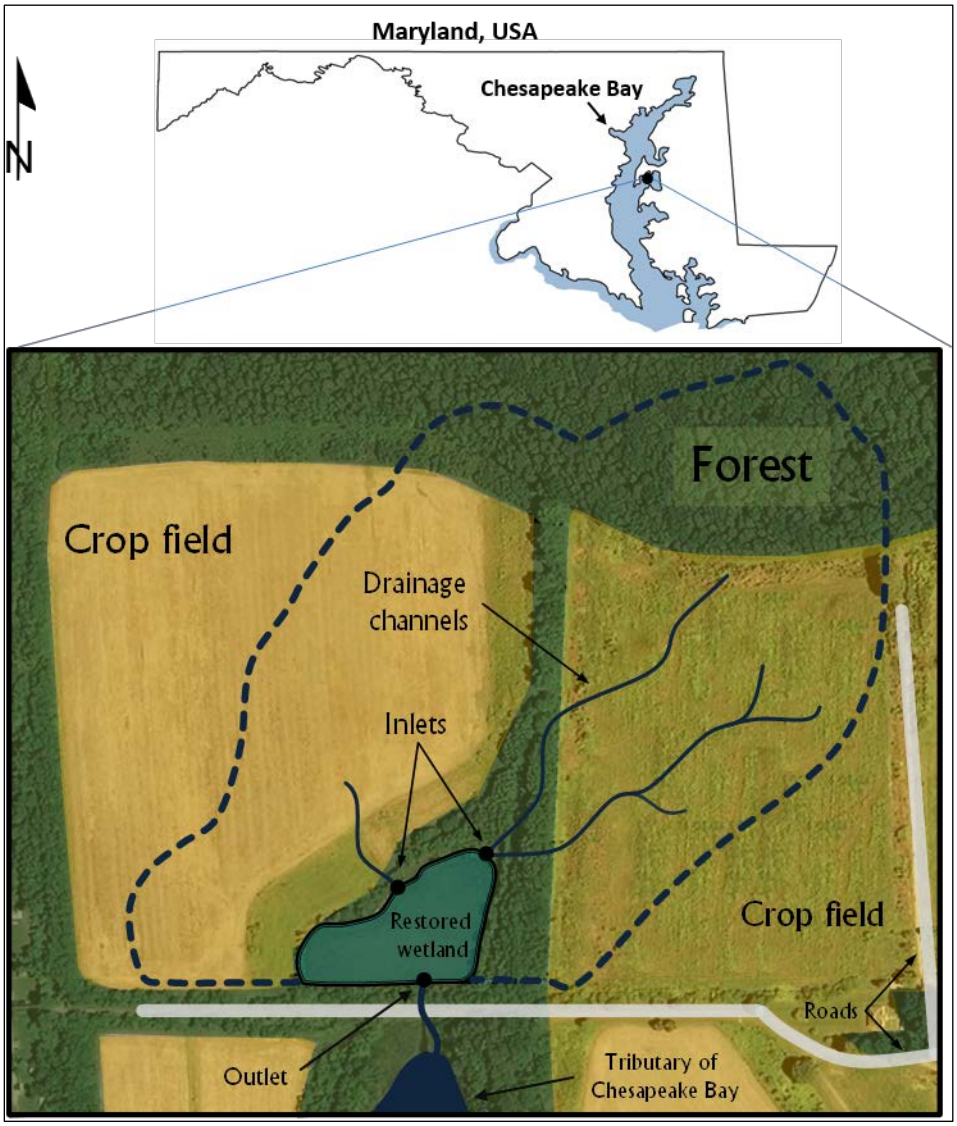


Figure 5.5: Study wetland and its watershed outlined by dashed line (reprinted from Sharifi et al. 2013, with permission from Elsevier and Copyright Clearance Center)

(a)

(b)

(c)

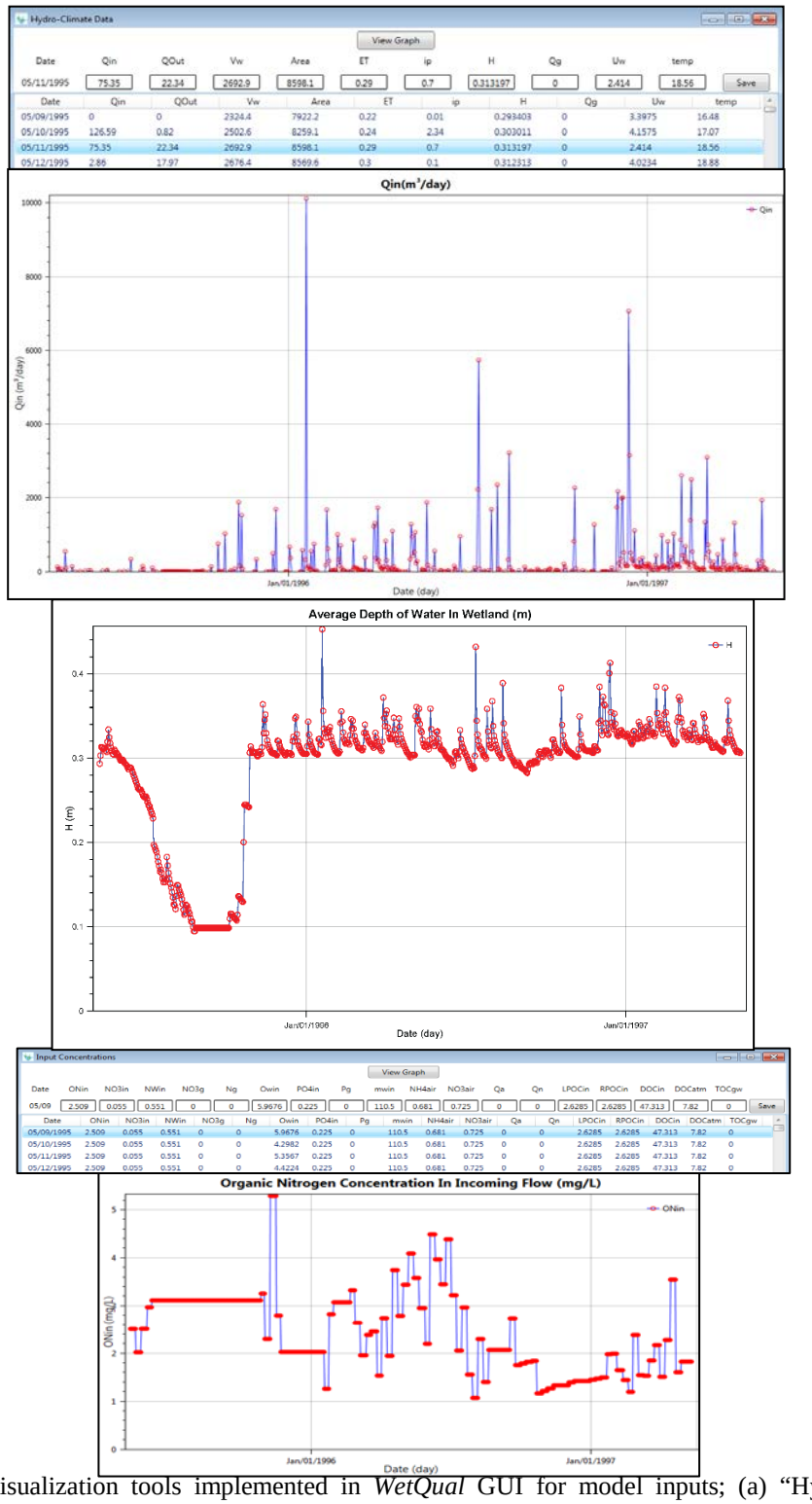


Figure 5.6: An example of visualization tools implemented in *WetQual* GUI for model inputs; (a) "Hydro-climate" data table and the graph for volumetric inflow rate ($Q_{in}$); (b) reference depth of water in the wetland, again from "Hydro-climate" data. (c) "Input concentration" data table and the graph of organic nitrogen concentration in incoming flow $N_{owi}$ (mg/L)

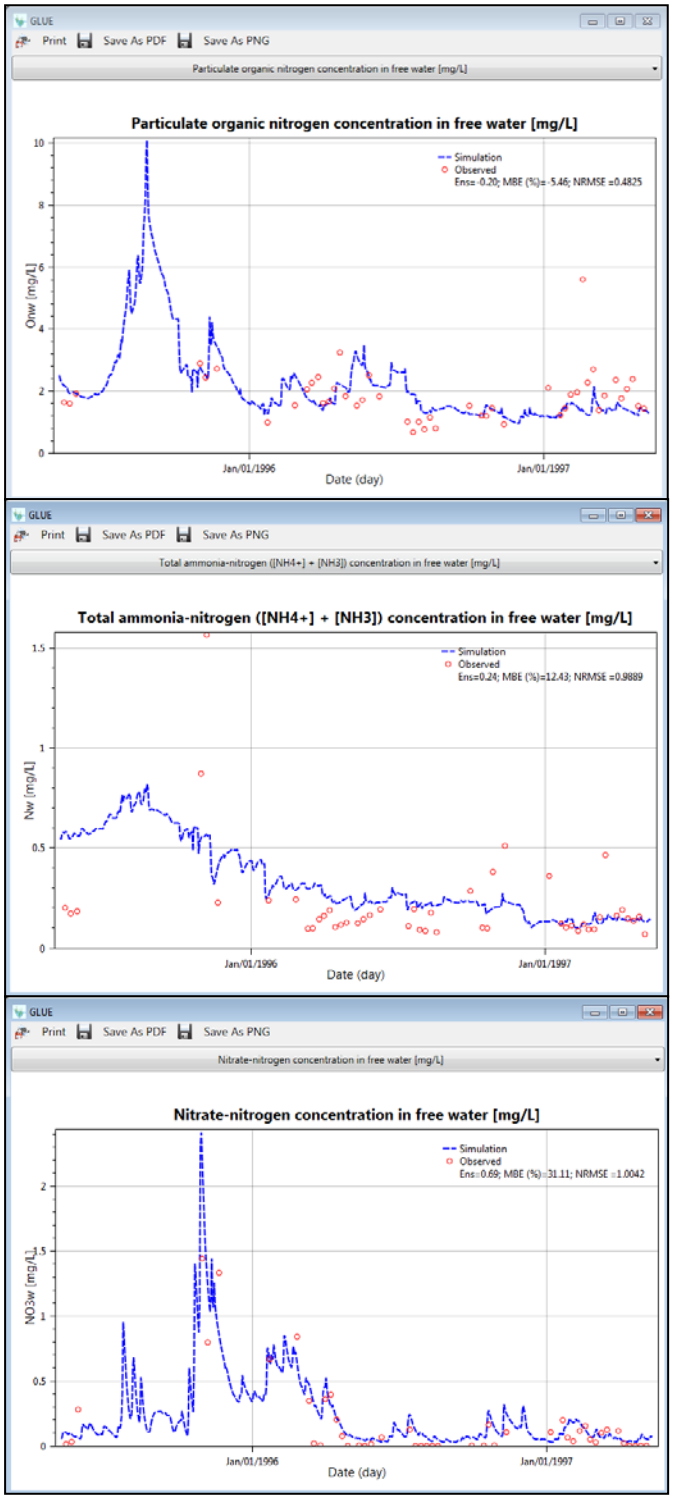


Figure 5.7: An example of visualization and post processing for deterministic model; the blue line and red circles represent simulated values and observations, respectively.

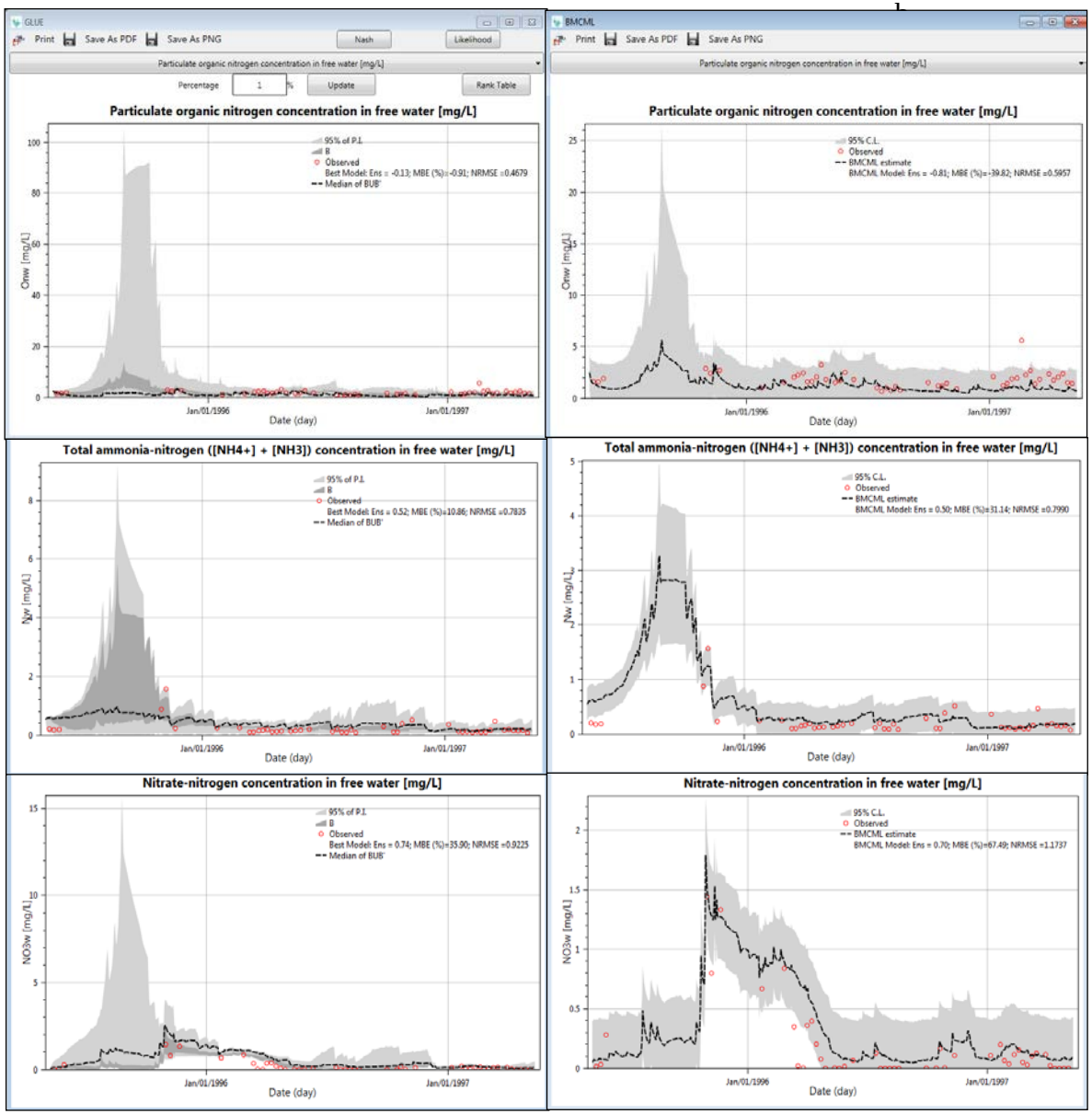


Figure 5.8: (a) Model generated 95% prediction interval (P.I.) from 50,000 MC simulations versus field observations. The results displayed respectively for $N_{ow}$, $N_{aw}$, and $N_{nw}$, from top to bottom. $B$ exhibits behavioral datasets whereas $B'$ represents non-behavioral datasets. Dashed line presents the median values for $BUB'$; (b) BMCML estimates and 95% confidence limits (C.L.) of $N_{ow}$, $N_{aw}$, and $N_{nw}$, from top to bottom.

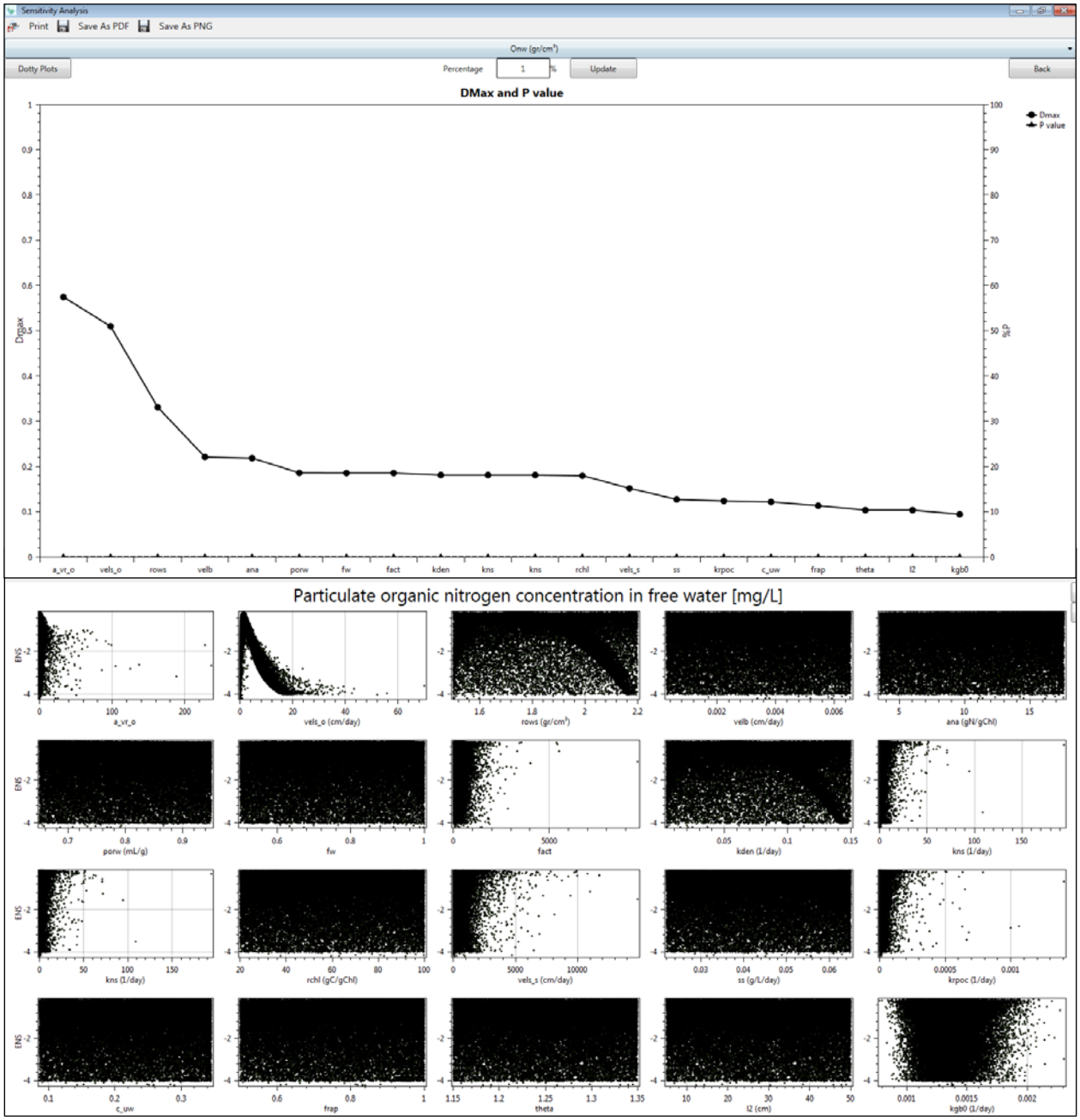


Figure 5.9: $D_{max}$ versus *p*-value (top figure) and dotty plots (bottom figure) for the 20 most sensitive parameters for predicting particulate organic nitrogen.

# Chapter 6 : Conclusions

Wetlands provide many important ecosystem services including water quality improvement through filtering, water storage and providing habitat. Changing and variable climate can impact wetland hydrologic processes and consequently have considerable implications for wetland soil biogeochemistry and nutrient cycles. In wetlands going through wetting/drying cycles, simulation of nutrient processes and biogeochemical reactions in both ponded and unsaturated wetland zones are needed for an improved understanding of wetland functioning for water quality improvement. In this study, we aimed to advance the current wetland hydrology knowledge by developing various models. We started with developing data-driven models and eventually expanded it to a physically-based modeling approach to predict various wetland hydrologic components. Sharifi et al. (2017) extended the ponded version of *WetQual* model (Hantush et al. 2013, Kalin et al. 2013, Sharifi et al. 2013) by adding a soil moisture accounting module, which solves Richards' Equation (RE), and improved biogeochemical relationships for N and C cycles in vadose zone of wetlands. The physically-based model of this dissertation was developed to make Sharifi et al. (2017) version of *WetQual* more practical and computationally efficient. Eventually, a flow routing module and a graphical user interface were added to ponded version of *WetQual*. In the first chapter, four primary objectives were presented. Each objective is summarized below, and following that, the most significant findings are listed.

***Objective 1: Develop ANN-based models to predict hourly water levels (WLs) in wetlands characterized by water tables at or near the surface that respond rapidly to rainfall events***

Two artificial neural network (ANN)-based methodologies were developed for wetlands whose WLs show (i) high correlation, and (ii) low to no correlation with WLs from nearby sites. A correlation analysis was employed to find the associations between/among the target wetland site and nearby site(s). In the case of having high correlation between WLs of target and nearby sites, Continuous Simulation Model (CSM), which used WL data from nearby sites and hourly precipitation data as input, is advised. When there is no or very low correlation, Event-based Model (EBM) is recommended which require partitioning of the WL hydrographs into high- and low-frequency components.

The two models were tested at two wetland sites named Site 17 and Site 32. Both sites are located in the southern portion of Baldwin County, Alabama. The following conclusion were drawn:

1. The use of WL data from nearby sites highly correlated with those from the target site can help prediction of hourly WL fluctuations with very high accuracy using the CSM.
2. Although Spearman's rank can be employed to find the sites with high level of correlation, those results cannot be considered as the ultimate input combinations. For example, adding hourly precipitation data having low correlation with WLs considerably improved the accuracy of the CSM.
3. In cases with low to no correlation between WL data from the target site and those from nearby sites, application of recursive digital filter can be an efficient method for splitting continuous hydrographs into high- and low-frequency (quick and delayed response) components and finding the optimal recession constant.

4. Bartlett's test and t-test are prominent tools for finding the optimal training and testing datasets in developing event-based ANN models.
5. EBMs showed the ability to accurately predict WLs up to six hours lead time during rain events at the study wetlands. The 6-hour lead time likely depends on the characteristics of wetlands.

***Objective 2: Develop a coupled SWAT-ANN model to predict WLs in headwater wetlands***

The idea behind the coupled hybrid model was to capture the hydrologic inputs from the contributing watershed to the study wetland. This model requires neither WL data from nearby wetlands nor antecedent WL data from the target wetland itself as input, which makes it practical for long term predictions.

The coupled SWAT-ANN model was applied to Site 17. The utility of the developed model was demonstrated with two applications, one of which assessed the potential impacts of future climate change on WLs, and the other explored the potential teleconnections between El Niño Southern Oscillation (ENSO) and WL fluctuations in the study wetland. The following conclusions were drawn:

1. Coupled SWAT-ANN model could be a viable tool in predicting daily WLs in wetlands. Availability of at least year-long WL data is needed to develop a reliable model.
2. Simulated future WLs by utilizing different global climate model (GCM) ensembles showed both decreasing and increasing trends. The increasing trend was dominant in medium WLs, and the declining trend was dominant in low and high WLs.

3. Winter will get wetter in terms of precipitation with statistically significant positive corellation with Niño index over El Niño phase. Winter WL also shows positive but non-significant correlation. However, WL reduction in spring during El Nino is expected.
4. The expected climate change and variability could have a significant impact on the overall vegetation of the study wetland. Understanding the ramifications of changes in WL on vegetation characteristics is beyond the scope of this dissertation.

***Objective 3: Develop and numerically solve a depth-averaged solution to highly non-linear Richards' (1931) Equation (RE) to predict soil moisture dynamics in wetlands***

Sharifi et al. (2017) extended the ponded version of *WetQual* model to account for N and C cycles in the unsaturated sections of wetlands. The primary purpose of this phase of the study was to make Sharifi et al. (2017) version of *WetQual* more practical and less computationally intensive by introducing the depth-averaged RE (DARE). DARE was verified versus Hydrus-1D (as a benchmark) which solves full RE. This was done in two successive steps: (i) gravity drainage condition, (ii) full-term equations by considering pressure head component. It was found that:

1. Gravity drainage version of DARE performed well compared to Hydrus-1D for all the assigned boundary conditions, climatic scenarios, and soil textures (sandy loam, loam, sandy clay loam, and sand).
2. The full-term version of DARE proved to estimate the soil moisture contents reasonably well in the root zone for three soil textures (sandy loam, loam, and sandy clay loam) under various boundary and climatic conditions. The accuracy of this model is lower for

the second layer. This model has partially captured soil moisture fluctuations in the loamy soil in the second later.

3. The non-convergence issue that often arises with the full-term RE no longer exists with the utilization of DARE. DARE is computationally efficient compared to Hydrus-1D which solves full RE.

***Objective 4: Add a flow routing module and develop a graphical user interface (GUI) for the ponded version of WetQual***

Earlier versions of *WetQual* required users take care of wetland hydrology independently. Users needed to either have pre-defined or measured hydrologic inputs or run a watershed model with a flow routing analysis outside the *WetQual* model. This GUI eliminated this issue by incorporating the hydrology and water quality under one umbrella. The GUI is also equipped with powerful post processing modules including Generalized Likelihood Uncertainty Estimation (GLUE), Bayesian Monte Carlo simulation and maximum likelihood estimation (BMCML) analyses, and Sensitivity Analysis modules. The utility of the developed GUI for *WetQual* model was demonstrated through a case study in a small restored wetland called Barnstable wetland, located in Kent Island, Maryland. It was found that:

1. The developed GUI has proven to be an efficient tool for tabular and graphical representations of *WetQual* inputs/outputs. This helps the users of *WetQual* model to easily find and fix the potential source of errors in model inputs. The added capability of analyzing model outputs assists in determining any issues (in the simulation process) in need of further investigation.

2. Inputs/Outputs visualization, post processing analyses by conducting GLUE and BMCML, and sensitivity analysis helped us have a better understanding of the internal processes in the study wetland.
3. The developed GUI has the capability of incorporating new modules to *WetQual*.

**1. Future research**

Several points can be further investigated which needs to be addressed in future studies. For the first objective of this study, we developed two ANN-based methods for predicting wetland water levels. There are other machine learning techniques that can be utilized for this purpose. For future research, I suggest conducting a comparison study between ANN and support vector machine (SVM) techniques to determine which model can better capture wetland WL fluctuations.

Regarding the second objective of this study, baseflow and stormflow estimates from the watershed draining to a wetland were considered from an uncalibrated SWAT. Since the ANN parameters (i.e., weights and biases) are conditioned on SWAT simulated inputs, by generating an ensemble of different inputs, we can better determine the robustness of the developed model for use in future projections. To build upon the findings of this study, I suggest sampling most sensitive SWAT parameters from the uniform distribution and conducting a Monte Carlo simulation so that an ensemble of SWAT outputs which serve as inputs to ANN is built. Due to the lack of a prior distribution of a parameter, uniform distribution was suggested because of its simplicity (Shen et al. 2012). Eventually, by obtaining the ANN outputs, an uncertainty analysis

is needed to obtain 95% prediction interval (regarding GLUE) or confidence limits (by using BMCML).

Concerning the third objective of this study, further analyses are needed to evaluate the full potential and applicability of the DARE. For future research, an evaluation of the developed model for different underlying soil layers is suggested. By performing that, the numerical stability of the model will be further assessed. Application of the developed model to other soil textures particularly to finer soil types such as clay are suggested. Utilization of DARE as a new module to *WetQual* for soil moisture accounting in the unsaturated section of wetlands is needed and should be considered for further development/application of *WetQual* model. By implementing this newly developed unsaturated flow module into *WetQual* as a part of its hydrology component, *WetQual* will also be ready for a broader development. I suggest an integration of the structurally-modified SWAT (i.e., SWAT+) with *WetQual* to represent wetland nutrient removal and cycling better at the watershed scale. Note that a short guideline for coupling SWAT+ with *WetQual* was prepared during working on this dissertation. It summarizes the main steps required for this coupling effort.

The GUI developed in this study for the *WetQual* model has the added hydrology component to the original *WetQual*. The hydrology component consists of a flow routing module which has a simple evapotranspiration (ET) calculation module based on Hamon method (Hamon, 1961) inside. For future research, adding some other options for ET calculations such as Penman–Monteith FAO 56 (Allen et al., 1998) would be a useful improvement in the ET module. Implementing the newly developed unsaturated flow module to the hydrology

component of *WetQual* GUI is also suggested. This modification will enhance the chance of public willingness to apply *WetQual* to non-flooded wetlands.

## References:


Abdelnour, A., Stieglitz, M., Pan, F., & McKane, R. (2011). Catchment hydrological response to forest harvest amount and spatial pattern. Water Resources Research, 47(9) http://dx.doi.org/10.1029/2010WR010165.

Acreman, M.C., Blake, J.R., Booker, D.J., Harding, R.J., Reynard, N., Mountford, J.O., & Stratford, C. J. (2009). A simple framework for evaluating regional wetland ecohydrological response to climate change with case studies from Great Britain. Ecohydrology, 2, 1–17.

Acreman, M.C., & Miller, F. (2007). Hydrological impact assessment of wetlands. In: Ragone S, Hernández-Mora N, de la Hera A, Bergkamp G, McKay J (eds) The global importance of groundwater in the 21st century: Proceedings of the International Symposium on Groundwater Sustainability. National Groundwater Association Press, Ohio.

AghaKouchak, A., Nakhjiri, N., & Habib, E. (2013). An educational model for ensemble streamflow simulation and uncertainty analysis, Hydrology and Earth System Sciences, 17, 445–452.

Alix, D. M., Anderson, C. J., Grand, J. B., & Guyer, C. (2014). Evaluating the effects of land use on headwater wetland amphibian assemblages in coastal Alabama. Wetlands, 34(5), 917–926.

Allen, R.G., Periera, L.S., Raes, D., & Smith, M. (1998). Crop evapotranspiration: guideline for computing crop water requirement. In: FAO Irrigation and Drainage Paper No. 56,. FAO, Rome, Italy.

Amari, S.-I., Murata, N., Muller, K.-R., Finke, M., & Yang, H.H. (1997). Asymptotic statistical theory of overtraining and cross-validation. IEEE Transactions on Neural Networks, 8(5), 985–996.

Amatya, D.M. (1993). Hydrologic Modeling of Drained Forested Lands (Unpublished Ph.D. dissertation). North Carolina State University, Raleigh, NC.

Amatya, D.M., Skaggs, R.W., & Gregory, J.D. (1997). Evaluation of a watershed scale forest hydrologic model. Agricultural Water Management, 32, 239–258.

Ang, A.H.-S., & Tang, W.H. (2007). In: Probability Concepts in Engineering, second ed. John Willey & Sons, INC, p. 406.

Arega, F. (2013). Hydrodynamic modeling and characterizing of Lagrangian flows in the West Scott Creek wetlands system, South Carolina. Journal of Hydro-environment Research, 7, 50–60.

Arnold, J. G., Srinivasan, R., Muttiah, R. S., & Williams, J. R. (1998). Large area hydrologic modeling and assessment: part I. Model development. Journal of American Water Resource Association, 34 (1), 73–89.

Barksdale, W. F. (2013). The effect of land use/land cover on headwater-slope wetlands in Baldwin County, Alabama. M. S. Thesis, Auburn University, Auburn, AL.

Barksdale, W. F., & Anderson, C. J. (2014). The influence of land use on forest structure, species composition, and soil conditions in headwater-slope wetlands of coastal Alabama, USA. International Journal of Biodiversity Science, Ecosystem Services & Management, 11(1), 61–70

Barksdale, W. F., Anderson, C. J., & Kalin, L. (2014). The influence of watershed run-off on the hydrology, forest floor litter and soil carbon of headwater wetlands. Ecohydrology, 7(2), 803–814.

Beven K. J., & Binley A. (2014). GLUE: 20 years on, Hydrological Processes, 28, 5897–5918.

Beven, K. J. (2006). A manifesto for the equifinality thesis, Journal of Hydrology, 320(1–2), 18 – 36.

Beven, K. J. (1989). Interflow, in Morel-Seytoux, H. J. (Ed.), Unsaturated Flow in Hydrological Modeling, D Reidel, Dordrecht.

Beven, K. J., & Binley, A.M. (1992). The future of distributed models: model calibration and uncertainty prediction. Hydrological Processes, 6, 279–298.

Beven, K. J., & Freer, J. (2001). Equifinality, data assimilation, and uncertainty estimation in mechanistic modelling of complex environmental systems using the GLUE methodology. Journal of Hydrology, 249(1–4), 11–29.

Beven, K. J., & Kirkby, M. (1979). A physically-based, variable contributing area model of basin hydrology. Hydrological Sciences Bulletin, 24, 43–69.

Bolster, C. H., & Saiers, J. E. (2002). Development and evaluation of a mathematical model for surface-water flow within the Shark River Slough of the Florida Everglades. Journal of Hydrology, 259, 221–35.

Bubier, J. L., & Moore, T. R. (1994). An ecological perspective on methane emissions from northern wetlands. Trends in Ecology & Evolution, 9, 460–464.

Bullock, A., & Acreman, M. (2003). The role of wetlands in the hydrological cycle. Hydrology and Earth System Sciences, 7(3), 358–389.

Burnash, R. J. C., Ferral, R. L., & McGuire, R. A. (1973). A generalized streamflow simulation system: conceptual modeling for digital computers." United States Dept. of Commerce, National Weather Service, and State of California, Dept. of Water Resources, Sacramento, Calif.

Burns, I. S., Scott, S. N., Levick, L. R., Semmens, D., Miller, S. N., Hernandez, M., Goodrich, D. C., & KEPNER, W. G. (2007). Automated Geospatial Watershed Assessment (AGWA)

Documentation Version 2.0. U.S. Environmental Protection Agency, Washington, DC, EPA/600/C-07/015 (NTIS PB2008-105118).

Carbone, M., Brunetti, G., & Piro, P. (2015). Modelling the hydraulic behavior of growing media with the explicit finite volume solution. Water, 7, 568–591.

Carsel, R.F., & Parrish, R. S. (1988). Developing joint probability distributions of soil water retention characteristics. Water Resources Research, 24, 755–769.

Chapra, S. C., & Canale, R. P. (2010). Numerical methods for engineers, Sixth Edition, McGraw-Hill Companies, Inc., 960 p.

Charley, W., Pabst, A., & Peters, J. (1995). The Hydrologic Modeling System (HEC-HMS): Design and Development Issues. Proc. Am. Soc. Civil Engrs. 2nd Congress on Computing in Civil Engineering. Atlanta, Georgia.

Chimner, R. A., & Cooper, D. J. (2003). Influence of water table levels on CO 2 emissions in a Colorado subalpine fen: an in situ microcosm study. Soil Biology and Biochemistry, 35(3), 345–351.

Chow, V. T., Maidment, D. R., & Mays, L. W. (1988). Applied hydrology. McGraw-Hill Series in Water Resources & Environmental Engineering. 572 pages.

Christensen, F. D. (2004). Coupling between the river basin management model (MIKE BASIN) and the 3D hydrological model (MIKE SHE) with use of the OpenMI system, in 6th International Conference on Hydroinformatics, Singapore.

Cigizoglu, H. K. (2003). Estimation, forecasting and extrapolation of river flows by artificial neural networks, Hydrological Sciences Journal, 48(3), 349–361.

Clair T.A. (1998). Canadian freshwater wetlands and climate change. Climatic Change, 40(2), 163–165.

Cohen, M. J. et al. (2016). Do geographically isolated wetlands influence landscape functions? Proceedings of the National Academy of the Sciences, 113(8), 1978–1986

Dadaser-Celik, F., Stefan, H. G., & Brezonik, P. L. (2006). Dynamic hydrologic model of the Örtülüakar Marsh in Turkey. Wetlands, 26, 1089–1102.

Dadaser-Celik, F., & Cengiz, E. (2013). A neural network model for simulation of water levels at the Sultan Marshes wetland in Turkey.’ Wetlands Ecology and Management, 21, 297–306.

Dai, T., Ambrose, R.B., Alvi, K., Wool, T., Manguerra, H., Choski, M., Yang, H., & Kraemer, S. (2005). Characterizing spatial and temporal dynamics: development of a grid-based watershed mercury loading model. In: Moglen, Glenn E. (Ed.), Managing Watersheds for Human and Natural Impacts: Engineering, Ecological, and Economic Challenges, Williamsburg, Virginia,

19-22 July 2005, ASCE Conference Proceedings. American Society of Civil Engineers, Reston, Virginia. http://dx.doi.org/10.1061/40763(178)56.

Dall'O, M., Kluge, W., & Bartels, F. (2001). FEUWAnet: a multi-box water level and lateral exchange model for riparian wetlands. Journal of Hydrology, 250, 40–62.

Daulat, W. E., & Clymo, R. S. (1998). Effects of temperature and water table on the efflux of methane from peatland surface cores. Atmospheric Environment, 32(19), 3207–3218.

Davidson, E., Belk, E., & Boone, R.D. (1998). Soil water content and temperature as independent or confounded factors controlling soil respiration in a temperate mixed hardwood forest. Global change biology, 4, 217–227.

Dawson, C. W., & Wilby, R. (1998). An artificial neural network approach to rainfall–runoff modeling. Hydrological Sciences Journal, 43(1), 47–66.

DeLaney, T. A. (1995). Benefits to downstream flood attenuation and water quality as a result of constructed wetlands in agricultural landscapes. Journal of Soil and Water Conservation, 50, 620–628.

DHI. (2007). MIKE SHE user manual. Volume 2: Reference guide.

Dile, Y. T., Daggupati, P., George, C., Srinivasan, R., & Arnold, J. (2016). Introducing a new open source GIS user interface for the SWAT model. Environmental Modelling & Software, 85, 129–138.

Drusch, M., Wood, E. F., & Gao, H. (2005). Observation operators for the direct assimilation of TRMM microwave imager retrieves soil moisture. Geophysical Research Letters, 32, L15403, doi:10.1029/2005GL023623.

Duda, P. B., Hummel, P. R., Donigian Jr., A. S., & Imhoff, J. C. (2012). BASINS/HSPF: Model use, calibration, and validation. Trans. ASABE, 55(4), 1523-1547.

Duda, P. B., Kittle Jr., J. L., Gray, M. H., Hummel, P. R., & Dusenbury, R. A. (2001). WinHSPF - An interactive Windows interface to HSPF: User's manual. Washington, D.C.: U.S. EPA Office of Water.

Ehrenfeld, J. G., Cutway, H. B., Hamilton, I. V. R., & Stander, E. (2003). Hydrologic description of forested wetland in northeastern New Jersey, USA – and urban/suburban region. Wetlands, 23, 685–700.

Ellis, J. T., Spruce, J. P., Swann, R. A., Smoot, J. C., & Hilbert, K.W. (2011). An assessment of coastal land-use and land-cover change from 1974-2008 in the vicinity of Mobile Bay, Alabama. Journal of Coastal Conservation, 15(1), 139–149.

EPA, (2010). Methane and Nitrous Oxide Emissions from Natural Sources. U.S. Environmental Protection Agency, Washington, DC, USA.

Erwin, K. L. (2009). Wetlands and global climate change: the role of wetland restoration in a changing world. Wetlands Ecology and Management, 17, 71–84.

Fan, Y., & Miguez-Macho, G. (2011). A simple hydrologic framework for simulating wetlands in climate and earth system models. Climate Dynamics, 37(1-2), 253-278.

Faulkner, S. (2004). Urbanization impacts on the structure and function of forested wetlands. Urban Ecosystems, 7, 89–106.

Feng, K., & Molz, F. J. (1997). A 2-D, diffusion-based, wetland flow model. Journal of Hydrology, 196(1–4), 230–250.

Feng, X. Q., Zhang, G. X., & Xu, Y. J. (2013). Simulation of hydrological processes in the Zhalong wetland within a river basin, Northeast China. Hydrology and Earth System Sciences, 17, 2797–2807.

Fortin, J., Turcotte, R., Massicotte, S., Moussa, R., Fitzback, J., & Villeneuve, J. (2001). Distributed Watershed Model Compatible with Remote Sensing and GIS Data. I: Description of Model. Journal of Hydrologic Engineering, 6(2), 91–99.

Fossey, M., Rousseau, A. N., Bensalma, F., Savary, S., & Royer, A. (2015). Integrating isolated and riparian wetland modules in the PHYSITEL/HYDROTEL modelling platform: model performance and diagnosis. Hydrological Processes, 29, 4683–4702.

Freni, G., Mannina, G., & Viviani, G. (2008). Uncertainty in urban stormwater quality modelling: the effect of acceptability threshold in the GLUE methodology. Water Research, 42, 2061–2072.

Golden, H. E., Lane, C. R., Amatya, D. M., Bandilla, K. W., Raanan Kiperwas, H., Knightes, C. D., & Ssegane, H. (2014). Hydrologic connectivity between geographically isolated wetlands and surface water systems: a review of select modeling methods. Environmental Modelling & Software, 53, 190–206.

Golden, H.E., Sander, H.A., Lane, C.R., Zhao, C., Price, K., D'Amico, E., & Christensen, J.R. (2016). Relative effects of geographically isolated wetlands on streamflow: a watershed-scale analysis. Ecohydrology, 9, 21–38.

Goodrich, D. C., Unkrich, C. L., Smith, R. E., & Woolhiser, D. A. (2006). KINEROS2—New features and capabilities, paper presented at 3rd federal Interagency Hydrologic Modeling Conference, Subcomm. on Hydrol., Reno, Nev.

Green, W. H., & Ampt, G. A. (1911). Studies on soil physics, part I, the flow of air and water through soils. Journal of Agricultural Science, 4(1), 1–24.

Guardo, M., & Tomasello, R. S. (1995). Hydrodynamic simulations of a constructed wetland in south Florida. Water Resources Bulletin, 31(4), 687-701.

Hakanson, L. (2000). The role of characteristic coefficients of variation in uncertainty and sensitivity analyses, with examples related to the structuring of lake eutrophication models. Ecological Modelling, 131(1), 1–20.

Hammer, D. E., & Kadlec, R. H. (1986). A model for wetland surface water dynamics. Water Resources Research, 22, 1951–1958.

Hamon, W. R. (1961). Estimating potential evapotranspiration. Journal of Hydraulics Division, Proceedings of the American Society of Civil Engineers, 871, 107–120.

Hantush M. M., Kalin L., Isik, S., & Yucekaya, A. (2013) Nutrient Dynamics in Flooded Wetlands. I: Model Development. Journal of Hydrologic Engineering, 18(12), 1709–1723.

Hantush, M. M., Kalin, L., & Govindaraju, R. (2011). Subsurface and Surface Water Flow Interactions. Groundwater Quantity and Quality Management, 295–393.

Harter, T., & Hopmans, J. W. (2004). Role of vadose zone flow processes in regional scale hydrology: Review, opportunities and challenges in Unsaturated Zone Modeling: Progress, Applications, and Challenges, edited by R. A. Feddes, G. H. de Rooij, and J. C. van Dam, , Kluwer, Dordrecht, Netherlands, 179 –208.

Hattermann, F. F., Krysanova, V., & Hesse, C. (2008). Modelling wetland processes in regional applications. Hydrological Sciences Journal, 53(5), 1001–1012.

Hodson, E. L., Poulter, B., Zimmermann, n. e., Prigent, c., & Kaplan, J. O. (2011). The El Niño-Southern Oscillation and wetland methane interannual variability. Geophysical Research Letters, 38, L08810, doi: 10.1029/2011GL046861.

Hosseinzadeh Talaee, P., Tabari, H., & Ardakani, S. (2014). Hydrological drought in the west of Iran and possible association with large-scale atmospheric circulation patterns. Hydrological Processes, 28, 764–773.

House, A. R., Thompson, J. R., & Acreman, M. C. (2016). Projecting impacts of climate change on hydrological conditions and biotic responses in a chalk valley riparian wetland. Journal of Hydrology 534: 178–192.

http://dx.doi.org/10.1061/(ASCE)HE.1943-5584.0000750.

Huang, C-W, Lin, Y-P., Chiang L-C., & Wang, Y-C. (2014). Using CV-GLUE procedure in analysis of wetland model predictive uncertainty. Journal of Environmental Management, 140, 83–92.

Hughes, D. A., Tshimanga, R., Tirivarombo, S., & Tanner, J. (2014). Simulating wetland impacts on stream flow in Southern Africa using a monthly hydrological model. Hydrological Processes, 28, 1775–1786.

IPCC, (2001). Climate change 2001: impacts, adaptation, and vulnerability. Technical summary, and summary for policymakers. Third assessment report of working group I of the intergovernmental panel on climatic change, URL: http://www.ipcc.ch

IPCC, (2007). IPCC Fourth Assessment Report: Climate Change 2007. (Accessed on 02/18/2016)

IPCC, (2014). Climate Change 2014: Synthesis Report. Contribution of Working Groups I, II and III to the Fifth Assessment Report of the Intergovernmental Panel on Climate Change [Core Writing Team, R.K. Pachauri and L.A. Meyer (eds.)]. IPCC, Geneva, Switzerland, 151 pp.

Jalalkamali, A., Sedghi, H., & Manshouri, M. (2011). Monthly groundwater level prediction using ANN and neuro-fuzzy models: a case study on Kerman plain, Iran. Journal of Hydroinformatics, 13(4), 867–876.

Jordan, T.E., Pittek, M.A., Hofmockel, K.H., & Whigham, D.F. (2003). Nutrient and sediment removal by a restored wetland receiving agricultural runoff. Journal of Environmental Quality 32, 1534–1547.

Kaastra, I., & Boyd, M.S. (1995). Forecasting futures trading volume using neural networks. The Journal of Futures Markets, 15(8), 953–970.

Kadlec, R. H. (1990). Overland flow in wetlands: vegetation resistance. Journal of Hydraulic Engineering, 116, 691–706.

Kadlec, R. H., & Wallace, D. C. (2009). Treatment wetlands. 2nd ed., CRC Press, 893 pp.

Kadlec, R. H., Hammer, D. E., Nam, I. S., & Wilkes, J. O. (1981). The hydrology of overland flow in wetlands. Chemical Engineering Communications, 9, 331–334.

Kalin, L., Hantush, M. M., & Rezaeianzadeh, M. (2017). Chapter 87: Wetland Hydrology. Singh, Vijay, Handbook of Applied Hydrology, Second Edition, © 2017 by McGraw-Hill Education.

Kalin, L., & Hantush, M.M. (2006). Hydrologic modeling of an eastern Pennsylvania watershed with NEXRAD and rain gauge data. Journal of Hydrologic Engineering 11, 555–569.

Kalin, L., Hantush, M., Isik, S., Yucekaya, A., & Jordan, T. (2013). Nutrient dynamics in flooded wetlands. II: Model application. Journal of Hydrologic Engineering, 1724–1738.

Kang, H., I. Jang, & Kim., S. (2012). Key processes in CH4 dynamics in wetlands and possible shifts with climate change. Pages 99–114, in B. A. Middleton, editor. Global change and the function and distribution of wetlands. Springer, New York, New York, USA.

Karthikeyan, L., Kumar, N., D., Graillot, D., & Gaur, S. (2013). Prediction of ground water levels in the uplands of a tropical coastal riparian wetland using artificial neural networks. Water Resources Management, 27,871–883.

Karunanithi, N., Grenney, W.J., Whitley, D., & Bovee, K. (1994). Neural networks for river flow prediction. Journal of Computing in Civil Engineering, 8(2), 201–220.

Kazezyilmaz-Alhan, C. M., Medina Jr, M. A., & Richardson, C. J. (2007). A wetland hydrology and water quality model incorporating surface water/groundwater interactions. Water Resources Research, 43, W04434. doi:10.1029/ 2006WR005003

Konyha, K. D., Shaw, D. T., & Weiler, K. W. (1995). Hydrologic design of a wetland – advantages of continuous modeling. Ecological engineering, 4 (2), 99–116.

Krysanova, V., & Arnold, J. G. (2008). Advances in ecohydrological modelling with SWAT– a review. Hydrological Sciences Journal, 53(5), 939–947.

LaBaugh JW (1986) Wetland ecosystem studies from a hydrologic perspective. Water Resources Bulletin, 22, 1–10.

Laio, F., Tamea, S., Ridolfi, L., D'Odorico, P., & Rodriguez-Iturbe, I. (2009). Ecohydrology of groundwater-dependent ecosystems: 1. Stochastic water table dynamics. Water Resources Research, 45:W05419. http://dx.doi.org/10.1029/2008wr007292.

Leavesley, G. H., Lichty, R. W., Troutman, B. M., & Saindon, L. G. (1983). Precipitation-runoff modeling system: User's manual. United States Dept. of the Interior, Geological Survey, Denver.

Lee, S.-K., Mapes, B. E., Wang, C., Enfield, D. B., & Weaver, S. J. (2014). Springtime ENSO phase evolution and its relation to rainfall in the continental U. S., Geophysical Research Letters, 41, 1673– 1680.

Linsley, R. K., Kohler, M. A., & Paulhus, J. L. H. (1958). Hydrology for engineers. McGraw-Hill, New York.

Liu, Y., Yang, W., & Wang, X. (2008). Development of a SWAT extension module to simulate riparian wetland hydrologic processes at a watershed scale. Hydrological Processes, 22, 2901–2915.

Liu, Y., & Gupta, H.V. (2007). Uncertainty in hydrologic modeling: toward an integrated data assimilation framework. Water Resources Research, 43, W07401.

Loukas, A., & Vasiliades, L. (2014). Streamflow simulation methods for ungauged and poorly gauged watersheds. Natural Hazards and Earth System Sciences, 14, 1641–1661.

Lowe, W.H. & Likens, G.E. (2005). Moving headwater streams to the head of the class. BioScience, 55, 196–197.

Lù, A., Jia, S., Zhu, W., Yan, H., Duan, S., & Yao, Z. (2011). El Niño -Southern Oscillation and water resources in the headwaters region of theYellow River: Links and potential for forecasting. Hydrology and Earth System Sciences, 15(4), 1273–1281.

Lu, J., Sun, G., Amatya, D.M., & McNulty, S.G. (2005). A Comparison of six potential evapotranspiration methods for regional use in the southeastern United States. Journal of American Water Resources Association 41, 621–633.

Lyne, V., & Hollick, M. (1979). Stochastic time variable rainfall runoff modeling. Hydrology and water resources symposium Berth 1979, proceedings, national committee on hydrology and water resources of the institution of engineers, Australia, pp. 89-92.

Maier, H.R., & Dandy, G.C., 2000. Neural networks for the prediction and forecasting of water resource variables: a review of modelling issues and applications. Environmental Modelling and Software 15, 101-124.

Majidzadeh, H., Wang, J., & Chow, A. T. (2015). Prescribed Fire Alters Dissolved Organic Matter and Disinfection By-Product Precursors in Forested Watersheds - Part I. A Controlled Laboratory Study. Recent Advances in Disinfection By-Products, Chapter 15, pp: 271–292.

Mannina, G. (2011). Uncertainty assessment of a water quality model for Ephemeral River using GLUE analysis. Journal of Environmental Engineering, 137(3), 177–186.

Mansell, R. S., Bloom, S. A., & Sun, G. (2000). A model for wetland hydrology: description and validation. Soil Science, 165(5), 384–397.

Martin, J. F., & Reddy, K. R. (1997). Interaction and spatial distribution of wetland nitrogen processes. Ecological Modelling, 105(1), 1–21.

Masters, T. (1993). Practical Neural Network Recipes in C++. Academic Press, San Diego, CA.

MathWork, Inc. (2010). Matlab user's manual, version 7.1.1. The MathWorks, Inc.

MathWorks, (2017). Integrate a .NET Assembly into a C# Application. https://www.mathworks.com/help/compiler_sdk/dotnet/integrate-your-net-assembly-into-a-c-application.html accessed on 01/09/2017.

Maurer, E. P., Hidalgo, H. G., Das, T., Dettinger, M. D., & Cayan, D. R. (2010). The utility of daily large-scale climate data in the assessment of climate change impacts on daily streamflow in California, Hydrol. Earth Syst. Sci., 14, 1125–1138.

McBride, E. H., & Burgess, L. H. (1964). Soil survey of Baldwin County, Alabama. U.S. Department of Agriculture. Soil Conservation Service. Soil Survey Report, 12, 110.

McCuen, R. H. (2002). Modeling Hydrologic Change: Statistical Methods. CRC Press, Science, 448 pages.

McKillop, R., Kouwen, N., & Soulis, E. D. (1999). Modeling the rainfall-runoff response of a headwater wetland. Water Resources Research, 35, 1165–1177.

McLaughlin, D. L., Kaplan, D.A., & Cohen, M. J. (2014). A significant nexus: Geographically isolated wetlands influence landscape hydrology. Water Resources Research, 50, 7153–7166.

McVoy, C.W., Said, W.P., Obeysekera, J., Van Arman, J.A., & Dreschel, T. W. (2011). Landscapes and hydrology of the predrainage Everglades. University Press of Florida, Gainesville

Mearns, L.O., Giorgi, F., Shields, C., & McDaniel, L. (2003). Climate scenarios for the southeastern US based on GCM and regional modeling simulations. Climatic Change, 60, 7–36.

Messina, M. G., & Conner, W. H. (1998). Southern Forested Wetlands: Ecology and Management. Lewis Publishers: Boca Raton, FL.

Min, J., Paudel, R., & Jawitz, J. W. (2010). Spatially distributed modeling of surface water flow dynamics in the Everglades ridge and slough landscape. Journal of Hydrology, 390, 1–12.

Mitsch, W. J. (1983). Ecological models for management of freshwater wetlands, in Application of Ecological Modeling in Environmental Management, edited by S. E. Jorgensen and W. J. Mitsch, Elsevier Science, New York, pp. 283–310.

Mitsch, W. J., & Gosselink, J. G. (2000). Wetlands, 3rd Edition. Van Nostrand Reinhold, New York, John Wiley & Sons, Inc., 920 pp.

Mitsch, W. J., & Gosselink, J. G. (2015). Wetlands, E-book, accessed 16 November 2015, <http://auburn.eblib.com/patron/FullRecord.aspx?p=1895927>.

Mo, K. C., & Schemm, J. E. (2008). Relationship between ENSO and drought over the Southeastern United States. Geophys Res Lett 35:L15701

Moffett, K. B., Gorelick, S. M., McLaren, R. G., & Sudicky, E. A. (2012). Salt marsh ecohydrological zonation due to heterogeneous vegetation – groundwater –surface water interactions. Water Resources Research, 48, W02516. http://dx.doi.org/10.1029/2011WR010874.

Mohanty, S., Jha, M. K., Kumar, A., & Panda, D. K. (2013). Comparative evaluation of numerical model and artificial neural network for simulating groundwater flow in Kathajodi–Surua Inter-basin of Odisha, India. Journal of Hydrology, 495, 38–51.

Mohanty, S., Jha, M. K., Kumar, A., & Sudheer, K. P. (2010). Artificial neural network modeling for groundwater level forecasting in a river island of eastern India. Water Resources Management, 24, 1845–1865.

MSDN, (2015). Microsoft Developer Network: Introduction to the C# Language and the .NET Framework. ⟨https://msdn.microsoft.com/en-us/library/z1zx9t92.aspx⟩ (Accessed on October. 19, 2015).

MSDN, (2017). Microsoft Developer Network: Type Safety and Security, .NET Framework. ⟨https://msdn.microsoft.com/en-us/library/hbzz1a9a(v=vs.110).aspx⟩ (Accessed on May. 29, 2017)

Nash, J. E., & Sutcliffe, J. V. (1970). River flow forecasting through conceptual models,1, A discussion of principles. Journal of Hydrology, 10, 282–290.

Nathan, R. J., & McMahon, T. A. (1990). Evaluation of automated techniques for baseflow and recession analysis. Water Resources Research, 26(7), 1465-1473.

Nayak, P. C., Satyaji Rao, Y. R., & Sudheer, K. P. (2006). Groundwater level forecasting in a shallow aquifer using artificial neural network approach. Water Resources Management, 20, 77–90.

Neitsch, S. L., Arnold, J. G., Kiniry, J. R., & Williams, J. R. (2011). Soil and water assessment tool: theoretical documentation, version 2009. Grassland, Soil and Water Research Laboratory-Agricultural Research Service, Blackland Research Center, Texas AgriLife Research, 647 pp.

Neitsch, S. L., Arnold, J. G., Kiniry, J. R., Williams, J. R., & King, K. W. (2005). Soil and water assessment tool: theoretical documentation. Grassland. Soil and Water Research Laboratory, Temple, TX.

Nilsson, K.A., Rains, M.C., Lewis, D.B., & Trout, K.E. (2013). Hydrologic characterization of 56 geographically isolated wetlands in west-central Florida using a probabilistic method. Wetlands Ecology and Management, 21, 1–14.

Niswonger, R.G., Prudic, D.E., & Regan, R.S. (2006). Documentation of the Unsaturated-Zone Flow (UZF1) Package for modeling unsaturated flow between the land surface and the water table with MODFLOW-2005: U.S. Geological Survey Techniques and Methods 6-A19, 62 p.

Noble, C. V., Wakeley, J. S., Roberts, T. H., & Henderson, C. (2007). Regional guidebook for applying the hydrogeomorphic approach to assessing the functions of headwater slope wetlands on the Mississippi and Alabama coastal plains. U.S. Army Corps of Engineers.

Noori, N., & Kalin, L. (2016). Coupling SWAT and ANN Models for Enhanced Daily Streamflow Prediction. Journal of Hydrology, 533, 141–151.

Nott, D. J., L. Marshall, & Brown, J. (2012). Generalized likelihood uncer-tainty estimation (GLUE) and approximate Bayesian computation: What's the connection? Water Resources Research, 48, W12602, doi:10.1029/2011WR011128.

Nourani, V., & Mano, A. (2007). Semi-distributed flood runoff model at the sub continental scale for southwestern Iran. Hydrological Processes, 21, 3173–3180.

Nourani, V., Mogaddam, A. A., & Nadiri, A. O. (2008). An ANN-based model for spatiotemporal groundwater level forecasting." Hydrological Processes, 22, 5054–66.

Nungesser, M., Saunders, C., Coronado-Molina, C., Obeysekera, J., Johnson, J., McVoy, C., & Benscoter, B. (2015). Potential effects of climate change on Florida's Everglades. Environmental Management, 55(4), 824–835.

Ogden, F. L., Lai, W., Steinke, R. C., Zhu, J., Talbot, C. A., & Wilson, J. L. (2015). A new general 1-D vadose zone flow solution method. Water Resources Research, 51, 4282–4300, doi: 10.1002/2015WR017126.

Olivera, F., M. Valenzuela, & Srinivasan, R. (2004). ArcGIS-SWAT: A GIS interface for the soil and water assessment tool (SWAT). ASCE World Water & Environmental Resources Congress 2004, June 27-July 1, Salt Lake City, U.T, 9 pages.

Olivera, F., Valenzuela, M., & Srinivasan, R. (2004). ArcGIS-SWAT: A GIS Interface for the Soil and Water Assessment Tool (SWAT). Critical Transitions in Water and Environmental Resources Management, 1–9.

Pandey, S. et al. (2017) Enhanced methane emissions from tropical wetlands during the 2011 La Niña. Scientific Reports, 7, 45759.

Paul, S., Jusel, K., & Alewell, C. (2006). Reduction processes in forest wetlands: tracking down heterogeneity of source/link functions with a combination of methods. Soil Biology and Biochemistry, 38, 1028–1039.

Rains, M. C., Leibowitz, S. G., Cohen, M. J., Creed, I. F., Golden, H. E., Jawitz, J. W., Kalla, P., Lane, C. R., Lang, M. W., McLaughlin, D. L. (2016). Geographically isolated wetlands are part of the hydrological landscape. Hydrological Processes, 30, 153–160

Rayburg, S., & Thoms, M. (2009). A coupled hydraulic–hydrologic modelling approach to deriving a water balance model for a complex floodplain wetland system. Hydrology Research 40(4), 364–379.

Reckhow, K., & Qian, S. (1994). Modeling phosphorus trapping in wetlands using generalized additive-models. Water Resources Research, 30(11), 3105–3114.

Reclamation, (2013). 'Downscaled CMIP3 and CMIP5 Climate and Hydrology Projections: Release of Downscaled CMIP5 Climate Projections, Comparison with preceding Information, and Summary of User Needs', prepared by the U.S. Department of the Interior, Bureau of Reclamation, Technical Services Center, Denver, Colorado. 47pp.

Records, R. M., Arabi, M., Fassnacht, S. R., Duffy, W. G., Ahmadi, M., & Hegewisch K. C. (2014). Climate change and wetland loss impacts on a western river's water quality. Hydrology and Earth System Sciences, 18, 4509–4527.

Reddy, K.R., & DeLaune, R.D. (2008). Biogeochemistry of wetlands: science and applications, 1 ed. CRC Press, Taylor & Francis Group, Boca Raton, FL

Renard, B., Kavetski, D., Kuczera, G., Thyer, M. & Franks, S. W. (2010). Understanding predictive uncertainty in hydrologic modeling: The challenge of identifying input and structural errors. Water Resources Research, 46, W05521, doi:10.1029/2009WR008328.

Restrepo, J. I., Montoya, A. M., & Obeysekera, J. (1998). A wetland simulation module for the MODFLOW ground water model. Groundwater, 36(5), 764–770.

Rezaeian Zadeh, M., Amin, S., Khalili, D., & Singh, V. P. (2010). Daily outflow prediction by multi layer perceptron with logistic sigmoid and tangent sigmoid activation functions. Water Resources Management, 24(11), 2673–2688.

Rezaeianzadeh, M., Kalin, L., & Anderson, C. (2015). Wetland Water-Level Prediction Using ANN in Conjunction with Base-Flow Recession Analysis. Journal of Hydrologic Engineering, 10.1061/(ASCE)HE.1943-5584.0001276 , D4015003.

Rezaeian-Zadeh, M., Zand-Parsa, S., Abghari, H., Zolghadr, M., & Singh, V.P. (2012). Hourly air temperature driven using multi-layer perceptron and radial basis function networks in arid and semi-arid regions. Theoretical and Applied Climatology, 109(3–4), 519–28.

Richards, L. A. (1931). Capillary conduction of liquids through porous mediums. Journal of Applied Physics, 1, 318–333.

Sahoo, S., & Jha, M. K. (2013). Groundwater-level prediction using multiple linear regression and artificial neural network techniques: a comparative assessment. Hydrogeology Journal, 21, 1865–1887.

Said, A., Ross, M., Trout, K., & Zhang, J. (2007). Simulation of surface water for un-gauged areas with storage-attenuation wetlands. Journal of the American Water Resources Association, 43(2), 546–556.

Sarhadi, A., & Soltani, S. (2013). Determination of water requirements of the Gavkhuni wetland, Iran: A hydrological approach. Journal of Arid Environments, 98, 27–40.

Savage, R., & Baker, V. (2007). The importance of headwater wetlands and water quality in North Carolina. ⟨http://water.epa.gov/type/wetlands/assessment/survey/presentations.cfm⟩ (Jan. 10, 2015).

Şen, Z. (2012). Innovative Trend Analysis Methodology. Journal of Hydrologic Engineering, 17(9), 1042–1046.

Shamsi, U. M. (2005). GIS Applications for Water, Wastewater, and Stormwater Systems. CRC Press, Boca Raton, FL, USA.

Sharda, V., Srivastava, P., Ingram, K., Chelliah, M., & Kalin, L., (2012). Quantification of El Niño Southern Oscillation (ENSO) impact on precipitation and stream flows for improved management of water resources in Alabama. Journal of Soil and Water Conservation, 67(3), 158–172.

Sharifi, A. (2013). Development and application of WetQual-C, a mechanistic model for simulating carbon dynamics, GHG gas emissions and carbon export from wetlands. (PhD Dissertation), Auburn University.

Sharifi, A., Hantush,M., & Kalin, L. (2017). Modeling nitrogen and carbon dynamics in wetland soils and water using a mechanistic wetland model. J. Hydrol. Eng., 10.1061/(ASCE)HE.1943-5584.0001441, D4016002.

Shen, Z. Y., Chen, L., & Chen, T. (2012). Analysis of parameter uncertainty in hydrological and sediment modeling using GLUE method: a case study of SWAT model applied to Three Gorges Reservoir Region, China. Hydrology and Earth System Sciences, 16, 121–32.

Shiri, J., & Kisi, O. (2011). Comparison of genetic programming with neuro-fuzzy systems for predicting short-term water table depth fluctuations. Computers & Geosciences, 37(10), 1692–1701.

Shiri, J., Kisi, O., Yoon, H., Lee, K. K., & Nazemi, A. H. (2013). Predicting groundwater level fluctuations with meteorological effect implications—a comparative study among soft computing techniques. Computers & Geosciences, 56, 32–44.

Shirmohammadi, B., Vafakhah, M., Moosavi, V., & Moghaddamnia, A. (2013). Application of several data-driven techniques for predicting groundwater level. Water Resources Management, 27(2), 419–432.

Siade, A., Nishikawa, T., & Martin, P., (2015). Natural recharge estimation and uncertainty analysis of an adjudicated groundwater basin using a regional-scale flow and subsidence model (Antelope Valley, California, USA). Hydrogeology Journal, 23, 1267–1291.

Šimůnek, J., Šejna, M., Saito, H., Sakai, M. & van Genuchten, M. Th. (2013). The HYDRUS-1D Software Package for Simulating the Movement of Water, Heat, and Multiple Solutes in Variably Saturated Media, Version 4.17, HYDRUS Software Series 3, Department of Environmental Sciences, University of California Riverside, Riverside, California, USA, pp. 343.

Singh, S., Srivastava, P., Abebe, A., & Mitra, S. (2015). Baseflow response to climate variability induced droughts in the Apalachicola–Chattahoochee–Flint River Basin, U.S.A. Journal of Hydrology, 528, 550–561.

Skaggs, R.W. (1978). A Water Management Model for Shallow Water Table Soils. Report No. 134. Water Res. Res. Inst. of The Univ. of North Carolina, NC State Univ., Raleigh, NC.

Solomatine, D., See, L. M., & Abrahart, R. J. (2008). Data-Driven Modelling: Concepts, Approaches and Experiences." Chap. 2 in Practical Hydroinformatics. In: Abrahart Robert J, See LindaM, Solomatine Dimitri P, editors. Springer Berlin Heidelberg: Water Science and Technology Library, 17–30.

Spieksma, J. F. M., & Schouwenaars, J. M. (1997). A simple procedure to model water level fluctuations in partially inundated wetlands. Journal of Hydrology, 196, 324–335.

Sutcliffe, A. (1989). Human-computer Interface Design. New York: Springer-Verlag.

Tamea, S., Laio, F., Ridolfi, L., D'Odorico, P., & Rodriguez-Iturbe, I. (2009). Ecohydrology of groundwater-dependent ecosystems: 2. stochastic soil moisture dynamics. Water Resources Research, 45:W05420. http://dx.doi.org/10.1029/2008wr007293.

Tamea, S., Muneepeerakul, R., Laio, F., Ridolfi, L., & Rodriguez-Iturbe, I. (2010). Stochastic description of water table fluctuations in wetlands. Geophysical Research Letters, 37, L06403. DOI: 10.1029/ 2009GL041633.

Taormina, R., wing Chau, K., & Sethi, R. (2012). Artificial neural network simulation of hourly groundwater levels in a coastal aquifer system of the Venice Lagoon. Engineering Applications of Artificial Intelligence, 25, 1670–1676.

Tebaldi, C., Smith, R. L., Nychka, D., & Mearns, L. O. (2005). Quantifying uncertainty in projections of regional climate change: a Bayesian approach to the analysis of multimodel ensembles. Journal of Climate, 18(10), 1524–1540.

Tetra Tech,. (2006). Development of Second-generation of Mercury Watershed Simulation Technology: Grid-based Mercury Model Version 2.0, User's Manual (Fairfax, Virginia).

Thompson, J. R., Sorenson, H. R., Gavin, H., & Refsgaard, A. (2004). Application of the coupled MIKE SHE/MIKE 11 modelling system to a lowland wet grassland in southeast England. Journal of Hydrology, 293, 151–179.

Thrasher, B., Maurer, E. P., McKellar, C., & Duffy, P. B. (2012). Technical Note: Bias correcting climate model simulated daily temperature extremes with quantile mapping. Hydrology and Earth System Sciences, 16, 3309–3314.

Tim, U.S. (1995). Emerging technologies for hydrologic and water quality modeling research. Trans. ASAE, 39(2), 465–476.

Todd, M.J., Muneepeerakul, R., Miralles-Wilhelm, F., Rinaldo, A., & Rodriguez-Iturbe, I. (2012). Possible climate change impacts on the hydrological and vegetative character of Everglades National Park, Florida. Ecohydrology, 5, 326–336.

van Dam, A. A., Dardona, A., Kelderman, P., & Kansiime, F. (2007). A simulation model for nitrogen retention in a papyrus wetland near Lake Victoria, Uganda (East Africa). Wetlands Ecology and Management, 15(6), 469–480.

van Dam, J.C., & Feddes, R.A. (2000). Numerical simulation of infiltration, evaporation and shallow groundwater levels with the Richards equation. Journal of Hydrology, 233, 72–85.

van der Valk, A., Volin, J., & Wetzel, P. (2015). Predicted changes in interannual water-level fluctuations due to climate change and its implications for the vegetation of the Florida Everglades. Environmental Management, 55(4), 799–806.

Villa, J. A., & Tobon, C. (2012). Modeling hydrologic dynamics of a created wetland, Colombia. Ecological Engineering, 40, 173–182.

Vogel, T., Huang, K., Zhang, R., & van Genuchten, M. Th. (1996). The HYDRUS code for simulating one-dimensional water flow, solute transport, and heat movement in variably-saturated media, Version 5.0, Research Report No 140, U.S. Salinity Laboratory, USDA, ARS, Riverside, CA.

Wagener, T., Lees, M. J., & Wheater, H. S. (2001). Monte-Carlo analysis toolbox user manual. Tech. Rep., Civil and Environmental Engineering Department, Imperial College of Science Technology and Medicine.

Walton, R., Chapman, R.S., & Davis, J.E. (1996). Development and application of the wetlands dynamic water budget model. Wetlands, 16, 347–357.

Wang, X. X., Shang, S. Y., Qu, Z. Y., Liu, T. X., Melesse, A. M., & Yang, W. H. (2010). Simulated wetland conservation-restoration effects on water quantity and quality at watershed scale. Journal of Environmental Management, 91(7), 1511–1525.

Weigend, A.S., Rumelhart, D.E., & Huberman, B.A. (1990). Predicting the future: A connectionist approach. International Journal of Neural Systems 1(3), 193–209.

Weinmann, P. E., & Laurenson, E. M. (1979). Approximate flood routing methods: a review. ASCE Proceedings. Journal of the Hydraulics Division, 105 (HY-12), 1521–1536.

Wilsnack, M. M., Welter, D. E., Montoya, A. M., Restrepo, J. I., & Obeysekera, J. (2001). Simulating flow in regional wetlands with the MODFLOW wetlands package. Journal of the American Water Resources Association, 37(3), 655–674.

Yoon, H., Jun, S. C., Hyun, Y., Bae, G., & Lee, K. K. (2011). A comparative study of artificial neural networks and support vector machines for predicting groundwater levels in costal aquifers. Journal of Hydrology, 396, 128–138.

Yuan, D., Lin, B., & Falconer, R. (2008). Simulating moving boundary using a linked groundwater and surface water model. Journal of Hydrology, 349(3–4), 524–535.

Zhang, J., Ross, M., Trout, K., & Zhou, D. (2009). Calibration of the HSPF model with a new coupled FTABLE generation method. Progress in Natural Science, 19, 1747–55.

Zhang, L., & Mitsch, W. (2005). Modelling hydrological processes in created freshwater wetlands: an integrated system approach. Environmental Modelling & Software, 20(7), 935–946.

Zhang, W., Li, T., & Dai, M. (2015). Uncertainty assessment of water quality modeling for a small-scale urban catchment using the GLUE methodology: a case study in Shanghai, China. Environmental Science and Pollution Research, 22(12), 9241–9249.

Zheng, Y., & Keller, A. A. (2007). Uncertainty assessment in watershed-scale water quality modeling and management: 1. Framework and application of generalized likelihood uncertainty estimation (GLUE) approach. Water Resources Research., 43, W08407, doi:10.1029/2006wr005345.

Zhu, Y., Shi, L., & Lin, L., Yang, J., Ye, M. (2012). A fully coupled numerical modeling for regional unsaturated-saturated water flow. Journal of Hydrology, 475, 188–203.